

Doctoral Dissertation

博士論文

**The nature of dark matter probed by  
strong gravitational lensing**

(強重力レンズ効果で探る暗黒物質の性質)

A Dissertation Submitted for the Degree of Doctor of Philosophy  
December, 2024

令和6年12月博士(理学)申請

Department of Physics, Graduate School of Science,  
The University of Tokyo

東京大学大学院 理学系研究科 物理学専攻

Hiroki Kawai

河合 宏紀



# Abstract

Dark matter is one of the major components of the universe and plays a crucial role in the history of structure formation. Although the existence of dark matter was first proposed over ninety years ago, its nature remains unknown. Observational cosmology, which combines theoretical studies of the universe with telescope-based observations, provides an effective approach to investigating the nature of dark matter. The standard model of the universe, which assumes that dark matter is cold and interacts with baryons and itself only through gravity (so-called cold dark matter, or CDM), successfully explains a wide range of observations. However, notable discrepancies exist between theoretical predictions and observations on small scales, indicating that the CDM assumption might be revised. Since the properties of dark matter have a direct impact on small-scale structures, studying these scales is crucial for understanding its nature.

One of the most effective methods for studying small-scale structures is gravitational lensing, a phenomenon in which light from background sources, such as galaxies and stars, is bent by foreground lens objects, such as galaxies and galaxy clusters. In particular, we focus on strong gravitational lensing, where multiple images are produced, accompanied by significant magnification. Strong gravitational lensing occurs near a characteristic line in the lens plane called a critical curve, where the magnification mathematically diverges to infinity. The corresponding line in the source plane is referred to as the caustic. When a background source lies near the caustics, highly magnified images are observed near the critical curves. Because mass distribution within the lens objects influences these critical curves and caustics, it is essential to understand how small-scale mass distributions affect their shape and configuration.

In this thesis, we first investigate the effect of microlenses near the macro-critical curve of a galaxy cluster, which generate micro-critical curves, on the observed number of highly magnified individual stars. We derive an analytic model for the high-magnification tail of the probability distribution function (PDF). Our model predicts that the probability is proportional to the independent number of micro-critical curves, showing excellent agreement with simulations that solve the lens equation. Using this analytic model, we constrain the parameter space of microlenses based on the observed number of Icarus-like events. Icarus is an individual star observed near the macro-critical curve of the MACS J1149 cluster, with a magnification factor estimated to be on the order of thousands. Finally, we consider primordial black holes (PBHs), one of the alternative candidates for CDM, as microlenses and constrain their mass and mass fraction, showing that a scenario with  $f_{\text{PBH}} \gtrsim 0.2$  with a mass around  $1 M_{\odot}$  cannot account for the observed number of Icarus-like events and is therefore excluded.

Second, we investigate how substructures, such as subhalos, perturb the shape of the macro-critical curve of a galaxy cluster. Perturbations to the macro-critical curve break the symmetry of the observed images, providing a potential method to infer the properties of substructures. A recent example of such perturbations is the observation of

Mothra, where an astrometric shift in the macro-critical curve might be indicated. We obtain the general analytic formula that connects the fluctuation of macro-critical curves with the fluctuation of the surface density caused by substructures. As an application of the analytic model, we first assess whether CDM subhalos can account for the observed location of Mothra. We find that this location can be explained if the maximum subhalo mass is approximately  $10^9 M_\odot/h$ . Next, we consider the fuzzy dark matter (FDM) model, a viable alternative candidate for CDM, which predicts the existence of granular structures within halos and subhalos. Our analysis shows that a particle mass of  $m \lesssim 10^{-24} \text{ eV}/c^2$  is required to explain the observed location of Mothra.

Finally, we numerically and analytically investigate the galaxy-galaxy strong lensing (GGSL) cross-section in galaxy clusters with the FDM model. The GGSL cross-section is defined as the total area covered by secondary caustics, which are generated by substructures. Observationally, the cross-section is reported to be an order of magnitude larger than what is predicted by the CDM model. Our findings show that FDM subhalos can produce larger cross-sections than CDM subhalos, primarily due to the soliton core, a distinctive structure at the center of FDM subhalos. The cross-section reaches its maximum when the soliton core radius aligns with the size of the critical curve. However, the peak ratio of cross-sections between FDM and CDM subhalos is approximately two when the baryonic distribution is included, suggesting that the FDM model, irrespective of the particle mass, may struggle to account for the observed GGSL cross-section.

With recent developments in observational capabilities, the observed number of strong gravitational lensing events is expected to increase significantly. Therefore, our studies presented in this thesis are particularly important, as they provide a crucial foundation for constraining small-scale mass distributions and uncovering the nature of dark matter through future observations.

# Contents

<b>1</b>	<b>Introduction</b>	<b>1</b>
<b>2</b>	<b>Standard model of the universe and small-scale problems</b>	<b>5</b>
2.1	Standard model of the universe . . . . .	6
2.1.1	Cold dark matter . . . . .	6
2.1.2	Large-scale structure . . . . .	7
2.1.3	Dark matter halo . . . . .	8
2.1.4	Baryon distribution . . . . .	12
2.2	Small-scale problems . . . . .	12
2.2.1	Core-cusp problem . . . . .	12
2.2.2	Missing satellite problem . . . . .	13
2.2.3	Diversity problem . . . . .	13
2.2.4	Too-big-to-fail problem . . . . .	13
2.3	Possible solutions . . . . .	14
2.3.1	Baryon physics . . . . .	14
2.3.2	Alternative dark matter models . . . . .	15
<b>3</b>	<b>Fuzzy dark matter</b>	<b>23</b>
3.1	Schrödinger-Poisson equation . . . . .	23
3.2	Linear structure formation . . . . .	27
3.3	FDM halo . . . . .	29
3.3.1	Soliton core . . . . .	29
3.3.2	Granular structures . . . . .	30
3.4	Core-halo mass relation . . . . .	33
3.4.1	Previous studies on the CHMR . . . . .	35
3.4.2	Modeling the CHMR . . . . .	36
3.4.3	Results . . . . .	38
3.4.4	Analysis in the Relaxation model . . . . .	39
3.4.5	Comparison of the degree of scatter . . . . .	50
3.4.6	Total density profile . . . . .	54
3.5	Subhalo distribution . . . . .	54
3.6	Sub-galactic matter power spectrum . . . . .	57
3.7	Previous constraints on the FDM mass . . . . .	59
<b>4</b>	<b>Strong gravitational lensing</b>	<b>63</b>
4.1	Lens equation . . . . .	64
4.2	Image distortion and magnification . . . . .	69
4.3	Critical curve and caustic . . . . .	71
4.4	Multiple images . . . . .	73

4.5	Magnification near critical curve and caustic . . . . .	74
4.6	Spherically symmetric lens . . . . .	77
4.6.1	Point mass lens . . . . .	79
4.6.2	Singular isothermal sphere . . . . .	80
4.7	Microlens in a smooth mass distribution . . . . .	81
4.8	Randomly distributed microlenses in a smooth mass distribution . . . . .	82
<b>5</b>	<b>The ultra-high magnification events due to microlenses</b>	<b>87</b>
5.1	Introduction . . . . .	87
5.2	High-magnification tail of probability distribution function . . . . .	89
5.3	Comparison with simulations . . . . .	93
5.3.1	Point source . . . . .	94
5.3.2	Finite source size . . . . .	97
5.4	Total probability distribution function . . . . .	99
5.5	Application to Icarus-like system . . . . .	100
5.5.1	MACS J1149 cluster and Icarus . . . . .	101
5.5.2	Location of highly magnified events . . . . .	105
5.5.3	The number of Icarus-like events . . . . .	106
5.5.4	Constraint on the PBH . . . . .	110
5.6	Summary and discussions . . . . .	111
<b>6</b>	<b>Perturbation of macro-critical curves by substructures</b>	<b>117</b>
6.1	Introduction . . . . .	117
6.2	Fluctuations of macro-critical curves . . . . .	118
6.3	Application to Mothra . . . . .	120
6.3.1	CDM subhalos . . . . .	122
6.3.2	Granular structures in FDM halos . . . . .	124
6.4	Summary and discussions . . . . .	127
<b>7</b>	<b>Galaxy-galaxy strong lensing cross-section with FDM model</b>	<b>129</b>
7.1	Introduction . . . . .	129
7.2	GGSL cross-section with FDM subhalos . . . . .	130
7.2.1	Single FDM subhalo . . . . .	131
7.2.2	Total GGSL cross-section . . . . .	134
7.3	Effects of baryons . . . . .	135
7.4	Summary and discussions . . . . .	137
<b>8</b>	<b>Conclusions</b>	<b>141</b>
	<b>Acknowledgement</b>	<b>143</b>

# List of Figures

1.1	Schematic illustration of dark matter experiments, including collider experiments, direct detection, and indirect detection. . . . .	2
2.1	Consistency of the linear matter power spectrum at redshift $z = 0$ with $\Lambda$ CDM model predictions. . . . .	9
2.2	The previous constraints on the PBH mass and mass fraction of PBH to the total dark matter. . . . .	22
3.1	The slice of the density profile of the FDM simulation at redshift $z = 0.1$ . .	30
3.2	The concentration-halo mass relation in CDM and FDM halos at redshift $z = 0$ . . . . .	34
3.3	The CHMR with the Jeans model at redshift $z = 0$ . . . . .	39
3.4	The CHMR with the Relaxation model at redshift $z = 0$ . . . . .	40
3.5	The CHMR with the Jeans model at redshift $z = 3$ . . . . .	41
3.6	The CHMR with the Relaxation model at redshift $z = 3$ . . . . .	42
3.7	The mass matching condition to determine the soliton core profile. . . . .	45
3.8	Semi-analytic expression of the CHMR with the Relaxation model at redshift $z = 0$ . . . . .	47
3.9	The FDM mass dependence of the Relaxation model. . . . .	49
3.10	The redshift dependence of the Relaxation model. . . . .	51
3.11	Semi-analytic expression of the CHMR with the Relaxation model at redshift $z = 3$ . . . . .	52
3.12	The probability distribution of the core mass with ten different halo masses at redshift $z = 3$ using the public code provided by Taruya and Saga 2022. . . . .	53
3.13	The probability distribution of the core mass with ten different halo mass bins at redshift $z = 3$ obtained from the FDM simulation. . . . .	54
3.14	The comparison of $1\sigma$ scatters of the core mass at redshift $z = 3$ . . . . .	55
3.15	The total density profile of the FDM halos with different FDM masses. . .	56
3.16	The projected subhalo mass functions within a FDM halo with different FDM masses. . . . .	57
3.17	The projected sub-galactic matter power spectrum in a FDM halo with different FDM masses. . . . .	60
3.18	The summary of the previous constraints on FDM mass. . . . .	61
4.1	Schematic illustration of gravitational lensing system under the thin lens approximation. . . . .	69
4.2	Schematic illustration of the gravitational lensing effects. . . . .	70
4.3	The caustics and critical curves, and the locations for multiple images for an elliptical lens. . . . .	73

4.4	The average magnification and its variance as a function of the distance from the caustic in the presence of multiple microlenses within a background smooth mass distribution. . . . .	86
5.1	The ultrahigh magnified individual star Icarus within the background spiral galaxy observed near the critical curve of the MACS J1149 galaxy cluster. . . . .	88
5.2	Rayleigh distribution of the nearest inter-microlens distance and the independent number of microlenses. . . . .	92
5.3	Comparison of the integrated probability distribution function regarding the high-magnification tail between the analytic model and the simulation data. . . . .	96
5.4	The suppression of the PDF from GERLUMPH data and fitting with the sigmoid function. . . . .	98
5.5	The total PDF of the magnification at $\theta = 0.039$ arcsec away from the macro-critical curve in the Icarus-like system. . . . .	100
5.6	The spectral energy distributions of Icarus, measured during the HFF project and during its peak magnification in May 2016 with a rescaling of the excess flux density. . . . .	103
5.7	The observed fluxes of Icarus from 2004 to 2017 and the best-matching simulated light curves. . . . .	104
5.8	The probability of the total magnification exceeding the observational threshold $\mu_{\text{obsth}}$ as a function of the distance from the macro-critical curve in the Icarus-like system. . . . .	107
5.9	Decomposition of the probability that total magnification exceeds the threshold into the contribution from the middle and the high magnification tail of the PDF. . . . .	108
5.10	The expected number of the observed Icarus-like ultrahigh magnification events as a function of distance from the macro-critical curve for different maximum source radii. . . . .	110
5.11	The expected number of the observed Icarus-like ultrahigh magnification events as a function of distance from the macro-critical curve for different mass fractions of microlenses. . . . .	111
5.12	The expected number of the observed Icarus-like ultrahigh magnification events as a function of distance from the macro-critical curve for different microlens masses. . . . .	112
5.13	Constraints on the microlens parameters derived from the observed number of high-magnification events in the Icarus-like system. . . . .	113
5.14	Constraints on the PBH parameters derived from the observed number of high-magnification events in the Icarus-like system during the two-year HST observation period. . . . .	114
6.1	Color image of the ultrahigh magnified binary stars Mothra and its surroundings. . . . .	121
6.2	Contours of fluctuations of the macro-critical curve for different minimum and maximum CDM subhalo masses. . . . .	123
6.3	The correlation between $\delta\theta_1$ and the magnification ratio between $c$ and $c'$ . . . . .	124
6.4	The FDM mass dependence of the fluctuation of the macro-critical curve in the Mothra-like system. . . . .	126

7.1	Discrepancy of the galaxy-galaxy strong lensing probability in galaxy clusters between the observational results and the $\Lambda$ CDM predictions. . . . .	131
7.2	Convergence maps and secondary-critical curves around subhalo positions in the CDM model and the FDM model with different FDM masses. . . . .	132
7.3	The GGSL cross-section of a single FDM subhalo in a galaxy cluster as a function of the FDM mass. . . . .	133
7.4	The ratio of the total GGSL cross-sections of the CDM and FDM subhalos as a function of the FDM mass. . . . .	136
7.5	Convergence maps and secondary-critical curves around subhalo positions in the CDM model and the FDM model with different FDM masses, including baryon distribution. . . . .	137
7.6	The GGSL cross-section of a single FDM subhalo in a galaxy cluster as a function of the FDM mass, including baryon distribution. . . . .	138
7.7	The ratio of the total GGSL cross-sections of the CDM and FDM subhalos as a function of the FDM mass, including baryon distribution. . . . .	139



# List of Tables

5.1	The simulation setups of CCTRAIN and the number of realizations. . . . .	94
5.2	The realizations of GERLUMPH used in Chap. 5. . . . .	95



# Chapter 1

## Introduction

The concept of dark matter has played a crucial role in shaping our understanding of the structure of the universe and its evolution. In the early twentieth century, the notion of unseen mass arose from discrepancies between observed and predicted motions of celestial objects. In 1933, Fritz Zwicky coined the term "dark matter" while studying the Coma Cluster, where the visible galaxies accounted for only a fraction of the gravitational forces inferred from their velocities [1, 2]. Decades later, in 1970, Vera Rubin and Kent Ford provided compelling evidence for dark matter by measuring the rotational velocities of the stars in the Andromeda galaxy, showing that stars at the outer edges of spiral galaxies move much faster than expected based on luminous matter alone [3]. In the same year, Ken Freeman also indicated the existence of the missing matter by measuring the rotation curve of spiral galaxies such as NGC300 and M33 [4]. These early findings laid the foundation for the modern understanding of dark matter as a fundamental yet enigmatic component of the universe, constituting approximately 27% of the total energy density in the universe [5]. Despite significant observational and theoretical advances, the true nature of dark matter remains one of the most profound open questions in physics.

The mystery of dark matter has driven a broad spectrum of research, developing five major experimental and theoretical approaches: particle physics, accelerator-based experiments, direct detection, indirect detection, and observational cosmology. Particle physics provides the theoretical foundation for dark matter, proposing candidates such as weakly interacting massive particles (WIMPs), axions, and sterile neutrinos. These models, rooted in extensions to the Standard Model such as supersymmetry, predict specific properties such as mass, interaction strength, and decay channels, guiding experimental searches [6, 7]. Accelerator experiments, such as those conducted at the Large Hadron Collider (LHC), test the predictions of various theories of particle physics through high-energy collisions. Since dark matter is expected to have negligible interaction with Standard Model particles, it would pass through detectors without being directly observed. By searching for missing energy signatures, experiments offer a pathway to uncovering the nature of dark matter [8, 9]. Direct detection experiments are designed to observe rare interactions between dark matter particles and atomic nuclei in ultra-sensitive detectors. These detectors, typically located deep underground to minimize background noise, rely on technologies like liquid xenon and cryogenic scintillators to detect minute energy deposits or ionization signals. Leading experiments such as XENONnT, LUX-ZEPLIN, and PANDA-X have set increasingly stringent limits on dark matter interaction cross-sections [10, 11, 12]. In contrast, indirect detection focuses on observing secondary particles, such as gamma rays, neutrinos, or positrons, that may result from dark matter annihilation

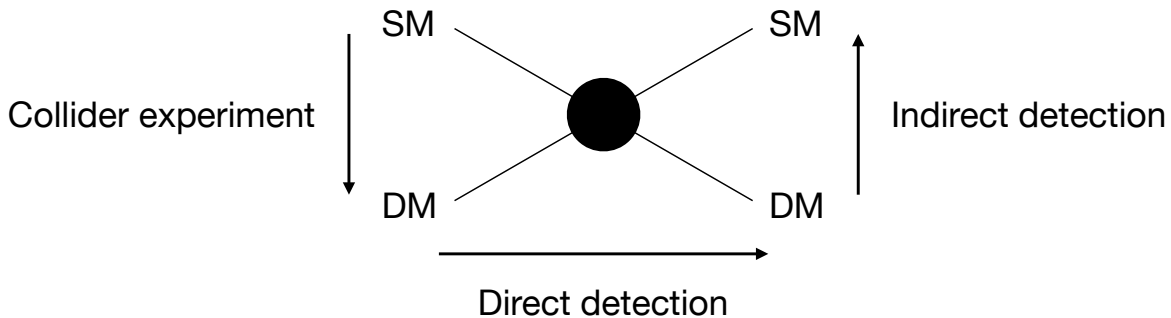


Figure 1.1: Schematic illustration of dark matter experiments, including collider experiments, direct detections, and indirect detections.

or decay in astrophysical environments. Observatories like the Fermi Gamma-ray Space Telescope and neutrino detectors such as IceCube and Super-Kamiokande have searched for these signatures in regions of high dark matter density, including the Galactic Center and dwarf spheroidal galaxies [13, 14, 15]. Figure 1.1 shows the schematic diagram of these experiments searching for dark matter. Each method addresses a unique aspect of dark matter, contributing to a comprehensive framework for understanding one of the universe’s most profound mysteries.

Observational cosmology provides a complementary avenue for studying dark matter by examining its effects on the structures of the universe. The standard model of the universe, known as the  $\Lambda$  Cold Dark Matter ( $\Lambda$ CDM) model, posits that dark matter is cold, i.e., non-relativistic, and interacts with both baryons and itself primarily through gravity. The WIMP, which is favored for existence in particle theory models, is considered to be a concrete dark matter model of the CDM. The standard model successfully explains a wide range of observational data. For instance, the anisotropies in the cosmic microwave background (CMB), as measured by observations such as Wilkinson Microwave Anisotropy Probe (WMAP) and Planck, align remarkably well with  $\Lambda$ CDM predictions [16, 5]. Similarly, the large-scale structure of the universe, as mapped by galaxy surveys such as Sloan Digital Sky Survey (SDSS) and Dark Energy Survey (DES), shows a hierarchical clustering pattern that matches simulations incorporating CDM [17, 18, 19, 20]. While these observational successes provide strong support for the  $\Lambda$ CDM model, there are some anomalies on a small scale, known as small-scale problems [21]. Some of the examples are the core-cusp problem [22, 23], the missing satellites problem [24], the diversity problem of rotation curves [25], and the too-big-to-fail problem [26]. There are two main approaches to alleviating small-scale discrepancies. One is to carefully consider the baryon physics such as star formation and supernova explosions within the framework of the standard model [27, 28, 29]. The other approach is to consider alternative dark matter models, such as warm dark matter (WDM) [30], self-interacting dark matter (SIDM) [31], primordial black holes (PBHs) [32, 33], and fuzzy dark matter (FDM) [34]. To be precise, PBHs might not be a direct solution to the small-scale problems, however, they are widely studied because they do not require new particles such as WIMPs to explain the existence of dark matter. Both strategies have demonstrated the potential to address these discrepancies while maintaining the success of the standard model at larger scales. As such, observational cosmology serves as a critical avenue for probing the fundamental nature of dark matter. To deepen our understanding, it is essential to explore the con-

nection between the mass distribution on small scales, as revealed through observation such as gravitational lensing, and the intrinsic properties of dark matter.

The history of gravitational lensing begins with its theoretical prediction by Einstein in 1915 as a consequence of General Relativity. Although the concept was also outlined by Orest Chwolson in 1924, Einstein formalized it in 1936 when he calculated the angular radius of an Einstein ring [35]. Fritz Zwicky further developed the idea in 1937, proposing that galaxy clusters could act as gravitational lenses, offering a way to measure masses independently of their luminosity and providing a tool to study dark matter [36]. Observationally, gravitational lensing was first confirmed in 1979 with the discovery of multiple imaging in the quasar QSO 0957+561 [37]. This was followed by the identification of giant luminous arcs in galaxy clusters [38, 39] and the first discovery of the Einstein ring [40]. Microlensing events were also detected [41, 42], revealing the possibility of constraining the abundance of the massive compact objects within the lens galaxies. The first detection of weak lensing was reported in 1990 [43], revealing systematic alignments in faint background galaxy images. These milestones solidified gravitational lensing as a powerful method for investigating both visible and dark matter in the universe.

In this thesis, we specifically focus on strong gravitational lensing as a tool for investigating the nature of dark matter. Strong gravitational lensing occurs near critical curves, which are characteristic lines on the lens plane where the magnification of background sources becomes extremely high. These critical curves are highly sensitive to the underlying mass distribution, enabling the estimation of small-scale mass structures by analyzing highly magnified images. The primary goal of this study is to analytically explore the relationship between the nature of dark matter, which affects the small-scale mass distribution, and the strong gravitational lensing signals. By utilizing the analytic models developed in this thesis, we aim to compare these theoretical predictions with actual observational data, thereby placing new constraints on the properties of dark matter.

The present thesis is organized as follows. We first review the standard model of the universe, the small-scale problems, and the possible solutions in Sec. 2. Then we review the FDM model in detail in Sec. 3. Here, we include the content of our recent paper on the core-halo mass relation in Sec. 3.4. We then review the basics of strong gravitational lensing in Sec. 4. In the following sections, we show our three different studies. In Sec. 5, we study the effect of microlenses on the number of ultrahigh magnification events and constrain the parameter space of PBHs from the observation of Icarus [44]. In Sec. 6, we study the fluctuations of the macro-critical curves induced by the substructures and show the preferred mass of FDM by comparing the observation of Mothra [45]. In Sec. 7, we focus on the galaxy-galaxy strong lensing (GGSL) cross-section with the FDM model and show the implication for the FDM mass. Finally in Sec. 8, we show the conclusion of this thesis. Throughout this thesis, unless otherwise stated, the cosmological parameters are set to the best-fit values from the Planck satellite observations [5]:  $\Omega_{m0} = 0.3111$ ,  $\Omega_{b0} = 0.0490$ , and  $H_0 = 67.66$  km/s/Mpc. Additionally, the size of the halo is defined as the radius at which the virial equilibrium condition holds, referred to as the virial radius, and the halo mass is defined as the total mass enclosed within the virial radius, i.e., the virial mass.

## List of papers

This thesis is based on the following publications:

1. K. T. Abe, H. Kawai, and M. Oguri, “Analytic approach to astrometric perturbations of critical curves by substructures,” *Phys. Rev. D*, vol. 109, no. 8, p. 083517, Apr. 2024, [46].  
— **Relevant Chapter:** Chap. 6
2. H. Kawai, A. Kamada, K. Kamada, and N. Yoshida, “Modeling the core-halo mass relation in fuzzy dark matter halos,” *Phys. Rev. D*, vol. 110, no. 2, p. 023519, July 2024, [47].  
— **Relevant Section:** Sec. 3.4
3. H. Kawai and M. Oguri, “Analytic model for the statistics of ultrahigh magnification events,” *Phys. Rev. D*, vol. 110, no. 8, p. 083514, Oct. 2024, [48].  
— **Relevant Chapter:** Chap. 5
4. H. Kawai and M. Meneghetti, “Galaxy-galaxy strong lensing cross-section with fuzzy dark matter model,” arXiv e-prints, p. arXiv:2410.14543, Oct. 2024, [49].  
— **Relevant Chapter:** Chap. 7
5. H. Kawai and M. Oguri, “Constraints on primordial black holes from the observed number of Icarus-like ultrahigh magnification events,” arXiv e-prints, p. arXiv:2411.13816, Nov. 2024, [50].  
— **Relevant Chapter:** Chap. 5

# Chapter 2

## Standard model of the universe and small-scale problems

In the early twentieth century, general relativity was formalized by Albert Einstein. The Einstein equation, which is the fundamental equation in general relativity, relates the geometry of spacetime to the underlying matter and energy distribution. Tests such as the precise tracking of the perihelion shift of Mercury, the deflection of light by the Sun observed during solar eclipses, and the detection of gravitational waves have confirmed predictions of general relativity. With these confirmations, general relativity has become one of the fundamental theories in modern physics, opening new windows to studying the structure and dynamics of the universe, which are known as astrophysics and cosmology.

Observational techniques in astronomy have advanced remarkably, and we have obtained a wealth of data from which we have gained a deeper understanding of the universe. Early milestones include Edwin Hubble's discovery of the expanding universe through galaxy redshift observations and the detection of the cosmic microwave background (CMB) by Penzias and Wilson, which provided strong evidence for the Big Bang theory. Subsequent missions such as the Cosmic Background Explorer (COBE), which provided detailed measurements of the anisotropy of the CMB, and the Hubble Space Telescope (HST), which provided a wide range of astronomical phenomena, have deepened our understanding of the universe. The Wilkinson Microwave Anisotropy Probe (WMAP) mission delivered precise data on the CMB across the entire sky, helping to determine cosmological parameters, and the Sloan Digital Sky Survey (SDSS) mapped millions of galaxies, unveiling the large-scale structure of the universe. Planck has improved the estimation of the cosmological parameters by increasing the sensitivity of the CMB, and the Dark Energy Survey (DES) and Hyper Suprime-Cam (HSC) have explored the nature of dark energy and galaxy distribution in more detail. More recently, the James Webb Space Telescope (JWST) has been revealing the early evolution of the universe through its sensitivity to the infrared region, and the Euclid satellite, mainly aiming at exploring the nature of dark energy and dark matter, launched in 2023.

These theoretical frameworks and observations have led to the development of the standard model of the universe, which can explain a wide range of observational data of the universe. Although the large-scale structure is well described by this standard model, there are several discrepancies between the theoretical predictions and the observation of the small-scale structures, indicating that the standard model might need to be revised.

In this chapter, we first review the standard model of the universe and its success in explaining the large-scale structures in Sec. 2.1. We then review the small-scale discrep-

ancies in Sec. 2.2. The possible approaches to alleviate the small-scale discrepancies are shown in Sec. 2.3.

## 2.1 Standard model of the universe

Our understanding of the universe has progressed from the latter half of the twentieth century thanks to the wide range of observations. Typical examples include the existence of unknown energy densities called dark matter and dark energy, the structure formation from the density fluctuations in a uniformly isotropic universe, the existence of inflation as a source of fluctuations, and Big Bang nucleosynthesis. In the standard model of the universe, so-called the  $\Lambda$  Cold Dark Matter (CDM) model, dark matter is assumed to interact primarily through gravity and be cold, which means it moves sufficiently slowly in the early universe, and dark energy is assumed to be the cosmological term in the Einstein equation. Our review of the standard model here mainly focuses on the CDM model as shown in Sec. 2.1.1. Then we show the theoretical prediction on the large-scale structures in Sec. 2.1.2 and small-scale structures in Sec. 2.1.3. In Sec. 2.1.4, we briefly review the baryon distribution within dark matter halos.

### 2.1.1 Cold dark matter

Observations of the CMB by Planck satellite indicate that dark matter accounts for about 27% of the total energy density in the universe, about five times as much as baryons [5]. Due to its large abundance, dark matter plays an important role in the structure formation of the universe. Although the nature of dark matter remains unknown, some of its properties have been uncovered. For instance, it exhibits extremely weak non-gravitational interactions and remains stable over the age of the universe. Therefore, the standard model of the universe phenomenologically assumes that dark matter has negligible non-gravitational interactions and its velocity dispersion is sufficiently small, the so-called CDM model. In the structure formation with the standard CDM model, there is no (or very small) cutoff scale because there is no collisionless damping of density fluctuations, and very low mass structures can be produced. If the particles constituting CDM are thermal relics, i.e., particles that were in thermal equilibrium in the early universe, but as the universe expanded their interactions became negligible and they subsequently behaved as free particles, then heavy particles are likely candidates. One viable example is the weakly interacting massive particle (WIMP) with a mass of approximately  $m \simeq 1 \text{ GeV}/c^2 - 1 \text{ TeV}/c^2$ . WIMP of this mass draws attention because it could potentially resolve the hierarchy problem in particle physics, which concerns the large gap between the energy scales of electroweak theory and the Planck scale [6], as well as it can explain the current amount of dark matter present in the universe. This coincidence is known as the "WIMP miracle". To closer look at this miracle, let us start with the current dark matter density assuming CDM is a thermal relic particle, which can be expressed as [51, 52]

$$\Omega_{\text{DM}} \simeq 0.1 \times \frac{3 \times 10^{-26} \text{ cm}^3/\text{s}}{\langle \sigma_{\text{ann}} v \rangle}. \quad (2.1)$$

Since the annihilation cross-section of the WIMP can be approximated as  $\langle \sigma_{\text{ann}} v \rangle \simeq cG_{\text{F}}^2 m_{\text{WIMP}}^2 / \hbar^4$  when  $m_{\text{WIMP}} \ll m_{\text{W}} \sim 100 \text{ GeV}$  and  $\langle \sigma_{\text{ann}} v \rangle \simeq cG_{\text{F}}^2 m_{\text{W}}^4 / (\hbar^4 m_{\text{WIMP}}^2)$  when  $m_{\text{WIMP}} \gg m_{\text{W}}$ , where  $G_{\text{F}}$  is the Fermi coupling constant and  $m_{\text{WIMP}}$  and  $m_{\text{W}}$  are

the WIMP mass and weak boson mass, respectively, the dark matter density calculated by Eq. (2.1) is consistent with the current universe when the WIMP mass is about  $1 \text{ GeV}/c^2$  to  $1 \text{ TeV}/c^2$ . This energy scale corresponds to the region where the new physics needed to explain Higgs condensation is expected, highlighting the WIMP as a viable candidate for addressing the hierarchy problem in particle physics. Thus, if CDM is composed of thermal relic particles, WIMP is regarded as a candidate to solve problems both in cosmology and particle physics.

Non-thermal relic particles can also constitute CDM. In this case, the CDM properties can be satisfied if particles are produced with non-relativistic velocity dispersion regardless of the particle mass. Specific examples include axions and axion-like particles (ALPs). Axions are particles necessary to solve the strong CP problem in quantum chromodynamics, while ALPs are predicted by string theory. ALPs have recently gained attention as a specific particle model for ultralight dark matter, often referred to as fuzzy dark matter (FDM), which we discuss in Chap. 3. In the context of the standard model of the universe, the term CDM typically refers to WIMPs, which are thermal relic particles. We follow this convention and treat other candidates as beyond CDM.

### 2.1.2 Large-scale structure

As mentioned in Sec. 2.1.1, dark matter has played a crucial role in the structure formation of the universe. This section discusses how the standard model has successfully explained observational results on large scales,  $k \lesssim 1 \text{ Mpc}^{-1}$  with  $k$  being the wavenumber of the matter fluctuation. Discussions often make use of statistical properties such as the two-point correlation function and the power spectrum. Considering the density fluctuation  $\delta(\mathbf{r}) = (\rho(\mathbf{r}) - \bar{\rho})/\bar{\rho}$  where  $\bar{\rho}$  is the mean density, the two-point correlation function of the density fluctuation is defined as

$$\xi(r_{12}) = \langle \delta(\mathbf{r}_1)\delta(\mathbf{r}_2) \rangle. \quad (2.2)$$

Here, the right-hand side calculates the ensemble average of the product of density fluctuations at two spatial points  $\mathbf{r}_1$  and  $\mathbf{r}_2$ , and  $r_{12}$  is the distance between the two points,  $r_{12} = |\mathbf{r}_1 - \mathbf{r}_2|$ . While the right-hand side involves taking an ensemble average over a large number of statistically equivalent universes, this is calculated by fixing the distance  $r_{12}$  and averaging over all locations in space using observational data, which is equivalent to assuming ergodicity. The power spectrum is defined using the Fourier transform of the density fluctuation  $\tilde{\delta}(\mathbf{k})$  as

$$\langle \tilde{\delta}(\mathbf{k})\tilde{\delta}(\mathbf{k}') \rangle = (2\pi)^3 \delta_D^{(3)}(\mathbf{k} + \mathbf{k}') P(k), \quad (2.3)$$

where  $\delta_D^{(3)}(\mathbf{k})$  is the Dirac delta function. The power spectrum corresponds to the Fourier transform of the two-point correlation function.

The initial density fluctuations generated by inflation follows  $P_{\text{in}}(k) \propto k^n$  with  $n \simeq 1$ , indicating an almost scale-invariant spectrum [5]. The fluctuations within the Hubble horizon grow or are suppressed due to various physical effects. Throughout the history of the universe, the Hubble horizon is very small at the time of inflation and then gradually increases through the radiation-dominant and matter-dominant eras [52]. Therefore, the fluctuations with shorter wavelengths re-enter the Hubble horizon at earlier times and undergo scale-dependent modifications. In the linear theory, where the density fluctuation satisfies  $\delta \ll 1$ , the evolution of fluctuations can be described by independent equations for

each wavenumber, and therefore, the amplitude of the fluctuation mode with wavenumber  $k$  is proportional to the amplitude of the initial fluctuation of the same mode. The scale-dependent modification is incorporated in the transition function  $T(k)$ . For scales that re-enter the Hubble horizon during the radiation-dominant era, the growth of fluctuations is suppressed due to the pressure of radiation, and the transfer function, disregarding the baryon abundance, can be approximated as [52]

$$T(k) = 12 \left( \frac{k}{k_{\text{eq}}} \right)^{-2} \ln \left( \frac{k}{8k_{\text{eq}}} \right), \quad (2.4)$$

where  $k_{\text{eq}}$  corresponds to the wavenumber associated with the size of the Hubble horizon at matter-radiation equality,  $k_{\text{eq}} \simeq 0.01 \text{ Mpc}^{-1}$  [5]. Since shorter wavelengths re-enter the Hubble horizon earlier, they experience a longer period of suppression, resulting in a smaller transfer function. The logarithmic growing mode indicates that the suppression is alleviated in the radiation-dominant era. On the other hand, fluctuations larger than the Hubble horizon at the age of matter-radiation equality re-enter the horizon during the matter-dominant era and avoid the suppression by the radiation, yielding  $T(k) \simeq 1$ . Therefore, the asymptotic behavior of the power spectrum with no baryon limit is given by

$$P(k) \propto T^2(k) P_{\text{in}}(k) \propto \begin{cases} k & k \lesssim k_{\text{eq}} \\ k^{-3} \ln\{k/(8k_{\text{eq}})\} & k \gtrsim k_{\text{eq}} \end{cases} \quad (2.5)$$

From this discussion, the key feature of the power spectrum is the turnover at matter-radiation equality. In the more realistic case where a small amount of baryon is present, the shape of the transfer function and the power spectrum is modified due to the silk damping and the baryon acoustic oscillation. Note that the discussion above is limited to structure formation in the linear regime, corresponding to scales larger than approximately 1 Mpc in the current universe.

Figure 2.1 shows a comparison of the linear matter power spectrum between the theoretical prediction by the standard  $\Lambda$ CDM model and the wide range of observations [53]. Here, they use the best-fitting cosmological parameters obtained from the CMB observations by the Planck satellite [5]. While the asymptotic behavior is consistent with Eq. (2.5), the oscillation and damping can be seen on a small scale originating from the baryonic effects. As shown in the figure, the standard model of the universe provides an excellent explanation for the observational results across various scales in the linear regime, with  $k \lesssim 1 \text{ Mpc}^{-1}$ .

### 2.1.3 Dark matter halo

In Sec. 2.1.2, we have focused on structure formation in the linear regime. While the evolution equation for matter fluctuations can be expressed independently for each wavenumber in the linear regime and therefore it is relatively easy to make theoretical predictions, it is not the case in the non-linear regime, resulting in the difficulty of analytical discussions. Here, the non-linear regime refers to the region where the density fluctuation is larger than unity,  $\delta \gtrsim 1$ . Examples of non-linear structures are dark matter halos and galaxies, where matter is highly concentrated compared to the average density of the universe. To study the non-linear structure formation, we need to rely on cosmological simulations (e.g., [55]). Here, we review the structure of CDM halos as revealed by  $\Lambda$ CDM simulations.

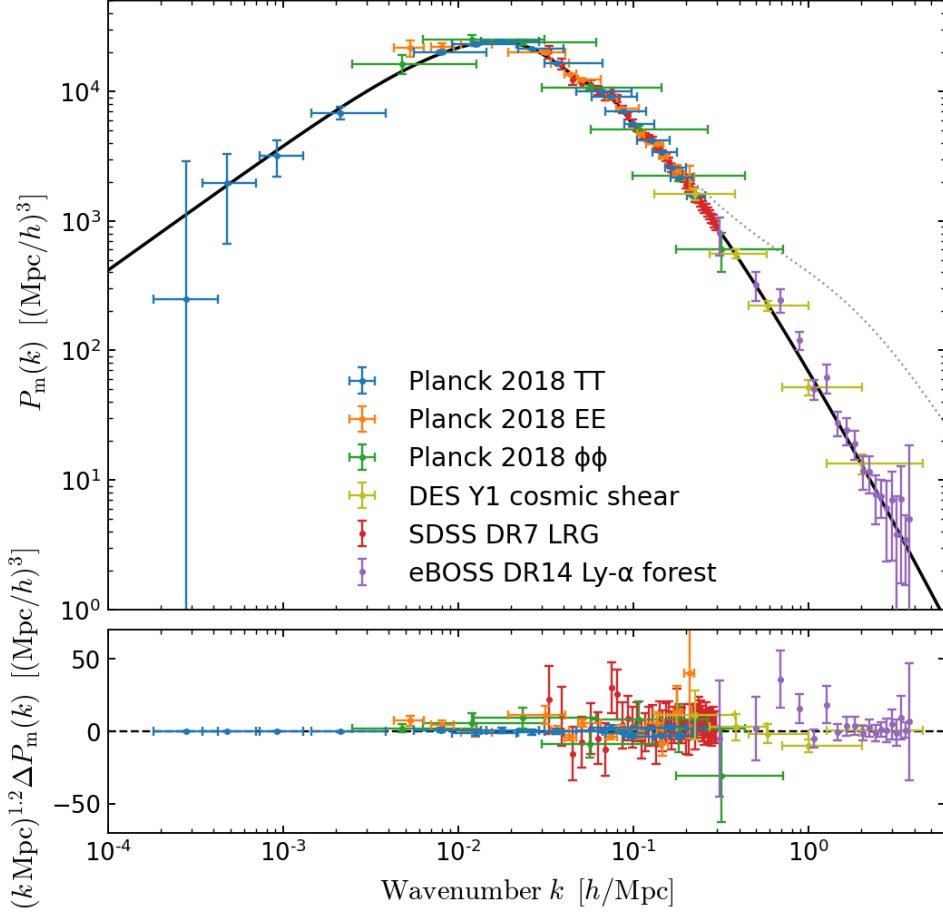


Figure 2.1: The linear matter power spectrum at redshift  $z = 0$  is shown. The black solid line represents the theoretical prediction by the standard  $\Lambda$ CDM model with cosmological parameters obtained by the Planck satellite [5]. The observed spectra are obtained by CMB with the Planck satellite on the largest scales [54], galaxy clustering with SDSS on intermediate scales [20], cosmic shear with DES [19], and Lyman- $\alpha$  clustering with SDSS [18] on the smallest scales. This figure is taken from [53].

The density profile of the CDM halos is known to be described by the Navarro-Frenk-White (NFW) profile [56], which can be expressed as

$$\rho_{\text{NFW}}(r) = \frac{\rho_s}{(r/r_s)(1+r/r_s)^2}, \quad (2.6)$$

where  $r_s$  and  $\rho_s$  are the scale radius and density, respectively. The density profile can be expressed by a double power law where the density profile is cusp-like  $\rho \propto r^{-1}$  near the center of the halo,  $r \lesssim r_s$ , and outside the density profile follows  $\rho \propto r^{-3}$ . The NFW profile can also be described using the total halo mass  $M_h$  and the concentration parameter  $c_{\text{vir}}$ , instead of the two parameters  $r_s$  and  $\rho_s$ . Here, the concentration parameter is defined as  $c_{\text{vir}} \equiv r_{\text{vir}}/r_s$ , with  $r_{\text{vir}}$  representing the virial radius of the halo. It is important to note that the definition of the concentration parameter varies depending on how the halo radius is defined. As mentioned in Chap. 1, we adopt the virial radius as the halo radius definition throughout the thesis. The enclosed mass of the NFW profile is expressed as

$$M_{\text{NFW}}(< r) = 4\pi\rho_s r_s^3 \left\{ \ln \left( 1 + \frac{r}{r_s} \right) - \frac{r/r_s}{1+r/r_s} \right\}. \quad (2.7)$$

Using this expression, the total halo mass can be written as

$$M_h = M_{\text{NFW}}(< r_{\text{vir}}) = 4\pi\rho_s r_s^3 f(c_{\text{vir}}), \quad (2.8)$$

where  $f(c_{\text{vir}})$  is defined as  $f(c_{\text{vir}}) \equiv \ln(1 + c_{\text{vir}}) - c_{\text{vir}}/(1 + c_{\text{vir}})$ . The virial halo mass is further related to the mean matter density  $\bar{\rho}$  at a given redshift  $z$  as

$$M_h = \frac{4}{3}\pi r_{\text{vir}}^3 \zeta(z) \bar{\rho}(z), \quad (2.9)$$

where  $\zeta(z)$  is given by

$$\zeta(z) = \frac{1}{\Omega_m(z)} \{18\pi^2 + 82(\Omega_m(z) - 1) - 39(\Omega_m(z) - 1)^2\}, \quad (2.10)$$

with  $\Omega_m(z)$  representing the matter density parameter at redshift  $z$  [57].

The relation between concentration and halo mass, so-called the  $c_{\text{vir}}-M_h$  relation, is actively studied (*e.g.*, [58, 55]). The mean concentration of halos with mass  $M_h$  at redshift  $z$  is approximated by [58]

$$c_{\text{vir}}^{\text{B}}(M_h, z; \text{CDM}) = A \frac{1 + z_{\text{coll}}(M_h; P_{\text{CDM}})}{1 + z}, \quad (2.11)$$

where  $P_{\text{CDM}}$  is the linear matter power spectrum at redshift  $z = 0$ , which is shown in Fig. 2.1, and the constant  $A$  is set to 3.13 [59]. The collapse redshift  $z_{\text{coll}}$  is determined through

$$D(z_{\text{coll}}) \sigma(f_{\text{coll}} M_h; P_{\text{CDM}}) = \delta_c, \quad (2.12)$$

where  $D(z)$  is the linear growth rate and  $\sigma(M)$  represents the linear root-mean-square density fluctuation on the comoving scale encompassing a mass  $M$  at redshift  $z = 0$ . The constant  $f_{\text{coll}}$  is set to 0.01, and the critical density fluctuation for collapse is given by  $\delta_c = 1.59 + 0.0314 \ln \sigma_8(z)$  with  $\sigma_8$  being the amplitude of the linear power spectrum on the scale of 8 Mpc/ $h$ . The  $c_{\text{vir}}-M_h$  relation derived from a cosmological CDM simulation with the largest box size of 140 Mpc/ $h$  [55] is consistent with the analytic model described above. The dependence of the concentration parameter on the halo mass at redshift  $z = 0$  in the CDM model is approximately

$$c_{\text{vir}} \propto M_h^{-0.06} \quad M_h \lesssim 10^{11} M_{\odot}/h \quad (2.13)$$

$$c_{\text{vir}} \propto M_h^{-0.12} \quad M_h \gtrsim 10^{11} M_{\odot}/h. \quad (2.14)$$

The concentration shows a scatter around its mean value, with a  $1\sigma$  scatter of approximately 0.16 dex [60]. This scatter is nearly independent of both halo mass and redshift.

Subhalos are smaller gravitationally bound structures within a larger dark matter halo. They are thought to be the remnants of smaller halos that have merged into a larger parent halo during the hierarchical structure formation of the universe. A key property of these subhalos is their mass distribution, commonly referred to as the subhalo mass function, describing the abundance of subhalos as a function of their mass within a parent halo. In the context of the CDM model, the subhalo mass function has been the subject of extensive investigation, both through numerical simulations and analytical approaches (*e.g.*, [61, 62, 63, 64, 65, 66, 67, 68, 69, 70, 71, 72, 73, 74, 75, 76]). The cumulative number of subhalos is approximated by a power-law relation, derived from numerical simulations, as [64, 67]

$$N_{\text{sh}}(> M_{\text{sh}}) \propto \left( \frac{M_{\text{sh}}}{M_{\text{hh}}} \right)^{-0.9}, \quad (2.15)$$

where  $M_{\text{hh}}$  and  $M_{\text{sh}}$  represent the host halo mass and the subhalo mass, respectively. This power-law behavior is consistent with theoretical predictions [65, 72]. However, deviations from a simple power law have been indicated in more detailed analyses. From simulations, it has been suggested that the subhalo mass function can be described with an exponential cutoff at the high-mass end as [68, 71, 76]

$$\frac{dN_{\text{sh}}}{d \ln M_{\text{sh}}} = 0.30 \left( \frac{M_{\text{sh}}}{M_{\text{hh}}} \right)^{-0.7} \exp \left[ -9.9 \left( \frac{M_{\text{sh}}}{M_{\text{hh}}} \right)^{2.5} \right]. \quad (2.16)$$

While the formula above is derived by fitting numerical results, a recent semi-analytic model provides a physical understanding of the CDM subhalo mass function [75]. In this model, the evolved mass function corresponding to the observable subhalo distribution in the present universe is calculated by combining the unevolved mass function with the effects of tidal evolution modeled by [72]. Here, the unevolved mass function assumes that the host halo grows solely through the accretion of smaller halos, with its mass determined by integrating the contributions from all accreted halos. This semi-analytic model based on the assumptions above successfully reproduces the subhalo mass function observed in simulations, providing a consistent explanation for the numerical results. Note that we can use the open source code <sup>1</sup> provided by [75] to calculate the subhalo mass function.

The spatial distribution of subhalos is thought to follow the density distribution of the host halo [69]. Here, let us consider the projection along the line of sight and obtain the projected subhalo mass function, which is important in the observation of gravitational lensing. The surface mass density profile is defined as

$$\Sigma(\mathbf{x}) = \int dz \rho(\mathbf{r}), \quad (2.17)$$

where  $\mathbf{x}$  is the two-dimensional coordinates on the projected density field. In the case of the spherical NFW profile, the analytic expression has been obtained [77],

$$\Sigma_{\text{NFW}}(x) = \frac{2\rho_{\text{s}}r_{\text{s}}^3}{x^2 - r_{\text{s}}^2} g\left(\frac{x}{r_{\text{s}}}\right), \quad (2.18)$$

with the function  $g(\xi)$  is defined by

$$g(x) = \begin{cases} 1 - \frac{2}{\sqrt{\xi^2 - 1}} \arctan \sqrt{\frac{\xi - 1}{\xi + 1}} & (\xi > 1), \\ 1 - \frac{2}{\sqrt{1 - \xi^2}} \operatorname{arctanh} \sqrt{\frac{1 - \xi}{1 + \xi}} & (\xi < 1), \\ 0 & (\xi = 1). \end{cases} \quad (2.19)$$

The surface number density of subhalos is proportional to the surface density profile of the host halo,

$$\frac{dN_{\text{sh}}}{dS} = \frac{N_{\text{sh}} \Sigma(d_{\text{sh}}; M_{\text{hh}})}{M_{\text{hh}}}, \quad (2.20)$$

where  $d_{\text{sh}}$  is the distance to the host halo center and  $dS = 2\pi d_{\text{sh}} dd_{\text{sh}}$  assuming the spherical symmetry. The projected subhalo mass function can be expressed as

$$\frac{d^2 N_{\text{sh}}}{dM_{\text{sh}} dS} = \frac{dN_{\text{sh}}}{dM_{\text{sh}}} \frac{\Sigma(d_{\text{sh}}; M_{\text{hh}})}{M_{\text{hh}}}. \quad (2.21)$$

Note that  $dN_{\text{sh}}/dM_{\text{sh}}$  is the subhalo mass function shown in the previous paragraph.

<sup>1</sup><https://github.com/shinichiroando/sashimi-c>

### 2.1.4 Baryon distribution

So far, we have focused on the distribution of CDM. Since structure formation is primarily driven by dark matter, given that the baryon abundance is five times smaller, the baryon distribution generally follows the dark matter density. Here, we provide a brief overview of the baryon distribution within the host halo that forms a galaxy.

The baryon profile is known to follow the Hernquist profile [78], which is expressed as

$$\rho_{\text{Hern}}(r) = \frac{\rho_{\text{g}}}{(r/r_{\text{g}})(1 + r/r_{\text{g}})^3}, \quad (2.22)$$

where  $r_{\text{g}}$  and  $\rho_{\text{g}}$  denote the characteristic radius and density, respectively. The characteristic density  $\rho_{\text{g}}$  can be written in terms of the characteristic radius and the total baryon mass  $M_{\text{s}}$  as

$$\rho_{\text{g}} = \frac{M_{\text{s}}}{2\pi r_{\text{g}}^3}. \quad (2.23)$$

The characteristic radius  $r_{\text{g}}$  is related to the effective radius of the Hernquist profile  $r_{\text{e}}$  as  $r_{\text{g}} = 0.551r_{\text{e}}$ . Therefore, the Hernquist profile is fully determined by the effective radius and the total baryon mass. Based on observations of 50,000 early-type galaxies in the SDSS, there is a relation between the effective radius and the total baryon mass as [79]

$$\log_{10} \left( \frac{r_{\text{e}}}{\text{kpc}} \right) = 7.55 - 1.84 \log_{10} \left( \frac{M_{\text{s}}}{M_{\odot}} \right) + 0.11 \left\{ \log_{10} \left( \frac{M_{\text{s}}}{M_{\odot}} \right) \right\}^2. \quad (2.24)$$

Additionally, the total baryon mass is linked to the host halo mass through the stellar-to-halo mass ratio [80]. The ratio depends on the halo mass but is typically on the order of 0.01. From the relations above, the baryon distribution within the host halo can be estimated for a given halo mass.

## 2.2 Small-scale problems

In Sec. 2.1, we briefly review the structure formation with the standard  $\Lambda$ CDM model and show that the linear theory is in good agreement with observational data. In this section, we focus on observational results in the nonlinear regime at scales  $k \gtrsim 1 \text{ Mpc}^{-1}$  and discuss the discrepancies identified in comparison to  $\Lambda$ CDM simulation outcomes. These discrepancies are collectively called small-scale problems, and the following four problems in particular have been identified [21].

### 2.2.1 Core-cusp problem

The core-cusp problem refers to the discrepancy between the central density profiles of halos predicted by  $\Lambda$ CDM simulations and those observed in dwarf galaxies and low-surface-brightness galaxies [22, 23, 81, 82, 83]. As shown in Sec. 2.1.3, CDM halos follow an NFW profile, where the density distribution near the center exhibits a cusp-like behavior,  $\rho \propto r^{-1}$ . In contrast, observations of the rotation curves of dwarf and low-surface-brightness galaxies indicate that their central density profiles are core-like,  $\rho = \text{const.}$  [84]. Since these systems are dominated by dark matter and have a small amount of baryon content, it is difficult to consider solutions to small-scale problems involving baryon physics as explained in Sec. 2.3.1.

### 2.2.2 Missing satellite problem

The missing satellite problem refers to the discrepancy between the number of subhaloes in a Milky Way-sized CDM halo and the number of dwarf galaxies observed around the Milky Way [24]. This comparison is based on the idea that simulated CDM subhalos with masses  $M \gtrsim 10^7 M_\odot$  are expected to host (dwarf) galaxies, making their numbers roughly comparable. However, the difference in their number is an order of magnitude, especially for structures with small masses. This discrepancy could be attributed to the power-law index of the subhalo mass function. As shown in Sec. 2.1.3, the  $\Lambda$ CDM simulations predict a value of about  $-1.9$ , while the observed galactic stellar mass function predicts about  $-1.47$  [85]. This leads to a large discrepancy in the number of low-mass objects.

However, recent observational advances and a better understanding of the galaxy-halo connection through baryon physics suggest that the missing satellite problem may be solved. Indeed, an increasing number of dwarf galaxies have been discovered within the Milky Way [86]. Additionally, it is expected that more dwarf galaxies will be detected through surveys such as the DES and the Large Synoptic Survey Telescope (LSST) [87]. It is shown that by considering the galaxy-halo mass scaling relations [88, 89, 90], the number of satellites predicted by the  $\Lambda$ CDM model agrees with the number of observed satellites after correcting for the detection efficiency of the SDSS [91]. These recent studies suggest that the missing satellite problem could already be resolved.

### 2.2.3 Diversity problem

The diversity problem refers to the discrepancy in the radial dependence of the inner rotation curves of galaxies. While in  $\Lambda$ CDM simulations, galaxies with the same maximum rotation velocity exhibit almost identical inner rotation curves, there is a wide variety of inner rotation curves in observations of dwarf galaxies [25]. This problem can be interpreted as a modern version of the core-cusp problem, as differences in the density profile near the center are reflected in the shape of rotation curves. However, some of the observed rotation curves show larger velocities than predicted by the  $\Lambda$ CDM model. The diversity problem might suggest that the dark matter density profile is influenced by the distribution of baryons, while the effects on the CDM distribution remain minimal due to the absence of non-gravitational interactions in the CDM framework. Therefore, it has been suggested that the diversity of the rotation curves can be achieved by considering the alternative dark matter model such as self-interacting dark matter (SIDM) as shown in Sec. 2.3.2.

### 2.2.4 Too-big-to-fail problem

The too-big-to-fail problem refers to the issue where the central densities of massive CDM subhalos within Milky Way-sized halos are too dense, leading to the formation of galaxies that are brighter than any of the observed dwarf galaxies [26]. The term “too big to fail” comes from the notion that massive subhalos require either strong tidal collapse or reduction in star formation efficiency to host the brightest dwarf galaxies observed, both of which are constrained by current observations, and that CDM subhalos should host larger galaxies. It is important to note that the core-cusp problem indicates discrepancies in the central density of systems with few baryons, whereas the too-big-to-fail problem focuses on massive subhalos where a sufficient amount of baryons exist. If the core-cusp

problem is resolved, it would reduce the central density, which in turn could solve the too-big-to-fail problem as well.

## 2.3 Possible solutions

In Sec. 2.2, we show the discrepancies between the theoretical predictions of the  $\Lambda$ CDM model and small-scale observations. It might indicate that the standard model is not the right model to explain the universe. To develop a theory that better explains the universe, the standard model must be modified to address inconsistencies at smaller scales while maintaining the success of the large-scale structure. Two main approaches have been researched as potential solutions to the small-scale problems. The first approach is to carefully include baryon physics such as star formation and supernova explosions, which are not incorporated in the original simulations solving the evolution of CDM distribution. The other approach involves considering alternative dark matter models, such as warm dark matter (WDM), SIDM, and FDM. In this section, we review both approaches. Note that FDM will be discussed in Chap. 3. Instead, in this section, we additionally review primordial black holes (PBHs), which are also viable dark matter candidates as an alternative to CDM.

### 2.3.1 Baryon physics

Baryon physics has been proposed as a potential solution to the small-scale problems within the standard model assuming CDM. Recent simulations that include the effects of star formation and supernova explosions, such as NIHAO [92] and FIRE-2 [29], have shown that the power-law index  $\alpha$  of the dark matter halo density profile near the center deviates from  $\alpha = -1$ , i.e., the NFW profile. This change in the density profile due to baryon physics is believed to depend on the total stellar (galaxy) mass or the stellar-to-halo mass ratio [93, 94, 27]. For small stellar-to-halo mass ratios of  $M_s/M_h \lesssim 10^{-4}$ , which corresponds to ultra-faint galaxies, the system is dominated by dark matter and the effect of star formation is minimal, resulting in a density profile close to the NFW profile,  $\alpha = -1$ . As the mass ratio increases, sufficient star formation occurs and supernova explosion of heavy stars reduces the central dark matter density. The effect of baryon physics is most pronounced around  $M_s/M_h \simeq 0.005$ , leading to a core-like density profile with  $\alpha \simeq 0$ . At this point, typical galaxy masses range from  $M_s \simeq 10^{8-9} M_\odot$ , corresponding to dwarf galaxies. As the mass ratio increases further, the gravitational potential of the baryons pulls back the dark matter ejected by the supernova explosion, making the density distribution more cuspy,  $\alpha \lesssim -1$ . As such, the power-law index of the dark matter density profile is mass-dependent, and the core profile can also be generated due to baryon physics, indicating that the small-scale problems such as the core-cusp problem [27].

In addition to the baryon physics within the satellite galaxies mentioned above, interactions between the satellite and the Milky Way including tidal stripping, disk shocking, and ram pressure stripping, act as additional mechanisms that reduce the central mass of the satellite galaxies. Tidal stripping occurs when the gravitational forces exerted by the host galaxy (Milky Way) exceed the gravitational binding force of the satellite galaxy, leading to the loss of mass, particularly in the outer regions of satellites. Disk shocking occurs when satellite galaxies pass through the disk of the host galaxy. The sudden change in gravitational potential causes stars and dark matter to gain energy and internal heating, facilitating matter escape. Ram pressure stripping occurs when a satellite

galaxy moves through the hot diffuse gas in the halo of the host galaxy. This gas exerts pressure on the interstellar medium of the satellite, removing gas and suppressing star formation. The importance of these phenomena has been shown in many galaxy formation simulations, and they might contribute to solving the too-big-to-fail problem [95, 96].

### 2.3.2 Alternative dark matter models

In Sec. 2.3.1, we discuss the possible solution to the small-scale problems within the framework of the  $\Lambda$ CDM model. In this section, we focus on an alternative approach to altering small-scale structures, which involves changing the dark matter model. Since CDM is a simple model that assumes non-relativistic when decoupled from the thermal bath and neglects collisionless damping, and that non-gravitational interactions are ignored, a natural modification to the CDM is to include collisionless damping and non-gravitational interactions. Here we first review WDM, in which collisionless damping becomes important, and then SIDM, which considers non-gravitational interactions. While PBHs might not directly solve the small-scale problems, they are also viable dark matter candidates without introducing new particles. Therefore, we also review them at the end of this subsection. Again, FDM will be reviewed in Chap. 3.

#### WDM

We consider a thermal relic dark matter model with a non-negligible velocity dispersion in the early universe. This dispersion causes collisionless damping, also known as free-streaming damping, where the free streaming of dark matter smooths out small-scale density perturbations, preventing their growth and thereby suppressing structure formation. The free streaming scale can be estimated as [97]

$$\lambda_{\text{fs}} \simeq \frac{ca_{\text{nr}}}{H_0\sqrt{\Omega_{\text{r}0}}}, \quad (2.25)$$

where  $a_{\text{nr}}$  is the scale factor when the dark matter becomes non-relativistic and  $\Omega_{\text{r}0}$  is the mean radiation density in the current universe. Here, we ignore the logarithmic term arising from the period between the non-relativistic transition and matter-radiation equality. The time when dark matter becomes non-relativistic can be approximated by the condition where its rest mass energy equals its thermal kinetic energy,

$$k_{\text{B}}T_{\text{nr}} = \frac{1}{3}mc^2. \quad (2.26)$$

where  $T_{\text{nr}}$  is the temperature at that time. Now we consider the warm relic with a mass on the order of  $\text{keV}/c^2$ . Then,  $T_{\text{nr}}$  is much lower than the electron-positron annihilation temperature of about  $1 \text{ MeV}/k_{\text{B}}$ , leading to the photon number density has already frozen at  $T_{\text{nr}}$ . Thus, the scale factor at the non-relativistic transition is expressed as

$$a_{\text{nr}} = \frac{T_0}{T_{\text{nr}}} = \frac{3k_{\text{B}}T_0}{mc^2}, \quad (2.27)$$

where  $T_0 = 2.725 \text{ K}$  is the current photon temperature. Substituting Eq. (2.27) into Eq. (2.25), the free-streaming scale can be represented as

$$\lambda_{\text{fs}} \simeq 82 \left( \frac{mc^2}{10 \text{ eV}} \right)^{-1} \text{ Mpc}. \quad (2.28)$$

As an example, if we consider the neutrino whose mass is below  $10 \text{ eV}/c^2$  as a dark matter candidate, the free-streaming scale exceeds that of galaxy clusters, making it inconsistent with the observed structure of the universe. Such particles with a mass on the order of  $\text{eV}/c^2$  are referred to as hot dark matter (HDM) and this dark matter model has been ruled out. To suppress only sub-galactic scales, the dark matter mass must be larger than that of HDM but smaller than that of CDM. Such a dark matter model, with properties intermediate between HDM and CDM, is called WDM.

The WDM simulation shows that the linear matter power spectrum is expressed by the following fitting formula [98, 99, 100, 21]

$$P_{\text{WDM}}(k) = P_{\text{CDM}}(k) \{1 + (\lambda_{\text{fs}} k)^{2\nu}\}^{-10/\nu} \quad (2.29)$$

with  $\nu = 1.12$ . Here, the free-streaming scale  $\lambda_{\text{fs}}$  is expressed by

$$\lambda_{\text{fs}} = 70 \left( \frac{mc^2}{1 \text{ keV}} \right)^{-1.11} \left( \frac{\Omega_{m0}}{0.25} \right)^{0.11} \left( \frac{h}{0.7} \right)^{0.22} \text{ kpc}, \quad (2.30)$$

which is roughly consistent with the analytic estimation shown in Eq. (2.28). The corresponding mass for this scale is

$$M_{\text{fs}} = \frac{4}{3} \pi \bar{\rho} \left( \frac{\lambda_{\text{fs}}}{2} \right)^3 \simeq 7.1 \times 10^6 \left( \frac{mc^2}{1 \text{ keV}} \right)^{-3.33} M_{\odot}, \quad (2.31)$$

assuming the Planck cosmological parameters [5]. In practice, the suppression of the matter power spectrum extends to scales larger than the free-streaming length. The scale that characterizes this suppression is called the half-mode scale, defined as the scale where the matter power spectrum is reduced by 1/4 compared to the CDM case. From Eq. (2.29), the half-mode scale can be expressed as

$$\lambda_{\text{hm}} = 2\pi \lambda_{\text{fs}} (2^{5/5} - 1)^{-\frac{1}{2\nu}} \simeq 13.93 \lambda_{\text{fs}}. \quad (2.32)$$

The half-mode mass  $M_{\text{hm}}$  is written as

$$M_{\text{hm}} = \frac{4}{3} \pi \bar{\rho} \left( \frac{\lambda_{\text{hm}}}{2} \right)^3 \simeq 2.7 \times 10^3 M_{\text{fs}} = 1.9 \times 10^{10} \left( \frac{mc^2}{1 \text{ keV}} \right)^{-3.33} M_{\odot}. \quad (2.33)$$

While we have shown the relation between the suppression scale of the structure formation and the WDM mass for thermal relic particles, these relations are not uniquely determined for non-thermal relic particles and depend on the specific production mechanism.

As shown above, the WDM model suppresses the small-scale structure formation, which might help alleviate the small-scale problems such as the missing satellites problem. The WDM model affects not only the number of small structures but also the formation of larger mass halos. Since the universe forms structures hierarchically, the suppression of small-scale perturbations delays the formation of halos with larger masses. Considering that the central density of halos reflects the density of the universe at the time of their formation, halos with masses close to  $M_{\text{hm}}$  experience a decrease in central density in the WDM model. This reduction might help resolve the too-big-to-fail problem [101]. While the concentration parameters of WDM halos are reduced compared to those of CDM halos, the central density profile remains cuspy [102], indicating that the core-cusp problem might not be solved with the WDM model.

The WDM mass is constrained by several observations. One such constraint comes from the number count of observed satellite galaxies within the Milky Way, which sets a lower limit on the number of subhalos and thus provides a lower bound on the WDM mass. The derived constraints are  $m > 2.3 \text{ keV}/c^2$  [103] and  $m > 1.6 \text{ keV}/c^2$  [104]. The differences in these limits arise from subtle variations in the assumptions, such as the mass of the Milky Way-sized halo and modeling of completeness limits for satellite detections. The strictest constraint is obtained from the power spectrum of stellar streams and the number of dwarf galaxies,  $m > 6.2 \text{ keV}/c^2$  [105]. It is worth noting that the stellar stream is sensitive to tidal stripping effects from passing subhalos nearby and thus provides a means of measuring their abundance, making it a valuable target for constraining dark matter models.

The potential candidates for WDM particles include the gravitino, the supersymmetric partner of the graviton, and the sterile neutrino, a hypothetical neutrino that does not interact via the weak nuclear force. Since both of them are theoretical particles beyond the standard model of elementary particle physics, confirming the existence of WDM would open a new window into new physics.

## SIDM

Next, we focus on the SIDM model [31], which includes non-gravitational interactions. The scattering cross-section is denoted by  $\sigma$ , whereas the model is often characterized by the scattering cross-section per unit mass  $\sigma/m$  since the mass of dark matter is not known.

The cross-section determines the mean free path, expressed as  $\lambda = (n\sigma)^{-1} = (\rho\sigma/m)^{-1}$ , where  $n$  is the number density of SIDM particles. In the high-density central region of the SIDM halo, the mean free path is shortened and scattering events occur frequently on local dynamical time scales. These interactions promote energy exchange between dark matter particles and shape the central density distribution of the SIDM halo into an isothermal form. Conversely, in the outer regions where the number density decreases, collisions become less frequent and the SIDM halo behaves like a CDM halo. The transition radius  $r_1$  at which this change occurs can be evaluated under the following conditions [106],

$$\frac{\langle\sigma v\rangle}{m}\rho(r_1)t_{\text{age}} \simeq 1, \quad (2.34)$$

which ensures that scattering occurs at least once during the halo age denoted by  $t_{\text{age}}$ . The ensemble average is taken over the velocity, which is assumed to follow the Maxwell-Boltzmann distribution [107]. With this transition radius  $r_1$ , the SIDM halo density profile can be written as,

$$\rho(r) = \begin{cases} \rho_{\text{iso}}(r) & r < r_1 \\ \rho_{\text{NFW}}(r) & r > r_1 \end{cases}, \quad (2.35)$$

where  $\rho_{\text{iso}}(r)$  denotes the isothermal density profile, and  $\rho_{\text{NFW}}(r)$  represents the NFW profile. The isothermal density profile in the inner region can be derived as follows. Since SIDM particles behave like an isothermal gas, the equation of state is given by  $p = \rho v_{\text{rms}}^2$ , where  $p$  is the pressure and  $v_{\text{rms}}$  is the velocity dispersion. Assuming hydrostatic equilibrium in the inner halo, the Euler equation  $\nabla p = -\rho\nabla\Phi_{\text{tot}}$  holds, where  $\Phi_{\text{tot}}$  is the total gravitational potential from dark matter and baryon. The total potential satisfies the Poisson equation,  $\nabla^2\Phi_{\text{tot}} = 4\pi G(\rho + \rho_b)$ , with  $\rho_b$  representing the baryon density. By

combining them, we can obtain the equation for the density,

$$v_{\text{rms}}^2 \nabla^2 \ln \rho = -4\pi G(\rho + \rho_b). \quad (2.36)$$

Setting the gravitational potential at the center as zero and defining the central density as  $\rho_0$ , the isothermal density profile can be expressed as [108]

$$\rho_{\text{iso}}(r) = \rho_0 \exp\left(\frac{-\Phi_{\text{tot}}(r)}{v_{\text{rms}}^2}\right), \quad (2.37)$$

from which we can see that a core, i.e.,  $\rho = \text{const.}$ , is formed near the center of the SIDM halo. The core radius depends on the cross-section; as the cross-section increases, thermal exchanges become more efficient, resulting in a larger core radius.

While the center of the SIDM halo has been thought to be expressed with a core profile as shown above, recent simulations suggest that the core-collapse occurs long after the core formation time [109, 110, 111, 112]. This is caused by the following mechanisms. Due to the scattering, heat flows from the inner hot region to the outer cool region. This heat loss causes the dark matter particles to infall, further increasing the temperature at the center. This negative heat capacity of a self-gravitating system accelerates the infall as the negative heat gradient becomes steeper, leading to a denser cuspy profile, known as the core-collapse process [113]. The relevant timescale for the core-collapse is approximately 10 times the core-formation time in a tidally truncated halo and around 100 times larger in an isolated (field) halo. Here, the core-formation (relaxation) timescale can be expressed as [113, 110, 114]

$$t_r \simeq \frac{m}{3\rho_s \langle \sigma v \rangle}. \quad (2.38)$$

with  $\rho_s$  is the scale density of the NFW profile. The central density profile of the core-collapsed SIDM halo follows  $\rho \propto r^{-3}$ , which is much steeper than the NFW profile [111].

Since the SIDM halo creates the cored density profile, before the core-collapse phase, the SIDM model might alleviate the core-cusp problem. [31]. Due to the reduction of the central density compared to the NFW profile, the too-big-to-fail problem might also be alleviated with the SIDM model [115]. The SIDM model is also known to address the diversity problem of galactic rotation curves [106]. This arises from the high sensitivity of SIDM cores to the underlying baryon distribution, as can be seen in Eq. (2.37), where the central density profile is determined by the gravitational potential, which relates to the baryon distribution. However, SIDM simulations show that the number of substructures is almost the same as in the CDM case, demonstrating that the SIDM model does not significantly alleviate the missing satellite problem [116].

Numerous studies have attempted to constrain the SIDM cross-section based on observations (see [117] for a recent review). For instance, analysis of strongly lensed images of galaxy clusters to measure dark matter density profiles excludes  $\sigma/m > 0.13 \text{ cm}^2/\text{g}$  [118]. The sphericity of the SIDM halo due to the scatterings places a constraint on the cross-section, excluding  $\sigma/m > 0.1 \text{ cm}^2/\text{g}$ , as determined by analyzing the central density of a galaxy cluster [119, 120]. A direct constraint on the cross-section has been obtained from analyses of the morphology of the hot gas, dark matter, and galaxies in a merging galaxy cluster, yielding an upper limit of  $\sigma/m < 1 \text{ cm}^2/\text{g}$  [121]. Considering the mean free path of the Milky Way halo to alleviate the core-cusp and the missing satellite problems, the cross-section is constrained to  $0.45 \lesssim \sigma/m \lesssim 450 \text{ cm}^2/\text{g}$ , which is comparable to

the neutron-neutron scattering cross-section [31]. For lower-mass systems such as dwarf galaxies, observed central densities are better explained by a larger cross-section, within the range  $\sigma/m < 30 - 100 \text{ cm}^2/\text{g}$  [122]. These constraints suggest that the cross-section should depend on the velocity to explain the data from dwarf galaxies ( $v \simeq 10 \text{ km/s}$ ) to galaxy clusters ( $v \simeq 1000 \text{ km/s}$ ); the cross-section needs to decrease as the velocity dispersion increases. Several models have been proposed where the cross-section depends on velocity. One such model describes self-interactions using a Yukawa potential, mediated by a dark photon. By setting the dark matter mass to  $15 \text{ GeV}/c^2$  and the dark photon mass to  $17 \text{ MeV}/c^2$ , the resulting cross-section aligns with observational constraints [106].

## PBH

PBHs are hypothetical black holes formed in the early universe [32, 33] (see [123, 124] for recent reviews). Although PBHs might not be a direct solution for small-scale problems, we review them here because PBHs are viable dark matter candidates and potential alternatives to CDM. Various formation scenarios are considered, such as the gravitational collapse during the matter-dominant era [125] and the collapse of large isocurvature perturbations [126, 127], however, the most plausible mechanism is the gravitational collapse of overdense regions during the radiation-dominant era following inflation [33]. One of the most interesting features is that PBHs can form across a wide range of masses depending on the collapsing time [128]. While the PBHs whose mass is lower than  $10^{15} \text{ g}$  would have evaporated through the Hawking radiation [129], the PBHs with larger masses could still exist in the current universe and potentially contribute to dark matter. This scenario is interesting since we do not need to assume the existence of new particles, such as WIMPs and supersymmetric particles, to explain dark matter, which is one of the main motivations for PBHs. Furthermore, PBHs might explain other astrophysical phenomena, including the unexpected observation of high-redshift massive galaxies [130] and the detection of stochastic gravitational waves [131], further motivating the study of PBHs.

PBHs forming during the radiation-dominant era have initial masses close to the Hubble horizon mass,  $M_{\text{H}}$ , given by

$$M_{\text{PBH}} = \gamma M_{\text{H}} = \frac{4\pi}{3} \gamma \bar{\rho} R_{\text{H}}^3 = \gamma \frac{c^3 t}{G} \simeq 2.03 \times 10^5 \gamma \left( \frac{t}{1 \text{ sec}} \right) M_{\odot}, \quad (2.39)$$

where  $\gamma \lesssim 1$  is the numerical factor and depends on the details of gravitational collapse. The mean density and the Hubble radius are denoted by  $\bar{\rho}$  and  $R_{\text{H}}$ , respectively. In the third equality, we use the relation  $R_{\text{H}} = c/H = 2ct$  with the Hubble parameter obtained from the Friedmann equation,

$$H^2 = \frac{8\pi G}{3c^2} \bar{\rho} = \frac{4\pi^3 G k_{\text{B}}^4}{45 \hbar^3 c^5} g_{\star} T^4, \quad (2.40)$$

where  $g_{\star}$  represents the number of relativistic degrees of freedom. The collapsing time  $t$  can be calculated by integrating the Friedmann equation, being expressed as,

$$t = \sqrt{\frac{45}{16\pi^3 g_{\star}}} \hbar c^2 m_{\text{Pl}} (k_{\text{B}} T)^{-2} \simeq 0.738 \left( \frac{g_{\star}}{10.75} \right)^{-\frac{1}{2}} \left( \frac{k_{\text{B}} T}{1 \text{ MeV}} \right)^{-2} \text{ sec}. \quad (2.41)$$

Here,  $m_{\text{Pl}} = \sqrt{\hbar c/G}$  represents the Planck mass. From Eq. (2.39), we can see that PBHs can form over a wide mass range, with the minimum mass corresponding to those that

collapsed at the Planck time,  $t \simeq 10^{-43}$  sec, yielding  $M_{\text{PBH}} \simeq 10^{-5}$  g. Assuming adiabatic expansion after PBH formation, the initial mass fraction can be expressed as

$$\begin{aligned} \beta(M_{\text{PBH}}) &= \frac{\rho_{\text{PBH}}(t_i)}{\bar{\rho}(t_i)} = \frac{4M_{\text{PBH}} n_{\text{PBH}}(t_0)}{3k_{\text{B}}T_i s(t_0)} \\ &\simeq 7.06 \times 10^{-18} \gamma^{-\frac{1}{2}} \left(\frac{h}{0.67}\right)^2 \left(\frac{g_{\star i}}{106.75}\right)^{\frac{1}{4}} \left(\frac{M_{\text{PBH}}}{10^{15} \text{ g}}\right)^{\frac{1}{2}} \Omega_{\text{PBH}}(M_{\text{PBH}}), \end{aligned} \quad (2.42)$$

where  $\Omega_{\text{PBH}}(M_{\text{PBH}})$  is the present-day density parameter defined by

$$\Omega_{\text{PBH}}(M_{\text{PBH}}) = \frac{\rho_{\text{PBH}}(t_0)}{\rho_{\text{cr}}(t_0)}, \quad (2.43)$$

with  $\rho_{\text{cr}}$  being the critical density. To derive Eq. (2.42), we use the relation  $\bar{\rho} = 3sk_{\text{B}}T/4$  and conservation of the ratio of the number density to the entropy density  $n_{\text{PBH}}/s$ . Note that the following variable is often used to simplify the expressions,

$$\beta'(M_{\text{PBH}}) = \gamma^{\frac{1}{2}} \left(\frac{h}{0.67}\right)^{-2} \left(\frac{g_{\star i}}{106.75}\right)^{-\frac{1}{4}} \beta(M_{\text{PBH}}). \quad (2.44)$$

While PBHs with masses smaller than  $10^{15}$  g would have evaporated by now due to Hawking radiation, those with masses larger than  $10^{15}$  g can survive to the present day and potentially contribute to the dark matter content of the universe. For non-evaporated PBHs, the fraction contributing to dark matter is parameterized by

$$f_{\text{PBH}}(M_{\text{PBH}}) = \frac{\Omega_{\text{PBH}}(M_{\text{PBH}})}{\Omega_{\text{CDM}}} \simeq 3.81 \times 10^8 \beta'(M_{\text{PBH}}) \left(\frac{M_{\text{PBH}}}{M_{\odot}}\right)^{-\frac{1}{2}}. \quad (2.45)$$

Thus, the current abundance of PBHs is parameterized by their mass  $M_{\text{PBH}}$  and their mass fraction  $f_{\text{PBH}}$ . Since the relation between these parameters depends on the formation mechanism of the PBHs, i.e.,  $\beta'$  in Eq. (2.45), observational constraints on these parameters are essential.

As an example, we consider the scenario where collapse occurs from inhomogeneities during the radiation-dominant era. When the equation of state is represented by  $p = \omega\rho c^2$  with  $\omega = 1/3$  for radiation, the overdensity must exceed the threshold value  $\delta_{\text{c}} \simeq \omega$  to overcome the pressure to collapse. The probability distribution of the smoothed density contrast over a scale corresponding to the horizon radius  $\delta(R_{\text{H}})$  is expressed with a Gaussian window function as

$$p(\delta(R_{\text{H}})) = \frac{1}{\sqrt{2\pi}\sigma(R_{\text{H}})} \exp\left(-\frac{\delta^2(R_{\text{H}})}{2\sigma^2(R_{\text{H}})}\right), \quad (2.46)$$

where  $\sigma(R_{\text{H}})$  is the variance of mass fluctuation within the Hubble horizon, given by,

$$\sigma^2(R_{\text{H}}) = \int_0^{\infty} \tilde{W}^2(kR_{\text{H}}) P_{\text{in}}(k) \frac{dk}{k}. \quad (2.47)$$

Here,  $\tilde{W}^2(kR_{\text{H}}) = \exp(-\frac{1}{2}k^2R_{\text{H}}^2)$  is the Fourier transform of the Gaussian window function, and  $P_{\text{in}}(k)$  is the primordial matter power spectrum. Using the Press-Schechter

formalism [132], the initial mass fraction of PBHs can be expressed with the complementary error function as,

$$\beta(M_{\text{PBH}}) = 2 \int_{\delta_c}^{\infty} p(\delta(R_{\text{H}})) d\delta(R_{\text{H}}) = \text{erfc} \left( \frac{\delta_c}{\sqrt{2}\sigma(R_{\text{H}})} \right). \quad (2.48)$$

Since the above expression shows the initial mass fraction for a given PBH mass, the relation between the PBH mass  $M_{\text{PBH}}$  and their mass fraction  $f_{\text{PBH}}$  is specified in this specific scenario [133].

The PBH mass and the mass fraction of PBH to total dark matter are constrained by broad observational targets. One of the most effective methods is the analysis of microlensing events. One example comes from the Subaru Hyper Suprime-Cam (HSC) observation of M31, where tens of millions of stars were monitored for seven hours. This search yielded only a single microlensing event, leading to an upper limit on the mass fraction with PBH mass in the range  $M_{\text{PBH}} = 10^{-11}$  to  $10^{-6} M_{\odot}$  [134]. This constraint is further refined by [135] using data from the Panchromatic Hubble Andromeda Treasury (PHAT) survey, resulting in a weaker limit. The ultra-high magnification event Icarus [44], observed during two-year HST observation, places constraints on PBHs in the range  $M_{\text{PBH}} = 10^{-5}$  to  $10^4 M_{\odot}$  by considering the peak magnification [136]. Similarly, the EROS-2 project, which monitored millions of stars in the Magellanic Clouds over 6.7 years, finds an optical depth lower than expected, constraining PBHs in the range  $0.6 \times 10^{-7} M_{\odot} < M_{\text{PBH}} < 15 M_{\odot}$  when combined with EROS-1 results [137]. The MACHO project places constraints in the range  $M_{\text{PBH}} = 10^{-6}$  to  $10^{-3} M_{\odot}$  based on the non-detection of long-duration microlensing events toward the Large Magellanic Cloud (LMC) [138]. Furthermore, the OGLE survey analyzes 2622 microlensing events from five years of Galactic bulge observations, constraining PBHs in the range  $M_{\text{PBH}} = 10^{-6}$  to  $10^{-3} M_{\odot}$  under the null hypothesis that PBH microlensing events are absent [139]. Extending the monitoring to 80 million stars in the LMC for 20 years, no events with durations longer than one year are found, resulting in the most stringent constraint to date for  $M_{\text{PBH}} = 10^{-6}$  to  $10^3 M_{\odot}$  [140]. Data from the two-year observation by the Kepler satellite, searching for short-duration microlensing bumps, excludes PBHs in the range  $M_{\text{PBH}} = 2 \times 10^{-9}$  to  $10^{-7} M_{\odot}$  due to the lack of detections [141, 142]. Gravitational lensing magnification probabilities of type Ia supernovae also constrain the mass fraction in the mass range  $M_{\text{PBH}} > 0.01 M_{\odot}$ , with the lower limit of the mass determined by the ratio of the supernova size to the lens Einstein radius [143]. Finally, millilens searches using high-quality very long baseline interferometry (VLBI) maps of 300 sources constrain PBHs in the mass range  $M_{\text{PBH}} = 10^6$  to  $10^8 M_{\odot}$  [144].

In addition to the constraints from microlensing events listed above, the parameter space of PBHs can also be constrained by dynamical processes. These include the dynamical evolution of stars in the dwarf galaxy Segue I [145], the effect of dynamical heating on the ultra-faint dwarf galaxy Eridanus II [146], the dynamical motion of 26 member stars in Eridanus II observed by the MUSE-Faint survey using the Multi Unit Spectroscopic Explorer on the Very Large Telescope (VLT) [147], and the disruption of wide binary systems [148]. Moreover, the impact of accreting PBHs on the CMB frequency spectrum, as well as on the angular temperature and polarization power spectra, provides constraints on the PBH abundance [149]. Additionally, the merger rate of black hole binaries detected by the Laser Interferometer Gravitational-Wave Observatory (LIGO), Virgo, and KAGRA constrain the PBH parameter space [150, 151]. These studies suggest that PBHs may not account for the entire dark matter components except for the mass window be-

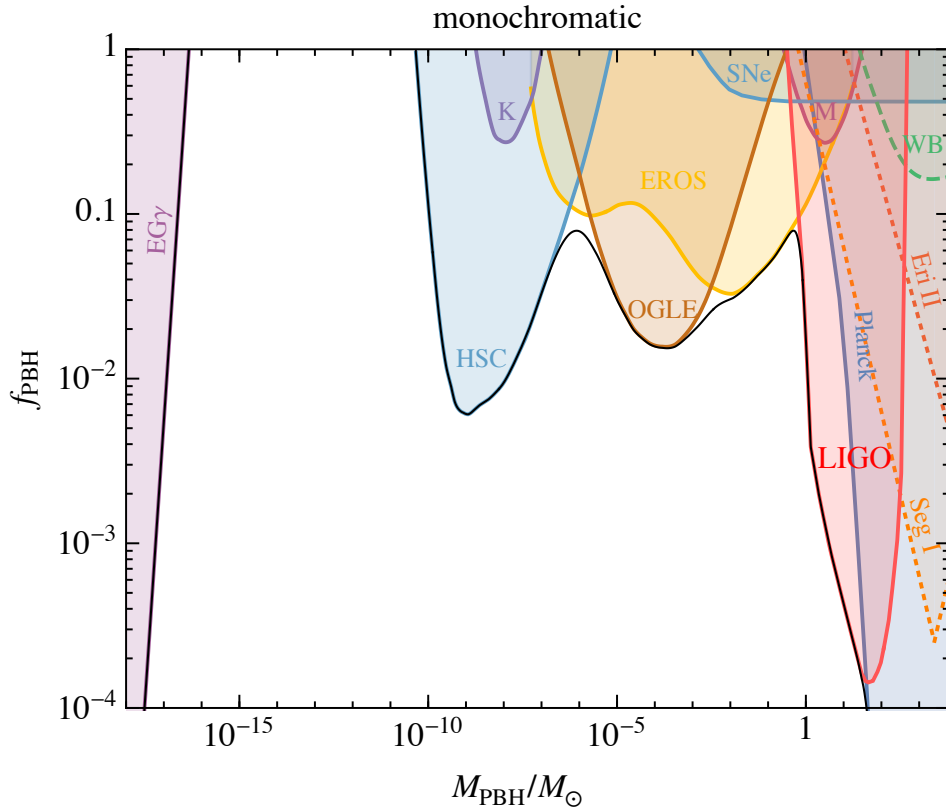


Figure 2.2: The previous constraints on the PBH mass and mass fraction of PBH to the total dark matter, assuming the monochromatic function. The purple region is excluded by evaporations [152]. The blue, violet, yellow, brown, purple and light blue regions by the microlensing results from HSC [134], Kepler [142], EROS [137], OGLE [139], MACHO [138] and supernovae (SNe) [143], respectively. The red and blue regions on the right are excluded by LIGO/Virgo [150] and Planck data [149]. The broken lines show the constraints from dynamical processes, including the survival of stars in Segue I (orange) [145] and Eridanus II (dark orange) [146], and the survival of wide binaries (green) [148]. The black solid lines show the combined constraint. This figure is adapted from [124].

tween  $M_{\text{PBH}} \simeq 10^{-15} - 10^{-11} M_{\odot}$ . In Fig. 2.2, the summary of the PBH constraints is shown.

# Chapter 3

## Fuzzy dark matter

Fuzzy dark matter (FDM) is one of the alternatives to cold dark matter (CDM) to alleviate small-scale problems [34]. The FDM consists of scalar particles minimally coupled to gravity with negligible self-interaction whose mass is around  $m \simeq 10^{-24} - 10^{-20} \text{ eV}/c^2$ . Such a small mass results in the de Broglie wavelengths on a cosmological scale,

$$\frac{\lambda_{\text{dB}}}{2\pi} = \frac{\hbar}{mv} = 1.92 \text{ kpc} \left( \frac{mc^2}{10^{-22} \text{ eV}} \right)^{-1} \left( \frac{v}{10 \text{ km/s}} \right)^{-1}. \quad (3.1)$$

Since the de Broglie wavelength defines the scale at which wave-like behavior dominates, the small-scale structure formation is influenced by the wave nature of the FDM, which could potentially address the small-scale problems.

In this chapter, we start with reviews of the basic equations in Sec. 3.1, the linear structure formation in Sec. 3.2, and the nonlinear structures in Sec. 3.3. In Sec. 3.4, we show the core-halo mass relation based on our recent work presented in [47]. In the rest of this chapter, we review the distribution of FDM subhalos in Sec. 3.5, and the sub-galactic matter power spectrum in Sec. 3.6. Finally, we show the current constraints on the FDM mass from various observations in Sec. 3.7. From the following in this chapter, we use the natural unit  $c = \hbar = k_{\text{B}} = 1$ .

### 3.1 Schrödinger-Poisson equation

To obtain the governing equation of the FDM, we start with the action of a scalar field minimally coupled to the gravity without self-interaction [153, 154, 155],

$$S = \int d^4x \sqrt{-g} \mathcal{L}, \quad (3.2)$$

where the Lagrangian is given by

$$\mathcal{L} = -\frac{1}{2} g^{\mu\nu} \partial_\mu \phi \partial_\nu \phi - \frac{1}{2} m^2 \phi^2, \quad (3.3)$$

with  $m$  being the mass of the FDM and  $g$  being the determinant of the metric  $g_{\mu\nu}$ . The first and second terms indicate the kinetic and mass terms, respectively. The equation of motion (EoM) of the scalar field can be obtained by taking the variation of the action, which results in the Euler-Lagrange equation,

$$\frac{\delta(\mathcal{L}\sqrt{-g})}{\delta\phi} - \partial_\mu \left( \frac{\delta(\mathcal{L}\sqrt{-g})}{\delta(\partial_\mu\phi)} \right) = 0. \quad (3.4)$$

By substituting the Lagrangian given by Eq. (3.3), we can obtain the EoM, known as the Klein-Gordon equation,

$$(\nabla^\mu \nabla_\mu - m^2) \phi = 0, \quad (3.5)$$

where  $\nabla_\mu$  is the covariant derivative and the first term can be rewritten as

$$\nabla^\mu \nabla_\mu \phi = \frac{1}{\sqrt{-g}} \partial_\mu (\sqrt{-g} \partial^\mu \phi). \quad (3.6)$$

Considering the homogeneous and isotropic metric in the expanding flat universe, known as the Friedmann-Lemaître-Robertson-Walker (FLRW) metric, with the perturbations corresponding to the Newtonian potential  $\Phi(t, \mathbf{x})$  and the spatial curvature  $\Psi(t, \mathbf{x})$ ,

$$g_{\mu\nu}(t, \mathbf{x}) = \begin{pmatrix} -1 - 2\Phi & 0 & 0 & 0 \\ 0 & a^2(t)(1 - 2\Psi) & 0 & 0 \\ 0 & 0 & a^2(t)(1 - 2\Psi) & 0 \\ 0 & 0 & 0 & a^2(t)(1 - 2\Psi) \end{pmatrix}, \quad (3.7)$$

with  $|\Phi|, |\Psi| \ll 1$ . Note that  $\mathbf{x}$  denotes the comoving coordinate. The inverse of the metric is expressed by

$$g^{\mu\nu}(t, \mathbf{x}) = \begin{pmatrix} -1 + 2\Phi & 0 & 0 & 0 \\ 0 & a^{-2}(t)(1 + 2\Psi) & 0 & 0 \\ 0 & 0 & a^{-2}(t)(1 + 2\Psi) & 0 \\ 0 & 0 & 0 & a^{-2}(t)(1 + 2\Psi) \end{pmatrix}. \quad (3.8)$$

Focusing on non-relativistic matter perturbations on scales far below the horizon, the anisotropic components of the stress tensor become negligible, leading to the relation  $\Psi = \Phi$ . Substituting the metric into the Klein-Gordon equation, Eq. (3.5), we can obtain the following equation,

$$(1 - 2\Phi) \frac{\partial^2 \phi}{\partial t^2} - 4(1 + 2\Phi) \frac{\partial \Phi}{\partial t} \frac{\partial \phi}{\partial t} + 3H(1 - 2\Phi) \frac{\partial \phi}{\partial t} - \frac{1}{a^2} (1 + 2\Phi) \nabla^2 \phi + m^2 \phi = 0. \quad (3.9)$$

Since the de Broglie wavelength of the FDM is larger than the inter-particle distance, the wavefunction of the FDM overlaps and the macroscopic number of the FDM particles are in the same state, *i.e.*, the coherent state, resulting in FDM behaving non-relativistically. To take the non-relativistic limit of the Klein-Gordon equation and obtain the wavefunction  $\psi$  of the coherent state, the following relation is used to remove the rest energy,

$$\phi(t, \mathbf{x}) = \frac{1}{\sqrt{2m}} (\psi(t, \mathbf{x}) e^{-imt} + \psi^*(t, \mathbf{x}) e^{imt}). \quad (3.10)$$

Here, the complex conjugate of the wavefunction in the second term corresponds to the antiparticle of the FDM. Note that the mass dependence of the coefficient is introduced to compensate for the difference of the mass dimensions,  $[\phi] = 1$  and  $[\psi] = 3/2$ . By substituting Eq. (3.10) into Eq. (3.9), the non-linear Schrödinger equation can be obtained,

$$i \left( \frac{\partial \psi}{\partial t} + \frac{3}{2} H \psi \right) = -\frac{1}{2ma^2} \nabla^2 \psi + m\Phi \psi, \quad (3.11)$$

where the non-relativistic relation  $i\partial/\partial t \ll m$  and  $\Phi \ll 1$  are used to obtain this equation.

Since the non-linear Schrödinger equation describes the dynamics of the coherent state, it can also be obtained from the Heisenberg equation of motion with the second-quantized N-body Hamiltonian [156],

$$\hat{H} = \int d^3x \hat{\Psi}^\dagger(\mathbf{x}) \left( -\frac{1}{2ma^2} \nabla^2 + m\Phi \right) \hat{\Psi}(\mathbf{x}), \quad (3.12)$$

where the Bose operators  $\hat{\Psi}^\dagger(\mathbf{x})$  and  $\hat{\Psi}(\mathbf{x})$  create and annihilate a particle at position  $\mathbf{x}$ , respectively. They satisfy the commutation relation  $[\hat{\Psi}(\mathbf{x}), \hat{\Psi}^\dagger(\mathbf{x}')] = \delta(\mathbf{x} - \mathbf{x}')$ . By using the creation operator  $\hat{a}_i^\dagger$  and the annihilation operator  $\hat{a}_i$  with the subscript  $i$  denoting the state, the Bose operators can be expressed as,

$$\hat{\Psi}^\dagger(\mathbf{x}) = \sum_i \hat{a}_i^\dagger \phi_i^*(\mathbf{x}), \quad (3.13)$$

$$\hat{\Psi}(\mathbf{x}) = \sum_i \hat{a}_i \phi_i(\mathbf{x}). \quad (3.14)$$

Here,  $\phi_i(\mathbf{x}) = \langle \mathbf{x} | 1_i \rangle$  represents the wavefunction for a single particle in the  $i$ -th state,  $|1_i\rangle$ , i.e., the square root of the probability of a single particle locating at  $\mathbf{x}$ . With the creation and annihilation operators, which satisfy the commutation relation  $[a_i, a_j^\dagger] = \delta_{ij}$ , the state can be expressed as  $\hat{a}_i^\dagger |0\rangle = |1_i\rangle$  and  $\hat{a}_i |1_i\rangle = |0\rangle$ . Now the Heisenberg equation is calculated as

$$i \frac{\partial \hat{\Psi}(t, \mathbf{x})}{\partial t} = [\hat{\Psi}(t, \mathbf{x}), H(t)] = \left( -\frac{1}{2ma^2} \nabla^2 + m\Phi \right) \hat{\Psi}(t, \mathbf{x}). \quad (3.15)$$

By applying the Bogoliubov's prescription or the mean-field approximation,

$$\hat{\Psi}(t, \mathbf{x}) = \langle \hat{\Psi}(t, \mathbf{x}) \rangle + \delta \hat{\Psi}(t, \mathbf{x}) \equiv \psi(t, \mathbf{x}) + \delta \hat{\Psi}(t, \mathbf{x}), \quad (3.16)$$

where the ensemble average is taken in terms of the second quantization, and by substituting Eq. (3.16) into Eq. (3.15), we can obtain the non-linear Schrödinger equation with the classical wavefunction  $\psi$ . Note that the wave nature is incorporated in the Schrödinger equation since  $\psi$  is first-quantized.

The Newtonian potential satisfies the Poisson equation, which can be obtained from the first-order perturbation of the time-time component of the Einstein equation. The Einstein equation is

$$G^\mu{}_\nu = 8\pi G T^\mu{}_\nu. \quad (3.17)$$

The energy-momentum tensor can be defined from the Lagrangian as

$$T_{\mu\nu} = -\frac{2}{\sqrt{-g}} \frac{\partial(\mathcal{L}\sqrt{-g})}{\partial g^{\mu\nu}}. \quad (3.18)$$

By substituting the Lagrangian of the scalar field, Eq. (3.3), it can be expressed as

$$T^\mu{}_\nu = g^{\mu\alpha} \frac{\partial\phi}{\partial x^\alpha} \frac{\partial\phi}{\partial x^\nu} - g^\mu{}_\nu \left( \frac{1}{2} g^{\alpha\beta} \frac{\partial\phi}{\partial x^\alpha} \frac{\partial\phi}{\partial x^\beta} + \frac{1}{2} m^2 \phi^2 \right). \quad (3.19)$$

The time-time component of the energy-momentum tensor is

$$T^0{}_0 = \frac{1}{2} (-1 + 2\Phi) \left( \frac{\partial\phi}{\partial t} \right)^2 - \frac{1}{2} a^{-2} (1 + 2\Phi) (\nabla\phi)^2 - \frac{1}{2} m^2 \phi^2. \quad (3.20)$$

Since the spatial derivative of  $\phi$  can be neglected for the homogeneous part of the field, it can be written as

$$T_0^0 \simeq -\frac{1}{2} \left( \frac{\partial \phi}{\partial t} \right)^2 - \frac{1}{2} m^2 \phi^2. \quad (3.21)$$

From the relation  $T_0^0 = g_{00} T^{00} \simeq -\rho$ , the density of the scalar field can be expressed as

$$\rho = \frac{1}{2} \left( \frac{\partial \phi}{\partial t} \right)^2 + \frac{1}{2} m^2 \phi^2. \quad (3.22)$$

By substituting Eq. (3.10) and using the condition  $i\partial/\partial t \ll m$ , the density can be written in terms of the wavefunction,

$$\rho = m|\psi|^2. \quad (3.23)$$

Therefore, the first-order perturbation of the right-hand side of the Einstein equation is

$$8\pi G \delta T_0^0 = 8\pi G (m|\psi|^2 - \bar{\rho}), \quad (3.24)$$

where the  $\bar{\rho}$  is the spatially-averaged matter density in the universe. Since the first-order perturbation of the time-time component of the Einstein tensor is expressed by [52]

$$\delta G_0^0 = 6H \frac{\partial \Phi}{\partial t} + 6\Phi H^2 + 2a^{-2} \nabla^2 \Phi, \quad (3.25)$$

we finally obtain the Poisson equation,

$$\nabla^2 \Phi = 4\pi G a^2 (m|\psi|^2 - \bar{\rho}), \quad (3.26)$$

where the super-horizon scale is ignored to obtain the Poisson equation. The Eqs. (3.11) and (3.26) are the governing equations of the FDM, called Schrödinger-Poisson (SP) equation, in the expanding universe.

The SP equation can be transformed into a fluid representation. To do this, we first decompose the wavefunction

$$\psi = |\psi| e^{i\theta} = \sqrt{\frac{\rho}{m}} e^{i\theta}, \quad (3.27)$$

where the phase of the wavefunction is related to the velocity,

$$\mathbf{v} = \frac{1}{ma} \nabla \theta. \quad (3.28)$$

By substituting Eqs. (3.27) and (3.28) into Eq. (3.11), the fluid equations are obtained, called the Madelung equation [157],

$$\frac{\partial \rho}{\partial t} + 3H\rho + \frac{1}{a} \nabla \cdot (\rho \mathbf{v}) = 0, \quad (3.29)$$

$$\frac{\partial \mathbf{v}}{\partial t} + H\mathbf{v} + \frac{1}{a} (\mathbf{v} \cdot \nabla) \mathbf{v} = -\frac{1}{a} \nabla \Phi + \frac{1}{2m^2 a^3} \nabla \left( \frac{\nabla^2 \sqrt{\rho}}{\sqrt{\rho}} \right). \quad (3.30)$$

Here, Eq. (3.29) represents the continuity equation and Eq. (3.30) is the Euler equation, which are obtained from the imaginary and real parts, respectively. The second term on the right-hand side of the Eq. (3.30) is called the quantum pressure term, which originates from the uncertainty principle. The Euler equation in the FDM model has a similar form to the Jeans equation obtained from the Boltzmann equation, however,

they have different natures of the pressure terms. While the quantum pressure term is solely determined by the density profile, the pressure term in the Jeans equation needs the local velocity dispersion as well as the density profile. It means that while the Madelung equation is the closed form, the latter needs an effective equation of state, which relates the velocity dispersion and the density, to solve the evolution of the system. The quantum pressure term is expressed by the divergence of the stress tensor as

$$\nabla \cdot \boldsymbol{\sigma} = \frac{\rho}{2m^2 a^2} \nabla \left( \frac{\nabla^2 \sqrt{\rho}}{\sqrt{\rho}} \right), \quad (3.31)$$

$$\sigma_{ij} = \frac{\rho}{4m^2 a^2} \frac{\partial^2 \log \rho}{\partial x_i \partial x_j}. \quad (3.32)$$

The Madelung equation is not fully consistent with the SP equation since the velocity is ill-defined where the density equals zero. Equivalently, the Madelung equation only considers a vortex-free fluid since the condition  $\nabla \times \mathbf{v} = \mathbf{0}$  satisfies. By imposing the additional quantization condition,

$$\oint_L \mathbf{v} \cdot d\mathbf{l} = 2\pi j \quad (3.33)$$

with  $j \in \mathbb{Z}$  is needed to be equivalent [158].

## 3.2 Linear structure formation

The linear structure formation can be studied using the Madelung equation. By taking the spatial average of the continuity equation, Eq. (3.29) can be expressed as

$$\frac{d}{dt}(\bar{\rho} a^3) = 0, \quad (3.34)$$

which is consistent with the conservation law of the matter density in the expanding universe. The fluctuation of the density can be obtained by subtracting the spatially averaged density,

$$\delta = \frac{\rho - \bar{\rho}}{\bar{\rho}}. \quad (3.35)$$

Now we can rewrite the Madelung equation in terms of the fluctuation  $\delta$ . In the linear regime where the conditions  $\delta, \mathbf{v}, \Phi \ll 1$  satisfy, the continuity equation becomes

$$\frac{\partial \delta}{\partial t} + \frac{1}{a} \nabla \cdot \mathbf{v} = 0, \quad (3.36)$$

and the Euler equation is

$$\frac{\partial \mathbf{v}}{\partial t} + H \mathbf{v} = -\frac{1}{a} \nabla \Phi + \frac{1}{4m^2 a^3} \nabla^3 \delta. \quad (3.37)$$

By applying  $(\partial/\partial t + 2H)$  to Eq. (3.36) and  $a^{-1} \nabla$  to Eq. (3.37), and then taking the difference of them, we can obtain the evolution equation of the density fluctuation,

$$\frac{\partial^2 \delta}{\partial t^2} + 2H \frac{\partial \delta}{\partial t} + \left( \frac{1}{4m^2 a^4} \nabla^4 - 4\pi G \bar{\rho} \right) \delta = 0. \quad (3.38)$$

It is useful to Fourier transform the fluctuation  $\delta$  as,

$$\delta(t, \mathbf{x}) = \int \frac{d^3k}{(2\pi)^3} e^{i\mathbf{k}\cdot\mathbf{x}} \tilde{\delta}(t, \mathbf{k}). \quad (3.39)$$

The evolution of the fluctuation in the Fourier mode is

$$\frac{\partial^2 \tilde{\delta}}{\partial t^2} + 2H \frac{\partial \tilde{\delta}}{\partial t} + \left( \frac{k^4}{4m^2 a^4} - 4\pi G \bar{\rho} \right) \tilde{\delta} = 0. \quad (3.40)$$

From the third term, the sound speed originating from the quantum pressure can be defined as

$$c_s^2 = \frac{k^2}{4m^2 a^2}. \quad (3.41)$$

Equation (3.40) is equivalent to the equation for a particle in motion undergoing friction in a time-varying potential,

$$V[\tilde{\delta}] = -\frac{1}{2} \left( 4\pi G \bar{\rho} - \frac{k^4}{4m^2 a^4} \right) \tilde{\delta}^2. \quad (3.42)$$

The comoving Jeans scale  $k_J$  can be defined from Eq. (3.40), below which the structure formation is suppressed. It can be expressed as [159]

$$\begin{aligned} k_J &= (16\pi G m^2 \bar{\rho} a^4)^{\frac{1}{4}} \\ &= 70 a^{\frac{1}{4}} \left( \frac{\Omega_{m0}}{0.3} \right)^{\frac{1}{4}} \left( \frac{H_0}{70 \text{ km s}^{-1} \text{ Mpc}^{-1}} \right)^{\frac{1}{2}} \left( \frac{mc^2}{10^{-22} \text{ eV}} \right)^{\frac{1}{2}} \text{ Mpc}^{-1}, \end{aligned} \quad (3.43)$$

where the Friedmann equation is used in the second equality. The corresponding Jeans mass is

$$M_J = \frac{4\pi}{3} \bar{\rho} \left( \frac{\pi}{k_J} \right)^3 \simeq 1.5 \times 10^7 a^{-\frac{3}{4}} \left( \frac{\Omega_{m0}}{0.3} \right)^{\frac{1}{4}} \left( \frac{m}{10^{-22} \text{ eV}} \right)^{-\frac{3}{2}} M_{\odot}. \quad (3.44)$$

When the scale of the fluctuation is larger than the Jeans scale,  $k \lesssim k_J$ , the potential given by Eq. (3.42) is a convex downward function and the fluctuation grows as the same as in the CDM universe. Below the Jeans scale,  $k \gtrsim k_J$ , the potential is a convex upward function, and the fluctuation evolved to zero, *i.e.*, the structure is suppressed. To be precise, the comoving Jeans scale evolves as  $k_J = \text{const.}$  in the radiation dominant era and  $k_J \propto a^{1/4}$  in the matter dominant era. From this behavior, the suppression of the linear matter power spectrum is expected to occur below the Jeans scale at the matter-radiation equality,

$$k_{\text{Jeq}} = 9 \left( \frac{mc^2}{10^{-22} \text{ eV}} \right)^{\frac{1}{2}} \text{ Mpc}^{-1}, \quad (3.45)$$

where we use the relation  $a_{\text{eq}} = \Omega_{r0}/\Omega_{m0}$  and  $\Omega_{r0} h^2 = 4.15 \times 10^{-5}$  [52] to obtain this equation. Indeed, the numerical simulation shows that the linear power in the FDM model is suppressed than that in the CDM model as [34],

$$P_{\text{FDM}}(k) = T_{\text{F}}^2(k) P_{\text{CDM}}(k), \quad (3.46)$$

where the suppression function is

$$T_{\text{F}}(k) \simeq \frac{\cos x^3}{1 + x^8}, \quad (3.47)$$

with  $x = 1.61(mc^2/10^{-22} \text{ eV})^{1/18} k/k_{\text{Jeq}}$ . The half-mode scale is defined where the linear power drops by a factor of four [34, 159],

$$k_{\text{hm}} \simeq 0.57 k_{\text{Jeq}} \left( \frac{mc^2}{10^{-22} \text{ eV}} \right)^{-\frac{1}{18}} = 5.1 \left( \frac{mc^2}{10^{-22} \text{ eV}} \right)^{\frac{4}{9}} \text{ Mpc}^{-1}. \quad (3.48)$$

The corresponding mass called half-mode mass is,

$$M_{\text{hm}} = \frac{4\pi}{3} \bar{\rho} \left( \frac{\pi}{k_{\text{hm}}} \right)^3 \simeq 3.8 \times 10^{10} M_{\odot} \left( \frac{mc^2}{10^{-22} \text{ eV}} \right)^{-\frac{4}{3}}. \quad (3.49)$$

Due to the suppression of the linear power spectrum, related properties such as the concentration parameter of halos and the subhalo mass function would be different as shown in the following sections.

### 3.3 FDM halo

The nonlinear structure formation, where the fluctuation is  $\delta \gtrsim 1$ , is studied with simulations [160, 161]. When considering the dynamics of collapsed objects, the effect of the cosmic expansion is minimal. In this case, the SP equation is expressed by

$$i \frac{\partial \psi}{\partial t} = -\frac{1}{2m} \nabla^2 \psi + m \Phi \psi, \quad (3.50)$$

$$\nabla^2 \Phi = 4\pi G m |\psi|^2. \quad (3.51)$$

Note that the Poisson equation is obtained directly from the time-time component of the Einstein equation, *i.e.*, not from the first-order perturbation. The SP equation is invariant under the following transformation [162],

$$\{x, t, \rho, m, \psi, \Phi, M\} \rightarrow \{\alpha x, \beta t, \beta^{-2} \rho, \alpha^{-2} \beta m, \alpha \beta^{-3/2} \psi, \alpha^2 \beta^{-2} \Phi, \alpha^3 \beta^{-2} M\}, \quad (3.52)$$

which is a crucial feature of the density profile of the FDM halo as described below.

The FDM halos have two important features, the soliton core located at the center of each halo and the granular structures existing all over the halos, as shown in Fig. 3.1. The presence of these non-linear structures has been revealed by the FDM simulations solving the SP equation (*e.g.*, [160, 161]). Although some simulations solve the Madelung equation (*e.g.*, [163]), they might not properly capture small-scale features since they cannot properly handle the dynamics at  $\rho = 0$ , as mentioned in Sec. 3.1.

#### 3.3.1 Soliton core

The soliton core is the ground state object and the density profile is empirically expressed as [160]

$$\rho_{\text{sol}}(r) = \frac{\rho_c}{\{1 + 0.091(r/r_c)^2\}^8}, \quad (3.53)$$

where  $r_c$  and  $\rho_c$  are the core radius and core density, respectively. The core radius is defined where the density drops by half. The core density is related to the core radius and the FDM mass as

$$\rho_c = 0.019 \left( \frac{mc^2}{10^{-22} \text{ eV}} \right)^{-2} \left( \frac{r_c}{\text{kpc}} \right)^{-4} M_{\odot} \text{ pc}^{-3}. \quad (3.54)$$

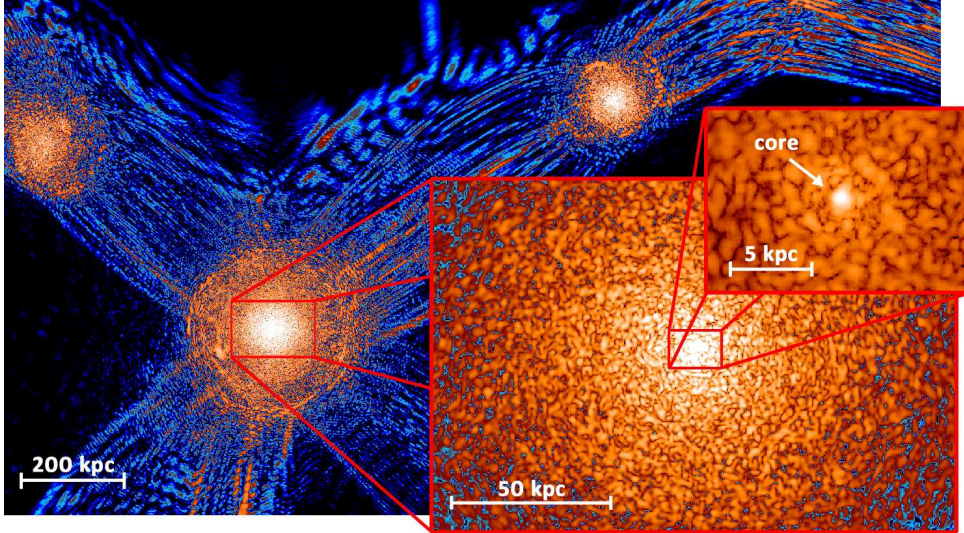


Figure 3.1: The slice of the density profile of the FDM simulation at redshift  $z = 0.1$ . The soliton core resides in the center of the halo, while the granular structure resides outside the core. These non-linear structures originate from the wave-like nature of FDM. This figure is taken from [160].

From the empirical form of the core profile, the density is constant as a function of the radius below the core radius and then drops sharply at radii larger than the core radius. Since the soliton core can be expressed by the ground state solution of the SP equation, the core radius can be estimated as the de Broglie wavelength of the FDM. The core mass is defined as the enclosed mass within the core radius,

$$M_c = M_{\text{sol}}(< r_c) = \int_0^{r_c} 4\pi r^2 dr \rho_{\text{sol}}(r) = 5.3 \times 10^7 \left( \frac{mc^2}{10^{-22} \text{ eV}} \right)^{-2} \left( \frac{r_c}{\text{kpc}} \right)^{-1} M_{\odot}. \quad (3.55)$$

For a given FDM mass, the shape of the soliton core can be determined by a single parameter such as the core radius or the core mass. As can be seen from Eqs. (3.54) and (3.55), the central density becomes smaller and the core mass becomes smaller with the larger core radius. These relations satisfy the scaling relation of the SP equation shown in Eq. (3.52).

### 3.3.2 Granular structures

The outer region of the halo consists of numerous granular structures, mainly originating from the interference of waves in excited states. Since the wavelength of each wavefunction is approximately the de Broglie wavelength, the size of the granular structures is also the same size. While the outskirts density profile is oscillating, the FDM simulations find that the spatially averaged density profile is expressed by the NFW profile. Here, we first present recent models of the outer density profile [164], which account for granular structures, followed by a review of the concentration parameter in FDM halos.

#### Outer density profile

Since the outer density profile consists of numerous granular structures, we begin by considering the internal density profile of each structure. The mass of a granular structure

at position  $\mathbf{r}'$ ,  $M_c(\mathbf{r}')$ , can be estimated using the local average density of the halo,  $\rho_{\text{NFW}}(\mathbf{r}')$ , as

$$M_c(\mathbf{r}') = \rho_{\text{NFW}}(\mathbf{r}')V_c, \quad (3.56)$$

where  $V_c$  is the volume of each granular structure determined by the de Broglie wavelength,

$$V_c = \frac{4}{3}\pi \left(\frac{\lambda_{\text{dB}}}{2}\right)^3. \quad (3.57)$$

The internal density profile of a granular structure can be expressed in terms of a normalized mass function  $u(\mathbf{r} - \mathbf{r}')$  as

$$\rho_c(\mathbf{r}; \mathbf{r}') = M_c(\mathbf{r}')u(\mathbf{r} - \mathbf{r}'). \quad (3.58)$$

To ensure proper normalization, the mass function must satisfy

$$\int_V d^3r u(\mathbf{r} - \mathbf{r}') = \int_{V_\epsilon(\mathbf{r}')} d^3r u(\mathbf{r} - \mathbf{r}') = 1, \quad (3.59)$$

where  $V_\epsilon(\mathbf{r}')$  is a three-dimensional sphere centered at  $\mathbf{r}'$ , which is small compared to the size of the halo but larger than the size of each clump. The mass function can be chosen as a Gaussian, with the variance set to half the de Broglie wavelength,

$$u(\mathbf{r} - \mathbf{r}') = \sqrt{\frac{2}{\pi\lambda_{\text{dB}}^2}} \exp\left(-\frac{2|\mathbf{r} - \mathbf{r}'|^2}{\lambda_{\text{dB}}^2}\right), \quad (3.60)$$

which is consistent with the numerical simulation conducted by [165], where the Widrow-Kaiser ansatz [166] is applied to reconstruct the density profile of the FDM halos. Assuming that the granular structures are randomly distributed on small scales while maintaining a fixed ensemble average for the number density, the density profile of the FDM halo can be described as a superposition of these randomly distributed clumps,

$$\rho_{\text{out}}(\mathbf{r}) = \int_V d^3r' \rho_c(\mathbf{r}; \mathbf{r}')n(\mathbf{r}') = \int_V d^3r' \rho_{\text{NFW}}(\mathbf{r}')V_c n(\mathbf{r}')u(\mathbf{r} - \mathbf{r}'), \quad (3.61)$$

where  $n(\mathbf{r})$  represents the number density of granular structures. Since  $\rho_{\text{NFW}}(\mathbf{r})$  is assumed to remain constant within the small  $V_\epsilon$  sphere, this can be further simplified to

$$\rho_{\text{out}}(\mathbf{r}) = \rho_{\text{NFW}}(\mathbf{r}) \int_{V_\epsilon} d^3r' V_c n(\mathbf{r}')u(\mathbf{r} - \mathbf{r}'), \quad (3.62)$$

which is a general formula to characterize the outer profile of the FDM halo incorporating the granular structures. Let each clump be indexed by  $j$ , with its center located at  $\mathbf{r}_j$ . Then, the number density  $n(\mathbf{r}')$  can be expressed using the Dirac delta function as

$$n(\mathbf{r}') = \sum_j \delta_{\text{D}}^{(3)}(\mathbf{r}' - \mathbf{r}_j). \quad (3.63)$$

Considering that the granular structures are distributed throughout the halos, the ensemble average of the number density  $\langle n(\mathbf{r}) \rangle$  should be set to  $V_c^{-1}$ . The ensemble average of the FDM density is then expressed as,

$$\langle \rho_{\text{out}}(\mathbf{r}) \rangle = \rho_{\text{NFW}}(\mathbf{r}), \quad (3.64)$$

which aligns with the assumed average halo profile.

### NFW profile

The spatially averaged density profile outside the soliton core is known to be described by the NFW profile. As reviewed in Sec. 2.1.3, the concentration parameter and halo mass determine the shape of the NFW profile. We review recent studies on the relation between the concentration parameter and the halo mass, i.e., the  $c_{\text{vir}}-M_{\text{h}}$  relation, in FDM halos [167, 168]. These studies predict the different halo mass dependence on the concentration parameter.

The  $c_{\text{vir}}-M_{\text{h}}$  relation studied in [167] is based on the warm dark matter (WDM) scenario discussed in [100], where the linear power spectrum is suppressed on small scales, similar to the case of FDM. The suppression of the linear power spectrum delays structure formation, leading to smaller values of the concentration parameter compared to the CDM case since it correlates with the average density of the universe at the time of collapse. However, WDM simulation indicates that the concentration parameter is suppressed at even lower halo masses than the theoretical prediction by [58], i.e., Eq. (2.11) with the suppressed linear power spectrum in the WDM model. This turnover behavior is likely attributed to fragmentation from a large halo rather than hierarchical structure formation at small scales. To account for this, the correction term is introduced. By setting the same cutoff scale, this approach can be applied to the FDM case, and it is demonstrated that the concentration parameters in FDM halos can be expressed as

$$c_{\text{vir}}(M_{\text{h}}, z; \text{FDM}) = c_{\text{vir}}^{\text{B}}(M_{\text{h}}, z; \text{FDM}) \Delta^{\text{FDM}}(M_0, \gamma_0, \gamma_1, \gamma_2). \quad (3.65)$$

Here,  $c_{\text{vir}}^{\text{B}}(M_{\text{h}}, z; \text{FDM})$  is calculated using Eq. (2.11) with the FDM linear power spectrum given by Eq. (3.46). The additional suppression factor is represented by  $\Delta^{\text{FDM}}$ , which is expressed as

$$\Delta^{\text{FDM}}(M_0, \gamma_0, \gamma_1, \gamma_2) = \left(1 + \frac{M_0}{f_{\text{coll}} M_{\text{h}}}\right)^{-\gamma_0} \left(1 + \gamma_1 \frac{M_0}{M_{\text{h}}}\right)^{-\gamma_2}, \quad (3.66)$$

where  $\gamma_0 = d \ln c_{\text{vir}}^{\text{B}} / d \ln M_{\text{h}}|_{M_{\text{h}}=4M_0}$ ,  $\gamma_1 = 15$ ,  $\gamma_2 = 0.3$ ,  $f_{\text{coll}} = 0.01$ , and

$$M_0 = 1.6 \times 10^{10} M_{\odot} \left(\frac{mc^2}{10^{-22} \text{ eV}}\right)^{-\frac{4}{3}}. \quad (3.67)$$

The concentration parameters in FDM halos given by Eq. (3.65) can be related to those in CDM halos in the following simpler form [47],

$$c_{\text{vir}}(M_{\text{h}}, z; \text{FDM}) = c_{\text{vir}}(M_{\text{h}}, z; \text{CDM}) F\left(\frac{M_{\text{h}}}{M_{\text{h}}^{\text{hm}}}\right), \quad (3.68)$$

where function  $F$  is defined as  $F(x) = (1 + ax^b)^c$  with  $(a, b, c) = (9.431, -1.175, -0.232)$ , and  $M_{\text{h}}^{\text{hm}}$  is the half mode mass given by Eq. (3.49).

The other  $c_{\text{vir}}-M_{\text{h}}$  relation in FDM halos studied in [168] refers to [169], which studies how the suppressed power spectrum by arbitrary dark matter models affects the concentration parameter. The inability of the theoretical model by [58] to capture the turnover behavior in the  $c_{\text{vir}}-M_{\text{h}}$  relation observed in the WDM simulation is attributed to its inaccurate estimation of the collapse redshift,  $z_{\text{coll}}$ . To resolve this problem, they propose that the concentration parameter  $c_{\text{vir}}^{\chi}$  for any dark matter scenario  $\chi$  can be determined by matching it to the concentration parameter of a CDM halo with the same collapse

redshift. Specifically, if  $z_{\text{coll}}^{\chi}$  represents the collapse redshift of a halo with mass  $M_{\text{h}}^{\chi}$  at redshift  $z$  in scenario  $\chi$ , then the concentration parameter  $c_{\text{vir}}^{\chi}$  is obtained by

$$c_{\text{vir}}^{\chi}(M_{\text{h}}^{\chi}, z) = c_{\text{vir}}(M_{\text{h}}^{\text{CDM}}, z), \quad (3.69)$$

where the halo mass  $M_{\text{h}}^{\text{CDM}}$  is determined by the same collapse redshift,

$$z_{\text{coll}}^{\chi}(M_{\text{h}}^{\chi}, z) = z_{\text{coll}}^{\text{CDM}}(M_{\text{h}}^{\text{CDM}}, z). \quad (3.70)$$

Here, the collapse redshifts can be calculated by Eq. (2.12) for given linear power spectra. This method allows the prediction of concentration parameters in various dark matter scenarios and shows good agreement with WDM simulation results. Based on this formulation, the  $c_{\text{vir}}-M_{\text{h}}$  relation in FDM halos can be expressed as [168]

$$c_{\text{vir}}(M_{\text{h}}, z; \text{FDM}) = c_{\text{vir}}(M_{\text{h}}, z; \text{CDM}) F\left(\frac{M_{\text{h}}}{M_{\text{h}}^{\text{hm}}}\right), \quad (3.71)$$

with the function  $F$  is the same as Eq. (3.68) but with different parameter sets,  $(a, b, c) = (5.496, -1.648, -0.417)$ .

Fig. 3.2 shows compare the  $c_{\text{vir}}-M_{\text{h}}$  relations between predictions by [167] and [168] as well as the CDM case. Here, the  $c_{\text{vir}}-M_{\text{h}}$  relation for CDM halos, which is derived by the largest CDM simulation [55], is shown by using the COLOSSUS [170]. While both models predict that the turnover of the  $c_{\text{vir}}-M_{\text{h}}$  relation occurs around  $M_{\text{h}} \simeq 4M_{\text{h}}^{\text{hm}} (\equiv M_{\text{h}}^{\text{4hm}})$ , four times larger than the half-mode mass, the relation obtained in [168] has a steeper turnover than that of [167]. Moreover, the concentration parameter obtained by [168] becomes  $c_{\text{vir}} < 1$  in halos with the Jeans mass, which might be unphysical. The halo mass dependence on the concentration parameters in the FDM halos can be estimated with that in the CDM halos, Eqs. (2.13) and (2.14), and the suppression factor  $F$ , leading to

$$c_{\text{vir}} \propto M_{\text{h}}^{0.21} \quad M_{\text{h}} \lesssim M_{\text{h}}^{\text{4hm}}, \quad (3.72)$$

$$c_{\text{vir}} \propto M_{\text{h}}^{-0.12} \quad M_{\text{h}} \gtrsim M_{\text{h}}^{\text{4hm}}. \quad (3.73)$$

In the following section, we present our recent work on the core-halo mass relation. We adopt the concentration derived by [167], as prediction by [168] appears to be underestimated for halos around the Jeans mass as mentioned earlier. Note that we also use the following fitting results,

$$f(c_{\text{vir}}) \propto M_{\text{h}}^{0.22} \quad M_{\text{h}} \lesssim M_{\text{h}}^{\text{4hm}}, \quad (3.74)$$

$$f(c_{\text{vir}}) \propto M_{\text{h}}^{-0.07} \quad M_{\text{h}} \gtrsim M_{\text{h}}^{\text{4hm}}, \quad (3.75)$$

where  $f(c_{\text{vir}}) \equiv \ln(1 + c_{\text{vir}}) - c_{\text{vir}}/(1 + c_{\text{vir}})$ .

### 3.4 Core-halo mass relation

Although we show the properties of the soliton core and the outer density profile in Sec. 3.3, an additional condition is required to fully determine the total density profile. Practically, the total density profile of the FDM halo can be expressed as

$$\rho(r) = \begin{cases} \rho_{\text{sol}}(r) & r < r_{\text{t}} \\ \rho_{\text{NFW}}(r) & r > r_{\text{t}}, \end{cases} \quad (3.76)$$

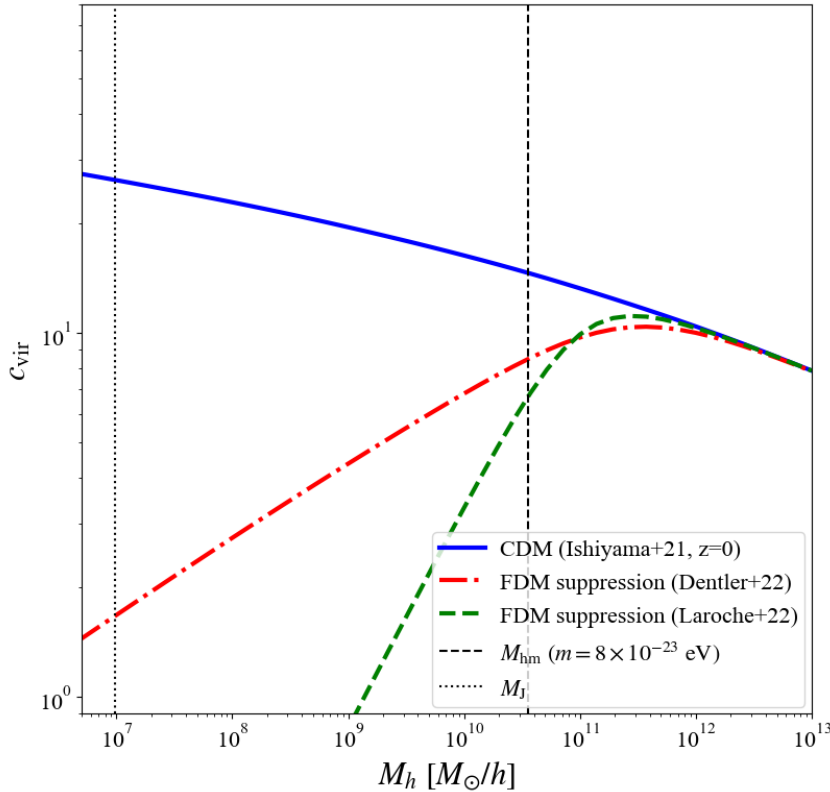


Figure 3.2: The suppressed  $c_{\text{vir}}-M_{\text{h}}$  relation in the FDM halos at redshift  $z = 0$ . The FDM mass is set to  $m = 8 \times 10^{-23}$  eV. The blue solid line shows the  $c_{\text{vir}}-M_{\text{h}}$  relation obtained from the largest cosmological CDM simulation [55]. To plot the red dash-dotted and green dashed lines, the FDM suppression factors obtained by [167] and [168] are considered, respectively. The vertical black dashed line and dotted lines indicate the half-mode mass and the Jeans mass, respectively. This figure is taken from [47].

where  $r_{\text{t}}$  represents the transition radius between the soliton core and the outer NFW profile, which is approximately three times the core radius [160]. Note that granular structures are neglected in this section.

Due to the scale symmetry of the SP system, i.e., Eq. (3.52), the soliton core can be characterized by a single parameter for a given FDM mass  $m$  such as the core mass or radius, which are related through Eq. (3.55). Meanwhile, the NFW profile is fully specified for a given halo mass  $M_{\text{h}}$  and an assumed  $c_{\text{vir}}-M_{\text{h}}$  relation. Thus, the total density profile can be constructed by establishing a relation between the soliton core mass and the halo mass, commonly referred to as the core-halo mass relation (CHMR). The primary goal of this section is to derive the total density profile of FDM halos for a given halo mass  $M_{\text{h}}$  and FDM particle mass  $m$  by considering CHMR.

This section builds upon our recent work on modeling the CHMR presented in [47] and is structured as follows. In Sec. 3.4.1, we review the CHMRs in the previous studies and outline the motivation for this study. Our modeling of the CHMR is presented in Sec. 3.4.2, followed by results and a detailed analysis in Sec. 3.4.3 and Sec. 3.4.4, respectively. A comparison between our model and previous studies is provided in Sec. 3.4.5. Finally, we show the total density profile based on the CHMR in Sec. 3.4.6. We adopt the concentration-halo mass relation for CDM halos as given by [55], and we use the suppression function of the concentration in the FDM model obtained by [167], as shown

in Eq. (3.68). In this section, we use the dimensionless Hubble parameter  $h = 0.7$ , the present-day matter density  $\Omega_{\text{m}0} = 0.30$ , and the dark energy density  $\Omega_0 = 0.70$ . Additionally, we revert from the natural unit to the SI unit in this section.

### 3.4.1 Previous studies on the CHMR

The FDM halo profile described by Eq. (3.76) does not inherently specify the connection between the core and halo masses. However, some underlying physical principles must link the inner soliton core to the outer NFW profile, and the CHMR provides this relation. In this sense, the CHMR is an important quantity in understanding the structure of FDM halos. The CHMR is first studied by [171], who combine analytical estimates with fits to FDM simulation data [160], providing the expression as

$$(1+z)^{-\frac{1}{2}} M_c = \frac{1}{4} \left( \sqrt{\frac{\zeta(z)}{\zeta(0)}} \frac{M_h}{M_{\text{min},0}} \right)^{\frac{1}{3}} M_{\text{min},0}, \quad (3.77)$$

where

$$M_{\text{min},0} = 4.4 \times 10^7 M_\odot \left( \frac{mc^2}{10^{-22} \text{ eV}} \right)^{-\frac{3}{2}} \left( \frac{\zeta(0)}{337.1} \right)^{\frac{1}{4}} \left( \frac{H_0}{70 \text{ km Mpc}^{-1} \text{ s}^{-1}} \right)^{-\frac{3}{2}} \times \left( \frac{\Omega_{\text{m}0}}{0.3} \right)^{-\frac{3}{4}} \left( \frac{\rho_{\text{m}0}}{40.8 M_\odot \text{ kpc}^{-3}} \right). \quad (3.78)$$

This relation takes the form of a simple power law,  $M_c \propto M_h^\alpha$ , with a power-law index  $\alpha = 1/3$ . This CHMR is derived by assuming that the core radius is determined by the de Broglie wavelength of FDM with the halo velocity dispersion, which scales as  $M_h^{1/3}$  at leading order. However, different FDM simulations suggest varying power-law indexes for the CHMR. For instance, [163] reports  $\alpha = 5/9$ , while [162] finds  $\alpha = 9/10$ . It is suggested that the discrepancy in the CHMR may arise from varying levels of tidal disruption of FDM halos, which are influenced by the simulation box size; halos in smaller boxes tend to be more tidally disrupted [162]. Nevertheless, the largest cosmological simulation conducted by [161], which includes a large number of FDM halos, also reports notable scatter in the CHMR. This suggests that the CHMR may intrinsically contain some scatter, regardless of simulation artifacts.

FDM simulations are computationally expensive due to the need for high spatial and time resolution, making (semi-)analytic approaches crucial for studying the CHMR. Several studies have attempted to (semi-)analytically construct the density profile of FDM halos and/or the CHMR without relying on simulations. The total density profile constructed by [172] uses the CHMR relation [171] to calculate the core radius for a given halo mass and imposes a continuity condition at a radius several times the core radius to determine the concentration parameter of the outer NFW profile. In this approach, the ratio between the core radius and the transition radius is allowed to vary with halo mass, while the physical motivation is unclear. Another interpretation of the CHMR relation [171] is discussed in [173], where the soliton core is determined by requiring that the total energy per unit mass is equal in both the soliton core and the halo. An alternative approach to study the density profile of FDM halos is taken by [174] and [175], who decompose the FDM halo profile into each eigenmode to investigate its time evolution by considering the time-averaged potential in the SP equation. With this approach, the

impact of the power-law index  $\alpha$  on the density profile is studied [175]. The CHMR is further investigated by solving the linearized SP equation with the NFW potential as a background, showing that the CHMR cannot be fully described by a single power law [176]. They also examine the impact of scatter in the  $c_{\text{vir}}-M_{\text{h}}$  relation on the CHMR, concluding that this scatter contributes partially (but not entirely) to the scatter observed in the FDM simulations.

While such dedicated studies exist, no (semi-)analytic models have been able to fully explain the scatter in the CHMR observed in simulations. This indicates that the CHMR is not yet fully understood, highlighting the need for a physically motivated (semi-)analytic model that can explain the scatter.

### 3.4.2 Modeling the CHMR

Our model assumes that the soliton core forms through the redistribution of mass from the NFW profile due to the wave nature of FDM. While this assumption may not fully capture the dynamics of FDM systems, it may be partially consistent with the setup used in cosmological FDM simulations that apply the CDM power spectrum to the initial conditions [160, 161]. In the following, we outline our physical model for the CHMR, focusing on a simplified scenario of static and spherically symmetric FDM halos.

For a given halo mass  $M_{\text{h}}$  and a redshift  $z$ , we first construct the NFW profile by using the  $c_{\text{vir}}-M_{\text{h}}$  relation derived from the largest cosmological CDM simulation [55] along with the FDM suppression factor obtained from [167]. Although FDM simulations use the CDM initial conditions, the linear power should be suppressed during the evolution, as they start from a sufficiently high redshift ( $z = 127$ ). Since the concentration parameter is derived from the linear power spectrum, we adopt the suppressed  $c_{\text{vir}}-M_{\text{h}}$  relation. The scatter of the concentration parameter around the mean value, which is specified by the  $c_{\text{vir}}-M_{\text{h}}$  relation, is assumed to follow a log-normal distribution with a  $1\sigma$  scatter of 0.16 dex for all halos, regardless of redshift [60]. As a reminder, we use the Python package COLOSSUS [170] to calculate the mean  $c_{\text{vir}}-M_{\text{h}}$  relation.

We then obtain the characteristic radius  $\tilde{r}_{\text{c}}$  from the NFW profile. Here we compare two different physically motivated conditions to calculate the characteristic radius. The first approach is based on the hydrostatic equilibrium condition, which we call the "Jeans model". The second approach is based on a relaxation time condition, which we refer to as the "Relaxation model".

The concept behind the Jeans model is that the characteristic radius is defined by the scale at which the pressure of a single granular structure balances the gravity in a halo that satisfies the hydrostatic equilibrium condition [177]. This radius can be determined by setting  $\mathbf{v} = 0$  in the Jeans equation, Eq. (3.30), leading to

$$\frac{GM_{\text{sol}}(< \tilde{r}_{\text{c}})}{\tilde{r}_{\text{c}}} \simeq \frac{\hbar^2}{m^2 \tilde{r}_{\text{c}}^2}. \quad (3.79)$$

Here,  $M_{\text{sol}}(< r)$  denotes the enclosed mass of the soliton core within a radius  $r$ . By approximating  $M_{\text{sol}}(< \tilde{r}_{\text{c}}) = M_{\text{NFW}}(< \tilde{r}_{\text{c}})$ , the characteristic radius can be determined from the NFW profile by solving Eq. (3.79). In this model, the characteristic radius corresponds to the de Broglie wavelength if we assume the Keplerian velocity  $v = \sqrt{GM_{\text{NFW}}(< r)/r}$  within halos,

$$\tilde{r}_{\text{c}} \simeq \frac{\lambda_{\text{dB}}(\tilde{r}_{\text{c}})}{2\pi}. \quad (3.80)$$

The model presented in [171] also approximates the core radius using the de Broglie wavelength, however, it simplifies the calculation by assuming a constant halo velocity dispersion, thereby neglecting the detailed internal density profile of the halo.

While the Jeans model determines the scale at which the wave nature of FDM becomes significant, it does not consider the dynamical evolution of FDM halos. To incorporate the effects of dynamical processes, we introduce the Relaxation model. The Relaxation model is based on the idea that the characteristic radius is determined where the relaxation time matches the age of the halo [153]. Considering granular structures, whose size is approximately equal to the de Broglie wavelength, as quasi-particles with an effective mass  $m_{\text{eff}} \simeq 4\pi\rho(\lambda_{\text{dB}}/2)^3/3$  where  $\rho$  represents the local density, the relaxation time can be estimated based on two-body relaxation processes as [178],

$$t_{\text{relax}}(r) \simeq \frac{0.1N}{\ln N} t_{\text{cr}}(r), \quad (3.81)$$

where  $N$  denotes the number of quasi-particles, which is evaluated as  $N \simeq M(< r)/m_{\text{eff}}$  with  $M(< r) \simeq 4\pi\rho r^3/3$  being the enclosed mass of halo within a radius  $r$ . The crossing time at a radius  $r$  is given by  $t_{\text{cr}}(r) = r/v$ . Substituting this into Eq. (3.81), we can derive an expression for the relaxation time at radius  $r$  as

$$t_{\text{relax}}(r) \simeq \frac{0.1}{10} \frac{m^3 v^2 r^4}{\pi^3 \hbar^3} \simeq 0.3 \text{ Gyr} \left( \frac{v}{100 \text{ km s}^{-1}} \right)^2 \left( \frac{r}{5 \text{ kpc}} \right)^4 \left( \frac{mc^2}{10^{-22} \text{ eV}} \right)^3. \quad (3.82)$$

For simplicity, we approximate  $\ln N$  as  $\ln N \sim 10$ , ignoring its dependence on parameters. This approximation is consistent within a factor of 2-3 for the mass range considered in this study, which spans  $M_{\text{h}} = 10^7 - 10^{13} M_{\odot}/h$  and  $mc^2 = 8 \times 10^{-24} - 8 \times 10^{-22} \text{ eV}$ . It is important to note that the  $\ln N$  factor is initially ignored in [153]. Given that the soliton core, representing the ground state, forms at the center of halos through relaxation, we define the characteristic radius as the radius where the relaxation time is equal to the age of the halo,

$$t_{\text{relax}}(\tilde{r}_{\text{c}}) = t_{\text{age}}, \quad (3.83)$$

with the right-hand side representing the halo age. In this study, we assume that the age of the halo at redshift  $z$  is the same as the age of the universe at that redshift.

After determining the characteristic radius, we calculate the mass-matching radius, representing the region where mass redistribution occurs. We allow a small discrepancy of order unity between the characteristic radius and the mass-matching radius, which is parameterized by a free parameter  $p_1$ , such that  $r_{\text{m}} = p_1 \tilde{r}_{\text{c}}$ . This parameter  $p_1$  is assumed to be constant for all halos at a given redshift. The introduction of  $p_1$  helps to account for uncertainties in the definitions of the characteristic radius.

Since the soliton core profile is fully defined by a single parameter for a given FDM mass  $m$ , we can determine the core mass  $M_{\text{c}}$  by solving the mass continuity equation at the mass-matching radius,  $M_{\text{NFW}}(< r_{\text{m}}) = M_{\text{sol}}(< r_{\text{m}})$  where the left-hand side represents the enclosed mass of the NFW profile, and the right-hand side corresponds to the mass within the soliton core profile. These steps yield the CHMR for the FDM halos in our model.

We select  $p_1$  to match the simulation results presented in [160] for low redshifts  $z < 1$  and [161] at  $z = 3$ , since these simulations solve the SP equation in a cosmological volume. After determining  $p_1$  by fitting, the core mass  $M_{\text{c}}$  in our model can be specified with four parameters: the halo mass  $M_{\text{h}}$ , the redshift  $z$ , the degree of the deviation  $n\sigma$  of the concentration parameter from the mean  $c_{\text{vir}}-M_{\text{h}}$  relation ( $c_{\text{vir}}^{(n)} = c_{\text{vir}}^{\text{mean}} \times 10^{0.16n}$ ), and the FDM mass  $m$ .

### 3.4.3 Results

In both models, once we determine  $\tilde{r}_c$ , we use a parameter  $p_1$  to set the matching radius and calculate the core mass. The redshift-dependent parameter  $p_1$  is obtained by fitting our results to the CHMR obtained from [160] for redshifts  $z < 1$  and from [161] at redshift  $z = 3$ . We adopt a fiducial FDM mass of  $mc^2 = 8.0 \times 10^{-23}$  eV, while the original simulations [160] and [161] use  $mc^2 = 7.5 \times 10^{-23}$  eV and  $7.0 \times 10^{-23}$  eV, respectively. To align with the fiducial FDM mass, we rescale the original CHMR data using the scaling relation of the SP equation. Both core and halo masses scale as  $M \propto m^{-3/2}$ , which can be obtained by setting  $\beta = 1$  in Eq. (3.52). It is important to note that this transformation does not affect the time scale in the simulation.

Figure 3.3 presents the comparison of the CHMR between the Jeans model at redshift  $z = 0$  and the simulation data from [160] at redshift  $z < 1$ . Figure 3.4 shows a similar comparison, but in this case, the Relaxation model is used. In both figures, the red solid lines represent the mean CHMR in our models, where we employ the mean  $c_{\text{vir}}-M_h$  relation. The values of  $p_1$  are adjusted to match the simulation data, indicated by the black dots. The best-fit values for  $p_1$  at low redshift ( $z < 1$ ) are found to be  $p_1 = 2.35$  in the Jeans model and  $p_1 = 0.11$  in the Relaxation model. In the Jeans model, the characteristic radius corresponds to the de Broglie wavelength, as shown in Eq. (3.80), and it is reasonable to expect  $p_1$  to range between two and three, which results in a matching radius larger than the de Broglie wavelength. In contrast, for the Relaxation model, where many granular structures relax to form the core at the center of the halo, the number of granular structures within the characteristic radius is much larger than one. Therefore, the characteristic radius is expected to be much larger than the core/mass-matching radius, and consequently,  $p_1$  should be smaller than unity. Both models show that the CHMR can be approximately described by a double power law. For halos with masses below  $10^{11} M_\odot/h$ , the CHMR aligns well with the empirical relation derived in [171], represented by the black dashed lines in the figures. However, for more massive halos, both models indicate a smaller power law index for the CHMR. The green dash-dotted and blue dashed lines in the figures incorporate the  $2\sigma$  scatter in the  $c_{\text{vir}}-M_h$  relation, where 0.16 dex is adopted as  $1\sigma$ . These  $2\sigma$  CHMR lines provide a reference for the degree of scatter. Notably, the three lines converge around a halo mass of  $M_h \simeq 10^{7-8} M_\odot/h$  which can be interpreted as the minimum halo mass, as discussed in Sec. 3.4.4. Additionally, the results reveal that more concentrated halos exhibit more massive cores. The scatter in the Relaxation model is found to be larger than in the Jeans model. While this difference can be clarified through a detailed analysis of the Jeans model, similar to what is done for the Relaxation model in Sec. 3.4.4, such an investigation is beyond the scope of this section, as it is not the primary focus.

Figure 3.5 compares the CHMR at redshift  $z = 3$  between the Jeans model and the simulation data from [161], while Fig. 3.6 presents the same comparison for the Relaxation model. In both figures, the red solid lines represent the mean CHMR predicted by our models, while the green dash-dotted and blue dashed lines correspond to the  $n = 2\sigma$  and  $-2\sigma$  CHMRs, respectively, derived by varying the concentration parameter as the same as Figs. 3.3 and 3.4. Again, we show these lines for reference to the degree of scatter, and further detailed analysis is shown in Sec. 3.4.5. To align with the simulation data shown in green dots, we introduce redshift-dependent values for  $p_1$ , setting  $p_1 = 2.00$  for the Jeans model and  $p_1 = 0.19$  for the Relaxation model. However, the Jeans model with any value of  $p_1$  cannot reproduce the expected scatter of the CHMR observed in the simulation. Specifically, the minimum halo mass, which corresponds to the crossing point of the three

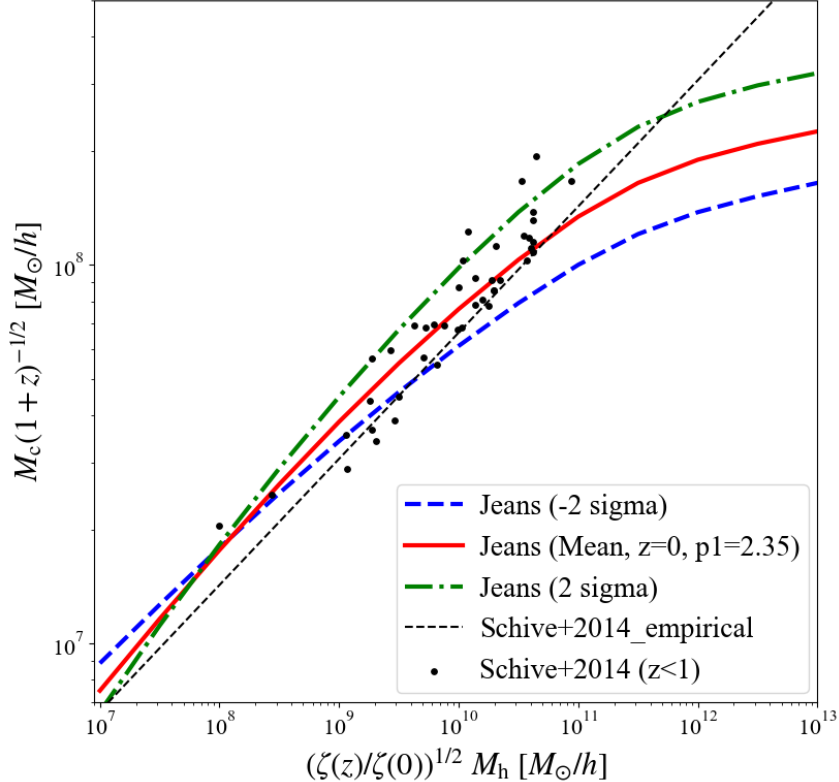


Figure 3.3: The comparison of the CHMR between the Jeans model at redshift  $z = 0$  and the simulation data obtained from [160] at redshift  $z < 1$ . We set the FDM mass to the fiducial value,  $mc^2 = 8.0 \times 10^{-23}$  eV. The red solid line shows the mean CHMR in the Jeans model at redshift  $z = 0$  using the mean  $c_{\text{vir}}-M_h$  relation. The green dash-dotted and blue dashed lines indicate the CHMRs when we consider the  $2\sigma$  scatter in the  $c_{\text{vir}}-M_h$  relation;  $n = 2, -2$ , respectively. By setting  $p_1 = 2.35$ , we successfully fit the CHMR obtained from [160] at redshift  $z < 1$ , which shows in black dots. The CHMR shown in [171] is plotted in a black dashed line. This figure is taken from [47].

lines, differs between the Jeans model and the simulation data. In contrast, the Relaxation model better reproduces the scatter observed in the CHMR and aligns more closely with the trends in the simulation data, including the location of the minimum halo mass. Note that the gray dotted lines in both figures represent the estimated scatter of the CHMR obtained by fitting to the simulation data, as presented in [162].

Based on these results, we conclude that the relaxation time condition, expressed in Eqs. (3.82) and (3.83), provides a more accurate framework for determining the mass-matching radius in describing FDM systems. Consequently, we focus on the Relaxation model in subsequent analysis to understand its behavior. The goal is to derive a semi-analytic expression for the CHMR within the framework of the Relaxation model.

### 3.4.4 Analysis in the Relaxation model

As demonstrated in Sec. 3.4.3, the Relaxation model successfully reproduces the simulation data and shows a larger scatter in the CHMR compared to the Jeans model. The Relaxation model exhibits two key characteristics: it is approximately described by a double power law, and CHMRs with varying concentration magnitudes converge near the

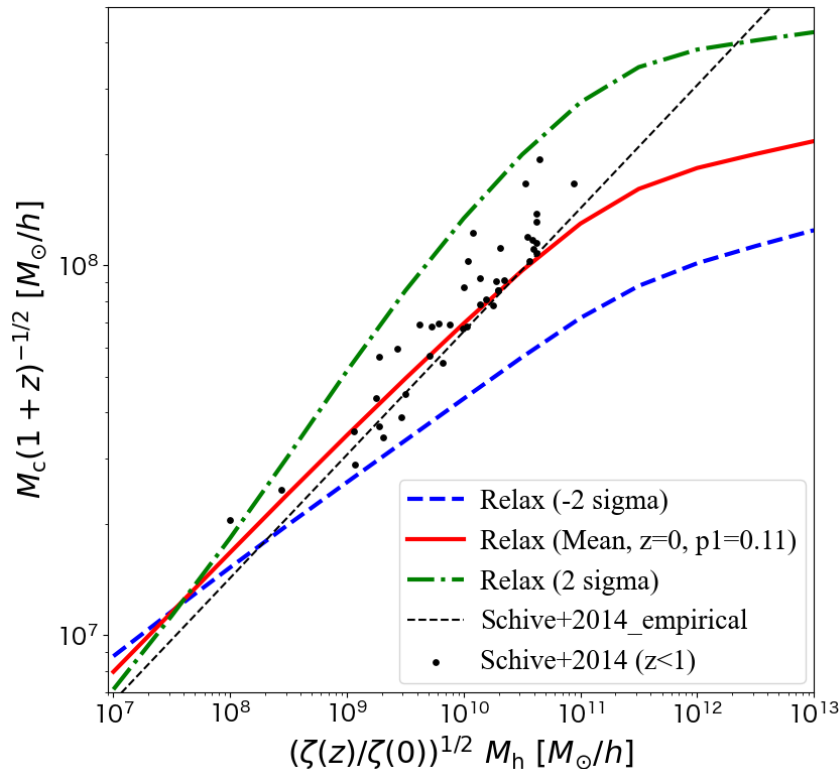


Figure 3.4: Similar to Fig. 3.3, but for the Relaxation model. By setting  $p_1 = 0.11$ , we successfully fit the CHMR obtained from [160] at redshift  $z < 1$ . This figure is taken from [47].

minimum halo mass. In this subsection, we analyze the Relaxation model at redshift  $z = 0$  to derive a simplified representation of the CHMR. Although the same methodology can be extended to analyze the Relaxation model at different redshifts, our primary interest lies in low-redshift systems, as they are crucial for comparison with observational data such as galaxy rotation curves and gravitational lensing studies. To obtain a simplified expression for the CHMR, we investigate the halo mass dependence of the characteristic radius and the enclosed mass within the mass-matching radius. In the following, we first explore the double power law behavior of the mean CHMR. Then, we analyze the scatter in the CHMR and determine the minimum halo mass. We also study the dependence of the CHMR on the FDM mass and derive a semi-analytic expression for the CHMR at  $z = 0$ . Finally, we discuss the redshift dependence of the CHMR.

### Mean relation

Let us recall the definition of the Relaxation model, given by Eqs. (3.82) and (3.83), which can be rewritten as

$$\tilde{r}_c^3 M_{\text{NFW}}(< \tilde{r}_c) = 7 \times 10^{13} \left( \frac{mc^2}{10^{-22} \text{ eV}} \right)^{-3} \left( \frac{t_{\text{age}}(z)}{13.8 \text{ Gyr}} \right) M_\odot \text{ kpc}^3. \quad (3.84)$$

Here, we take  $v$  as the circular velocity. Considering two cases whether the radius of interest is greater or smaller than the scale radius  $r_s$ , the enclosed mass of the NFW

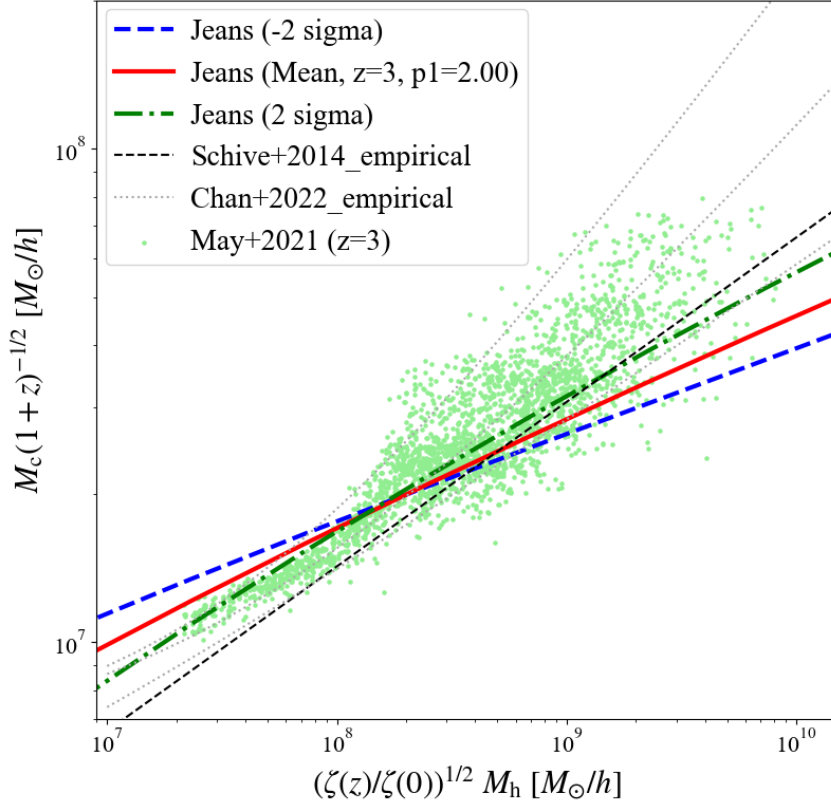


Figure 3.5: The comparison of the CHMR at redshift  $z = 3$  between the Jeans model and the simulation data obtained from [161]. The FDM mass is set to the fiducial value,  $mc^2 = 8.0 \times 10^{-23}$  eV. The red solid line shows the mean CHMR in the Jeans model at redshift  $z = 3$  using the mean  $c_{\text{vir}}-M_{\text{h}}$  relation. The green dash-dotted and blue dashed lines indicate the CHMR when we consider the  $2\sigma$  scatter in the  $c_{\text{vir}}-M_{\text{h}}$  relation;  $n = 2, -2$ , respectively. We set  $p_1 = 2.00$  in this plot. Although we try different  $p_1$  values, the Jeans model cannot reproduce the estimated scatter of the CHMR obtained from [161] at redshift  $z = 3$ , which shows in green dots. The gray dotted lines show the estimated scatter of the CHMR presented in [162], and the black dashed line shows the CHMR obtained by [171]. This figure is taken from [47].

profile, Eq. (2.7), can be approximated as

$$M_{\text{NFW}}(< r) \simeq \begin{cases} 2\pi\rho_s r_s r^2 & r \ll r_s \\ 4\pi\rho_s r_s^3 \left\{ \ln\left(\frac{r}{r_s}\right) - 1 \right\} & r \gg r_s \end{cases}. \quad (3.85)$$

It can be expected that CHMR can be divided into two cases depending on whether the characteristic radius is larger or smaller than the scale radius, which would lead to the double power law behavior. Since  $\tilde{r}_c$  decreases monotonically with increasing halo mass (as we verify later) and  $r_s$  exhibits the opposite trend, the halo mass at the boundary of these two cases is uniquely determined, which can be obtained from the condition  $\tilde{r}_c = r_s$ . Using the relation  $r_{\text{vir}} = c_{\text{vir}} r_s$  and Eq. (2.9), the boundary halo mass at a given redshift

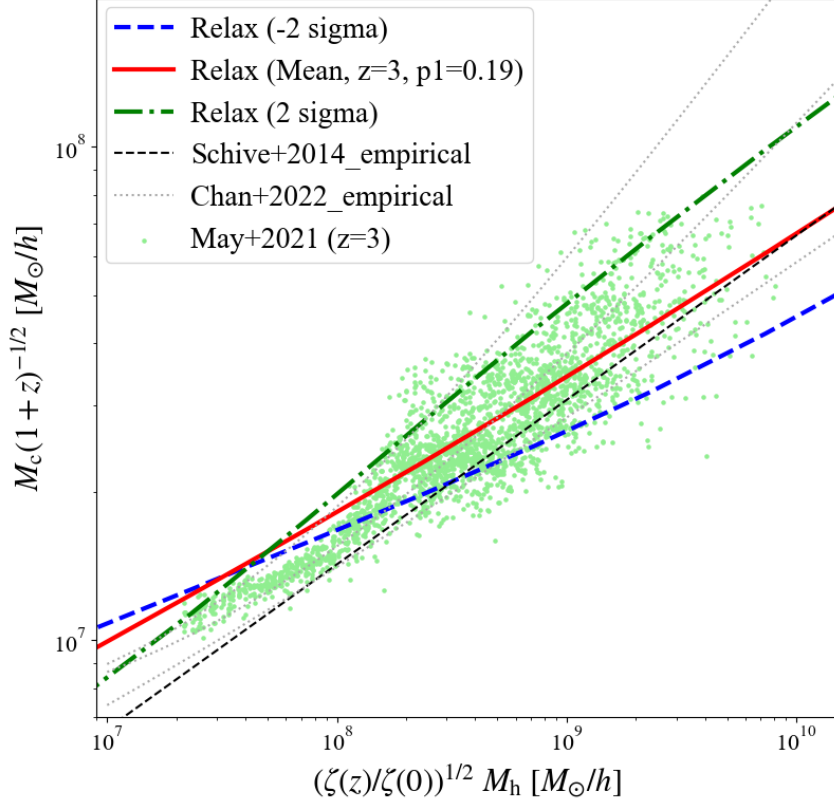


Figure 3.6: Similar to Fig. 3.5, but for the Relaxation model. By setting  $p_1 = 0.19$ , the larger scatter can be reproduced than the Jeans model and the Relaxation model captures a similar trend including the minimum halo mass to the simulation data obtained from [161] at redshift  $z = 3$ . This figure is taken from [47].

$z$  can be expressed as

$$M_h^B(z) \simeq 1 \times 10^{11} M_\odot (1+z)^{\frac{3}{4}} \left( \frac{\zeta(z)}{\zeta(0)} \right)^{\frac{1}{2}} \left( \frac{mc^2}{10^{-22} \text{ eV}} \right)^{-\frac{3}{2}} \times \left( \frac{c_{\text{vir}}^3 \{ \ln(1+c_{\text{vir}}) - c_{\text{vir}}/(1+c_{\text{vir}}) \}}{1000} \right)^{\frac{1}{2}} \left( \frac{\rho_{\text{m0}}}{40.8 M_\odot \text{ kpc}^{-3}} \right)^{\frac{1}{2}} \left( \frac{t_0}{13.8 \text{ Gyr}} \right)^{\frac{1}{2}}. \quad (3.86)$$

We approximate the halo age as  $t_{\text{age}}(z) \simeq t_0(1+z)^{-\frac{3}{2}}$ , where  $t_0$  represents the current age of the universe. To compute  $\zeta(0)$ , as defined in Eq. (2.10), we adopt  $\Omega_{\text{m0}} = 0.30$ . It is important to note that the right-hand side of Eq. (3.86) includes the concentration parameter, which depends on the halo mass.

Another characteristic halo mass influencing the CHMR is four times the half-mode mass, where the  $c_{\text{vir}}-M_h$  relation shows a turnover. As a result, the CHMR would exhibit a triple power law behavior, rather than the double power law discussed earlier. However, for FDM masses  $mc^2 \simeq 10^{-23} - 10^{-21}$  eV, the boundary halo mass derived in Eq. (3.86) at  $z = 0$  is approximately equivalent to four times the half-mode mass,

$$M_h^B(z=0) \simeq M_h^{4\text{hm}}. \quad (3.87)$$

Thus, we do not account for the intermediate mass range between the boundary halo mass defined in Eq. (3.86) and  $M_h^{4\text{hm}}$  at  $z = 0$ . Instead, we focus on two scenarios: halos

with masses either larger or smaller than the boundary mass and four times the half-mode mass. Halos with  $M_h < M_h^{4\text{hm}}$  are referred to as "low-mass halos", while those with  $M_h > M_h^{4\text{hm}}$  are called "high-mass halos".

For low-mass halos,  $\tilde{r}_c \gtrsim r_s$ , Eq. (3.84) simplifies to  $\tilde{r}_c^3 \ln(\tilde{r}_c/r_s) \cdot 4\pi\rho_s r_s^3 \simeq \text{const.}$ , neglecting the subdominant term. Considering the halo mass dependence of the concentration parameter in this regime at  $z = 0$ , Eq. (3.74), and using Eq. (2.8), we find  $4\pi\rho_s r_s^3 \propto M_h^{0.78}$ . This gives the halo mass dependence of the characteristic radius as  $\tilde{r}_c \propto M_h^{-0.26 \div -0.20}$ , where the uncertainty arises from the logarithmic term. Numerical calculations yield a best-fit power law index of  $-0.21$ , which aligns with this theoretical estimate. For high-mass halos,  $\tilde{r}_c \lesssim r_s$ , Eq. (3.84) reduces to  $\tilde{r}_c^5 \cdot 2\pi\rho_s r_s = \text{const.}$ . Using the halo mass dependence of the concentration parameter, Eqs. (3.73) and (3.75), we find  $2\pi\rho_s r_s \propto M_h^{0.16}$ , leading to  $\tilde{r}_c \propto M_h^{-0.032}$ . However, numerical calculations suggest a best-fit power law index of  $-0.06$ . The discrepancy likely arises because the fitting region,  $M_h < 10^{13} M_\odot/h$ , is insufficiently high to validate the approximation used in Eq. (3.85). In summary, the halo mass dependence of the characteristic radius is

$$\tilde{r}_c \propto M_h^{-0.21} \quad \text{low-mass halos,} \quad (3.88)$$

$$\tilde{r}_c \propto M_h^{-0.06} \quad \text{high-mass halos.} \quad (3.89)$$

We observe that  $\tilde{r}_c$  decreases monotonically as a function of halo mass, which supports our earlier discussion regarding the boundary halo mass. Additionally, the power law index shifts around the boundary halo mass and four times the half-mode mass, confirming the change in behavior as described earlier.

Next, we examine the halo mass dependence of the enclosed mass within the matching radius,  $r_m = p_1 \tilde{r}_c$  with  $p_1 = 0.11$ . From the definition of the the Relaxation model shown in Eq. (3.84), the relation  $M_{\text{NFW}}(< \tilde{r}_c) \propto \tilde{r}_c^{-3}$  holds. If  $p_1 \simeq 1$ , it follows that  $M_{\text{NFW}}(< \tilde{r}_m) \propto \tilde{r}_m^{-3}$ , as  $r_m \simeq \tilde{r}_c$  under this condition. Even if  $p_1 \simeq 1$  does not hold, this relation remains valid when both  $\tilde{r}_c$  and  $r_m$  satisfy  $\tilde{r}_c, r_m \gg r_s$  or  $\tilde{r}_c, r_m \ll r_s$ . This is because the ratio of the enclosed mass at the matching radius to that at the characteristic radius can be approximated as  $M_{\text{NFW}}(< r_m)/M_{\text{NFW}}(< \tilde{r}_c) = \ln(r_m/r_s)/\ln(\tilde{r}_c/r_s)$  for low-mass halos and  $(r_m/\tilde{r}_c)^2$  for high-mass halos. However, since  $r_m \simeq r_s$  for low-mass halos due to the small value of  $p_1 = 0.11$ , and  $\tilde{r}_c \simeq r_s$  for high-mass halos as discussed earlier, this simple scaling no longer holds. To capture the actual behavior, we use numerical fitting, which reveals that  $M_{\text{NFW}}(< r_m) \propto r_m^{-2.2}$  for low-mass halos and  $M_{\text{NFW}}(< r_m) \propto r_m^{-1.1}$  for high-mass halos. Combining these with Eqs. (3.88) and (3.89), we derive the following halo mass dependence for the enclosed mass,

$$M_{\text{NFW}}(< r_m) \propto M_h^{0.46} \quad \text{low-mass halos,} \quad (3.90)$$

$$M_{\text{NFW}}(< r_m) \propto M_h^{0.07} \quad \text{high-mass halos.} \quad (3.91)$$

This result is further validated by numerical calculations.

Since the soliton core profile is determined by imposing the mass continuity condition at the matching radius,  $M_{\text{sol}}(< r_m) = M_{\text{NFW}}(< r_m)$ , we next investigate the relation between the enclosed soliton mass within the matching radius,  $M_{\text{sol}}(< r_m)$ , and the core mass  $M_c = M_{\text{sol}}(< r_c)$ . Figure 3.7 illustrates the enclosed soliton core mass within a radius  $R = r$ ,  $M_{\text{sol}}(< r)$ , for various soliton core radii at a fixed FDM mass of  $mc^2 = 8 \times 10^{-23}$  eV (rainbow-colored lines), alongside  $M_{\text{NFW}}(< r_m)$  as a function of  $R = r_m$  for halos with masses  $M_h = 10^7 - 10^{13} M_\odot/h$  (red solid line). As shown earlier, halos with higher masses correspond to smaller matching radii. Since  $r_m$  is uniquely determined by the halo mass

$M_h$ , the soliton core profile is determined by a line through the point  $(r_m, M_{\text{NFW}}(< r_m))$ . Using this procedure, we obtain the soliton core mass for a given halo mass. The behavior of the rainbow-colored lines can be approximated by the following relation,

$$M_{\text{sol}}(< r) \simeq \begin{cases} \frac{4}{3}\pi\rho_c r^3 \propto m^6 M_c^4 & (r < 0.5r_c) \\ M_s \propto M_c & (r > 3.5r_c) \end{cases}, \quad (3.92)$$

where the total core mass denoted by  $M_s$  can be calculated using Eq. (3.55) with the upper limit of the integration extended to infinity. The parameter dependence in Eq. (3.92) is determined by using Eqs. (3.54) and (3.55). Since the density profile of the soliton core drops rapidly, the enclosed mass of the soliton core within a radius exceeding 3.5 times the core radius closely approximates  $M_s$ .

To understand the halo mass dependence of the core mass, we divide it into two cases based on whether the matching radius  $r_m$  exceeds  $3.5r_c$  or not. The transition halo mass between these two cases, where the red solid line intersects the black dotted line in Fig. 3.7, closely aligns with the boundary mass distinguishing low-mass halos from high-mass halos, where the power law index of the red solid line changes. Thus, no further subdivisions are necessary. For high-mass halos, where  $r_m > 3.5r_c$ , the relation  $M_{\text{NFW}}(< r_m) = M_s \propto M_c$  holds, leading to the halo mass dependence  $M_c \propto M_h^{0.07}$ . For low-mass halos, precise estimation is more challenging because the matching radius lies between  $0.5r_c$  and  $3.5r_c$ . However, we can approximate the halo mass dependence of the core mass by using the upper relation in Eq. (3.92), Eq. (3.90), and the relation  $r_m \propto M_h^{-0.21}$  derived from Eq. (3.88). This analytic approach yields  $M_c \propto M_h^{0.27}$ . Numerical fitting results in  $M_c \propto M_h^{0.32}$ , showing reasonable agreement with the analytic estimation.

In summary, we find that the CHMR in FDM halos obtained from the Relaxation model approximately follows a double power law behavior,

$$M_c \propto M_h^{0.32} \quad \text{low-mass halos}, \quad (3.93)$$

$$M_c \propto M_h^{0.07} \quad \text{high-mass halos}. \quad (3.94)$$

The transition in the CHMR corresponds to a halo mass four times the half-mode mass  $M_h^{4\text{hm}}$ , where the  $c_{\text{vir}}-M_h$  relation shows a turnover. While the power law index of the CHMR also shifts near the boundary mass given in Eq. (3.86), this transition is subtler compared to the change around  $M_h^{4\text{hm}}$ . Furthermore, as previously discussed, the boundary mass aligns closely with  $M_h^{4\text{hm}}$  at redshift  $z = 0$ .

The CHMR presented in [171] shows that the power-law index derived for low-mass halos at redshift  $z = 0$  aligns well with the predictions of the Relaxation model. However, significant deviations are observed between the Relaxation model and their findings in the case of high-mass halos. The double power-law behavior is highlighted in [176], albeit under a different framework. They investigate CHMR by solving the linearized SP equation with the NFW potential as the background, concluding that the power-law index is approximately 1/3 for low-mass halos but decreases for high-mass halos, i.e., a trend consistent with the Relaxation model. Further data on high-mass halos may allow us to distinguish the Relaxation model from the model proposed in [176].

## Scatter

We next account for the scatter in the  $c_{\text{vir}}-M_h$  relation and show its impact on the scatter in the CHMR. As a reminder, we assume the scatter in the  $c_{\text{vir}}-M_h$  relation to be 0.16 dex at the  $1\sigma$  level.

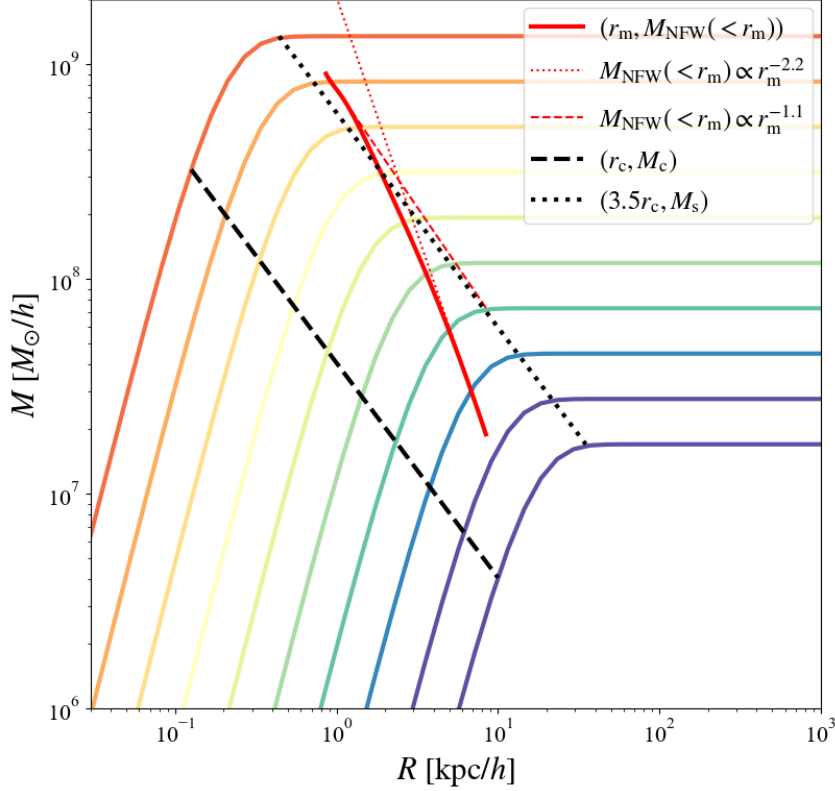


Figure 3.7: The enclosed masses within a radius  $R = r$  or  $r_m$  are shown, from which the soliton core mass is determined using the mass-matching condition. The red solid line shows the enclosed mass of the NFW profile at the matching radius  $r_m$  with halo mass range  $M_h = 10^7 - 10^{13} M_\odot/h$ . The rainbow-colored lines indicate the enclosed masses of the soliton cores as a function of radius  $r$  for different core radii with the fixed FDM mass,  $mc^2 = 8 \times 10^{-23}$  eV. For a given halo mass  $M_h$ , we first obtain  $(r_m, M_{\text{NFW}}(<r_m))$ , and then determine the core radius and mass such that the corresponding soliton core passes through this point. The red dotted line shows the power law relation for the low-mass halos,  $M_{\text{NFW}}(<r_m) \propto r_m^{-2.2}$ , and the red dashed line shows for the high-mass halos,  $M_{\text{NFW}}(<r_m) \propto r_m^{-1.1}$ . The relation between the core radius  $r_c$  and the core mass  $M_c$  is shown in the black dashed line. The black dotted line represents the relation between the  $3.5r_c$  and the total core mass  $M_s$ . This figure is taken from [47].

Since only the magnitude of the concentration parameter is modified, the power law index of the  $c_{\text{vir}}-M_h$  relation remains unchanged. However, the dependence of  $f(c_{\text{vir}})$  on halo mass is slightly changed, leading to the different dependence of the relevant combinations of the NFW parameters on the halo mass;  $4\pi\rho_s r_s^3|_{\text{low}M_h} \propto M_h^{0.78+0.025n}$  and  $2\pi\rho_s r_s|_{\text{high}M_h} \propto M_h^{0.16-0.01n}$ . In the first combination, the power law index increases as the concentration parameter becomes larger, while the second combination shows an opposite trend. These variations in halo mass dependence lead to changes in the power law indices of the CHMR. The method for determining the power law index in each case follows the same procedure as the mean case. We finally obtain the following relation through fitting,

$$M_c \propto M_h^{0.32+0.05n} \quad \text{low-mass halos} \quad (3.95)$$

$$M_c \propto M_h^{0.07-0.01n} \quad \text{high-mass halos.} \quad (3.96)$$

As anticipated, the dependence of the power law index on the scatter shows the opposite

trends for low-mass and high-mass halos.

In Fig. 3.4, we observe that the three lines, each corresponding to different magnitudes of the concentration parameter, intersect at nearly the same halo mass,  $M_h \simeq 10^{7.5} M_\odot/h$ . This halo mass represents the minimum halo mass, as discussed below. We define the minimum halo mass  $M_h^{\min}$  as the mass where the matching radius  $r_m$  equals the virial radius  $r_{\text{vir}}$ . For halos with  $r_m > r_{\text{vir}}$ , we cannot use the halo mass definition given in Eq. (2.9), and thus such halos do not exist. Using the condition  $r_m = r_{\text{vir}}$  and Eq. (3.84), we can analytically derive the minimum halo mass for a given redshift  $z$  as

$$M_h^{\min}(z) \simeq 4 \times 10^7 M_\odot (1+z)^{\frac{3}{4}} \left( \frac{\zeta(z)}{\zeta(0)} \right)^{\frac{1}{2}} \left( \frac{mc^2}{10^{-22} \text{ eV}} \right)^{-\frac{3}{2}} \left( \frac{p_1}{0.11} \right)^{1.8} \\ \times \left( \frac{1}{p_1^{0.6}} \frac{f(c_{\text{vir}})}{f(\tilde{c}_{\text{vir}})} \right)^{\frac{1}{2}} \left( \frac{\rho_{\text{m}0}}{40.8 M_\odot \text{ kpc}^{-3}} \right)^{\frac{1}{2}} \left( \frac{t_0}{13.8 \text{ Gyr}} \right)^{\frac{1}{2}}. \quad (3.97)$$

Here, we define  $\tilde{c}_{\text{vir}} = p_1^{-1} c_{\text{vir}}$ . The scatter in the minimum halo mass due to variations in the concentration parameter is relatively small because the factor  $f(c_{\text{vir}})/f(\tilde{c}_{\text{vir}})$  does not change significantly. The core mass of the minimum halo is nearly identical to the halo mass by definition, and more precisely,  $M_c^{\min} \simeq 0.34 M_h^{\min} (n=0)$ . This explains why the three lines in Fig. 3.4 intersect around the minimum halo mass for FDM halos. We verify that the mass at the intersection in the numerical calculation closely matches the analytically estimated minimum halo mass, differing only by a factor of  $\mathcal{O}(1)$  even when considering different redshifts and FDM masses. It is important to note that although we plot the CHMR below the minimum halo mass, those small halos may not be physically meaningful. On the other hand, there are no upper limits to the core and halo mass, as our model does not impose a lower limit on the core radius.

We briefly discuss the scatter in the boundary halo mass given by Eq. (3.86). We find that the boundary mass varies approximately 5 times larger or smaller than the mean case when considering the  $2/-2 \sigma$  scatter. However, the mass at which the power law index in the CHMR changes does not exhibit significant variation. This leads us to conclude that the variation in the power law index around the boundary mass is less pronounced than the variation around the four times the half-mode mass  $M_h^{4\text{hm}}$ , where the  $c_{\text{vir}}-M_h$  relation shows a turnover.

Combining all the results up to this point, we can express the CHMR at redshift  $z=0$  in a simpler semi-analytic way as,

$$M_c = \begin{cases} M_c^{\min} \left( \frac{M_h}{M_h^{\min}} \right)^{0.32+0.05n} & (M_h^{\min} < M_h < M_h^{4\text{hm}}) \\ M_{c,n}^{4\text{hm}} \left( \frac{M_h}{M_h^{4\text{hm}}} \right)^{0.07-0.01n} & (M_h > M_h^{4\text{hm}}) \end{cases}, \quad (3.98)$$

where we define  $M_{c,n}^{4\text{hm}}$  to ensure core mass continuity at  $M_h = M_h^{4\text{hm}}$  for a given  $n$ . As shown in Fig. 3.8, the semi-analytic form given in Eq. (3.98) closely matches the numerical results of the Relaxation model, with discrepancies on the order of  $\mathcal{O}(1)$ .

### FDM mass

Another important aspect of the CHMR is its dependence on the FDM mass, which is constrained by various observational data, including rotation curve measurements and gravitational lensing events.

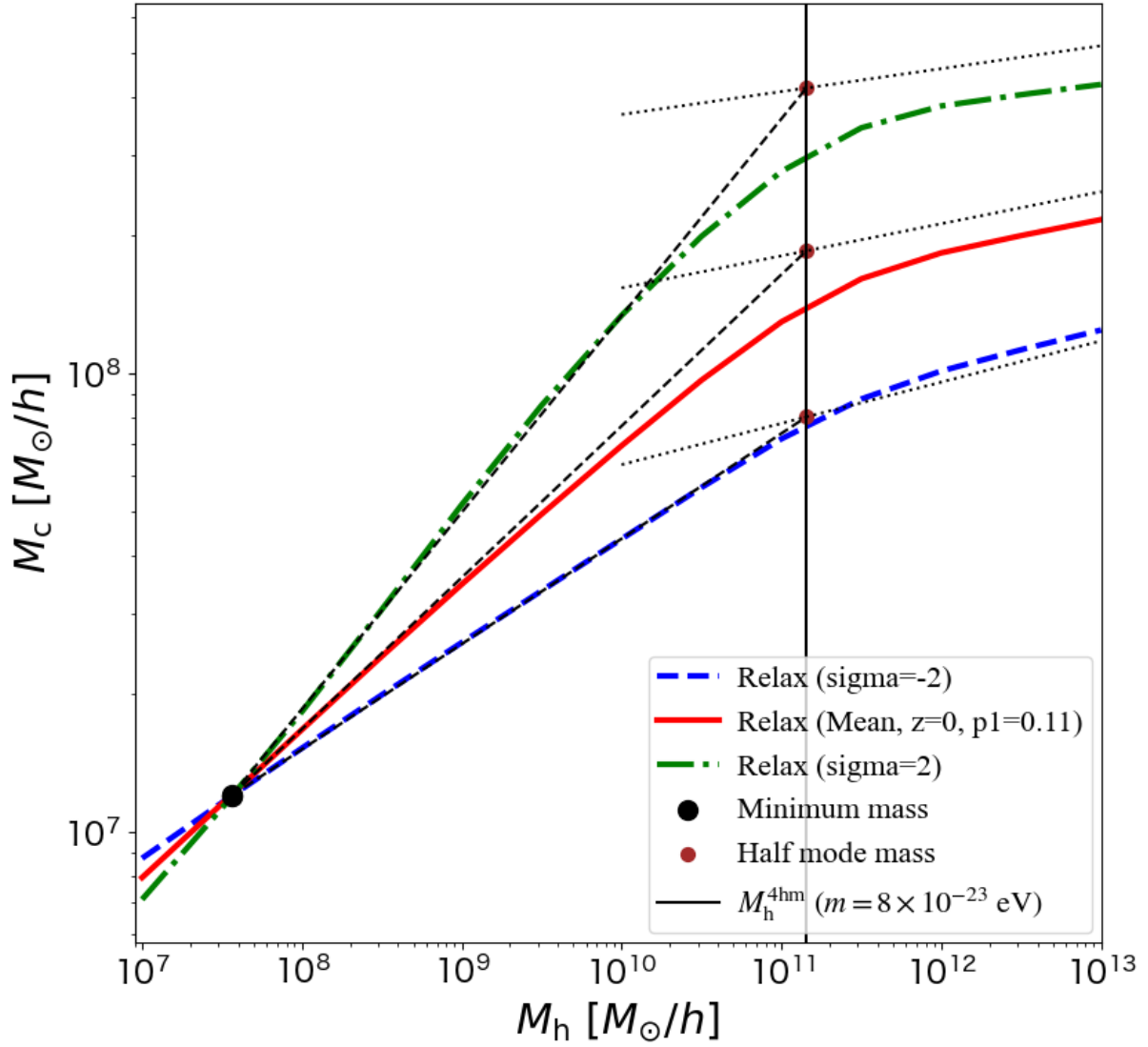


Figure 3.8: The CHMR with the Relaxation model and its semi-analytic expression at redshift  $z = 0$ . The red solid, green dash-dotted, and blue dashed lines are the same as Fig. 3.4. The black big point represents the minimum halo mass and the brown small points indicate the four times the half-mode mass. We use the semi-analytic expressions shown in Eq. (3.98) to plot the black dashed and dotted lines. This figure is taken from [47].

The FDM mass dependence in the Relaxation model can be interpreted in the same way as the previous analysis. Since we already know the FDM mass dependence for both the minimum mass and the half-mode mass, where the CHMR exhibits a transition in its double power-law behavior, the primary remaining point of discussion is how the power law index itself changes with the FDM mass. We rely on fitting to get the exact value for the power law index since the combinations of the NFW parameters such as the enclosed mass include the logarithmic dependence on the halo mass. Interestingly, we observe that the power law index of the CHMR is almost independent of the mass of FDM within the relevant range.

The minimum halo and core masses approximately follow the scaling relation  $M^{\min} \propto m^{-3/2}$ , as shown in Eq. (3.97), while the half-mode mass scales as  $M_h^{4\text{hm}} \propto m^{-4/3}$ , as can be seen in Eq. (3.49). Additionally, the core mass corresponding to the halo mass of four times the half-mode mass scales as  $M_{c,n}^{4\text{hm}} \propto m^{-(8.68-0.05n)/6}$ , which can be derived from the upper relation in Eq. (3.98) by setting  $M_h = M_h^{4\text{hm}}$ . These scaling relations align closely with those predicted by the SP equation:  $M_h \propto m^{-3/2}$  and  $M_c \propto m^{-3/2}$ , which are obtained by setting  $\beta = 1$  in Eq. (3.52). This consistency is illustrated in Fig. 3.9, where the scaling relation is compared to the numerical results of the Relaxation model. The red solid line represents the CHMR with the fiducial FDM mass, while the green dash-dotted and blue dashed lines correspond to the cases with ten times larger and smaller FDM masses, respectively. The black dashed and dotted lines represent the scaling relation applied to the red solid line. From this result, we can conclude that the Relaxation model successfully captures the scaling features of the SP equation.

To be more precise, we observe slight deviations between the scaling relation of the SP equation and the Relaxation model. These deviations arise from the  $c_{\text{vir}}-M_h$  relation in FDM halos, given by Eq. (3.71). Both factors on the right-hand side of Eq. (3.71), namely  $c_{\text{vir}}(M_h, z; \text{CDM})$  and  $F(M_h/M_h^{\text{hm}})$ , contribute to breaking the scaling relation. We can check these deviations as follows. Regarding the first factor, since the concentration parameter is not constant across all halo masses due to the scale-variant power spectrum and the concentration parameter remains unchanged under scaling while the halo mass changes, the scaling relation is broken. Even though the primordial power spectrum of the density perturbation is scale-invariant, it becomes scale-variant due to the evolution of perturbations at the super-horizon scale and during the radiation-dominant era, which are described by the (CDM) transfer function. Regarding the second factor, the half-mode mass does not follow the scaling relation due to the violation of the scaling law in the FDM transfer function, which is modified by  $T_F(k)$  compared to the CDM transfer function as shown in Eq. (3.46). This modification incorporates a factor of  $(mc^2/10^{-22} \text{ eV})^{1/18}$ , which also originates from the evolution of perturbations at the super-horizon scale during the radiation-dominated era, and is responsible for breaking the scaling relation. Therefore, the deviations between the Relaxation model and the scaling relation in the SP equation arise from these two factors. It is worth noting that in the semi-analytic form of the Relaxation model, Eq. (3.98), the contribution of the first factor is found to be negligible within the range of FDM masses of interest. Otherwise, the power law indices of the CHMR would be expected to depend on the FDM mass.

The previous simulations are carried out with nearly the same FDM mass around our fiducial value, along with the CDM initial conditions, which only incorporate the first factor. Therefore, it is crucial to perform simulations with varying FDM masses and with the FDM initial condition. These simulations would allow us to test the FDM mass dependence of the CHMR and the validity of the Relaxation model.

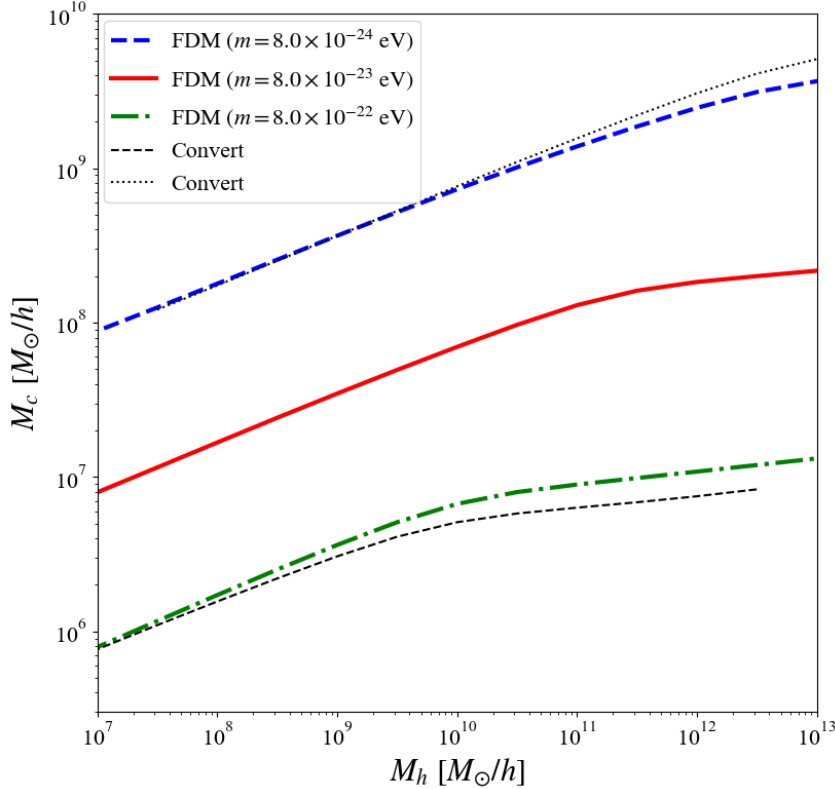


Figure 3.9: The dependence of the Relaxation model on the FDM mass and the comparison with the scaling relation of the SP equation. The Relaxation models with different FDM masses are plotted in the blue dashed, red solid, and green dash-dotted lines. The concentration parameter is taken to be the mean value. The black dotted and dashed lines are plotted by applying the scaling relation  $M \propto m^{-3/2}$  to the red solid line. This figure is taken from [47].

## Redshift

Up to this point, we have primarily focused on the CHMR at redshift  $z = 0$ . Here, we briefly explore the redshift dependence of the Relaxation model.

In the Relaxation model, the redshift dependence arises from the concentration parameter, the halo age, and the parameter  $p_1$ . The concentration parameter for low-mass halos follows the scaling relation  $c_{\text{vir}} \propto (1+z)^{-1}$ , and the power law index of the  $c_{\text{vir}}-M_h$  relation remains unchanged. However, the redshift dependence is not monotonic for high-mass halos, as these halos are rare at high redshifts. Nevertheless, we can understand the behavior in the same way as the previous analyses. We present the outcomes of the Relaxation model, without explaining the details of the analysis.

First, we fix  $p_1 = 0.11$  for simplicity. According to [171], the redshift dependence of the CHMR can be absorbed by plotting it in the  $\sqrt{\zeta(z)/\zeta(0)}M_h-M_c/\sqrt{1+z}$  plane. However, when we plot the results from the Relaxation model in this plane, we still observe redshift dependence (with  $M_c/\sqrt{1+z}$  being smaller at higher redshifts). Additionally, the Relaxation model can explain the simulation data from [161] when  $p_1 = 0.19$  (not 0.11) at  $z = 3$ . Therefore, we allow  $p_1$  to depend on redshift. Since a larger core mass is required at higher redshifts to match the three lines,  $p_1$  must increase as redshift increases. We find that we can effectively absorb the redshift dependence of the CHMR, as shown in

Fig. 3.10, where we set  $p_1 = 0.11$  at  $z = 0$ ,  $0.15$  at  $z = 1$ , and  $0.19$  at  $z = 3$ . The resulting power law index of the CHMR in the  $\sqrt{\zeta(z)/\zeta(0)}M_h - M_c/\sqrt{1+z}$  plane for the low-mass halos is approximately 0.30, which is in reasonable agreement with the relation found in [171].

The empirical and practical reason for requiring a larger  $p_1$  at higher redshifts is to compensate for the smaller core mass associated with a shorter halo age  $t_{\text{age}}$ . As mentioned earlier, the Relaxation model incorporates redshift dependence in the concentration  $c_{\text{vir}}$ , halo age  $t_{\text{age}}$ , and  $p_1$ . When  $t_{\text{age}}(z)$  is fixed to the current age of the universe  $t_{\text{age}}(0)$ , we find that the CHMRs at different redshifts coincide in the  $\sqrt{\zeta(z)/\zeta(0)}M_h - M_c/\sqrt{1+z}$  plane. However, when the redshift dependence of  $t_{\text{age}}$  is taken into account, the core mass becomes smaller at higher redshifts. To compensate for this,  $p_1$  must be increased to reproduce the larger core mass as the redshift becomes larger.<sup>1</sup>

We can derive the semi-analytic expression at redshift  $z = 3$  in the same manner,

$$M_c = \begin{cases} \tilde{M}_c^{\text{min}} \left( \frac{M_h}{M_h^{\text{min}}} \right)^{0.30+0.04n} & (M_h^{\text{min}} < M_h < M_h^{4\text{hm}}) \\ M_{c,n}^{4\text{hm}} \left( \frac{M_h}{M_h^{4\text{hm}}} \right)^{0.22} & (M_h > M_h^{4\text{hm}}). \end{cases} \quad (3.99)$$

To improve the fit to the numerical calculations, we introduce  $\tilde{M}_h^{\text{min}} = M_h^{\text{min}}/2.5$ . The minimum halo mass is estimated using the mean concentration ( $n = 0$ ), and we find that  $\tilde{M}_c^{\text{min}} \simeq 0.45\tilde{M}_h^{\text{min}}$ . As with the  $z = 0$  case, we define  $M_{c,n}^{4\text{hm}}$  to ensure continuity of the expression at  $M_h = M_h^{4\text{hm}}$  for a given  $n$ . The difference in the power law indices between the expressions at redshift  $z = 0$ , i.e., Eq. (3.98), and at redshift  $z = 3$ , i.e., Eq. (3.99), arises from the different halo mass dependence of  $c_{\text{vir}}$ ,  $f(c_{\text{vir}})$ , and the varying value of  $p_1$ . While the power law index remains nearly the same for low-mass halos, it diverges for high-mass halos. This is due to the substantial difference in the halo mass dependence of the concentration parameter; the upturn in the  $c_{\text{vir}} - M_h$  relation at higher redshifts, as described in [55]. Interestingly, the power law index of high-mass halos is found to be independent of  $n$ . Note that the scatter of the core mass for high-mass halos is encapsulated in  $M_{c,n}^{4\text{hm}}$ . In Fig. 3.11, we compare the semi-analytic expression with the numerical results at redshift  $z = 3$ , showing good agreement between them. We use the semi-analytic expression, Eq. (3.99), in Sec. 3.4.5 to examine the scatter of the CHMR.

### 3.4.5 Comparison of the degree of scatter

In this subsection, we assess how variations in the  $c_{\text{vir}} - M_h$  relation influence the scatter of the CHMR. Revisiting Fig. 3.6, the Relaxation model shows a significant reduction in scatter around the minimum halo mass. While [176] also show a similar trend by considering the scatter in the  $c_{\text{vir}} - M_h$  relation, it seems that the variation in scatter with respect to halo mass is not sufficient to match the simulation data.

To quantitatively evaluate the scatter of the CHMR in the Relaxation model, we analyze the distribution of core masses for a given halo mass. Here, we consider the

<sup>1</sup>This behavior raises questions about the validity of the  $c_{\text{vir}} - M_h$  relation in FDM halos, particularly below the half-mode mass, where we apply the suppression model from [167]. A notable issue with this model is that it predicts  $c_{\text{vir}} < 1$  for low-mass halos at high redshift, which is physically unrealistic. In reality, these halos likely have a concentration  $c_{\text{vir}} > 1$ , suggesting that the concentration parameter may be underestimated at higher redshifts. Since a lower concentration leads to a smaller core mass, adjusting  $p_1$  to larger values may compensate for this discrepancy. To gain a clearer understanding of the redshift dependence of  $p_1$ , further investigation is needed into the  $c_{\text{vir}} - M_h$  relation in FDM halos through simulations or semi-analytic approaches.

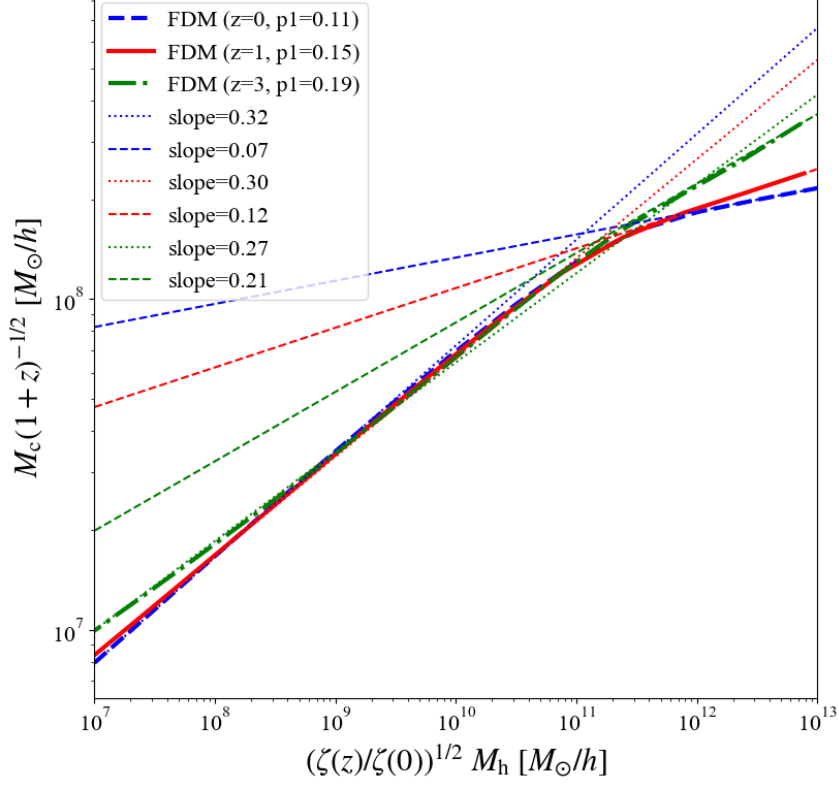


Figure 3.10: The CHMR in the Relaxation model with redshift-dependent  $p_1$ . We show the results of  $z = 0$  (blue dashed),  $z = 1$  (red solid), and  $z = 3$  (green dash-dotted). We set  $p_1 = 0.11$  at  $z = 0$ ,  $0.15$  at  $z = 1$ , and  $0.19$  at  $z = 3$  to absorb the redshift dependence. This figure is taken from [47].

CHMR at redshift  $z = 3$  and use the expression given in Eq. (3.99) to compare the simulation results from [161]. In the Relaxation model, the distribution of the scatter can be derived as follows. Since the concentration parameter is known to follow a log-normal distribution with a constant scatter of approximately 0.16 dex, the probability distribution of the concentration can be expressed as

$$dP = \frac{d \log_{10} c_{\text{vir}}}{\sqrt{2\pi\sigma_{\log_{10} c_{\text{vir}}}^2}} \exp\left(-\frac{(\log_{10} c_{\text{vir}} - \log_{10} c_{\text{vir}}^{\text{mean}})^2}{2\sigma_{\log_{10} c_{\text{vir}}}^2}\right), \quad (3.100)$$

where  $\sigma_{\log_{10} c_{\text{vir}}} = 0.16$  is the variance of the concentration parameter. Since we use the relation  $c_{\text{vir}} = c_{\text{vir}}^{\text{mean}} \times 10^{0.16n}$ , we can express as

$$n = \sigma_{\log_{10} c_{\text{vir}}}^{-1} \log_{10} \left( \frac{c_{\text{vir}}}{c_{\text{vir}}^{\text{mean}}} \right). \quad (3.101)$$

Using the semi-analytic expressions in Eqs. (3.99), (3.100), and (3.101), we can show that the core mass also follows a log-normal distribution,

$$dP = \frac{d \log_{10} M_c}{\sqrt{2\pi\sigma_{\log_{10} M_c}^2}} \exp\left(-\frac{(\log_{10} M_c - \log_{10} M_c^{\text{mean}})^2}{2\sigma_{\log_{10} M_c}^2}\right), \quad (3.102)$$

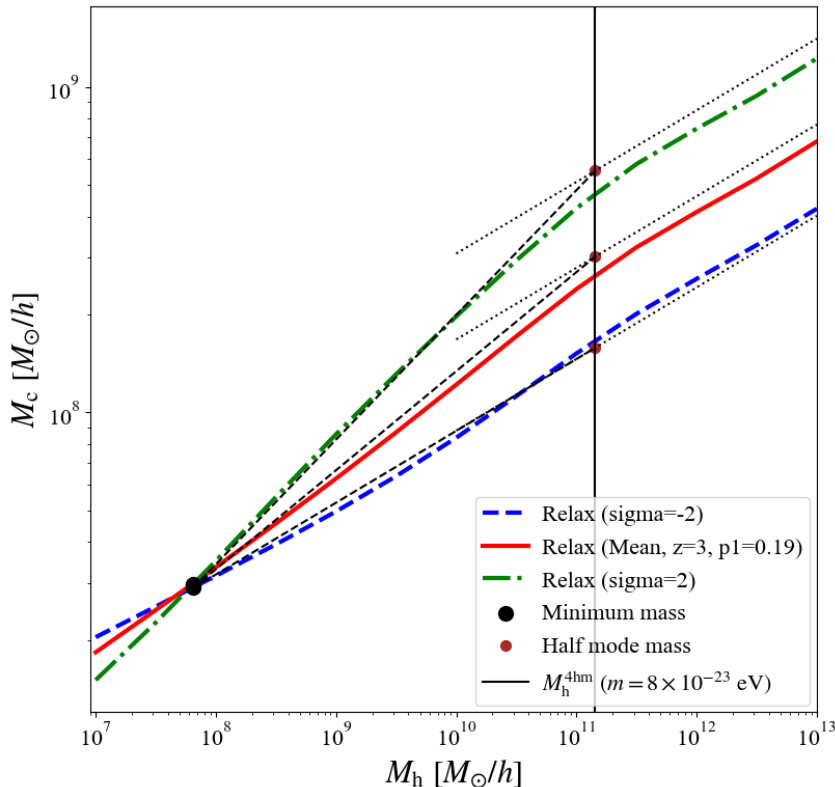


Figure 3.11: The same as Fig. 3.8, but in the case of the redshift  $z = 3$ . The semi-analytic expression is given by Eq. (3.99), plotted by the black dashed and dotted lines. Here we show the minimum mass denoted by  $\tilde{M}_h^{\min}$ . This figure is taken from [47].

where the core mass calculated with the mean concentration is denoted by  $M_c^{\text{mean}}$ , and the scatter of the core mass can be expressed as

$$\sigma_{\log_{10} M_c} = \begin{cases} 0.04 \log_{10} \left( \frac{M_h}{M_h^{\min}} \right) & (M_h^{\min} < M_h < M_h^{4\text{hm}}) \\ 0.04 \log_{10} \left( \frac{M_h^{4\text{hm}}}{M_h^{\min}} \right) & (M_h > M_h^{4\text{hm}}). \end{cases} \quad (3.103)$$

From Eq. (3.103), the degree of the scatter of the core mass increases as halo mass becomes larger for low-mass halos and remains constant for high-mass halos. It is important to note that, due to the monotonic dependence of the  $c_{\text{vir}}-M_h$  relation on the CHMR, the core mass corresponding to an  $n\sigma$  variance of the concentration parameter directly reflects the same variance for the core mass, as shown in Figs. 3.3 to 3.6. Note that the degree of scatter at redshift  $z = 0$  can also be estimated similarly by using Eq. (3.98) instead of Eq. (3.99).

We also examine the core mass distribution derived analytically in [176] using their publicly available code <sup>2</sup>. For a given halo mass, we generate 100,000 realizations of the concentration parameter, assuming a log-normal distribution. The mean concentration is determined by the  $c_{\text{vir}}-M_h$  relation from [55] with the suppression factor from [167], and the scatter is set to 0.16 dex, consistent with the Relaxation model. We compute the core masses by using these concentration parameters, resulting in 100,000 realizations of the core mass for each halo mass. The core mass distributions for ten different halo masses are shown in Fig. 3.12. These distributions are well-fitted by log-normal functions, consistent

<sup>2</sup><https://github.com/ataruya/FDM>

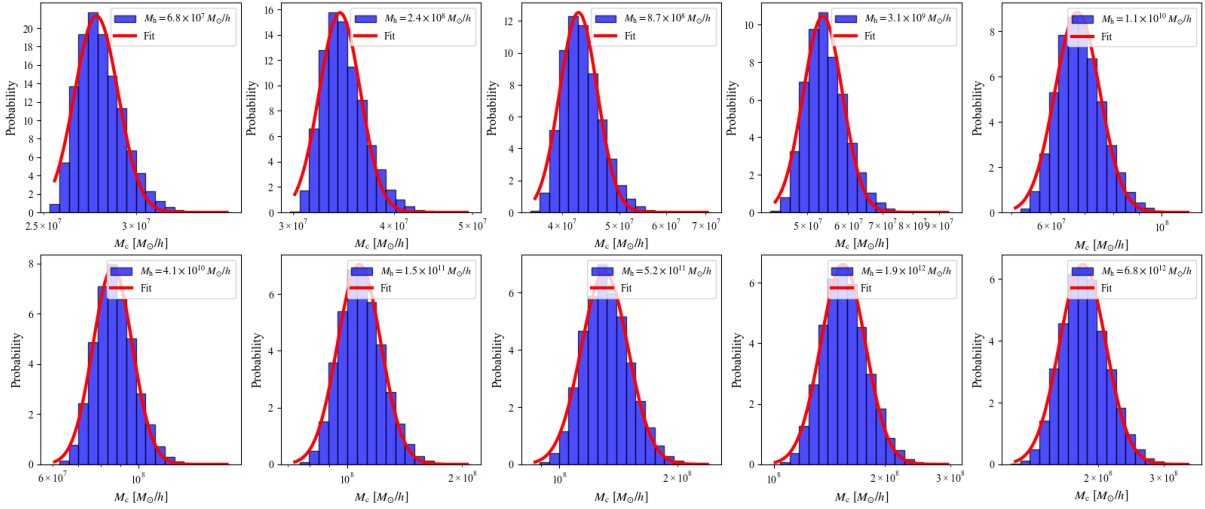


Figure 3.12: The probability distribution of the core mass with ten different halo masses at redshift  $z = 3$  obtained from the analytic study [176] using their public code. For a given halo mass, we compute the 100,000 realizations of the core mass by considering the log-normal scatter of the concentration parameter. The mean concentration is obtained by the  $c_{\text{vir}}-M_h$  relation [55] with the suppression factor presented in [167], and the variance of the concentration parameter is set to 0.16 dex. The red lines show the result of the log-normal fitting to the core mass distribution. This figure is taken from [47].

with the prediction of the Relaxation model. Additionally, we analyze the core mass distribution in the simulation data from [161]. The data is divided into ten logarithmic bins based on halo mass, and the histograms of core mass are plotted in Fig. 3.13. The red lines represent log-normal fits, indicating that the core mass distributions are in good agreement with the log-normal distribution.

Having confirmed that the core mass distributions predicted by both models and observed in simulation data follow a log-normal distribution, we compare the  $1\sigma$  scatter of the core mass. The results are presented in Fig. 3.14. As mentioned earlier, the scatter in the Relaxation model expressed in Eq. (3.103) increases with halo mass for low-mass halos and becomes constant for high-mass halos. While the model by [176] exhibits a similar trend to the Relaxation model, the amplitude of the variance is generally smaller, except for halo masses below  $10^8 M_\odot/h$ . We employ two approaches to estimate the degree of scatter of the core mass for a given halo mass in the simulation data. The first approach is by fitting the core mass distribution with a log-normal function to obtain the scatter, represented by red square dots. In the second approach, we evaluate the scatter using quantiles, following the method presented in [176]. Specifically, we identify two quantiles, where 16% of the data lies below one and above the other, and take half of the difference of the two quantiles as  $1\sigma$ . The results of the second method are shown in orange circle dots. Since the core mass distribution aligns well with the log-normal function, both methods yield nearly identical scatter estimates. In Fig. 3.14, we observe that neither the Relaxation model nor the model presented by [176], which incorporates the scatter in the  $c_{\text{vir}}-M_h$  relation, fully explain the scatter of the CHMR observed in the simulation. While the scatter in the simulation is about 1.5 times larger than that predicted by the Relaxation model, the dependence of the scatter on halo mass shows good agreement between them. These findings suggest that the scatter in core mass at a given

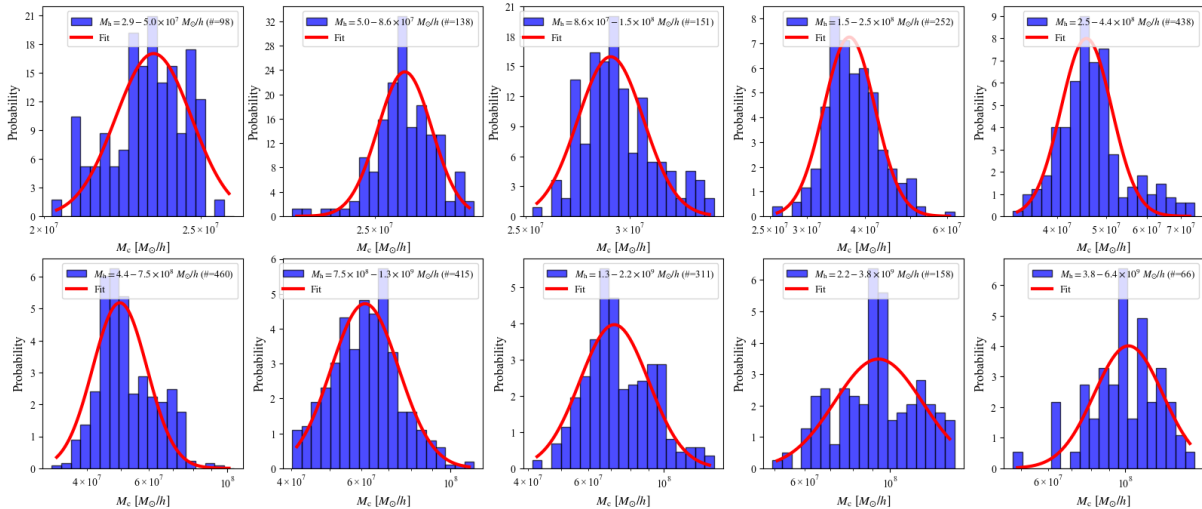


Figure 3.13: The probability distribution of the core mass with ten different halo mass bins obtained from the largest FDM simulation at redshift  $z = 3$  [161]. The red lines show the result of the log-normal fitting. This figure is taken from [47].

halo mass may partially stem from the scatter in halo concentration parameter, which itself likely originates from the assembly history of individual halos. Indeed, additional factors such as the shape of halos may also contribute to the log-normal distribution of core masses and the larger scatter observed in simulations [179]. Since the only degree of freedom for scatter in the current Relaxation model is the concentration parameter, extending the model to account for effects such as non-spherical halos would improve its prediction, which we leave for future studies.

### 3.4.6 Total density profile

While the CHMR might be further investigated in future studies, we obtain the analytic expression for the CHMR at redshift  $z = 0$ , Eq. (3.98). The total density profile, which is the main goal of this section, can be expressed as

$$\rho(r) = \begin{cases} \rho_{\text{sol}}(r) & (r < r_c/2) \\ \max[\rho_{\text{sol}}(r), \rho_{\text{NFW}}(r)] & (r > r_c/2) \end{cases}. \quad (3.104)$$

In Fig. 3.15, we present the density profile of the FDM halo with a halo mass of  $M_h = 10^{11} M_\odot$  at redshift  $z = 0$ , compared with the CDM density profile. The profiles are shown for different FDM particle masses. As the FDM particle mass increases, the core radius decreases, and the central density becomes higher. The FDM density profile surpasses the standard CDM profile near the core radius due to the presence of the soliton core, which affects the strong gravitational signal as shown in Chap. 7.

## 3.5 Subhalo distribution

Due to the wave nature of FDM, the linear power spectrum is suppressed, leading to a reduced abundance of subhalos compared to the CDM case. This suppression takes place

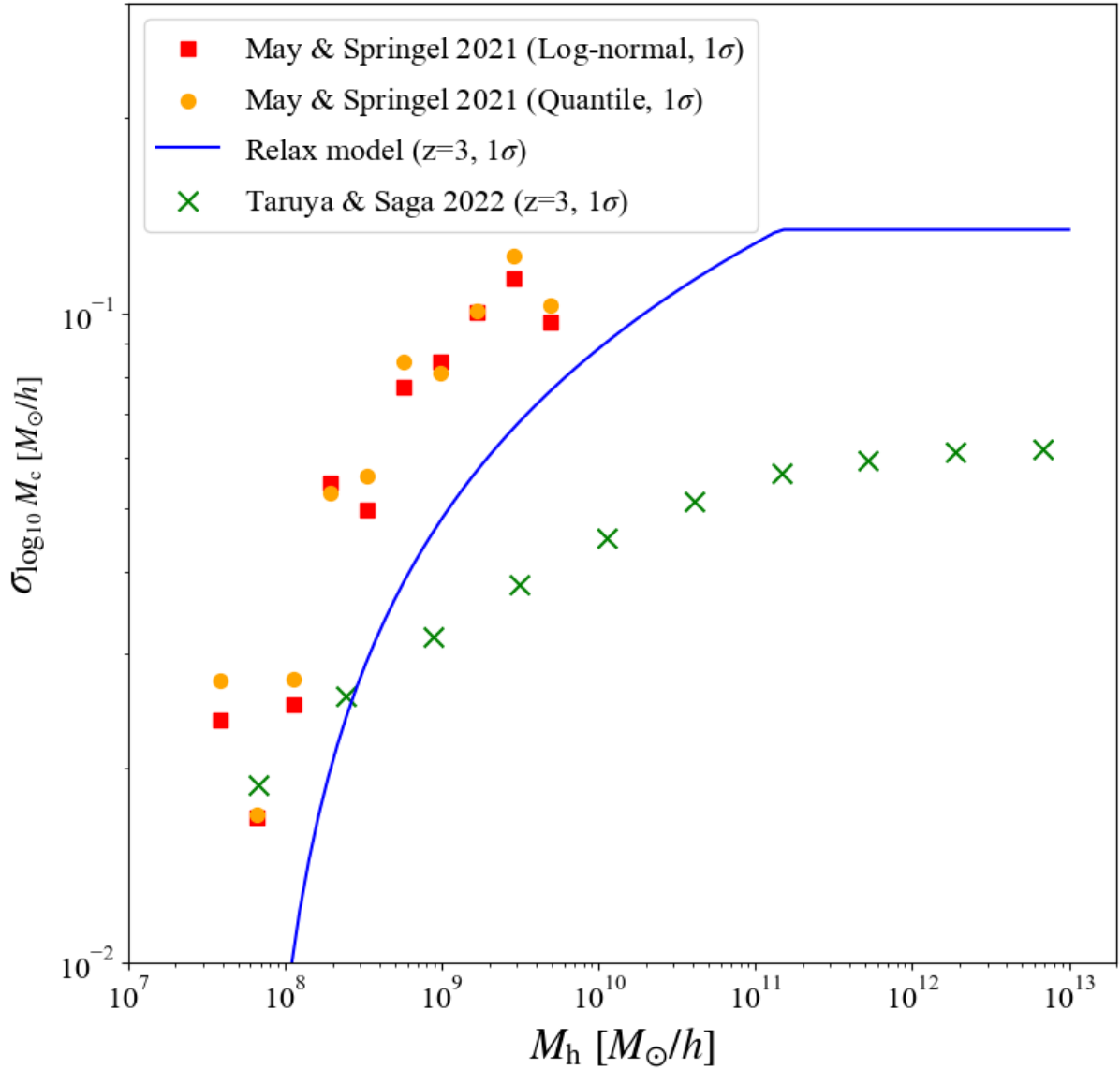


Figure 3.14: The degree of  $1\sigma$  scatters of the core mass at redshift  $z = 3$ . The red square and orange circle dots represent scatters obtained from the simulation results conducted by [161], where the former is estimated by fitting the core mass distribution with the log-normal function, and the latter is estimated by computing quantiles of the 68% around the median core mass. The blue solid line indicates the estimated scatter of the core mass due to the scatter of the concentration parameter using the Relaxation model, Eq. (3.103). The green dots with the cross symbol represent the scatter of the core mass estimated by [176]. This figure is taken from [47].

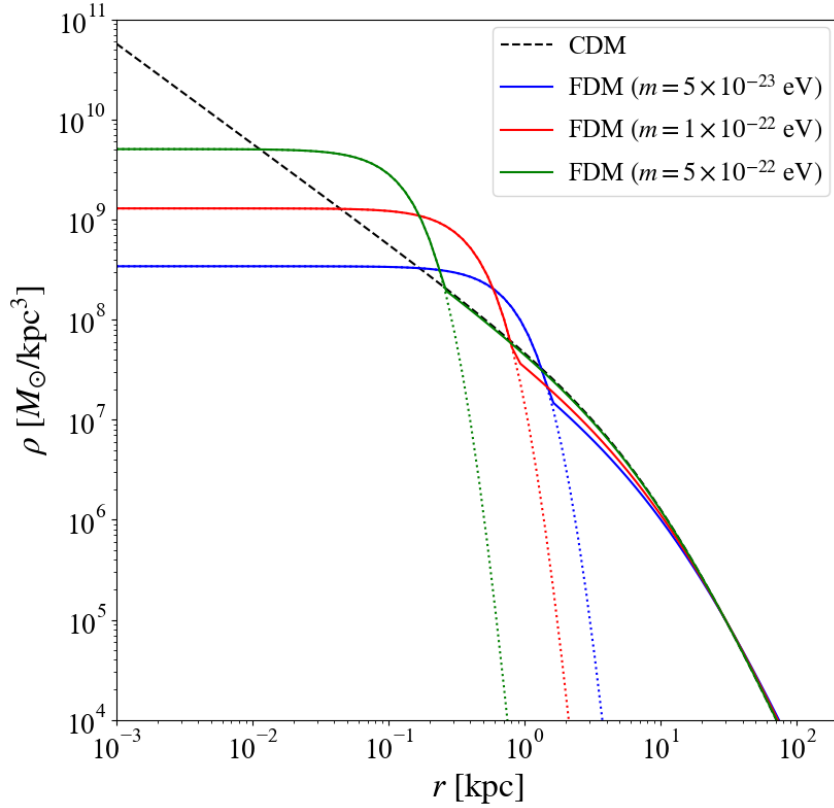


Figure 3.15: The CDM and the FDM density profiles with different FDM masses of halos with mass  $M_h = 10^{11} M_\odot$  at redshift  $z = 0$ . The black dashed line represents the NFW profile in the CDM halo. The blue, red, and green solid and dotted lines show the total density profiles of the FDM halo and their soliton core profiles with  $m = 5 \times 10^{-23} \text{eV}/c^2$ ,  $1 \times 10^{-22} \text{eV}/c^2$ , and  $5 \times 10^{-22} \text{eV}/c^2$ , respectively. We use the  $c_{\text{vir}}-M_h$  relation to obtain the concentration parameter of the CDM halo and multiply the suppression function to obtain that of the FDM halos. This figure is taken from [49].

below the half-mode mass and the subhalo mass function can be expressed as [159, 168],

$$\left. \frac{dN_{\text{sh}}}{dM_{\text{sh}}} \right|_{\text{FDM}} = \left. \frac{dN_{\text{sh}}}{dM_{\text{sh}}} \right|_{\text{CDM}} F \left( \frac{M_{\text{sh}}}{M_h^{\text{hm}}} \right), \quad (3.105)$$

where the suppression function  $F$  is the same as Eq. (3.71), but now the parameters are  $(a, b, c) = (0.36, -1.1, -2.2)$  [168]. The first component in the right-hand side of Eq. (3.105) denotes the CDM subhalo mass functions, i.e., Eq. (2.16) for instance. The projected subhalo mass function can be expressed as

$$\left. \frac{d^2 N_{\text{sh}}}{dM_{\text{sh}} dS} \right|_{\text{FDM}} = \left. \frac{d^2 N_{\text{sh}}}{dM_{\text{sh}} dS} \right|_{\text{CDM}} F \left( \frac{M_{\text{sh}}}{M_h^{\text{hm}}} \right), \quad (3.106)$$

with the same values of  $(a, b, c)$ . Again the first component in the right-hand side of Eq. (3.106) denotes the projected CDM subhalo mass functions defined by Eq. (2.21). In Fig. 3.16, we present the evolved projected subhalo mass function for both CDM and FDM models. As the FDM mass decreases, the turnover shifts to a higher subhalo mass, which is attributed to the larger de Broglie wavelength.

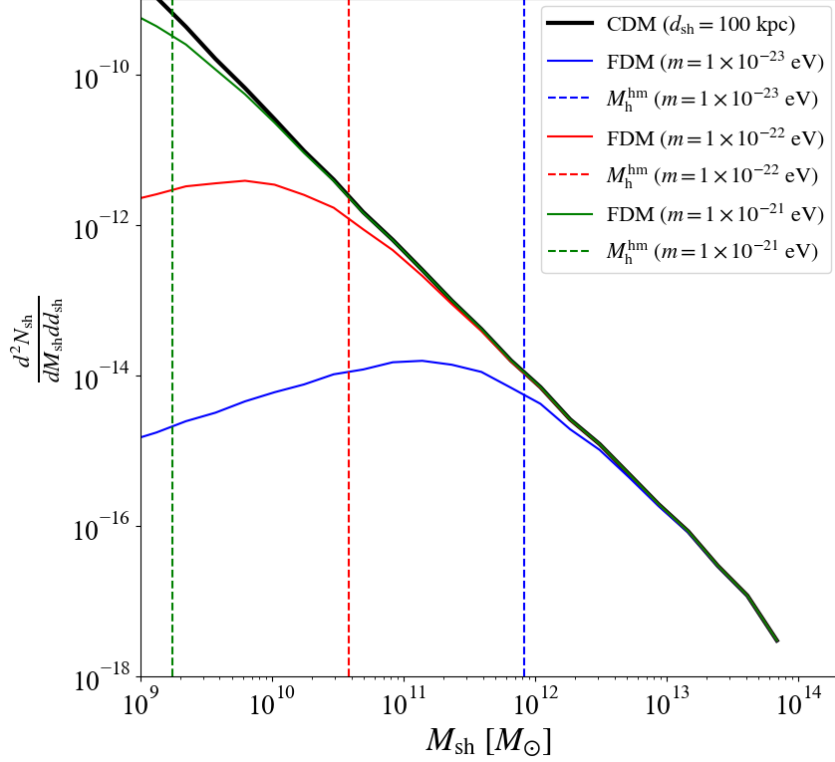


Figure 3.16: The evolved projected subhalo mass function in the case of CDM and FDM models with different FDM masses. Host halo mass is set to  $M_{\text{hh}} = 10^{15} M_{\odot}$  and its density profile is assumed to follow the NFW profile. We use the concentration-halo mass relation obtained by [55]. The position of the subhalos is set to  $d_{\text{sh}} = 100$  kpc and we use the relation  $dS = 2\pi d_{\text{sh}} dd_{\text{sh}}$ . The black solid line indicates the CDM case calculated by [75] with their provided code. The blue, red, and green solid lines are the FDM cases with FDM masses  $m = 1 \times 10^{-23} \text{ eV}/c^2$ ,  $1 \times 10^{-22} \text{ eV}/c^2$ , and  $1 \times 10^{-21} \text{ eV}/c^2$ , respectively. The suppression of the subhalo mass function below the half-mode masses, which are shown in the vertical dashed lines, is calculated by the function  $F$  with  $(a, b, c) = (0.36, -1.1, -2.2)$ . This figure is taken from [49].

### 3.6 Sub-galactic matter power spectrum

In Sec. 3.2, the linear matter power spectrum is discussed. Here, we show the sub-galactic matter power spectrum, where granular structures are the primary contributors, based on the analytical study presented in [164]. Assuming that granular structures are uniformly and randomly distributed within spherical halos and have a constant size determined by the halo velocity dispersion,

$$v = \sqrt{\frac{3GM_{\text{tot}}}{2r_{\text{vir}}}}, \quad (3.107)$$

where the total mass  $M_{\text{tot}}$  refers to the sum of the halo and stellar masses, and  $r_{\text{vir}}$  is the virial radius of the halo. Using Eq. (3.62), the fluctuation around the spatially averaged NFW profile can be written as

$$\delta(\mathbf{r}) = \frac{\rho(\mathbf{r}) - \rho_{\text{NFW}}(\mathbf{r})}{\rho_{\text{NFW}}(\mathbf{r})} = V_c \int_{V_c} d^3r' u(\mathbf{r} - \mathbf{r}') n(\mathbf{r}') - 1. \quad (3.108)$$

The Fourier transform of the density fluctuation can be expressed as,

$$\begin{aligned}
\delta_{\mathbf{k}} &= \int_{V_\epsilon} d^3r \delta(\mathbf{r}) e^{-i\mathbf{k}\cdot\mathbf{r}} \\
&= V_c \int_{V_\epsilon} d^3r' n(\mathbf{r}') e^{-i\mathbf{k}\cdot\mathbf{r}'} \int_{V_\epsilon} d^3r'' u(\mathbf{r}'') e^{-i\mathbf{k}\cdot\mathbf{r}''} \\
&= V_c \tilde{u}_{\mathbf{k}} \int_{V_\epsilon} d^3r' n(\mathbf{r}') e^{-i\mathbf{k}\cdot\mathbf{r}'} \tag{3.109}
\end{aligned}$$

where  $\mathbf{k}$  is the three-dimensional wavenumber of the fluctuation. Note that a discrete Fourier transform is applied here since the radius of concern is finite, i.e., the size of the halo. Since the density fluctuation with the wavenumber  $\mathbf{k} = \mathbf{0}$  is not important, the constant term in Eq. (3.108) is ignored. In the second equality, the variable transformation  $\mathbf{r}'' = \mathbf{r} - \mathbf{r}'$  is performed. The Fourier transform of the normalized mass density profile is denoted by  $\tilde{u}_{\mathbf{k}}$ .

The definition of the three-dimensional power spectrum is

$$\langle \delta_{\mathbf{k}} \delta_{\mathbf{k}'} \rangle = V_c \delta_{\mathbf{k}+\mathbf{k}',\mathbf{0}}^{(3)} P(k). \tag{3.110}$$

The left hand side of Eq. (3.110) can be further calculated by substituting Eq. (3.109) as,

$$\begin{aligned}
\langle \delta_{\mathbf{k}} \delta_{\mathbf{k}'} \rangle &= V_c^2 \tilde{u}_{\mathbf{k}} \tilde{u}_{\mathbf{k}'} \int_{V_\epsilon} d^3r \int_{V_\epsilon} d^3r' e^{-i\mathbf{k}\cdot\mathbf{r}} e^{-i\mathbf{k}'\cdot\mathbf{r}'} \langle n(\mathbf{r}) n(\mathbf{r}') \rangle \\
&= V_c \tilde{u}_{\mathbf{k}} \tilde{u}_{\mathbf{k}'} \int_{V_\epsilon} d^3r e^{-i(\mathbf{k}+\mathbf{k}')\cdot\mathbf{r}} \\
&= V_c V_c \delta_{\mathbf{k}+\mathbf{k}',\mathbf{0}}^{(3)} |\tilde{u}_{\mathbf{k}}|^2. \tag{3.111}
\end{aligned}$$

In the second equality, the correlation between the number density of the granular structures is assumed to be ignored, i.e.,  $\langle n(\mathbf{r}) n(\mathbf{r}') \rangle = \delta^{(3)}(\mathbf{r} - \mathbf{r}')/V_c$ . Therefore, the sub-galactic matter power spectrum is expressed as

$$P(k) = V_c |\tilde{u}_{\mathbf{k}}|^2, \tag{3.112}$$

where the sphericity of the normalized mass density is assumed. When the normalized mass function  $u$  is given by the Gaussian, Eq. (3.60), it can be further expressed as

$$P(k) = V_c \exp\left(-\frac{\lambda_{\text{dB}}^2}{4} k^2\right). \tag{3.113}$$

The sub-galactic matter power spectrum resembles white noise on large angular scales but exhibits exponential suppression on small scales below the de Broglie wavelength.

A similar analysis can be applied to the projected density field. The sub-galactic matter power spectrum at a location  $x = |\mathbf{x}|$  in the projected density is given by

$$P(K) = \frac{V_c}{r_{\text{NFW}}(x)} |\tilde{u}_K|^2, \tag{3.114}$$

where  $K = |\mathbf{K}|$  is the two-dimensional wavenumber, and  $r_{\text{NFW}}(x)$  is the effective radius of the NFW profile, defined as

$$r_{\text{NFW}}(x) = \frac{\left\{ \int dz \rho_{\text{NFW}}(r) \right\}^2}{\int dz \rho_{\text{NFW}}^2(r)}, \tag{3.115}$$

with the integration along the line of sight performed at the point  $x$ . The two-dimensional normalized mass function  $\tilde{u}_K$  is related to the three-dimensional counterpart, as  $\tilde{u}_K = \tilde{u}_k|_{k_z=0}$ . By considering the Gaussian mass density profile, the projected sub-galactic matter power spectrum is further expressed as

$$P(K) = \frac{V_c}{r_{\text{NFW}}(x)} \exp\left(-\frac{\lambda_{\text{dB}}^2}{4} K^2\right). \quad (3.116)$$

When considering the smooth baryon distribution described by the Hernquist profile, Eq. (2.22), in addition to the FDM density profile, the amplitude of the matter power spectrum is suppressed,

$$P(K) = \left(\frac{\Sigma_{\text{NFW}}(x)}{\Sigma_{\text{NFW}}(x) + \Sigma_{\text{Hern}}(x)}\right)^2 \frac{V_c}{r_{\text{NFW}}(x)} \exp\left(-\frac{\lambda_{\text{dB}}^2}{4} K^2\right), \quad (3.117)$$

where  $\Sigma_{\text{Hern}}$  is the projected density of the Hernquist profile. This is because the smooth baryon profiles reduce the density contrast of fluctuations. It is important to note that any modification of the FDM density profile due to the presence of the baryonic component is ignored in this representation.

Figure 3.17 illustrates the projected sub-galactic matter power spectrum for different FDM masses. The amplitude, which is proportional to the volume of the granular structures, exhibits a strong dependence on the FDM mass, scaling as  $V_c \propto \lambda_{\text{dB}}^3 \propto m^{-3}$ . Considering that each granular structure contributes a fluctuation of  $\mathcal{O}(1)$ , the overall fluctuation is reduced and estimated to be  $\mathcal{O}(1/\sqrt{N})$ , where  $N$  is the number of granular structures along the line of sight. As the FDM mass increases or the halo size becomes larger, the number of granular structures increases, leading to a smaller power spectrum. Additionally, damping occurs at scales corresponding to the size of granular structures,  $K \propto \lambda_{\text{dB}}^{-1} \propto m$ .

### 3.7 Previous constraints on the FDM mass

The FDM mass is constrained by various observations (see [156] for a recent review). The suppression of small-scale structures affects the integrated Sachs-Wolfe effect, where photons from the cosmic microwave background (CMB) are gravitationally redshifted by intervening matter between the last scattering surface and the Earth, influencing the CMB anisotropies and pattern of power spectra. By comparing the CMB power spectra obtained by the Wilkinson Microwave Anisotropy Probe (WMAP), Planck satellite, Atacama Cosmology Telescope, and South Pole Telescope, the FDM mass is excluded in the range between  $m = 10^{-33} - 10^{-24}$  eV at the 95% confidence interval (CI) [180, 181]. The Lyman-alpha forests, a series of absorption lines corresponding to the rest frame wavelength of 121.6 nm, formed when light excites neutral hydrogen left in the intergalactic medium (IGM) at various redshifts after the reionization, provide a crucial means to probe small-scale structures. The suppressed linear matter power spectrum in the FDM model results in the suppressed structure of the IGM, which in turn affects the Lyman- $\alpha$  flux power spectrum. From the Baryon Oscillation Spectroscopic Survey (BOSS) in the Sloan Digital Sky Survey (SDSS), XQ-100, and HIRES/MIKE, the FDM mass  $m \lesssim 2 \times 10^{-20}$  eV is excluded at the 95% CI, which is the most stringent constraint [182, 183, 184, 185]. The 21 cm line is a spectral feature produced by the transition between parallel and antiparallel spin states of the proton and electron in a neutral hydrogen atom. Since the

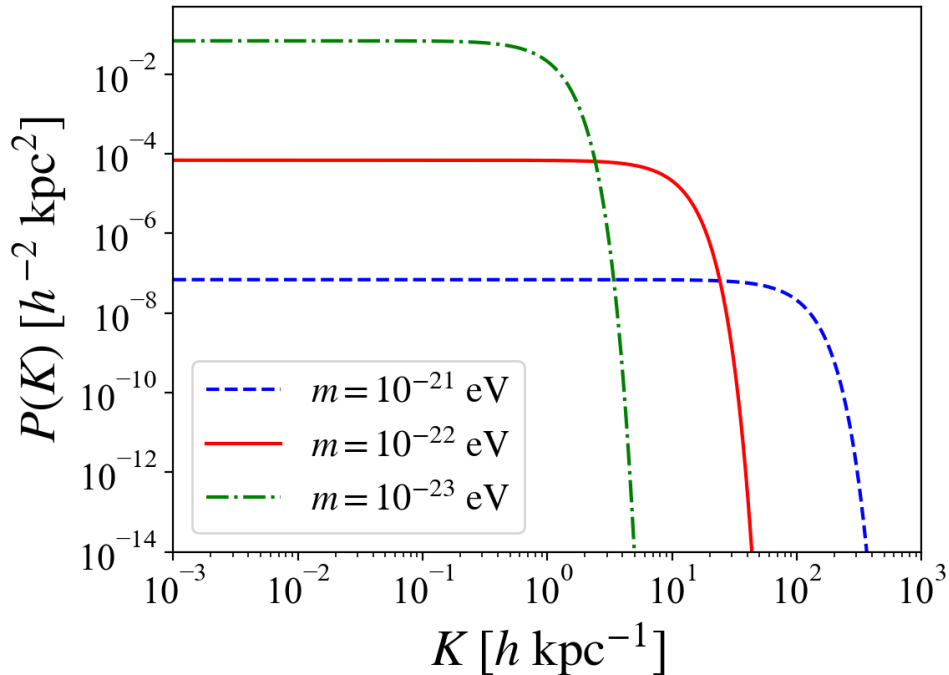


Figure 3.17: The projected sub-galactic matter power spectrum in an FDM halo due to the presence of the granular structures. The three lines represent the results for different FDM masses:  $m = 1 \times 10^{-23}$  eV (green dash-dotted line),  $m = 1 \times 10^{-22}$  eV (red solid line), and  $m = 1 \times 10^{-21}$  eV (blue dashed line). The halo and baryon profiles are given by the NFW and Hernquist profile with total masses being set to  $M_h = 10^{13} M_\odot/h$  and  $M_s = 10^{11} M_\odot/h$ , respectively. We use the  $c_{\text{vir}}-M_h$  relation obtained by [55] and the relation between the effective radius and the total baryon mass shown in Eq. (2.24). We set the position  $x$  by one-hundredth of the halo virial radius, corresponding to  $x \simeq 4.4$  kpc/ $h$ . This figure is adapted from [164].

observations of the 21 cm line trace the neutral hydrogen before and around the epoch of the reionization, it is also useful to probe the abundance of small-scale structures. From the first detection of such an absorption signal at redshift  $z \simeq 17$  in the Experiment to Detect the Global Epoch of Reionization Signature (EDGES) survey, the FDM mass of  $m \lesssim 8 \times 10^{-21}$  eV is constrained [186, 187]. The upcoming power spectrum measurements from the Hydrogen Epoch of Reionization Array (HERA) also constrain the FDM mass around  $m \simeq 10^{-21}$  eV [188]. While these constraints stem from large-scale structure observations, small-scale studies also provide implications for the FDM mass. By estimating the low-mass end of halos through strong gravitational lensing of quasars and the perturbations in the motion of stars in stellar streams within the Milky Way, the FDM mass of  $m < 2.1 \times 10^{-21}$  eV [189] or  $m < 5.2 \times 10^{-21}$  eV [190] has been constrained, with the difference comes from assumed subhalo mass function. In [191], the stellar kinematics of eight dwarf spheroidal galaxies (dSphs) are analyzed, concluding that the FDM mass of  $m \simeq 10^{-22}$  eV is consistent with observations. For two specific dSphs, Fornax and Sculptor, which exhibit the core density profiles, the FDM mass is constrained to  $m \lesssim 4 \times 10^{-23}$  eV [192]. However, combining data of dSphs and ultra-faint dwarfs (UFDs) places a stronger lower bound on the FDM mass, constraining it to  $m \gtrsim 6 \times 10^{-22}$  eV [193]. This is further supported by an analysis of the density profiles of 18 Galactic UFD galaxies, which suggests an even tighter constraint of  $m \gtrsim 10^{-21}$  eV

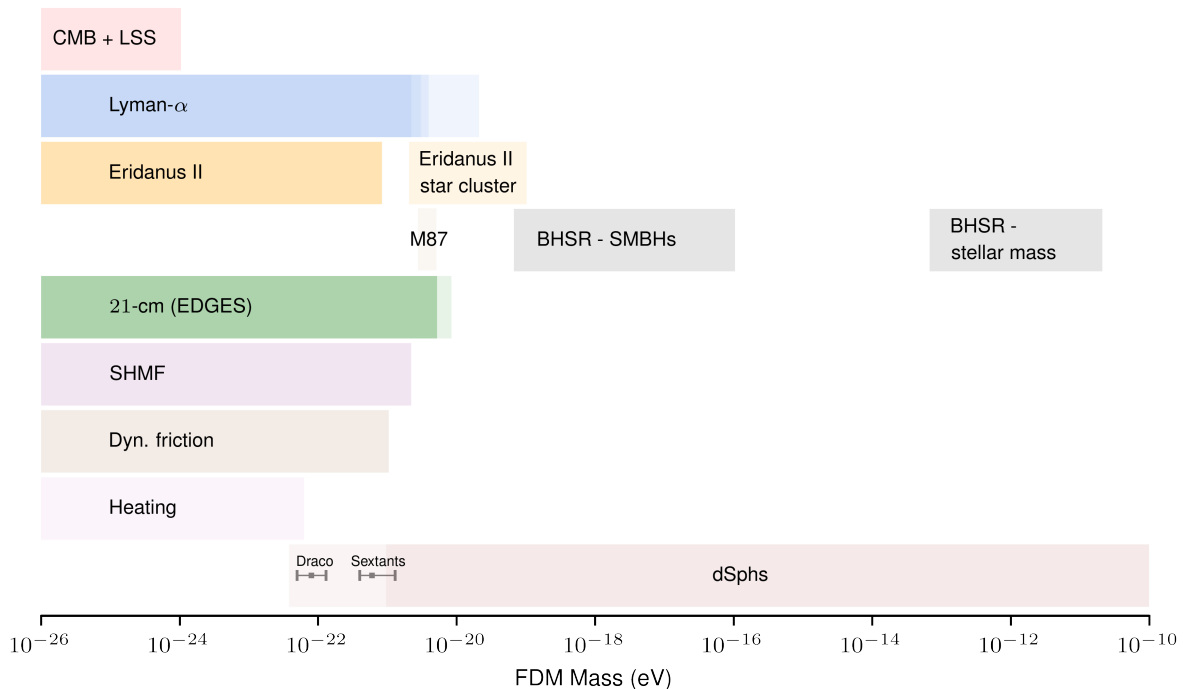


Figure 3.18: The summary of previous constraints on the FDM mass, assuming that FDM constitutes the entirety of the dark matter. The colored regions are excluded by observations. The constraints come from the CMB anisotropy and the large-scale structure [180, 181] Lyman- $\alpha$  forest [182, 183, 184, 185], Eridanus II [198], black hole superradiance [199, 200], 21 cm absorption line [186, 187], quasar strong lensing and stellar streams using the subhalo mass function (SHMF) [189], dynamical friction [196], heating of the Milky Way discs [197], and dSphs and UFDs [191, 192, 193, 194]. This figure is taken from [156].

[194]. Additionally, the constraints have been obtained from the rotation curve of the Milky Way [195], the effects of dynamical friction [196], the heating of Milky Way disc stars by granular structures [197], the heating of old star clusters in Eridanus II due to the soliton core oscillation [198], and black hole superradiance [199, 200]. Note that black hole superradiance is a phenomenon where rotating black holes lose energy and angular momentum by amplifying waves with a Compton wavelength comparable to or larger than the black hole size, thereby constraining the FDM mass based on its efficiency.

Combining all these constraints, no single FDM mass is strongly favored, implying that FDM alone might not fully account for the dark matter component in the universe. However, since some of these constraints may be affected by uncertainties in baryonic physics, further detailed studies are needed. The constraints on the FDM mass listed above are summarized in Fig. 3.18.



# Chapter 4

## Strong gravitational lensing

Before the advent of general relativity (GR), Newtonian theory was the standard framework for explaining motion in gravitational fields. According to Newtonian mechanics, acceleration  $\mathbf{a} = \mathbf{F}/m$  is independent of mass. Thus, if light behaves as a particle, it should also be influenced by a gravitational field. Using Newtonian gravity, the deflection angle of light by a spherical mass  $M$  is calculated as  $\hat{\alpha} = 2GM/c^2\xi$ , where  $\xi$  is the impact parameter. In 1915, Albert Einstein formulated the GR and recalculated the deflection of light, revealing that the Newtonian result underestimated the angle by a factor of two. This discrepancy arises from the curvature in the presence of mass predicted by the GR, which increases the deflection angle. According to the GR, the deflection angle is given by

$$\hat{\alpha} = \frac{4GM}{c^2\xi} = 1''.75 \left( \frac{M}{M_\odot} \right) \left( \frac{\xi}{R_\odot} \right)^{-1}. \quad (4.1)$$

This theoretical prediction, first validated by Eddington's observations during a solar eclipse in 1919, has been confirmed by numerous subsequent observations. These theoretical and observational advancements laid the foundation for using gravitational lensing to study the mass distribution in the universe.

In this chapter, we specifically focus on strong gravitational lensing, which produces multiple images. These images are observed near the characteristic lines called critical curves, where magnification becomes mathematically infinity. The Einstein ring is an example of the critical curve, a ring-shaped image that forms when the source, lens, and observer are aligned along a straight line. The size of the Einstein ring, i.e., the Einstein radius, varies depending on the mass of the lensing object. When the lensing object has a stellar mass, the Einstein radius is on the order of micro-arcseconds, and such lensing objects are often referred to as microlenses. In the case of galaxy-size lenses, where the mass is around  $10^{10} - 10^{12} M_\odot$ , the Einstein radius is on the order of arcseconds. For galaxy clusters with masses around  $10^{15} M_\odot$ , the Einstein ring can reach sizes on the order of ten to hundred arcseconds. Since these underlying lens objects influence the shape and distribution of critical curves, small-scale mass distribution in the universe. These lensing objects determine the shape and distribution of critical curves and influence strong gravitational lensing events. With the discovery of numerous strong gravitational lensing events through observations, the theoretical framework regarding the relationship between the underlying mass distribution and lensing properties such as magnification and image locations has been developed.

In this chapter, we first derive the lens equation from the geodesic equation in Sec. 4.1. The image distortion and magnification are shown in Sec. 4.2, followed by a review of the

critical curve and caustic in Sec. 4.3 and multiple images in Sec. 4.4. Since our main focus is the strong gravitational lensing, in which multiple images are observed near critical curves, we show the magnification behavior in these regions in Sec. 4.5. As an example of a lens system, we consider the spherically symmetric lens in Sec. 4.6. Next, we consider specific cases involving microlenses. The case of a single microlens embedded in a smooth mass distribution is explored in Sec. 4.7, while that of randomly distributed microlenses is examined in Sec. 4.8. Note that the discussions in Secs. 4.1, 4.2, and 4.6 are primarily taken from the gravitational lensing textbook by Professor Masamune Oguri [201]. Additionally, the contents of Secs. 4.3 and 4.4 are based on the textbook of [202].

## 4.1 Lens equation

The GR shows that light follows a "straight" line in curved spacetime, known as the geodesic. The geodesic equation is

$$\frac{d^2 x^\mu}{d\lambda^2} + \Gamma_{\alpha\beta}^\mu \frac{dx^\alpha}{d\lambda} \frac{dx^\beta}{d\lambda} = 0, \quad (4.2)$$

where  $x^\mu = (ct, \mathbf{x})$  with  $\mathbf{x}$  being the comoving coordinates,  $\lambda$  is an affine parameter, and  $\Gamma_{\alpha\beta}^\mu$  is the Christoffel symbol, which encodes the geometry of curved spacetime,

$$\Gamma_{\alpha\beta}^\mu = \frac{1}{2} g^{\mu\nu} (g_{\nu\alpha,\beta} + g_{\beta\nu,\alpha} - g_{\alpha\beta,\nu}), \quad (4.3)$$

with  $g_{\mu\nu}$  denoting the metric of spacetime and  $g_{\alpha\beta,\nu} = \partial g_{\alpha\beta} / \partial x^\nu$ . In the case of the Minkowski spacetime, the geodesic equation reduces to the Newtonian equation of motion. The geodesic equation can be transformed into the useful form,

$$\frac{d}{d\lambda} \left( g_{\mu\nu} \frac{dx^\nu}{d\lambda} \right) - \frac{1}{2} g_{\alpha\beta,\mu} \frac{dx^\alpha}{d\lambda} \frac{dx^\beta}{d\lambda} = 0, \quad (4.4)$$

from which we see that  $g_{\mu\nu} dx^\nu / d\lambda$  conserves along geodesics when the metric tensor does not depend explicitly on some coordinate  $x^\mu$ . This corresponds to the energy-momentum conservation in the presence of shift symmetry. For massless particles, the line element is null,

$$ds^2 = g_{\mu\nu} dx^\mu dx^\nu = 0, \quad (4.5)$$

and the affine parameter is defined by

$$\frac{dx^\mu}{d\lambda} = k^\mu, \quad (4.6)$$

where  $k^\mu$  is the four-dimensional wavenumber vector. The zeroth component of this vector corresponds to the angular frequency  $\omega/c$ , and the spatial components represent the three-dimensional wavevector,  $\mathbf{k}$ . The null condition can be expressed with the four-vector as

$$k^\mu k_\mu = 0, \quad (4.7)$$

and the geodesic equation, Eq. (4.2), for massless particles becomes

$$\frac{dk^\mu}{d\lambda} + \Gamma_{\alpha\beta}^\mu k^\alpha k^\beta = 0. \quad (4.8)$$

Equivalently, the geodesic equation given in Eq. (4.4) can be expressed as

$$\frac{dk_\mu}{d\lambda} - \frac{1}{2}g_{\alpha\beta,\mu}k^\alpha k^\beta = 0. \quad (4.9)$$

These equations serve as the foundation for deriving the lens equation.

We first consider the homogeneous and isotropic universe, whose spacetime can be expressed by the Friedmann-Lemaître-Robertson-Walker (FLRW) metric,

$$ds^2 = -c^2 dt^2 + a^2 [d\chi^2 + f_K^2(\chi)(d\theta^2 + \sin^2\theta d\phi^2)], \quad (4.10)$$

with  $f_K(\chi)$  being the function related to the curvature  $K$ , given by

$$f_K(\chi) = \begin{cases} \frac{1}{\sqrt{K}} \sin(\sqrt{K}\chi) & (K > 0), \\ \chi & (K = 0), \\ \frac{1}{\sqrt{-K}} \sinh(\sqrt{-K}\chi) & (K < 0). \end{cases} \quad (4.11)$$

Here,  $\chi$  is the radial coordinate of the polar coordinates, and  $\theta$  and  $\phi$  are the angular coordinates. Since the metric does not depend on the azimuthal angle  $\phi$ , Eq. (4.4) can be expressed as

$$g_{3\nu} \frac{dx^\nu}{d\lambda} = a^2 f_K^2 \sin^2\theta \frac{d\phi}{d\lambda} = 0, \quad (4.12)$$

where the boundary condition,  $f_K(\chi = 0) = 0$ , is applied to obtain the second equality. Therefore, we obtain

$$\frac{d\phi}{d\lambda} = 0. \quad (4.13)$$

Next, we consider the geodesic equation with  $\mu = 2$ . From Eq. (4.4), we obtain

$$\frac{d}{d\lambda} \left( g_{2\nu} \frac{dx^\nu}{d\lambda} \right) = \frac{1}{2} g_{\alpha\beta,2} \frac{dx^\alpha}{d\lambda} \frac{dx^\beta}{d\lambda} = 0, \quad (4.14)$$

where Eq. (4.13) is used to derive the last equality. Considering the boundary condition at  $\chi = 0$ , we obtain

$$\frac{d\theta}{d\lambda} = 0. \quad (4.15)$$

The first component of the geodesic equation can similarly be written as

$$\frac{d}{d\lambda} \left( g_{1\nu} \frac{dx^\nu}{d\lambda} \right) = \frac{1}{2} g_{\alpha\beta,1} \frac{dx^\alpha}{d\lambda} \frac{dx^\beta}{d\lambda} = 0. \quad (4.16)$$

By integrating both sides of the above equation and setting the integration constant to unity, which can be achieved by choosing an appropriate affine parameter, we obtain

$$\frac{d\chi}{d\lambda} = \frac{1}{a^2}. \quad (4.17)$$

Finally, the zeroth component of the geodesic equation is

$$\frac{d}{d\lambda} \left( g_{0\nu} \frac{dx^\nu}{d\lambda} \right) = \frac{1}{2} g_{\alpha\beta,0} \frac{dx^\alpha}{d\lambda} \frac{dx^\beta}{d\lambda} = \frac{\dot{a}}{a^3}. \quad (4.18)$$

This can be further simplified to

$$\frac{cdt}{d\lambda} = \pm \frac{1}{a}. \quad (4.19)$$

Note that Eq. (4.19) can also be derived from the null condition. Since we are interested in the light propagation towards the observer, we choose the minus sign in Eq. (4.19) in the following.

To derive the lens equation, which describes how light is deflected in the presence of mass, we consider the perturbation to the FLRW metric,

$$ds^2 = - \left( 1 + \frac{2\Phi}{c^2} \right) c^2 dt^2 + a^2 \left( 1 - \frac{2\Psi}{c^2} \right) \gamma_{ij} dx^i dx^j, \quad (4.20)$$

where  $\gamma_{ij}$  denotes the spatial tensor given by

$$\gamma_{ij} dx^i dx^j = d\chi^2 + f_K^2(\chi) \omega_{ab} dx^a dx^b \quad (4.21)$$

with

$$\omega_{ab} dx^a dx^b = d\theta^2 + \sin^2 \theta d\phi^2. \quad (4.22)$$

Here  $\Phi$  and  $\Psi$  are the gravitational potential and the curvature perturbation, respectively. They are assumed to be small,  $|\Phi/c^2| \ll 1$ ,  $|\Psi/c^2| \ll 1$ , and the relation  $\Phi = \Psi$  holds since there is no anisotropic stress at least to first order in the GR. Considering the first-order perturbation of the geodesic equations, the angular components of the geodesic equation become

$$\frac{d}{d\chi} \left[ f_K^2(\chi) \frac{dx^a}{d\chi} \right] + \frac{2}{c^2} \omega^{ab} \Phi_{,b} = 0. \quad (4.23)$$

This equation shows how the light ray is bent by the presence of the gravitational potential. The factor of two in the second term comes from the contribution of curvature perturbation  $\Psi$  in addition to the gravitational potential  $\Phi$ , which is different from Newtonian mechanics. By integrating in terms of the radial coordinate  $\chi$ , we can obtain

$$\begin{aligned} x^a(\chi_s) - x^a(0) &= -\frac{2}{c^2} \int_0^{\chi_s} d\chi' \frac{1}{f_K^2(\chi')} \int_0^{\chi'} d\chi \omega^{ab} \Phi_{,b}(\chi, \boldsymbol{\theta}(\chi)) \\ &= -\frac{2}{c^2} \int_0^{\chi_s} d\chi \omega^{ab} \Phi_{,b}(\chi, \boldsymbol{\theta}(\chi)) \int_\chi^{\chi_s} d\chi' \frac{1}{f_K^2(\chi')}, \end{aligned} \quad (4.24)$$

where  $\chi_s$  denotes the radial coordinate of the source and the observer is located at  $\chi = 0$ . By calculating the second integral and using the relation  $\omega^{ab} \Phi_{,b} = (\nabla_{\boldsymbol{\theta}} \Phi)^a$ , we can simplify the above equation as

$$\boldsymbol{\theta}(\chi_s) = \boldsymbol{\theta}(0) - \frac{2}{c^2} \int_0^{\chi_s} d\chi \frac{f_K(\chi_s - \chi)}{f_K(\chi) f_K(\chi_s)} \nabla_{\boldsymbol{\theta}} \Phi(\chi, \boldsymbol{\theta}(\chi)). \quad (4.25)$$

This represents the lens equation, which relates the light from an object at the comoving distance  $\chi_s$  and celestial coordinates  $\boldsymbol{\theta}(\chi_s)$  to the observed celestial coordinates  $\boldsymbol{\theta}(0)$ . The bending of light occurs due to the influence of the intervening mass distribution.

Since the gravitational potential on the right-hand side of Eq. (4.25) depends on  $\boldsymbol{\theta}(\chi)$ , which itself is determined by the lens equation, it takes the form of an integral equation. A common approximation is to evaluate the gravitational potential at the position of the observer. With this simplification, the lens equation becomes

$$\boldsymbol{\theta}(\chi_s) = \boldsymbol{\theta}(0) - \frac{2}{c^2} \int_0^{\chi_s} d\chi \frac{f_K(\chi_s - \chi)}{f_K(\chi) f_K(\chi_s)} \nabla_{\boldsymbol{\theta}} \Phi(\chi, \mathbf{0}). \quad (4.26)$$

The location of the source is often denoted by  $\boldsymbol{\beta} = \boldsymbol{\theta}(\chi_s)$  and the location of the observed image is denoted by  $\boldsymbol{\theta} = \boldsymbol{\theta}(0)$ , leading to

$$\boldsymbol{\beta} = \boldsymbol{\theta} - \frac{2}{c^2} \int_0^{\chi_s} d\chi \frac{f_K(\chi_s - \chi)}{f_K(\chi)f_K(\chi_s)} \nabla_{\boldsymbol{\theta}} \Phi(\chi, \boldsymbol{\theta}). \quad (4.27)$$

The lens equation given in Eq. (4.27) can be interpreted as a mapping from the lens plane to the source plane. Furthermore, since the deflection angle is relatively small, we can approximate the light-passing region as locally flat and use Cartesian coordinates instead of celestial coordinates. In this framework, the source and image positions are represented as  $\boldsymbol{\beta} = (\beta_1, \beta_2)$  and  $\boldsymbol{\theta} = (\theta_1, \theta_2)$ , respectively, and the gradient with respect to  $\boldsymbol{\theta}$  is expressed as  $\nabla_{\boldsymbol{\theta}} = (\partial/\partial\theta_1, \partial/\partial\theta_2)$ . More simpler form of the lens equation is expressed by

$$\boldsymbol{\beta} = \boldsymbol{\theta} - \boldsymbol{\alpha}(\boldsymbol{\theta}), \quad (4.28)$$

where the  $\boldsymbol{\alpha}(\boldsymbol{\theta})$  is the deflection angle. By introducing the lens potential  $\psi(\boldsymbol{\theta})$  given by

$$\psi(\boldsymbol{\theta}) = \frac{2}{c^2} \int_0^{\chi_s} d\chi \frac{f_K(\chi_s - \chi)}{f_K(\chi)f_K(\chi_s)} \Phi(\chi, \boldsymbol{\theta}), \quad (4.29)$$

the deflection angle can be expressed by

$$\boldsymbol{\alpha}(\boldsymbol{\theta}) = \nabla_{\boldsymbol{\theta}} \psi(\boldsymbol{\theta}) = \frac{2}{c^2} \int_0^{\chi_s} d\chi \frac{f_K(\chi_s - \chi)}{f_K(\chi)f_K(\chi_s)} \nabla_{\boldsymbol{\theta}} \Phi(\chi, \boldsymbol{\theta}). \quad (4.30)$$

In most cases, gravitational lensing is caused by a single object such as a galaxy and galaxy cluster. Since the size of these lenses is much smaller than their distance to the source, the thin lens approximation, which treats lenses as having negligible thickness along the line of sight, is commonly applied. When the lens object is located at redshift  $z_\ell$ , or corresponding to the scale factor  $a_\ell$ , its density profile can be approximated as

$$\rho(\mathbf{r}) \simeq \delta_D(Z) \Sigma(\mathbf{r}_\perp), \quad (4.31)$$

where  $\mathbf{r}_\perp = a_\ell f_K(\chi_\ell) \boldsymbol{\theta}$  with  $\chi_\ell = \chi(z_\ell)$ ,  $Z$  represents the coordinate along the line of sight with  $Z = 0$  at the location of the lens, and  $\Sigma$  denotes the surface density. The density profile is related to the gravitational potential as

$$\Phi(\mathbf{r}) = - \int d^3 r' \frac{G\rho(\mathbf{r}')}{|\mathbf{r} - \mathbf{r}'|} \simeq -G \int d^2 r'_\perp \frac{\Sigma(\mathbf{r}'_\perp)}{\sqrt{|\mathbf{r}_\perp - \mathbf{r}'_\perp|^2 + Z^2}}, \quad (4.32)$$

from which the gradient of the gravitational potential can be expressed as

$$\begin{aligned} \nabla_{\boldsymbol{\theta}} \Phi &\simeq G a_\ell f_K(\chi_\ell) \int d^2 r'_\perp \frac{\mathbf{r}_\perp - \mathbf{r}'_\perp}{\{|\mathbf{r}_\perp - \mathbf{r}'_\perp|^2 + Z^2\}^{\frac{3}{2}}} \Sigma(\mathbf{r}'_\perp) \\ &\simeq 2G f_K(\chi_\ell) \delta_D(\chi - \chi_\ell) \int d^2 r'_\perp \frac{\mathbf{r}_\perp - \mathbf{r}'_\perp}{|\mathbf{r}_\perp - \mathbf{r}'_\perp|^2} \Sigma(\mathbf{r}'_\perp) \\ &= 2G a_\ell \{f_K(\chi_\ell)\}^2 \delta_D(\chi - \chi_\ell) \int d^2 \theta' \frac{\boldsymbol{\theta} - \boldsymbol{\theta}'}{|\boldsymbol{\theta} - \boldsymbol{\theta}'|^2} \Sigma(\boldsymbol{\theta}'). \end{aligned} \quad (4.33)$$

In the second equality, the following approximation is applied,

$$\frac{1}{\{|\mathbf{r}_\perp - \mathbf{r}'_\perp|^2 + Z^2\}^{\frac{3}{2}}} \simeq \frac{2\delta_D(Z)}{|\mathbf{r}_\perp - \mathbf{r}'_\perp|^2} \simeq \frac{2a_\ell^{-1} \delta_D(\chi - \chi_\ell)}{|\mathbf{r}_\perp - \mathbf{r}'_\perp|^2}. \quad (4.34)$$

By substituting Eq. (4.33) into Eq. (4.30), the deflection angle under the thin lens approximation can be expressed as

$$\boldsymbol{\alpha}(\boldsymbol{\theta}) = \frac{1}{\pi} \int d^2\theta' \kappa(\boldsymbol{\theta}') \frac{\boldsymbol{\theta} - \boldsymbol{\theta}'}{|\boldsymbol{\theta} - \boldsymbol{\theta}'|^2}, \quad (4.35)$$

where  $\kappa$  is the convergence, defined as

$$\kappa(\boldsymbol{\theta}) = \frac{\Sigma(\boldsymbol{\theta})}{\Sigma_{\text{cr}}} \quad (4.36)$$

and  $\Sigma_{\text{cr}}$  is the critical surface density, given by

$$\Sigma_{\text{cr}} = \frac{c^2}{4\pi G} \frac{D_{\text{os}}}{D_{\text{ol}}D_{\text{ls}}}. \quad (4.37)$$

Here,  $D_{\text{ol}}$ ,  $D_{\text{os}}$ , and  $D_{\text{ls}}$  are the angular diameter distances from the observer to the lens, from the observer to the source, and from the lens to the source, respectively. These distances can be expressed as

$$D_{\text{ol}} = \frac{f_K(\chi_\ell)}{1 + z_\ell} = a_\ell f_K(\chi_\ell), \quad (4.38)$$

$$D_{\text{os}} = \frac{f_K(\chi_s)}{1 + z_s} = a_s f_K(\chi_s), \quad (4.39)$$

$$D_{\text{ls}} = \frac{f_K(\chi_s - \chi_\ell)}{1 + z_s} = a_s f_K(\chi_s - \chi_\ell), \quad (4.40)$$

where  $a_s$  is the scale factor corresponding to the source redshifts  $z_s$ . Note that the lens potential can be written as

$$\psi(\boldsymbol{\theta}) = \frac{1}{\pi} \int d^2\theta' \kappa(\boldsymbol{\theta}') \ln |\boldsymbol{\theta} - \boldsymbol{\theta}'|, \quad (4.41)$$

under the thin lens approximation. In Fig. 4.1, we show the schematic picture of the gravitational lensing system.

The lens equation, Eq. (4.28), can also be derived from the scalar function, called Fermat potential,

$$\tau(\boldsymbol{\theta}; \boldsymbol{\beta}) = \frac{1}{2}(\boldsymbol{\theta} - \boldsymbol{\beta})^2 - \psi(\boldsymbol{\theta}), \quad (4.42)$$

which is the function of  $\boldsymbol{\theta}$  with  $\boldsymbol{\beta}$  entering as a parameter. The Fermat potential corresponds to the time it takes for light emitted from the coordinate point  $\boldsymbol{\beta}$  in the source plane to pass through the coordinate point  $\boldsymbol{\theta}$  in the lens plane and reach the observer, up to an affine transformation [203]. The lens equation can be obtained from

$$\nabla_{\boldsymbol{\theta}} \tau(\boldsymbol{\theta}; \boldsymbol{\beta}) = 0, \quad (4.43)$$

expressing the principle that physical light rays travel along paths whose travel time is stationary.

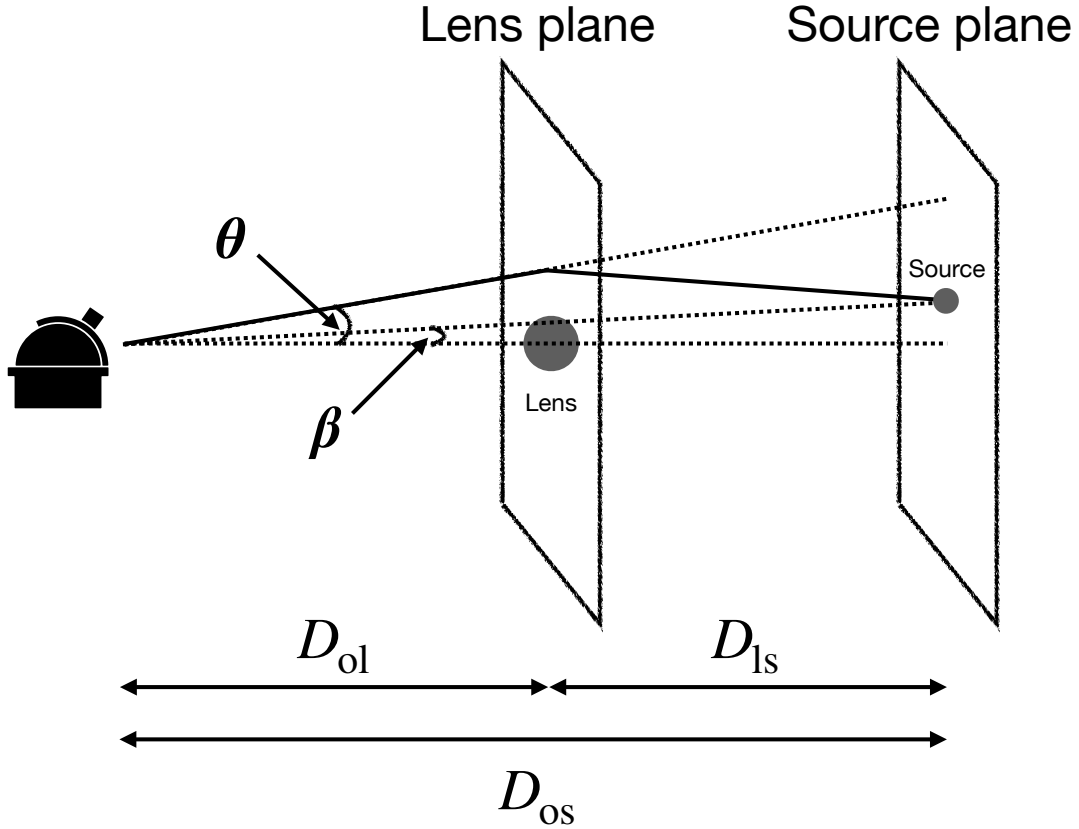


Figure 4.1: Schematic illustration of gravitational lensing system under the thin lens approximation.

## 4.2 Image distortion and magnification

In Sec. 4.1, we derive the lens equation, which describes how the light emitted from a source propagates through the spacetime in the presence of a lens mass distribution. Using the lens equation, we explore the distortion of images and their magnification in this section.

Since the lens equation maps the image plane to the source plane, the distortion of images is characterized by the Jacobian matrix,

$$A(\boldsymbol{\theta}) = \frac{\partial \boldsymbol{\beta}}{\partial \boldsymbol{\theta}} = \left( \delta_{ij} - \frac{\partial^2 \psi(\boldsymbol{\theta})}{\partial \theta_i \partial \theta_j} \right) = \begin{pmatrix} 1 - \kappa - \gamma_1 & -\gamma_2 \\ -\gamma_2 & 1 - \kappa + \gamma_1 \end{pmatrix}, \quad (4.44)$$

where  $\kappa$  is the convergence as defined in Eq. (4.36), and  $\gamma_1$  and  $\gamma_2$  are the two components of the shear. The convergence and shear components can be expressed in terms of the lens potential as

$$\kappa = \frac{1}{2} \left( \frac{\partial^2 \psi}{\partial \theta_1^2} + \frac{\partial^2 \psi}{\partial \theta_2^2} \right), \quad (4.45)$$

$$\gamma_1 = \frac{1}{2} \left( \frac{\partial^2 \psi}{\partial \theta_1^2} - \frac{\partial^2 \psi}{\partial \theta_2^2} \right), \quad (4.46)$$

$$\gamma_2 = \frac{\partial^2 \psi}{\partial \theta_1 \partial \theta_2}. \quad (4.47)$$

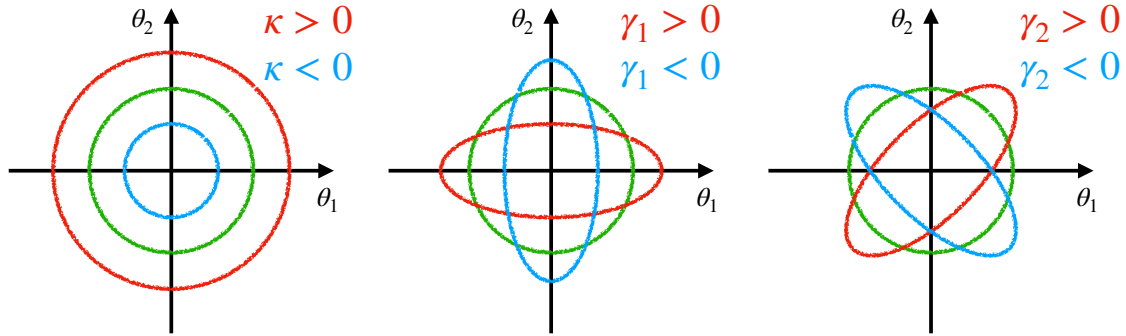


Figure 4.2: The effect of the convergence  $\kappa$  (left) and the shear components  $\gamma_1$  (middle),  $\gamma_2$  (right) on the shape of the observed images. The green lines indicate the original shape of the background source. The red and light blue lines indicate the observed shape of the images.

The total shear is defined as  $\gamma = \sqrt{\gamma_1^2 + \gamma_2^2}$ . While the convergence  $\kappa$  affects the size of the image, it does not alter its shape. In contrast, the shear  $\gamma$  distorts the image, causing changes in its shape due to the tidal gravitational field. These characteristics can be understood by analyzing the eigenvalues and eigenvectors of the Jacobian matrix. Since  $\kappa$  is the coefficient of the identity matrix, it isotropically scales the image size. Specifically, the image size increases if  $\kappa > 0$  and decreases if  $\kappa < 0$ , without affecting the shape of the images. For the shear component  $\gamma_1$ , the eigenvectors are aligned with the coordinate axes,  $(\theta_1, \theta_2) = (1, 0)$  and  $(0, 1)$ . A positive  $\gamma_1$  stretches the image along the  $\theta_1$  axis and compresses it along the  $\theta_2$  axis, transforming a circular source into an ellipse elongated in the  $\theta_1$ -direction. Conversely, if  $\gamma_1 < 0$ , the image is stretched in the  $\theta_2$ -direction. For the shear component  $\gamma_2$ , the eigenvectors are tilted by 45 degrees from the coordinate axes,  $(\theta_1, \theta_2) = (1, 1)$  and  $(1, -1)$ . A positive  $\gamma_2$  elongates the image along the  $(1, 1)$  direction while compressing it along the  $(1, -1)$  direction, and vice versa for a negative  $\gamma_2$ . Figure 4.2 illustrates the schematic effect of convergence and shear components on the shapes of images, highlighting how  $\kappa$  expands or contracts the image and how  $\gamma_1$  and  $\gamma_2$  distort the image.

In gravitational lensing, the surface brightness remains conserved, as described by the relation

$$I(\boldsymbol{\theta}) = I^{(s)}[\boldsymbol{\beta}(\boldsymbol{\theta})]. \quad (4.48)$$

Here,  $I(\boldsymbol{\theta})$  denotes the surface brightness of the image, while  $I^{(s)}[\boldsymbol{\beta}(\boldsymbol{\theta})]$  represents the intrinsic surface brightness of the source. The surface brightness is defined as the energy per unit time, area, solid angle, and frequency, i.e.,  $I$  [erg/s/m<sup>2</sup>/sr/Hz]. To show this conservation law, we provide a brief derivation based on the Liouville theorem. The Liouville theorem states that the phase-space density of photons remains constant. Considering that light rays travel from a solid angle  $d\Omega$  into an area  $dA$ , then the phase-space volume can be written as

$$d^3x = c dt dA, \quad (4.49)$$

$$d^3p = dp_x dp_y dp_z d\Omega = p^2 dp d\Omega = \frac{E^2}{c^3} dE d\Omega, \quad (4.50)$$

where the relation  $E = cp$  is used in the last equality. With  $E = h\nu$ , the Liouville theorem

asserts that

$$\frac{N}{d^3x d^3p} = \frac{Nc^2}{h^3\nu^2 dt dA d\Omega d\nu} = \text{const.}, \quad (4.51)$$

with  $N$  being the number of photons. The surface brightness can be expressed as

$$I_\nu = \frac{Nh\nu}{dt dA d\Omega d\nu} \propto \frac{N}{d^3x d^3p} \nu^3. \quad (4.52)$$

Since the frequency  $\nu$  remains unchanged in a gravitational lens system, the surface brightness conservation theorem can be obtained from Eq. (4.52).

Due to the surface brightness conservation theorem, the magnification of a small source can be expressed as

$$\mu(\boldsymbol{\theta}) = \frac{F_{\text{image}}}{F_{\text{source}}} = \frac{I(\boldsymbol{\theta}) d\Omega_{\text{image}}}{I^{(s)}[\boldsymbol{\beta}(\boldsymbol{\theta})] d\Omega_{\text{source}}} = \frac{d\Omega_{\text{image}}}{d\Omega_{\text{source}}} = \frac{1}{\det A(\boldsymbol{\theta})} = \frac{1}{(1 - \kappa(\boldsymbol{\theta}))^2 - |\gamma(\boldsymbol{\theta})|^2}, \quad (4.53)$$

where  $F$  is the flux,  $F$  [erg/s/m<sup>2</sup>/Hz], and  $d\Omega_{\text{source}}$  and  $d\Omega_{\text{image}}$  denote the open angle of the source and the observed image, respectively. The magnification,  $\mu$ , can have either a positive or negative sign, with the sign indicating the parity of the image. Negative-parity images are mirror-symmetric to the source. The origin of magnification lies in the fact that gravitational lensing bends light that would not normally reach a given region and makes it reach there. For an extended source, the total magnification can be expressed as the weighted sum of the magnifications at all points

$$\mu = \left[ \int d^2\beta I^{(s)}(\boldsymbol{\beta}) \right]^{-1} \int d^2\beta I^{(s)}(\boldsymbol{\beta}) \mu_p(\boldsymbol{\beta}), \quad (4.54)$$

where  $\mu_p(\boldsymbol{\beta})$  is the total magnification summed over all observed images for a point source located at  $\boldsymbol{\beta}$ ,

$$\mu_p(\boldsymbol{\beta}) = \sum_i |\mu(\boldsymbol{\theta}_i)|. \quad (4.55)$$

### 4.3 Critical curve and caustic

The magnification derived from Eq. (4.53) diverges to infinity when the following condition is satisfied,

$$\det A = (1 - \kappa - \gamma)(1 - \kappa + \gamma) = 0. \quad (4.56)$$

This condition generally holds along a curve in the lens plane, known as the critical curve. The magnification can be expressed as the product of the tangential magnification,  $\mu_t = (1 - \kappa - \gamma)^{-1}$ , and the radial magnification,  $\mu_r = (1 - \kappa + \gamma)^{-1}$ . The tangential critical curve corresponds to the locus where the tangential magnification diverges, while the radial critical curve is defined analogously as the locus where the radial magnification becomes infinite. When the critical curves on the lens plane are mapped to the source plane using the lens equation, Eq. (4.28), the resulting lines in the source plane are called caustics. These are further classified into tangential caustics and radial caustics.

On the critical curves, the magnification formally diverges. However, this infinite magnification is unphysical and is prevented by two main factors: the finite source size and the breakdown of the geometrical optics approximation, which requires wave optics. Nevertheless, sources near the caustics produce highly magnified images, observed near

the critical curves. The number of images depends on the relative position of the source to the caustics. For larger  $\beta$ , a single image is observed near  $\theta \simeq \beta$ , where the lens mapping is locally invertible since  $\det A \neq 0$ . In this region, the number of images is unchanged, however, when the source crosses a caustic, a pair of images is either created or destroyed near the corresponding critical curve. The number of images increases (decreases) by two when the source moves from the outer (inner) side to the inner (outer) side of the caustic, following the odd-number theorem introduced in Sec. 4.4. A source located near the inner side of the caustics produces a pair of highly magnified images with opposite parities, i.e., the opposite signs of magnification.

While the critical curves are smooth, the caustics are not necessarily smooth; they consist of smooth folds and cusps. To examine this, let  $\xi$  be the parameter describing the critical curve,  $\theta(\xi)$ . The corresponding caustic is given by  $\beta(\theta(\xi))$ . The tangent vector to the caustic can be written as

$$\frac{d\beta(\theta(\xi))}{d\xi} = \frac{\partial\beta}{\partial\theta} \frac{d\theta(\xi)}{d\xi} = A(\theta(\xi)) \frac{d\theta(\xi)}{d\xi}. \quad (4.57)$$

When the tangent vector to the critical curve,  $d\theta(\xi)/d\xi$ , is parallel to the eigenvector of  $A$  corresponding to the eigenvalue zero, it follows that  $d\beta/d\xi = 0$ . Since the caustic is a closed curve, this condition indicates the presence of a cusp. If the source lies close to and inside a cusp, it generates three highly magnified images near the corresponding point on the critical curve. In this case, the sum of the absolute magnifications of the two outer images equals that of the central image as shown in Sec. 4.5.

In this way, the geometry of a lens mapping can be quantitatively understood with critical curves and caustics. The critical curves separate the lens plane into regions of positive ( $\mu > 0$ ) and negative ( $\mu < 0$ ) parity. The caustics divide the source plane into regions with different numbers of observed images. Each time the source crosses the caustics, the number of images changes by two, either increasing or decreasing. When an extended source is positioned on the caustic, the two or three (in the case of a cusp) images merge. As one of the eigenvalues of  $A$  vanishes along the critical curves, the images become highly distorted in the direction of the corresponding eigenvector, i.e., tangential or radial direction.

Figure 4.3 shows an example of critical curves on the lens plane and caustics on the source plane. The two lines on each plane correspond to the tangential and radial critical curves or caustics, respectively. In this case, the tangential caustic lies inside the radial caustic, while the tangential critical curve is located outside the radial critical curve. The tangential caustic can be divided into fold and cusp caustics. Note that the magnification becomes significantly high near both the tangential and radial critical curves, however, images near the radial critical curve are difficult to observe since the central region of the lens is typically very bright. Thus, highly magnified images are generally observed around the tangential critical curves. As shown in the figure, the outermost source (purple) produces a single image. When the source crosses the radial caustic, the number of images increases by two, and it further increases when crossing the tangential caustic. For a finite-sized source located on a caustic, the two images near the corresponding critical curve merge, forming an elongated arc stretched in the tangential or radial direction.

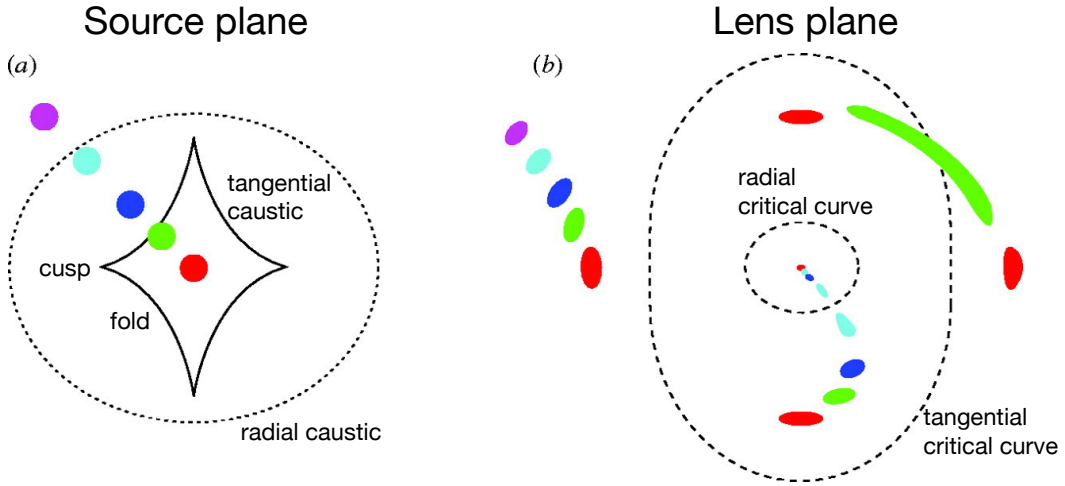


Figure 4.3: The caustics and critical curves, and the locations for multiple images for an elliptical lens are shown. In the left panel, five sources on the source plane are shown. Their corresponding images on the lens plane are displayed with the same colors in the right panel. This figure is adapted from [204].

## 4.4 Multiple images

Multiple images are formed in strong gravitational lensing. In this section, we first classify the multiple images, then show the magnification theorem and the odd-number theorem, and finally present the necessary and sufficient conditions for multiple images to be formed.

To classify the multiple images, the Fermat potential  $\tau(\boldsymbol{\theta}; \boldsymbol{\beta})$  defined in Eq. (4.42) is useful. Since the images correspond to the stationary points of the Fermat potential, as described in Eq. (4.43), they can be classified as minima, maxima, or saddle points of the Fermat potential. Since the Jacobian matrix can be expressed by the Hessian of the Fermat potential,

$$A_{ij} = \delta_{ij} - \frac{\partial^2 \psi}{\partial \theta_i \partial \theta_j} = \frac{\partial^2 \tau}{\partial \theta_i \partial \theta_j}, \quad (4.58)$$

the classification of these stationary points is determined by the signs of the two eigenvalues of  $A$ . At a minimum of the Fermat potential, both eigenvalues are positive, leading to  $\det A > 0$  and  $\text{tr} A > 0$ . At a maximum, both eigenvalues are negative, thus  $\det A > 0$  and  $\text{tr} A < 0$ . At a saddle point, the eigenvalues have opposite signs, resulting in  $\det A < 0$ . Since the trace of the Jacobian matrix is expressed as

$$\text{tr} A = 2(1 - \kappa), \quad (4.59)$$

the minima (maxima) occur at positions where the convergence satisfies  $\kappa < 1$  ( $\kappa > 1$ ). Considering the classification condition, the single image corresponds to the minima. Furthermore, the images corresponding to minima are magnified when  $\kappa \geq 0$ , known as the magnification theorem [205], which can be understood from the following relation,

$$0 < \det A = (1 - \kappa)^2 - \gamma^2 < 1. \quad (4.60)$$

Since each source is mapped onto at least one minimum image, the total magnification of all sources exceeds unity in positive-density regions.

When the source crosses the caustics, a pair of images forms or disappears. These images correspond either to a saddle point and a maximum or to a saddle point and a minimum. Since these image pairs have opposite signs of magnification, the critical curve, which divides the lens plane into regions of positive and negative parity, must lie between them. Thus, the creation and annihilation of images at the critical curve can also be understood in terms of the Fermat potential (time delay) surface. The number of multiple images is always expected to be odd since images are always created and annihilated in pairs of two. This property is known as the odd-number theorem [206], which holds when the Fermat potential is smooth and continuous. One proof of this theorem is based on Morse theory. By considering a manifold where the time delay surface is closed at the top, and denoting the numbers of minima, saddle points, and maxima as  $n_{\min}$ ,  $n_{\text{sad}}$ , and  $n_{\max}$ , respectively, the Morse theory gives the following relation,

$$n_{\min} - n_{\text{sad}} + n_{\max} + 1 = \chi, \quad (4.61)$$

where the Euler characteristic  $\chi$  is two for a two-dimensional sphere. From this relation, we find

$$n_{\text{tot}} = n_{\min} + n_{\text{sad}} + n_{\max} = 1 + 2n_{\text{sad}} \quad (4.62)$$

which demonstrates that the total number of images is always odd.

There are two general criteria for the occurrence of multiple images. The first criterion is that multiple images are formed if, and only if, there exists a point  $\boldsymbol{\theta}$  where the condition  $\det A(\boldsymbol{\theta}) < 0$  satisfies. When  $\det A > 0$  across the entire lens plane, the lens equation is globally invertible, resulting in a single image corresponding to the minimum. However, if  $\det A < 0$  at some point, the image at that point corresponds to a saddle point, and according to the odd-number theorem, at least two additional images must form. The second criterion provides a sufficient but not necessary condition for multiple imaging: multiple images are produced when there is a point where  $\kappa > 1$ . In such regions, images do not correspond to minima, as minima occur only when  $\kappa < 1$ , and thus, multiple images form. Again, the image at that point corresponds to a maximum or a saddle point (not a minimum), resulting in multiple images from the odd-number theorem. While the second criterion is not the necessary condition for multiple images, it shows that the critical surface density  $\Sigma_{\text{cr}}$  is the characteristic surface mass density for strong gravitational lensing.

## 4.5 Magnification near critical curve and caustic

This section reviews magnification near critical curves and caustics. We begin by examining the fold caustic, focusing on how the magnification depends on the distance to the critical curve and caustic. Next, we briefly show the magnification near the cusp caustic. Finally, we show the effects of finite source size on the magnification and present the probability distribution function (PDF) for high magnifications.

To analyze magnification near the critical curve and the fold caustic, it is convenient to place the origins of the lens plane and the source plane on the critical curve and caustic, respectively, and expand the lens potential around these origins. The Taylor expansion of the lens potential is expressed as

$$\begin{aligned} \psi(\boldsymbol{\theta}) = & \psi(\mathbf{0}) + (\psi_{,1}(\mathbf{0})\theta_1 + \psi_{,2}(\mathbf{0})\theta_2) + \frac{1}{2}(\psi_{,11}(\mathbf{0})\theta_1^2 + 2\psi_{,12}(\mathbf{0})\theta_1\theta_2 + \psi_{,22}(\mathbf{0})\theta_2^2) \\ & + \frac{1}{6}(\psi_{,111}(\mathbf{0})\theta_1^3 + 3\psi_{,112}(\mathbf{0})\theta_1^2\theta_2 + 3\psi_{,122}(\mathbf{0})\theta_1\theta_2^2 + \psi_{,222}(\mathbf{0})\theta_2^3), \quad (4.63) \end{aligned}$$

where the subscription of , 1 and , 2 indicate partial derivatives with respect to  $\theta_1$  and  $\theta_2$ , respectively. The zeroth and first-order terms of the lens potential can be omitted, as they only introduce constant shifts in the potential and the deflection angle. The convergence at the origin, denoted as  $\kappa_0$ , is expressed in terms of the lens potential as

$$\kappa_0 = \frac{1}{2}(\psi_{,11}(\mathbf{0}) + \psi_{,22}(\mathbf{0})). \quad (4.64)$$

Then, we can express the second derivative of the lens potential at the origin as

$$\psi_{,11}(\mathbf{0}) = \kappa_0 + (1 - \kappa_0) \cos \omega, \quad (4.65)$$

$$\psi_{,22}(\mathbf{0}) = \kappa_0 - (1 - \kappa_0) \cos \omega, \quad (4.66)$$

where  $\omega$  is an arbitrary constant. Since the origin lies on the critical curve, the determinant of the lensing Jacobian matrix vanishes at the origin,  $\det A(\mathbf{0}) = 0$ . This condition leads to

$$\psi_{,12}(\mathbf{0}) = -(1 - \kappa_0) \sin \omega. \quad (4.67)$$

For simplicity,  $\omega = 0$  can be chosen. We further consider a completely orthogonal configuration, where the train of micro-images is oriented perpendicular to the critical curve. Aligning the critical curve with the  $\theta_2$  axis such that  $\det A((0, \theta_2)) = 0$ , it follows that  $\psi_{,112}(\mathbf{0}) = \psi_{,122}(\mathbf{0}) = 0$ . Additionally, symmetry about the critical curve for images produced by the same source leads to  $\psi_{,222}(\mathbf{0}) = 0$ . Finally, defining  $\psi_{,111}(\mathbf{0}) = -\epsilon$ , proportional to the curvature of the critical curve as shown in Sec. 4.6.1, the lens potential can be expressed as [46, 207]

$$\psi(\boldsymbol{\theta}) = \frac{1}{2}\{\kappa_0(\theta_1^2 + \theta_2^2) + (1 - \kappa_0)(\theta_1^2 - \theta_2^2)\} - \frac{\epsilon}{6}\theta_1^3. \quad (4.68)$$

Using Eq. (4.30), the deflection angle can be calculated as

$$\boldsymbol{\alpha}(\boldsymbol{\theta}) = \begin{pmatrix} \theta_1 - \frac{\epsilon}{2}\theta_1^2 \\ (2\kappa_0 - 1)\theta_2 \end{pmatrix}. \quad (4.69)$$

The lens equations can be expressed as

$$\beta_1 = \frac{\epsilon}{2}\theta_1^2, \quad (4.70)$$

$$\beta_2 = 2(1 - \kappa_0)\theta_2, \quad (4.71)$$

from which the Jacobian lens matrix can be derived as

$$A(\boldsymbol{\theta}) = \begin{pmatrix} \epsilon\theta_1 & 0 \\ 0 & 2(1 - \kappa_0) \end{pmatrix}. \quad (4.72)$$

The convergence and the shear at the position  $\boldsymbol{\theta}$  can be calculated from the lens potential by using Eqs. (4.45), (4.46), and (4.47), which are expressed as

$$\kappa(\boldsymbol{\theta}) = \kappa_0 - \frac{\epsilon}{2}\theta_1, \quad (4.73)$$

$$\gamma_1(\boldsymbol{\theta}) = 1 - \kappa_0 - \frac{\epsilon}{2}\theta_1, \quad (4.74)$$

$$\gamma_2(\boldsymbol{\theta}) = 0, \quad (4.75)$$

$$\gamma(\boldsymbol{\theta}) = 1 - \kappa_0 - \frac{\epsilon}{2}\theta_1. \quad (4.76)$$

The magnification is obtained as the inverse of the determinant of the Jacobian matrix, expressed as

$$\mu(\boldsymbol{\theta}) = \frac{1}{|\det A(\boldsymbol{\theta})|} = \frac{1}{2\epsilon(1 - \kappa_0)} \cdot \frac{1}{\theta_1}. \quad (4.77)$$

Equation (4.77) indicates that the critical curve corresponds to a straight line on the lens plane, given by  $\theta_1 = 0$  as expected, and the magnification is inversely proportional to the distance from the critical curve. By applying Eq. (4.70), the magnification on the source plane can be expressed as

$$\mu(\boldsymbol{\beta}) = \frac{1}{\sqrt{2\epsilon(1 - \kappa_0)}} \cdot \frac{1}{\sqrt{\beta_1}}. \quad (4.78)$$

To derive this relation, a factor of two is included because two images with equal magnification appear symmetrically on either side of the critical curve when the source lies inside the caustic. On the source plane, the caustic corresponds to a straight line,  $\beta_1 = 0$ , and the magnification depends on the distance as  $\mu \propto \beta^{-1/2}$ .

In the case of the cusp caustic, it is helpful to use the lens potential expressed as

$$\psi(\boldsymbol{\theta}) = \frac{1}{2}(1 - b_c)\theta_1^2 + \frac{1}{2}\theta_2^2 - \frac{1}{4}a_c\theta_2^4 - \frac{1}{2}c_c\theta_1\theta_2^2. \quad (4.79)$$

The Jacobian matrix can be expressed as

$$A(\boldsymbol{\theta}) = \begin{pmatrix} b_c & c_c\theta_2 \\ c_c\theta_2 & 3a_c\theta_2^2 + c_c\theta_1 \end{pmatrix}, \quad (4.80)$$

and the magnification is written as

$$\mu(\boldsymbol{\theta}) = \frac{1}{(3a_cb_c - c_c^2)\theta_2^2 + b_cc_c\theta_1}. \quad (4.81)$$

The critical curve corresponds to a parabola with  $\theta_2 = 0$  as its axis, and the associated caustic follows the relation  $\beta_2^2 \propto \beta_1^3$ , indicating that the origin is in a cusp. Considering a source located along the  $\beta_1$  axis, i.e.,  $\beta_2 = 0$ , when the source lies outside the caustic ( $\beta_1 < 0$ ), a single image is observed at  $(\theta_1, \theta_2) = (\beta_1/b_c, 0)$ . When the source is located inside the caustic ( $\beta_1 > 0$ ), two additional images appear at  $(\theta_1, \theta_2) = (2a_c\beta_1/(2a_cb_c - c_c^2), \pm\sqrt{2c_c\beta_1/(c_c^2 - 2a_cb_c)})$ . These two additional images emerge symmetrically along the  $\theta_1$  axis. The magnification of these three images can be calculated as

$$\mu = \frac{1}{c_cb_1}, \quad -\frac{1}{2c_cb_1}, \quad -\frac{1}{2c_cb_1}. \quad (4.82)$$

From this equation, we can see that the magnification scales as  $\mu \propto \beta_1^{-1}$ . Furthermore, the sign of the magnification for the central image on the  $\theta_1$  axis differs from that of the other two images, and its absolute magnification is twice as large.

Given that the occurrence of the cusp caustic is rarer than that of the fold caustic, we primarily focus on the fold caustic in the subsequent discussion. When considering a source with a finite size  $\sigma_W$ , the magnification Eq. (4.78) is averaged over the size of the source as

$$\mu(\boldsymbol{\beta}) = \frac{1}{\sqrt{2\epsilon(1 - \kappa_0)}} \frac{1}{\sqrt{2\pi\sigma_W^2}} \int_0^\infty d\beta'_1 \frac{1}{\sqrt{\beta'_1}} \exp\left[-\frac{(\beta'_1 - \beta_1)^2}{2\sigma_W^2}\right], \quad (4.83)$$

where a Gaussian surface brightness profile is applied. While the magnification of the point source mathematically diverges on critical curves, there is a maximum magnification in the case of the finite-sized source due to the average effect, with the peak magnification being expressed as

$$\mu_{\max} \simeq \frac{1}{\sqrt{2\epsilon(1-\kappa_0)}} \cdot \frac{1}{\sqrt{\sigma_W}}. \quad (4.84)$$

Next, we examine the area on the lens plane where the magnification exceeds  $\mu$ , which is denoted by  $a_\ell(> \mu)$  [208]. The area can be obtained by integrating along the critical curve with the help of Eq. (4.77), leading to

$$a_\ell(> \mu) \simeq \oint d\xi \frac{dl}{d\xi} \frac{1}{2\epsilon(1-\kappa_0)\mu} \propto \frac{1}{\mu}, \quad (4.85)$$

where  $\xi$  is the parameter of the critical curve. By differentiating with respect to the magnification, the area where the magnification is between  $\mu$  and  $\mu + d\mu$  is expressed as

$$\left| \frac{da_\ell(> \mu)}{d\mu} \right| d\mu \propto \frac{1}{\mu^2} d\mu. \quad (4.86)$$

The cross-section is defined as the area on the source plane where the magnification lies between  $\mu$  and  $\mu + d\mu$ . This can be obtained by mapping the corresponding area on the lens plane onto the source plane,

$$\left| \frac{da_s(> \mu)}{d\mu} \right| d\mu = \frac{2}{\mu} \left| \frac{da_\ell(> \mu)}{d\mu} \right| d\mu \propto \frac{1}{\mu^3} d\mu. \quad (4.87)$$

A factor of two appears in the middle term because the images are on both sides of the critical curve. Therefore, the area on the source plane where the magnification exceeds  $\mu$ , which is denoted by  $a_s(> \mu)$ , is given by

$$a_s(> \mu) \propto \frac{1}{\mu^2}. \quad (4.88)$$

The above relations indicate that when the source is randomly distributed on the source plane, the probability that the magnification becomes  $\mu$ , i.e., the high-magnification tail of the PDF, is given by

$$\frac{dP}{d\mu} \propto \mu^{-3}, \quad (4.89)$$

or equivalently,

$$\frac{dP}{d \log_{10} \mu} \propto \mu^{-2}. \quad (4.90)$$

We show the detailed modeling for the high-magnification tail of the PDF including its parameter dependence in Chap. 5.

## 4.6 Spherically symmetric lens

As a specific example of a lens model, we focus on the spherically symmetric lens, a foundational and useful case. Due to the spherical symmetry, the coordinates on the lens

plane can be reduced to  $\theta = |\boldsymbol{\theta}|$ . Utilizing the definition of the lens potential given in Eq. (4.41), it can be rewritten as

$$\begin{aligned}\psi(\theta) &= \frac{1}{\pi} \int_0^\infty d\theta' \int_0^{2\pi} d\varphi' \theta' \kappa(\theta') \ln \sqrt{\theta^2 + \theta'^2 - 2\theta\theta' \cos \varphi'} \\ &= 2 \int_0^\theta d\theta' \theta' \kappa(\theta') \ln \theta + 2 \int_\theta^\infty d\theta' \theta' \kappa(\theta') \ln \theta'\end{aligned}\quad (4.91)$$

Since a constant shift in the lens potential has no physical impact, we redefine the lens potential as

$$\psi(\theta) - 2 \int_0^\infty d\theta' \theta' \kappa(\theta') \ln \theta', \quad (4.92)$$

which simplifies the expression of the lens potential to,

$$\psi(\theta) = 2 \int_0^\theta d\theta' \theta' \kappa(\theta') \frac{\theta}{\theta'}. \quad (4.93)$$

The deflection angle can be derived from Eq. (4.30), leading to

$$\boldsymbol{\alpha}(\boldsymbol{\theta}) = \bar{\kappa}(< \theta) \boldsymbol{\theta}, \quad (4.94)$$

where  $\bar{\kappa}(< \theta)$  represents the mean convergence within a circular region of a radius  $\theta$ ,

$$\bar{\kappa}(< \theta) = \frac{2}{\theta^2} \int_0^\theta d\theta' \theta' \kappa(\theta'). \quad (4.95)$$

The deflection angle in Eq. (4.94) implies that the source lies along the same direction as the image, as indicated by the lens equation in Eq. (4.28). Thus, introducing the notation  $\beta = |\boldsymbol{\beta}|$ , the lens equation can be rewritten as

$$\beta = \theta - \alpha(\theta) = (1 - \bar{\kappa}(< \theta))\theta, \quad (4.96)$$

where  $\alpha(\theta)$  is the magnitude of the deflection angle. The shear components can be expressed with the convergence as

$$\gamma_1(\theta) = -(\bar{\kappa}(< \theta) - \kappa(\theta)) \cos(2\phi), \quad (4.97)$$

$$\gamma_2(\theta) = -(\bar{\kappa}(< \theta) - \kappa(\theta)) \sin(2\phi), \quad (4.98)$$

$$\gamma(\theta) = |\bar{\kappa}(< \theta) - \kappa(\theta)|, \quad (4.99)$$

where  $\phi$  represents the argument of the vector  $\boldsymbol{\theta}$ , given by  $\phi = \arctan(\theta_2/\theta_1)$ . Note that for a spherically symmetric lens, the system can be characterized using the tangential shear, which is defined as

$$\gamma_+(\theta) = \bar{\kappa}(< \theta) - \kappa(\theta). \quad (4.100)$$

The magnification can be expressed using Eq. (4.53), which reduces to

$$\mu(\theta) = \frac{1}{(1 - \bar{\kappa})(1 - 2\kappa + \bar{\kappa})}. \quad (4.101)$$

The tangential and radial magnifications correspond to the first and second factors in the denominator of the above expression, respectively.

When the source is located at  $\beta = 0$ , the image forms a ring, known as the Einstein ring. The radius of this ring, called the Einstein radius, is defined by the condition,

$$\bar{\kappa}(< \theta_{\text{Ein}}) = 1. \quad (4.102)$$

By defining the cylinder mass, which is the enclosed mass of the surface mass density,

$$M(< \theta) = D_{\text{ol}}^2 \int_0^\theta d\theta' 2\pi\theta'\Sigma(\theta'), \quad (4.103)$$

the Einstein radius, as defined by Eq. (4.102), can be expressed as

$$\theta_{\text{Ein}} = \sqrt{\frac{4GM(< \theta_{\text{Ein}})}{c^2} \frac{D_{\text{ls}}}{D_{\text{ol}}D_{\text{os}}}}. \quad (4.104)$$

Since the above expression does not assume any specific mass distribution for the radial density profile, it indicates that the total enclosed mass can be reliably estimated once the Einstein radius is measured.

### 4.6.1 Point mass lens

A point mass lens is a specific example of a spherically symmetric lens, which can be applied when considering microlensing. The density profile of a point mass lens is given by

$$\rho(\mathbf{r}) = M\delta_{\text{D}}^{(3)}(\mathbf{r}). \quad (4.105)$$

By integrating the density along the line of sight, the convergence can be expressed by

$$\kappa(\boldsymbol{\theta}) = \frac{4\pi GM}{c^2} \frac{D_{\text{ls}}}{D_{\text{ol}}D_{\text{os}}} \delta_{\text{D}}^{(2)}(\boldsymbol{\theta}). \quad (4.106)$$

The average convergence within a radius  $\theta$  is

$$\bar{\kappa}(< \theta) = \frac{1}{\pi\theta^2} \int_{|\boldsymbol{\theta}'| < \theta} d^2\theta' \kappa(\boldsymbol{\theta}') = \frac{4GM}{c^2} \frac{D_{\text{ls}}}{D_{\text{ol}}D_{\text{os}}} \frac{1}{\theta^2} = \frac{\theta_{\text{Ein}}^2}{\theta^2}, \quad (4.107)$$

where the Einstein radius  $\theta_{\text{Ein}}$ , obtained by Eq. (4.104), is

$$\theta_{\text{Ein}} = \sqrt{\frac{4GM}{c^2} \frac{D_{\text{ls}}}{D_{\text{ol}}D_{\text{os}}}}. \quad (4.108)$$

Note that the Einstein radius depends on the mass of the lens and it can be calculated as

$$\theta_{\text{Ein}} \simeq \left( \frac{M}{10^{11} M_{\odot}} \right)^{\frac{1}{2}} \left( \frac{D_{\text{ol}}D_{\text{os}}/D_{\text{ls}}}{\text{Gpc}} \right)^{-\frac{1}{2}} \text{arcsec}, \quad (4.109)$$

from which the Einstein radius of a stellar-mass object is on the order of micro-arcseconds. This is why such lenses are referred to as microlenses. In contrast, the Einstein radii are typically on the order of arcseconds for galaxy-mass lenses, and ten to hundred arcseconds for galaxy cluster lenses. Substituting Eq. (4.106) into the lens equation, Eq. (4.96), we obtain,

$$\beta = \theta - \frac{\theta_{\text{Ein}}^2}{\theta}, \quad (4.110)$$

from which the lens potential can be expressed as

$$\psi(\theta) = \theta_{\text{Ein}}^2 \ln \theta. \quad (4.111)$$

Here, we briefly check that the quantity  $\epsilon$  in the lens potential Eq. (4.68), which is defined by the minus of the third-order derivative of the lens potential with respect to  $\theta_1$ , is proportional to the curvature of the critical curve. By expanding the lens potential around a point on the critical curve in the radial direction,  $\theta = \theta_{\text{Ein}} + \delta\theta$ , we can express the third-order term as

$$\psi_{3\text{rd}}(\delta\theta) \simeq \frac{1}{3\theta_{\text{Ein}}} (\delta\theta)^3, \quad (4.112)$$

from which it follows that  $\epsilon \propto \theta_{\text{Ein}}^{-1}$ .

From the lens equation, the Jacobian matrix can be expressed as

$$A(\theta) = \begin{pmatrix} 1 + \frac{\theta_{\text{E}}^2}{\theta^2} \cos 2\phi & \frac{\theta_{\text{E}}^2}{\theta^2} \sin 2\phi \\ \frac{\theta_{\text{E}}^2}{\theta^2} \sin 2\phi & 1 - \frac{\theta_{\text{E}}^2}{\theta^2} \cos 2\phi \end{pmatrix}. \quad (4.113)$$

Since the convergence is zero except at the origin, the magnitude of the shear obtained from Eq. (4.99) is

$$\gamma(\theta) = \frac{\theta_{\text{Ein}}^2}{\theta^2}. \quad (4.114)$$

The magnification is determined entirely by the shear and is given by

$$\mu(\theta) = \left\{ 1 - \left( \frac{\theta_{\text{Ein}}}{\theta} \right)^4 \right\}^{-1}. \quad (4.115)$$

As indicated by Eq. (4.115), the Einstein radius represents the location where the magnification diverges to infinity. Consequently, the Einstein ring aligns with the critical curve on the lens plane. When the source is located at  $\beta$ , two images are observed at

$$\theta_{\pm} = \frac{1}{2} \left( \beta \pm \sqrt{\beta^2 + 4\theta_{\text{Ein}}^2} \right). \quad (4.116)$$

Notably, the number of images is always two, which appears to violate the odd-number theorem. However, this discrepancy arises due to the singular density distribution, violating the assumption of a smooth and continuous Fermat potential surface required for the odd-number theorem to hold.

## 4.6.2 Singular isothermal sphere

The singular isothermal sphere (SIS) is the mass model often employed for galaxies and galaxy clusters. Its density profile can be expressed as

$$\rho(r) = \frac{\sigma^2}{2\pi G r^2}, \quad (4.117)$$

where  $\sigma$  is the velocity dispersion. The convergence and the average convergence for the SIS lens model are given by

$$\kappa(\theta) = \frac{\theta_{\text{Ein}}}{2\theta}, \quad (4.118)$$

$$\bar{\kappa}(<\theta) = \frac{\theta_{\text{Ein}}}{\theta}, \quad (4.119)$$

where the Einstein radius is given by

$$\theta_{\text{Ein}} = \frac{4\pi\sigma^2 D_{\text{ls}}}{c^2 D_{\text{os}}}. \quad (4.120)$$

The deflection angle can be derived using the relation  $\alpha(\theta) = \bar{\kappa}(<\theta)\theta$  for a spherically symmetric lens, yielding the constant deflection angle,

$$\alpha(\theta) = \theta_{\text{Ein}}. \quad (4.121)$$

The shear is calculated as

$$\gamma(\theta) = \bar{\kappa}(<\theta) - \kappa(\theta) = \frac{\theta_{\text{Ein}}}{\theta}, \quad (4.122)$$

from which the convergence and shear are equal for the SIS lens model.

## 4.7 Microlens in a smooth mass distribution

In this section, we consider a point mass lens embedded in the constant convergence  $\kappa_{\text{B}}$  and total shear  $\gamma_{\text{B}}$  as the background. We show that the size of the critical curve becomes larger when a smooth mass distribution exists in the background [136].

We first start from the lens equation, which is modified from Eq. (4.110) and has additional terms regarding the background mass distribution,

$$\beta_1 = \frac{\theta_1}{\mu_{\text{t,B}}} - \frac{\theta_{\text{Ein}}^2 \theta_1}{\theta^2}, \quad (4.123)$$

$$\beta_2 = \frac{\theta_2}{\mu_{\text{r,B}}} - \frac{\theta_{\text{Ein}}^2 \theta_2}{\theta^2}, \quad (4.124)$$

where the tangential and radial magnifications by the background smooth component are given by

$$\mu_{\text{t,B}} = (1 - \kappa_{\text{B}} - \gamma_{\text{B}})^{-1}, \quad (4.125)$$

$$\mu_{\text{r,B}} = (1 - \kappa_{\text{B}} + \gamma_{\text{B}})^{-1}. \quad (4.126)$$

The total magnification due to the smooth background mass distribution is expressed by  $\mu_{\text{B}} = \mu_{\text{t,B}}\mu_{\text{r,B}}$ . In regions close to the tangential critical curve,  $\mu_{\text{t,B}}$  becomes significantly large, while  $\mu_{\text{r,B}}$  remains approximately equal to unity. The corresponding Jacobian matrix is expressed as

$$A(\boldsymbol{\theta}) = \begin{pmatrix} \mu_{\text{t,B}}^{-1} + \frac{\theta_{\text{E}}^2}{\theta^2} \cos 2\phi & \frac{\theta_{\text{E}}^2}{\theta^2} \sin 2\phi \\ \frac{\theta_{\text{E}}^2}{\theta^2} \sin 2\phi & \mu_{\text{r,B}}^{-1} - \frac{\theta_{\text{E}}^2}{\theta^2} \cos 2\phi \end{pmatrix}. \quad (4.127)$$

The determinant of the Jacobian matrix is

$$\det A = \mu_{\text{t,B}}^{-1}\mu_{\text{r,B}}^{-1} + (\mu_{\text{r,B}}^{-1} - \mu_{\text{t,B}}^{-1})\frac{\theta_{\text{Ein}}^2}{\theta^2} \cos 2\phi - \frac{\theta_{\text{Ein}}^4}{\theta^4}. \quad (4.128)$$

In the direction of  $\phi = \pi/2$ , the magnification can be expressed as,

$$\begin{aligned} \mu(\theta) &= \mu_{\text{t,B}}\mu_{\text{r,B}} \frac{1}{1 - (\mu_{\text{t,B}} - \mu_{\text{r,B}})\frac{\theta_{\text{E}}^2}{\theta^2} - \mu_{\text{t,B}}\mu_{\text{r,B}}\frac{\theta_{\text{Ein}}^4}{\theta^4}} \\ &\simeq \mu_{\text{t,B}}\mu_{\text{r,B}} \frac{1}{1 - \left(\frac{\mu_{\text{t,B}}\theta_{\text{Ein}}^2}{\theta^2}\right)^2}. \end{aligned} \quad (4.129)$$

Comparing Eqs. (4.115) and (4.129), we see that the Einstein radius increases by a factor of  $\sqrt{\mu_{t,B}}$  in the presence of the background smooth component. This enhancement arises because the area of the tangential critical curve is scaled by a factor of  $\mu_B \simeq \mu_{t,B}$ . It is worth noting that since the expansion rate of the critical curve is unity in the  $\phi = 0$  direction, the actual shape of the critical curve is gourd-like [136].

The magnification behavior near the critical curve and caustic can be approximated as follows. Expanding the magnification derived in Eq. (4.129) around the critical curve at  $\theta = \sqrt{\mu_{t,B}}\theta_{\text{Ein}} + \Delta\theta$ , we can express the magnification as a function of the distance from the critical curve on the lens plane as

$$\mu(\Delta\theta) = \frac{1}{2}\mu_{t,B}\mu_{r,B} \left( \frac{\sqrt{\mu_{t,B}}\theta_{\text{Ein}}}{\Delta\theta} \right). \quad (4.130)$$

We can confirm that the dependence aligns with Eq. (4.77). Now, let us examine the magnification near the caustic on the source plane. Since the caustic exhibits an asteroid-like shape as numerically confirmed by [136], and the direction  $\phi = \pi/2$  corresponds to the cusp, where caustic crossings are infrequent, we focus on directions near but not exactly at  $\phi = \pi/2$ . In this region, the normal vector to the caustic is approximately along the  $\beta_1$  axis. We thus consider a point on the source plane given by  $(\beta_1, \beta_2) = (\Delta\beta_1, \theta_{\text{Ein}}\sqrt{\mu_{t,B}}/\mu_{r,B})$ , where  $\Delta\beta_1$  represents the distance to the caustic and the second component corresponds to the caustic size along the  $\beta_2$  axis. The corresponding point on the lens plane is  $(\theta_1, \theta_2) = (\Delta\theta_1, \sqrt{\mu_{t,B}}\theta_{\text{Ein}})$ , where  $\Delta\theta_1$  is given by

$$\Delta\theta_1 = \sqrt{\frac{1}{2}\mu_{t,B}^{\frac{3}{2}}\theta_{\text{Ein}}\Delta\beta_1}. \quad (4.131)$$

Assuming that the distance to the critical curve  $\Delta\theta$  can be approximated by  $\Delta\theta_1$ , the magnification near the caustic can be obtained by substituting Eq. (4.131) into Eq. (4.130),

$$\mu(\Delta\beta) = \frac{1}{\sqrt{2}}\mu_{t,B}\mu_{r,B} \sqrt{\frac{\theta_{\text{Ein}}}{\sqrt{\mu_{t,B}}\Delta\beta}}. \quad (4.132)$$

Here, the notation  $\Delta\beta_1$  has been generalized to  $\Delta\beta$ . The magnification behavior is consistent with the dependence given in Eq. (4.78). Moreover, while this approximation may not be fully accurate, Eq. (4.132) is in agreement with the numerical results presented in [136].

## 4.8 Randomly distributed microlenses in a smooth mass distribution

In the previous section, we focus on a single microlens within a smooth mass distribution. In this section, we extend the analysis to multiple randomly distributed microlenses and show the ensemble average of the total magnification and its variance across many realizations. It is important to note that the total magnification refers to the sum of the magnifications of the multiple micro-images produced by the individual microlenses.

We consider the case where the background convergence and shear are given by  $\kappa_B$  and  $\gamma_B$ , respectively, and randomly distribute microlenses with the same masses, i.e., the

same Einstein radii. The average convergence of microlenses is denoted by  $\kappa_*$ . In this setup, the average magnification  $\mu_{\text{av}} = \langle \mu_{\text{tot}} \rangle$  is given by

$$\mu_{\text{av}}(\boldsymbol{\beta}) = \frac{1}{2\pi(\sigma_{\text{ml}}^2 + \sigma_{\text{W}}^2)} \int d^2\theta \exp \left[ -\frac{|\boldsymbol{\theta} - \boldsymbol{\beta} - \boldsymbol{\alpha}_{\text{B}}|^2}{2(\sigma_{\text{ml}}^2 + \sigma_{\text{W}}^2)} \right], \quad (4.133)$$

as analytically shown by [209]. Here,  $\boldsymbol{\alpha}_{\text{B}}$  denotes the deflection angle arising from the background smooth mass distribution, and  $\sigma_{\text{ml}}^2$  represents the variance of the random deflection angle caused by the microlenses,

$$\sigma_{\text{ml}}^2(R_*, l_*) = \kappa_* \theta_{\text{Ein}}^2 \left( 1 - \gamma_{\text{E}} + \ln \frac{2R_*}{\theta_{\text{Ein}}^2 l_*} \right), \quad (4.134)$$

with  $\gamma_{\text{E}}$  being the Euler-Mascheroni constant, and  $R_*$  and  $l_*$  being given by

$$R_* = \mu_{\text{B}} \sigma_{\text{eff}}, \quad (4.135)$$

$$l_* = \frac{1}{\sigma_{\text{eff}}}, \quad (4.136)$$

$$\sigma_{\text{eff}} = \sqrt{\sigma_{\text{W}}^2 + \kappa_* \theta_{\text{Ein}}^2}. \quad (4.137)$$

The variance of the total magnification,  $\langle \mu_{\text{tot}}^2 \rangle$ , can be expressed as

$$\langle \mu_{\text{tot}}(\boldsymbol{\beta})^2 \rangle = \int d^2\theta' \int d^2\theta'' \frac{\exp \left[ -\frac{1}{2} \mathbf{u}^{\text{T}} (C_{\text{ml}}(\tilde{\boldsymbol{\theta}}) + \sigma_{\text{W}}^2 I)^{-1} \mathbf{u} \right]}{(2\pi)^2 \sqrt{\det(C_{\text{ml}}(\tilde{\boldsymbol{\theta}}) + \sigma_{\text{W}}^2 I)}}, \quad (4.138)$$

where the two-dimensional vector  $\tilde{\boldsymbol{\theta}}$  is defined by  $\tilde{\boldsymbol{\theta}} = \boldsymbol{\theta}'' - \boldsymbol{\theta}'$ , and  $\mathbf{u}$  is the four-dimensional vector given by

$$\mathbf{u}(\boldsymbol{\theta}', \boldsymbol{\theta}''; \boldsymbol{\beta}) = \begin{pmatrix} \theta'_1 - \beta_1 - \alpha_{\text{B1}}(\boldsymbol{\theta}') \\ \theta'_2 - \beta_2 - \alpha_{\text{B2}}(\boldsymbol{\theta}') \\ \theta''_1 - \beta_1 - \alpha_{\text{B1}}(\boldsymbol{\theta}'') \\ \theta''_2 - \beta_2 - \alpha_{\text{B2}}(\boldsymbol{\theta}'') \end{pmatrix}. \quad (4.139)$$

The matrix  $C_{\text{ml}}(\tilde{\boldsymbol{\theta}})$  in the integrand is the square matrix of order four, which is represented by

$$C_{\text{ml}}(\tilde{\boldsymbol{\theta}}) = \begin{pmatrix} \sigma_{\text{ml}}^2 & 0 & C_{13}^{\text{ml}} & C_{14}^{\text{ml}} \\ 0 & \sigma_{\text{ml}}^2 & C_{14}^{\text{ml}} & C_{24}^{\text{ml}} \\ C_{13}^{\text{ml}} & C_{14}^{\text{ml}} & \sigma_{\text{ml}}^2 & 0 \\ C_{14}^{\text{ml}} & C_{24}^{\text{ml}} & 0 & \sigma_{\text{ml}}^2 \end{pmatrix}, \quad (4.140)$$

with each component being given by

$$C_{13}^{\text{ml}}(\tilde{\boldsymbol{\theta}}) = C_{\parallel}^{\text{ml}}(\tilde{\theta}) \cos^2 \phi + C_{\perp}^{\text{ml}} \sin^2 \phi, \quad (4.141)$$

$$C_{14}^{\text{ml}}(\tilde{\boldsymbol{\theta}}) = C_{\parallel}^{\text{ml}}(\tilde{\theta}) \cos \phi \sin \phi - C_{\perp}^{\text{ml}}(\tilde{\theta}) \cos \phi \sin \phi, \quad (4.142)$$

$$C_{24}^{\text{ml}}(\tilde{\boldsymbol{\theta}}) = C_{\parallel}^{\text{ml}}(\tilde{\theta}) \sin^2 \phi + C_{\perp}^{\text{ml}}(\tilde{\theta}) \cos^2 \phi, \quad (4.143)$$

where  $\phi$  is the polar angle of  $\tilde{\boldsymbol{\theta}}$ , and  $C_{\parallel}^{\text{ml}}(\tilde{\theta})$  and  $C_{\perp}^{\text{ml}}(\tilde{\theta})$  are expressed as

$$C_{\parallel}^{\text{ml}}(\tilde{\theta}) = \kappa_* \theta_{\text{Ein}}^2 \left[ \ln \frac{R_*}{\tilde{\theta}} + \ln \sqrt{1 + \frac{\tilde{\theta}^2}{4R_*^2}} - \frac{1}{2} \right], \quad (4.144)$$

$$C_{\perp}^{\text{ml}}(\tilde{\theta}) = \kappa_* \theta_{\text{Ein}}^2 \left[ \ln \frac{R_*}{\tilde{\theta}} + \ln \sqrt{1 + \frac{\tilde{\theta}^2}{4R_*^2}} + \frac{1}{2} \right]. \quad (4.145)$$

The standard deviation of the total magnification is calculated from Eqs. (4.133) and (4.138) as

$$\text{Std}[\mu_{\text{tot}}(\boldsymbol{\beta})] = \sqrt{\langle \mu_{\text{tot}}^2(\boldsymbol{\beta}) \rangle - \mu_{\text{av}}^2(\boldsymbol{\beta})}. \quad (4.146)$$

It is important to note that these analytical estimates are not valid when  $\tilde{\theta} \gg R_\star$  and  $\tilde{\theta} \ll \theta_{\text{Ein}}^2 l_\star$ . Therefore, this analytic model does not accurately predict the high-magnification tail of the PDF that we focus on in Chap. 5.

In the specific case where the background convergence  $\kappa_{\text{B}}$  and shear  $\gamma_{\text{B}}$  are constant, these equations can be expressed in simpler forms. The average magnification is given by

$$\mu_{\text{av}} = \mu_{\text{B}} = \frac{1}{|(1 - \kappa_{\text{B}})^2 - \gamma_{\text{B}}^2|}, \quad (4.147)$$

and the variance of the total magnification is

$$\langle \mu_{\text{tot}}^2 \rangle = \frac{\mu_{\text{av}}^2}{4\pi} \int d^2\tilde{\Theta} \frac{\exp\left[-\frac{1}{2}\tilde{\Theta}^T \cdot D(\tilde{\theta}) \cdot \tilde{\Theta}\right]}{\sqrt{B_{\text{ml}}(\tilde{\theta})}}, \quad (4.148)$$

where  $B_{\text{ml}}(\tilde{\theta})$  in the denominator is given by

$$B_{\text{ml}}(\tilde{\theta}) = (\sigma_{\text{ml}}^2 + \sigma_{\text{W}}^2 - C_{\parallel}^{\text{ml}}(\tilde{\theta}))(\sigma_{\text{ml}}^2 + \sigma_{\text{W}}^2 - C_{\perp}^{\text{ml}}(\tilde{\theta})). \quad (4.149)$$

Here, the two-dimensional vector  $\tilde{\Theta}$  is defined by  $\tilde{\Theta} = \Theta'' - \Theta'$ , with  $\tilde{\Theta}$  being the rescaled coordinate on the lens plane,

$$\Theta = \begin{pmatrix} |1 - \kappa_{\text{B}} - \gamma_{\text{B}}|\theta_1 \\ |1 - \kappa_{\text{B}} + \gamma_{\text{B}}|\theta_2 \end{pmatrix}. \quad (4.150)$$

Each component of the two dimensional matrix  $D(\tilde{\theta})$  is

$$D_{11} = \frac{1}{4B_{\text{ml}}(\tilde{\theta})} \{2\sigma_{\text{ml}}^2 + 2\sigma_{\text{W}}^2 - (C_{\parallel}^{\text{ml}}(\tilde{\theta}) + C_{\perp}^{\text{ml}}(\tilde{\theta})) + (C_{\parallel}^{\text{ml}}(\tilde{\theta}) - C_{\perp}^{\text{ml}}(\tilde{\theta})) \cos 2\phi\}, \quad (4.151)$$

$$D_{12} = D_{21} = \frac{1}{4B_{\text{ml}}(\tilde{\theta})} (C_{\parallel}^{\text{ml}}(\tilde{\theta}) - C_{\perp}^{\text{ml}}(\tilde{\theta})) \sin 2\phi, \quad (4.152)$$

$$D_{22} = \frac{1}{4B_{\text{ml}}(\tilde{\theta})} \{2\sigma_{\text{ml}}^2 + 2\sigma_{\text{W}}^2 - (C_{\parallel}^{\text{ml}}(\tilde{\theta}) + C_{\perp}^{\text{ml}}(\tilde{\theta})) - (C_{\parallel}^{\text{ml}}(\tilde{\theta}) - C_{\perp}^{\text{ml}}(\tilde{\theta})) \cos 2\phi\}. \quad (4.153)$$

In this thesis, we choose  $\phi = 0$  to calculate these values.

Another useful example is when the lens potential is given by Eq. (4.68), which is important to study the magnification near the critical curve and the caustic. The deflection angle by a background smooth mass distribution,  $\boldsymbol{\alpha}_{\text{B}}$ , is given by Eq. (4.69). In this case, the Gaussian integral for  $\theta_2$  can be easily performed, and we obtain the expression for the average magnification as

$$\mu_{\text{av}}(\boldsymbol{\beta}) = \frac{1}{\sqrt{2\epsilon}(1 - \kappa_0)} \frac{1}{\sqrt{2\pi(\sigma_{\text{ml}}^2 + \sigma_{\text{W}}^2)}} \int_0^\infty d\beta'_1 \frac{1}{\sqrt{\beta'_1}} \exp\left[-\frac{(\beta'_1 - \beta_1)^2}{2(\sigma_{\text{ml}}^2 + \sigma_{\text{W}}^2)}\right]. \quad (4.154)$$

Note that Eq. (4.154) is identical to Eq. (4.83), with the only difference being the term corresponding to the source size.

Figure 4.4 shows an example of the average magnification and its  $1\sigma$  standard deviation. The lens potential is given by Eq. (4.68) with parameters  $\kappa_0 = 0.7$  and  $\epsilon = 10^{-5}$ . The average magnification is computed using Eq. (4.154), with  $\kappa_\star = 0.004$ ,  $\theta_{\text{Ein}} = 1.0$ , and  $\sigma_W = 0.05$ . Following the approach of [209], we set  $R_\star = 1500$ , which differs from the original value defined by Eq. (4.135). To compute the dispersion, we do not directly use Eq. (4.138) due to computational limitations. Instead, we first calculate the background convergence and shear using the average magnification from Eq. (4.147), assuming  $\kappa_B = \gamma_B$ , for each point  $\beta_1$ . Next, we use Eq. (4.148) to determine the dispersion of the total magnification. Even with this simplified calculation, the derived values are in close agreement with those obtained from Eq. (4.138). Finally, the standard deviation is obtained using Eq. (4.146). To prevent computational breakdowns in the regions  $\tilde{\theta} \gg R_\star$  and  $\tilde{\theta} \ll \theta_{\text{Ein}}^2 l_\star$ , we apply the following formula instead of Eqs. (4.144) and (4.145), as introduced by [209],

$$C_{X,\text{reg}}^{\text{ml}}(\tilde{\theta}) = \sigma_{\text{ml}}^2 \text{sgn}(C_X^{\text{ml}}(\tilde{\theta})) \left[ 1 + \left( \frac{\sigma_{\text{ml}}^2}{|C_X^{\text{ml}}(\tilde{\theta})| e^{-(\tilde{\theta}/(\nu R_\star))^2}} \right)^n \right]^{-1/n}, \quad (4.155)$$

with  $n = 10$  and  $\nu = 1$ . We employ the Monte Carlo algorithm VEGAS [210, 211] to perform the integration. Note that physical units are ignored here, as the main focus is on presenting the numerical results for the magnification.

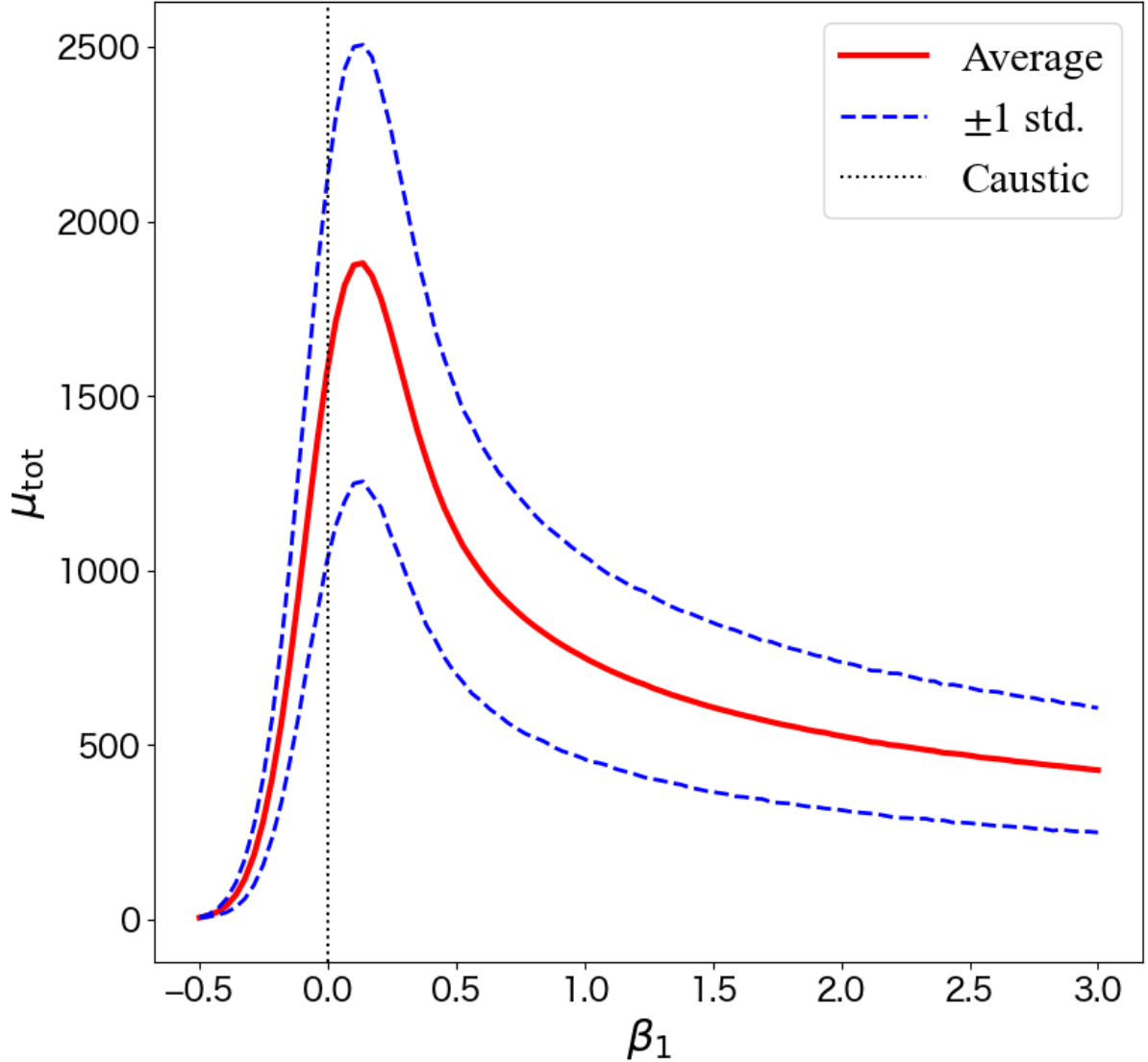


Figure 4.4: The average (red solid line) and  $1\sigma$  standard deviation (blue dashed lines) of the total magnifications as a function of the distance from the (macro-)caustic in the presence of multiple microlenses within a background smooth mass distribution. The vertical dotted line shows the position of the (macro-)caustic. We set the parameters as  $\kappa_0 = 0.7$ ,  $\epsilon = 10^{-5}$ ,  $\kappa_\star = 0.004$ ,  $\theta_{\text{Ein}} = 1.0$ ,  $\sigma_W = 0.05$ , and  $R_\star = 1500$ . Here, we omit the physical units of these parameters. The average magnification and dispersion are calculated from Eqs. (4.154) and (4.148). Note that  $\kappa_B$  and  $\gamma_B$  are obtained from Eq. (4.147) assuming  $\kappa_B = \gamma_B$  for each point  $\beta_1$ . The standard deviation is calculated from Eq. (4.146). This figure is taken from [48].

# Chapter 5

## The ultra-high magnification events due to microlenses

### 5.1 Introduction

Advancements in observational techniques have led to a significant increase in the number of observed gravitational lensing events. Notably, individual stars experiencing extreme magnification near the critical curves of galaxy clusters have been observed. The first example of such an event is Icarus, a blue supergiant star within a spiral galaxy hosting the supernova (SN) Refsdal [212] at a redshift  $z = 1.49$ , observed near the critical curve of the MACS J1149 galaxy cluster at redshift  $z = 0.544$ , with its magnification estimated to exceed a factor of two thousand (see Fig. 5.1) [44]. The high magnification lasts for less than two weeks, indicating that microlenses, such as intracluster light (ICL) stars, contribute to the event. The discovery of Icarus originates from the observations of the MACS J1149 cluster, which was selected as one of the targets in the Hubble Frontier Fields (HFF) project of Hubble Space Telescope (HST) [213]. The project was conducted between 2013 and 2015, during which the gravitationally lensed SN Refsdal images were discovered [212]. As SN Refsdal provided a unique opportunity to determine the Hubble constant through time-delay measurements [214], follow-up observations were carried out [215]. These frequent monitoring observations of the MACS J1149 cluster for approximately two years of observations in total led to the discovery of Icarus in 2016 and the measurement of its light curve. Another notable case is Earendel, a star at very high redshift  $z = 6.7$ , identified through HST observations [216]. Earendel is located on the critical curve of the galaxy cluster WHL0137–08 at redshift  $z = 0.566$  and the magnification is estimated to exceed a factor of thousand, with the peak magnification continuing for over 3.5 years. This phenomenon is attributed to the influence of microlenses forming a corrugated band near the critical curve [207]. Despite the similarities of Icarus and Earendel such as extreme magnification due to microlenses near critical curves of galaxy clusters, these events differ in terms of the locations and durations of their peak magnifications. The number of highly magnified events has been increasing rapidly (e.g., [45, 217]), paving the way for statistical analyses of such phenomena.

Highly magnified stars are observed near the critical curves of lens objects, with their shapes determined by the mass distributions. Critical curves can generally be classified into two types. The first type arises from the overall density profile of the lensing object, resulting in macro-critical curves. These curves are typically several tens of arcseconds in size for galaxy clusters as shown in Sec. 4.6. The shape of the macro-critical curve is

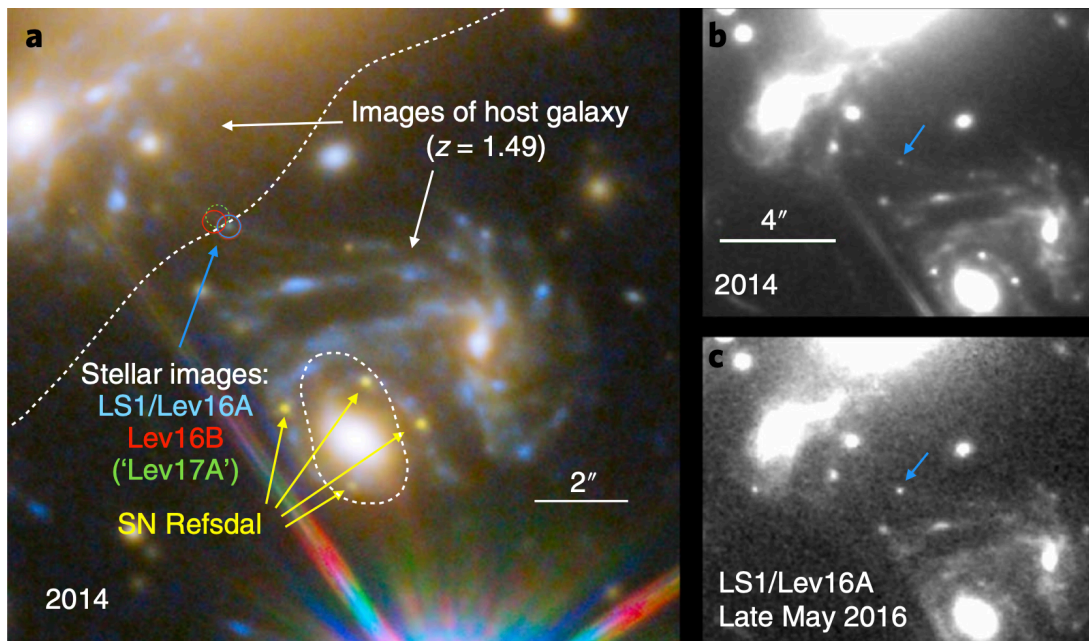


Figure 5.1: The ultrahigh magnified individual star Icarus (formally called LS1) in the spiral galaxy hosting SN Refsdal was observed near the critical curve of the MACS J1149 galaxy cluster (white dashed line) by HST observation. The peak magnification of Icarus was identified in May 2016 as shown in the lower right panel. This figure is taken from [44].

perturbed by the existence of subhalos [46], which we show in Chap. 6. Cold dark matter (CDM) subhalos with masses in the range  $M_h = 10^6 - 10^8 M_\odot$  can induce distortions on the order of ten milli-arcseconds [218]. The second type consists of micro-critical curves created by microlenses such as stars and black holes within the lens objects. These micro-critical curves are typically much smaller, often less than milli-arcseconds. In galaxy clusters, intracluster light (ICL) stars play a role as microlenses. Alongside ICL stars, other compact objects such as primordial black holes (PBHs), which are potential alternatives to the standard CDM model as discussed in Sec. 2.3.2, can also act as microlenses.

The presence of microlenses within lens objects influences the observed features of highly magnified stars [219]. Microlenses produce frequent peak magnifications and numerous micro-images due to their micro-critical curves. The analytic work by [220] explores key characteristics of the systems such as the width of the corrugated network near macro-critical curves, the frequency of caustic-crossing events, and peak magnifications. They further use these results to constrain the parameter space for massive compact halo objects as dark matter. The detailed ray-tracing simulations are conducted by [221] to investigate the corrugated networks near macro-critical curves. Similarly, [136] study microlensing effects near critical curves and estimate the event rate of Icarus using the GLAFIC software [222]. Furthermore, [223] consider the presence of axion minihalos in galaxy clusters, showing that these minihalos induce surface density fluctuations and irregular light curves. The average and dispersion of magnification in a random microlensing field within a smooth mass distribution are analytically derived by [209], where they extend the foundational work of [224], as reviewed in Sec. 4.8. The inverse ray-shooting simulations are conducted by [225] and [226], and they derive probability distribution functions (PDFs) under various parameter sets and provide fitting formulae to describe

these PDFs. While these studies have advanced our understanding of the statistical properties of highly magnified events near critical curves in galaxy clusters, a comprehensive physical model for the high-magnification tail of the PDF applicable across a wide range of parameters has yet to be developed. Addressing this gap serves as the primary motivation for our study.

In this chapter, we first introduce an analytic model for the high-magnification tail of the PDF, based on the number of independent micro-critical curves. Using the CCTRAIN simulation, which is a modified version of GLAFIC [222] designed to calculate caustic crossing events, we derive the PDF for point sources. We find that the combination of the surface mass density of microlenses and the background (average) magnification is a key quantity for describing the PDF across all parameter regions. Next, we address the case of finite source sizes, which limit the maximum magnification and suppress the high-magnification tail of the PDF. Leveraging simulations from the GPU-Enabled High-Resolution cosmological MicroLensing parameter survey (GERLUMPH) [225], we show that this suppression is accurately modeled using a sigmoid function. Our analytic model demonstrates good agreement with these simulation results, including parameter dependencies on the background average magnification, the mass fraction of microlenses, and finite source size effects. For practical applications, we focus on the Icarus-like system to estimate the number of highly magnified stars and the probability distribution of their observed positions. Given that the peak magnification of Icarus continues for about two weeks during a two-year HST survey, the observed mean number of Icarus-like events per snapshot can be approximated as  $1/52 \simeq 0.019$ . Our results indicate that ICL stars are consistent with the constraints on microlenses derived from the number of observed events in HST data. Furthermore, we place constraints on the mass and mass fraction of PBHs, assuming a monochromatic mass function for PBHs and the coexistence of ICL stars.

This chapter is structured as follows. In Sec. 5.2, we present our analytic model for the high-magnification tail of the PDF. In Sec. 5.3, we validate our model by comparing it with simulation results. To account for the contribution of probabilities around the average magnification, we show the model for the total PDF in Sec. 5.4. As an application of the model, Sec. 5.5 focuses on the Icarus-like system, where we calculate the number of highly magnified star events, the probability distribution of their observed locations, and place constraints on the parameter space of microlenses and PBHs. Finally, we provide a summary and discussion in Sec. 5.6. This chapter is based on our recent works presented in [48, 50].

## 5.2 High-magnification tail of probability distribution function

In this section, we outline our modeling for the high-magnification tail of the PDF. We consider a scenario where microlenses exist within a uniform smooth background. The total average convergence and shear are represented by  $\kappa_{\text{tot}}$  and  $\gamma_{\text{tot}}$ , respectively. Since ultra-high magnification events are observed near the critical curves of galaxy clusters, where the mass distribution is often approximated by a singular isothermal sphere profile as reviewed in Sec. 4.6.2, we adopt the relation  $\kappa_{\text{tot}} = \gamma_{\text{tot}}$ . The average convergence due to microlenses is denoted by  $\kappa_{\star}$ , and the microlens mass fraction,  $f_{\star}$ , is defined as  $\kappa_{\star} = f_{\star}\kappa_{\text{tot}}$ . We assume that all microlenses have identical masses and are uniformly

distributed randomly on the lens plane. Note that these assumptions may not fully capture reality, as microlenses should follow a mass function, and some may form binary systems, which we discuss further in Sec. 5.6. All microlenses have the same (original) Einstein radius, denoted by  $\theta_{\text{Ein}}$ , and the total number of microlenses,  $N_{\star}^{\text{tot}}$ , is proportional to the microlens mass fraction,  $f_{\star}$ . The average magnification depends on the total mass but is independent of  $f_{\star}$ , as shown in Eq. (4.147), and can be expressed as

$$\mu_{\text{av}} = \frac{1}{|(1 - \kappa_{\text{tot}})^2 - \gamma_{\text{tot}}^2|} = \frac{1}{|1 - 2\kappa_{\text{tot}}|}. \quad (5.1)$$

To be precise, while the background convergence is given by  $\kappa_{\text{B}} = \kappa_{\text{tot}} - \kappa_{\star}$  due to the fixed total convergence, the results from simulations conducted by GERLUMPH [225] also support this formula. Note that the average magnification can be separated into tangential magnification,  $\mu_{\text{t,av}}$ , and radial magnification,  $\mu_{\text{r,av}}$ . Under the assumption  $\kappa_{\text{tot}} = \gamma_{\text{tot}}$ , these components satisfy  $\mu_{\text{t,av}} = \mu_{\text{av}}$  and  $\mu_{\text{r,av}} = 1$ .

We study the parameter dependence of the high magnification tail of the PDF on the average magnification  $\mu_{\text{av}}$ , which depends solely on the total convergence, and the mass fraction of microlenses  $f_{\star}$ . For convenience, we introduce the normalized magnification

$$r = \frac{\mu_{\text{tot}}}{\mu_{\text{av}}} \quad (5.2)$$

and focus on the high magnification regime,  $r \gtrsim 10$ . Note that, since the average magnification is determined by the distance from the macro-critical curve or caustic, e.g., Eq. (4.133), our model allows us to study how the high-magnification events appear near the macro-critical curve, as discussed in Sec. 5.5.

We find that the high-magnification tail of the PDF can be effectively modeled as

$$\frac{dP}{d \log_{10} r} \propto N_{\star}^{\text{indep}} \sqrt{\mu_{\text{av}}} r^{-2} S(r; r_{\text{max}}). \quad (5.3)$$

Here,  $N_{\star}^{\text{indep}}$  represents the number of independent micro-critical curves, and  $S(r; r_{\text{max}})$  is the suppression factor due to the finite source size, effectively applied above the maximum magnification  $r_{\text{max}}$ . For point sources, the suppression factor is unity;  $S(r; r_{\text{max}}) = 1$ . The factor  $\sqrt{\mu_{\text{av}}}$  accounts for the stretching of the length of each micro-critical curve (and corresponding micro-caustic) in the smooth background, as explained in Sec. 4.7. The  $r^{-2}$  dependence emerges from the width around the micro-critical curve, where the magnification is between  $\log_{10} r$  and  $\log_{10} r + d \log_{10} r$ , as shown in Eq. (4.90). In summary, the first three components on the right-hand side,  $N_{\star}^{\text{indep}} \sqrt{\mu_{\text{av}}} r^{-2}$ , represent the total area where the magnification lies between  $\log_{10} r$  and  $\log_{10} r + d \log_{10} r$ , with the effect of the finite source size included in  $S(r; r_{\text{max}})$ .

The independent micro-critical curve is one that is generated by a microlens, whose distance to its nearest neighboring microlens is larger than the size of its own micro-critical curve. To determine the number of independent micro-critical curves, we begin by deriving the distribution of nearest inter-microlens distances, denoted as  $\theta_{\text{mid}}$ , for microlenses randomly distributed across the lens plane.

Consider a scenario where microlenses are randomly distributed across a two-dimensional lens plane with a number density  $n_{\star}$ ,

$$n_{\star} = \frac{f_{\star} \kappa_{\text{tot}}}{\pi \theta_{\text{Ein}}^2}. \quad (5.4)$$

The average number of microlenses within an area  $S$  is given by  $\bar{N}_\star = n_\star S$ . Assuming the number of microlenses follows a Poisson distribution, the probability of having  $N_\star$  microlenses within the area  $S$  can be expressed as

$$P(N_\star; S) = \frac{1}{N_\star!} e^{-n_\star S} (n_\star S)^{N_\star}. \quad (5.5)$$

To derive the distribution of the nearest inter-microlens distance from a single microlens, we examine the distribution that satisfies the following two conditions. The first condition is that there are no microlenses within a circle of radius  $\theta_{\text{nid}}$  from a given microlens. The second condition is that at least one microlens exists within a small annular region with radii  $\theta_{\text{nid}}$  and  $\theta_{\text{nid}} + d\theta_{\text{nid}}$ . The probability that satisfies the first condition is

$$P(N_\star = 0; S = \pi\theta_{\text{nid}}^2) = e^{-n_\star\pi\theta_{\text{nid}}^2}, \quad (5.6)$$

and the probability satisfying the second condition is

$$\begin{aligned} 1 - P(N_\star = 0; S = 2\pi\theta_{\text{nid}}d\theta_{\text{nid}}) &= 1 - e^{-2n_\star\pi\theta_{\text{nid}}d\theta_{\text{nid}}} \\ &\simeq 2n_\star\pi\theta_{\text{nid}}d\theta_{\text{nid}}. \end{aligned} \quad (5.7)$$

Thus, the probability of satisfying both conditions is given by

$$\frac{dQ}{d\theta_{\text{nid}}} = 2n_\star\pi\theta_{\text{nid}}e^{-n_\star\pi\theta_{\text{nid}}^2}, \quad (5.8)$$

from which it follows that the nearest inter-microlens distance follows a Rayleigh distribution. The mean of the nearest inter-microlens distance is expressed as

$$\bar{\theta}_{\text{nid}} = \int_0^\infty \theta_{\text{nid}} \frac{dQ}{d\theta_{\text{nid}}} d\theta_{\text{nid}} = \frac{1}{2\sqrt{n_\star}}. \quad (5.9)$$

Following the distribution of nearest inter-microlens distances, we can obtain the independent number of micro-critical curves,  $N_\star^{\text{indep}}$ . Considering that the typical size of each micro-critical curve is  $\sqrt{\mu_{\text{av}}}\theta_{\text{Ein}}$ , the probability that a micro-critical curve is independent can be calculated as

$$Q(\theta_{\text{nid}} > \sqrt{\mu_{\text{av}}}\theta_{\text{Ein}}) = \int_{\sqrt{\mu_{\text{av}}}\theta_{\text{Ein}}}^\infty \frac{dQ}{d\theta_{\text{nid}}} d\theta_{\text{nid}} = \exp(-f_\star\kappa_{\text{tot}}\mu_{\text{av}}). \quad (5.10)$$

Thus, the number of the independent micro-critical curves is expressed as

$$\begin{aligned} N_\star^{\text{indep}} &= N_\star^{\text{tot}} Q(\theta_{\text{nid}} > \sqrt{\mu_{\text{av}}}\theta_{\text{Ein}}) \\ &\propto f_\star\kappa_{\text{tot}} \exp(-f_\star\kappa_{\text{tot}}\mu_{\text{av}}). \end{aligned} \quad (5.11)$$

When the fraction of microlenses is sufficiently small, the nearest inter-microlens distance is typically larger than the size of each micro-critical curve, leading to  $Q(\theta_{\text{nid}} > \sqrt{\mu_{\text{av}}}\theta_{\text{Ein}}) \simeq 1$  and  $N_\star^{\text{indep}} \simeq N_\star^{\text{tot}}$ . As the microlens fraction or the average magnification increases, the typical nearest inter-microlens distance becomes smaller than the size of each micro-critical curve, leading to a decrease in the number of independent micro-critical curves below the total number of microlenses,  $N_\star^{\text{indep}} < N_\star^{\text{tot}}$ . We refer to the former as the "linear regime" and the latter as the "nonlinear regime". The boundary between these two regimes can be determined by comparing the mean nearest inter-microlens

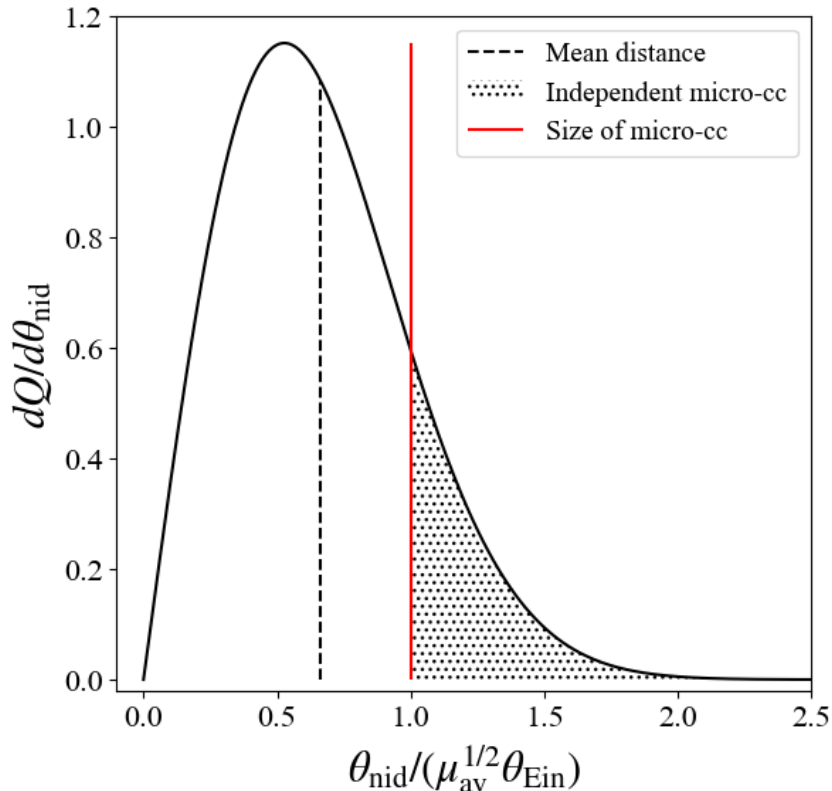


Figure 5.2: Distribution of the nearest inter-microlens distance (black solid line). The size of the micro-critical curve is shown in the vertical red solid line, and the mean of the nearest inter-microlens distance is shown in the vertical black dashed line. The dotted region is where the microlenses are independent. Here we set  $\theta_{\text{Ein}} = 0.2$  arcsec,  $\kappa_{\text{tot}} = 0.48$ ,  $f_{\star} = 0.15$ . This figure is taken from [48].

distance  $\bar{\theta}_{\text{nid}}$ , as given by Eq. (5.9), with the size of each micro-critical curve  $\sqrt{\mu_{\text{av}}}\theta_{\text{Ein}}$ , which results in

$$f_{\star}\kappa_{\text{tot}}\mu_{\text{av}} \simeq 1. \quad (5.12)$$

In the linear regime, where  $f_{\star}\kappa_{\text{tot}}\mu_{\text{av}} \lesssim 1$ , the number of independent micro-critical curves scales directly with the microlens fraction, i.e.,  $N_{\star}^{\text{indep}} \propto f_{\star}$ , as demonstrated by Eq. (5.11). In contrast, the number of independent micro-critical curves undergoes exponential suppression in the nonlinear regime. When considering the limit of  $f_{\star} \rightarrow 1$ , all matter components are effectively captured by the microlenses, which leads to a distribution that closely resembles the smooth matter distribution. This explains the suppression observed in the nonlinear regime.

In Fig. 5.2, we show the distribution of the nearest inter-microlens distance (black solid line), with its mean indicated by the vertical black dashed line, and compare it to the size of the micro-critical curve (vertical red solid line). The microlenses with the nearest inter-microlens distance larger than the size of the micro-critical curve (black dotted region) contribute to the independent micro-critical curves. In this case, only a small fraction of the microlenses are independent, as the mean nearest inter-microlens distance is smaller than the size of the micro-critical curve, indicating the nonlinear regime.

For a point source, where the suppression factor is  $S(r; r_{\text{max}}) = 1$ , we can derive the

high-magnification tail of the PDF by integrating all of these results to obtain

$$\frac{dP}{d\log_{10} r} \propto f_{\star} \kappa_{\text{tot}} \exp(-f_{\star} \kappa_{\text{tot}} \mu_{\text{av}}) \sqrt{\mu_{\text{av}}} r^{-2}. \quad (5.13)$$

The integrated probability above a magnification threshold  $r_{\text{th}}$  can be derived as

$$\begin{aligned} P^{\text{PS}}(r > r_{\text{th}}) &= \int_{r_{\text{th}}}^{\infty} \frac{dP}{d\log_{10} r} d\log_{10} r \\ &\propto f_{\star} \kappa_{\text{tot}} \sqrt{\mu_{\text{av}}} \exp(-f_{\star} \kappa_{\text{tot}} \mu_{\text{av}}) \left(\frac{1}{r_{\text{th}}}\right)^2, \end{aligned} \quad (5.14)$$

where PS refers to the point source. It can be shown that, by multiplying both sides by  $\sqrt{\mu_{\text{av}}}$ , Eq. (5.14) can be rewritten in a simpler form as

$$Y \propto X \exp(-X), \quad (5.15)$$

with  $X = f_{\star} \kappa_{\text{tot}} \mu_{\text{av}}$  and  $Y = P^{\text{PS}}(r > r_{\text{th}}) \sqrt{\mu_{\text{av}}}$ . The boundary between the linear and nonlinear regimes is given by  $X \simeq 1$ . For the first time, we show that by considering this combination of parameters, the dependence of the high-magnification PDF on  $f_{\star}$  and  $\mu_{\text{av}}$  can be analyzed in a unified way that covers both the linear and nonlinear regimes. A discussion of the suppression factor due to the finite source size is provided in Sec. 5.3.

### 5.3 Comparison with simulations

To validate our model presented in Sec. 5.2, we perform detailed ray-tracing simulations using our new code, CCTRAIN, which employs the same algorithm for solving the lens equation as GLAFIC [222]. Note that CCTRAIN has also been utilized in [207] to investigate magnification patterns near macro-critical curves. In addition to using an adaptive grid for efficiently solving lens equations, CCTRAIN incorporates a hierarchical tree algorithm to accelerate the computation of deflection angles for large populations of microlenses [227]. Magnifications of each source are calculated from the second derivatives of the lens potential as  $\mu = 1/\{(1 - \kappa)^2 - \gamma^2\}$ , where  $\kappa$  and  $\gamma$  represent the convergence and shear at the image position, respectively. As a result, the magnifications obtained from CCTRAIN correspond to those for point sources, with no effects from finite source sizes included. In addition to the ray-tracing simulations performed with CCTRAIN, we utilize publicly available magnification maps from GERLUMPH [225] in our analysis. The GERLUMPH simulations employ the inverse ray-shooting method, where magnifications are determined based on the number of inverse rays that converge within a single pixel on the source plane. Consequently, the pixel size on the source plane can be interpreted as the effective source size in the GERLUMPH simulations.

For both CCTRAIN and GERLUMPH, we analyze the cases where microlenses are randomly distributed in a smooth background characterized by constant convergence and shear with  $\kappa_{\text{tot}} = \gamma_{\text{tot}}$ , consistent with the setup described in Sec. 5.2. Note that GERLUMPH uses the smooth matter fraction  $s$ , which relates to the microlens fraction via  $f_{\star} = 1 - s$ . For CCTRAIN, we generate multiple realizations by varying the microlens distributions for a given parameter set, as detailed in Tab. 5.1. In contrast, for GERLUMPH, we use publicly available data provided through its online platform at <https://gerlumph.swin.edu.au>, with the specific realizations listed in Tab. 5.2. Here, many

Table 5.1: The simulation setups of CCTRAIN and the number of realizations. The lengths of the box size in the  $x$ - and  $y$ -directions are denoted by  $l_x$  and  $l_y$ , respectively. The box size and the resolution on the "lens" plane are in the unit of the Einstein radius of a point mass lens. This table is taken from [48].

$\kappa_{\text{tot}}$	$\mu_{\text{av}}$	$f_{\star}$	$(l_x, l_y)$	resolution	realization
0.45	10	0.0015625	(15, 2)	0.003125	100,000
0.45	10	0.003125	(15, 2)	0.003125	100,000
0.45	10	0.00625	(15, 2)	0.003125	100,000
0.45	10	0.0125	(15, 2)	0.003125	100,000
0.45	10	0.025	(20, 3)	0.003125	100,000
0.45	10	0.05	(20, 3)	0.003125	100,000
0.45	10	0.10	(30, 3)	0.003125	61,549
0.45	10	0.25	(50, 4)	0.003125	349
0.49	50	0.0003125	(9, 2)	0.0125	100,000
0.49	50	0.000625	(12, 2)	0.0125	100,000
0.49	50	0.00125	(18, 2)	0.0125	100,000
0.49	50	0.0025	(25, 2)	0.0125	100,000
0.49	50	0.005	(35, 2)	0.0125	100,000
0.49	50	0.01	(50, 2)	0.0125	100,000
0.49	50	0.02	(70, 2)	0.0125	100,000
0.49	50	0.04	(100, 2)	0.0125	100,000
0.49	50	0.056	(119, 4)	0.0125	10,000
0.49	50	0.08	(140, 4)	0.0125	10,000
0.49	50	0.112	(166, 4)	0.0125	10,000
0.49	50	0.16	(200, 4)	0.0125	10,000
0.49	50	0.32	(280, 5.6)	0.0125	3,926

realizations are obtained by varying the source position while keeping the microlens distribution fixed. From these realizations, we construct the PDF for the total magnification, the sum of the absolute magnifications of multiple images. Specifically, we focus on the regime where the condition  $\mu_{\text{tot}} \gtrsim 10\mu_{\text{av}}$  satisfies, which translates to  $r \gtrsim r_{\text{th}}$  with the normalized magnification threshold approximately given by  $r_{\text{th}} \simeq 10$ .

In the following subsections, we investigate two cases to test our model: one for a point source and another for a finite-sized source. The point source case is examined using CCTRAIN, while the finite source size case is tested with GERLUMPH. In Sec. 5.3.1, we present the results for the point source case, followed by those for the finite source case in Sec. 5.3.2.

### 5.3.1 Point source

For the point source case, the suppression term can be neglected and  $S(r; r_{\text{max}}) = 1$  in Eq. (5.3). As shown in Eq. (5.15), the dependence of the parameters on the high magnification tail of the PDF can be absorbed using the variables  $X$  and  $Y$ . Consequently, the data should ideally follow along a single line on the  $X$ - $Y$  plane. We introduce two fitting parameters,  $A_0$  and  $B_0$ . The parameter  $A_0$  is used to determine the normalization of the PDF, while  $B_0$  accounts for the uncertainty in Eq. (5.12). Thus,  $B_0$  should be of the order  $\mathcal{O}(1)$ . With  $A_0$  and  $B_0$ , our model for the magnification PDF is then expressed

Table 5.2: The realizations of GERLUMPH used in this study. The resolution on the "source" plane is expressed in the unit of the Einstein radius of a point mass lens. The number of realizations is given for each value of  $f_\star$ . This table is taken from [48].

$\kappa_{\text{tot}}$	$\mu_{\text{av}}$	$f_\star$	resolution	realization
0.30	2.50	0.01, 0.05, 0.1, 0.2, 0.3, 0.4, 0.5, 0.6, 0.7, 0.8, 0.9, 1	0.0025	100,000,000
0.33	2.94	0.01, 0.05, 0.1, 0.2, 0.3, 0.4, 0.5, 0.6, 0.7, 0.8, 0.9, 1	0.0025	100,000,000
0.36	3.57	0.01, 0.05, 0.1, 0.2, 0.3, 0.4, 0.5, 0.6, 0.7, 0.8, 0.9, 1	0.0025	100,000,000
0.37	3.85	0.01, 0.05, 0.1, 0.2, 0.3, 0.4, 0.5, 0.6, 0.7, 0.8, 0.9, 1	0.0025	100,000,000
0.38	4.12	0.01, 0.05, 0.1, 0.2, 0.3, 0.4, 0.5, 0.6, 0.7, 0.8, 0.9, 1	0.0025	100,000,000
0.39	4.55	0.01, 0.05, 0.1, 0.2, 0.3, 0.4, 0.5, 0.6, 0.7, 0.8, 0.9, 1	0.0025	100,000,000
0.40	5.00	0.01, 0.05, 0.1, 0.2, 0.3, 0.4, 0.5, 0.6, 0.7, 0.8, 0.9, 1	0.0025	100,000,000
0.41	5.56	0.01, 0.05, 0.1, 0.2, 0.3, 0.4, 0.5, 0.6, 0.7, 0.8, 0.9, 1	0.0025	100,000,000
0.42	6.25	0.01, 0.05, 0.1, 0.2, 0.3, 0.4, 0.5, 0.6, 0.7, 0.8, 0.9, 1	0.0025	100,000,000
0.43	7.14	0.01, 0.05, 0.1, 0.2, 0.3, 0.4, 0.5, 0.6, 0.7, 0.8, 0.9, 1	0.0025	100,000,000
0.44	8.33	0.01, 0.05, 0.1, 0.2, 0.3, 0.4, 0.5, 0.6, 0.7, 0.8, 0.9, 1	0.0025	100,000,000
0.45	10.0	0.01, 0.05, 0.1, 0.2, 0.3, 0.4, 0.5, 0.6, 0.7, 0.8, 0.9, 1	0.0025	100,000,000
0.46	1.25	0.01, 0.05, 0.1, 0.2, 0.3, 0.4, 0.5, 0.6, 0.7, 0.8, 0.9, 1	0.0025	100,000,000
0.47	16.7	0.01, 0.05, 0.1, 0.2, 0.3, 0.4, 0.5, 0.6, 0.7, 0.8, 0.9, 1	0.0025	100,000,000
0.48	25.0	0.01, 0.05, 0.1, 0.2, 0.3, 0.4, 0.5, 0.6, 0.7, 0.8, 0.9, 1	0.0025	100,000,000

as

$$P^{\text{PS}}(r > r_{\text{th}})\sqrt{\mu_{\text{av}}} = \frac{A_0}{2.4} f_\star \kappa_{\text{tot}} \mu_{\text{av}} \exp(-B_0 f_\star \kappa_{\text{tot}} \mu_{\text{av}}) \left(\frac{10}{r_{\text{th}}}\right)^2. \quad (5.16)$$

We determine the parameters by fitting the simulation data obtained from CCTRAIN, using a magnification threshold of  $r_{\text{th}} = 10$ .

In Fig. 5.3, we present the fitting results. The best-fitting parameters are found to be  $A_0 = 0.057$  and  $B_0 = 0.394$ . The integrated PDF exhibits the turnover between linear and nonlinear regimes, which is accurately reproduced by our model. As anticipated, the simulation data for different parameter sets align closely along a single line in this plane, with the best-fit value of  $B_0$  being of order  $\mathcal{O}(1)$ . To be precise, small discrepancies between our model and the simulation data can be seen even in the simple linear regime. Since the integrated probability scales almost linearly with the microlens mass fraction  $f_\star$  in the linear regime for a given average magnification  $\mu_{\text{av}}$ , the discrepancy might suggest that the simple assumption of the size of the micro-critical curve expanding by  $\sqrt{\mu_{\text{av}}}$  times the original Einstein radius is not entirely accurate. As mentioned in Sec. 4.7, the actual micro-critical curve shapes like a gourd, expanding at a rate of  $\sqrt{\mu_{\text{av}}}$  in the  $\phi = \pi/2$  direction, while the expansion rate is unity in the  $\phi = 0$  direction. This leads to an overestimate of the size of the micro-critical curve, potentially explaining the discrepancy between the cases of  $\mu_{\text{av}} = 10$  and  $\mu_{\text{av}} = 50$ . Moreover, the variation in the central value tends to exceed the Poisson error for a given average magnification. This may also be attributed to an inadequate estimation of the micro-critical curve size and an insufficient number of realizations. Since the size of micro-critical curves is influenced by the shear from neighboring microlenses, it might introduce scatter in the probability, leading to a misalignment of the central value. Increasing the number of realizations is expected to reduce this variation. Despite these discrepancies, our model successfully explains the PDF within the scope of the zeroth-order approximation.

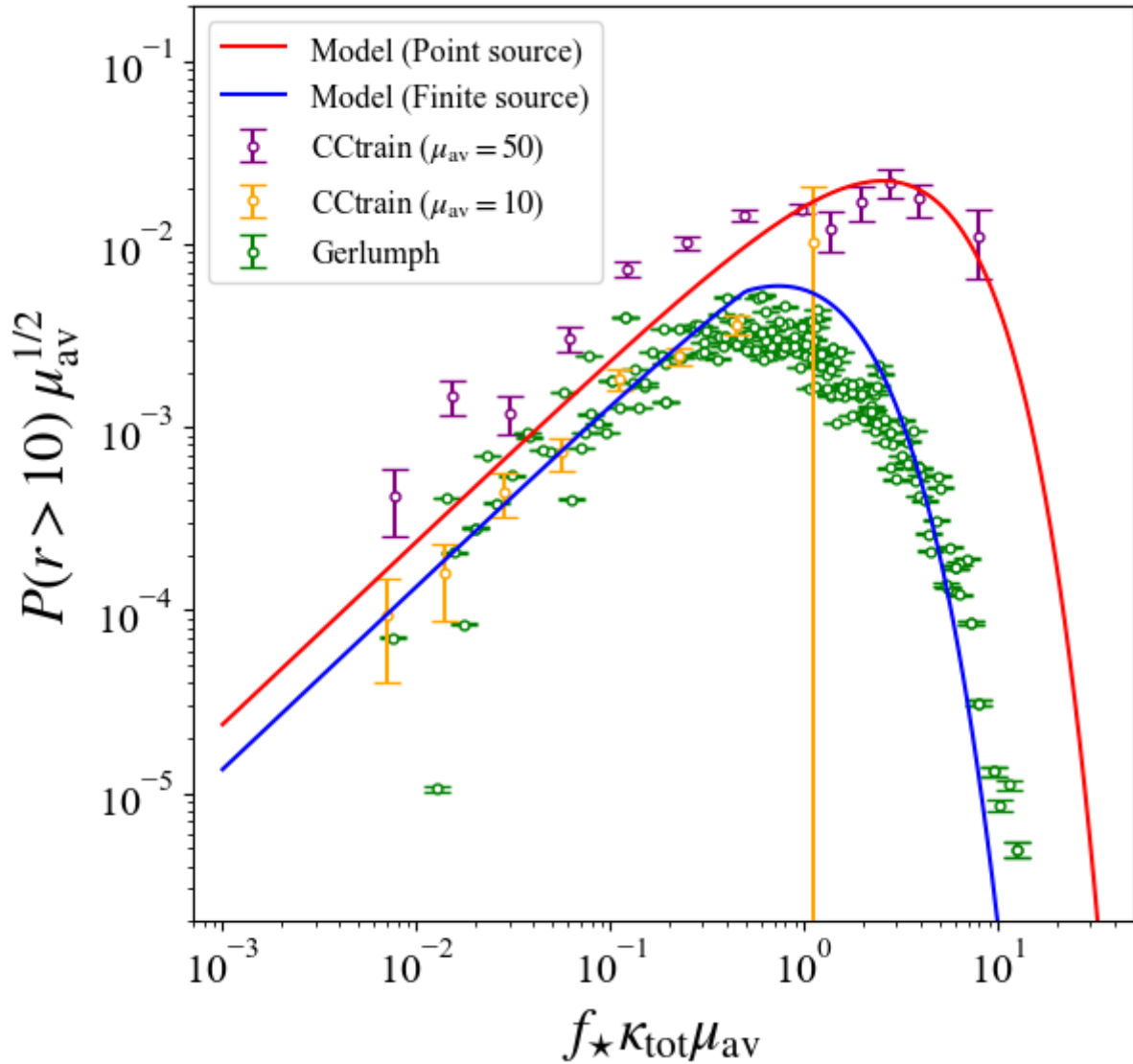


Figure 5.3: Comparison of the integrated PDF between the simulations and our model. The purple and orange dots are obtained by the CCTRAIN with  $\kappa_{\text{tot}} = 0.49$  and  $0.45$ , respectively. The green dots are the simulation data from GERLUMPH. The realizations are listed in Tab. 5.1 and 5.2. The error bars are determined based on the Poisson distribution of the number of realizations exceeding  $r > 10$ . The red line shows the fitting result of our model in the case of the point source with fitting parameters  $A_0 = 0.057$  and  $B_0 = 0.394$ . The blue line shows the fitting result of our model with the finite source case with a fitting parameter  $C_0 = 2.0$ . This figure is taken from [48].

### 5.3.2 Finite source size

When considering the finite source size, the model for the high-magnification tail of the PDF becomes

$$\frac{dP}{d \log_{10} r} = 2 \ln 10 P^{\text{PS}}(r > r_{\text{th}}) S(r; r_{\text{max}}) \left( \frac{r}{r_{\text{th}}} \right)^{-2}. \quad (5.17)$$

In this subsection, we discuss the suppression function  $S(r; r_{\text{max}})$  resulting from the finite source size, based on the simulation data obtained from GERLUMPH.

For the case of a finite source size, a maximum magnification arises due to the averaging effect, as discussed in Sec. 4.5. The resolution on the source plane in GERLUMPH corresponds to the effective source size, expressed as  $\sigma_{\text{W}} = 0.0025\theta_{\text{Ein}}$ . In the linear regime, where the micro-critical curves and micro-caustics are independent of each other, the maximum magnification can be estimated using Eq. (4.132) as

$$r_{\text{max}} \simeq \sqrt{\frac{\theta_{\text{Ein}}}{\sqrt{\mu_{\text{av}}\sigma_{\text{W}}}}}, \quad (5.18)$$

where we neglect the  $\mathcal{O}(1)$  prefactor. In the nonlinear regime, the size of the micro-critical curves can be approximated by the average nearest inter-microlens distance [220]. Using Eqs. (5.4) and (5.9), this distance can be written as

$$\bar{\theta}_{\text{nid}} \simeq \frac{\theta_{\text{Ein}}}{\sqrt{f_{\star}\kappa_{\text{tot}}}}, \quad (5.19)$$

where we neglect the factor of two. Thus, in the nonlinear regime, the maximum magnification can be derived by replacing  $\sqrt{\mu_{\text{av}}}$  to  $1/\sqrt{f_{\star}\kappa_{\text{tot}}}$  in Eq. (5.18). This gives the maximum magnification in the nonlinear regime as

$$r_{\text{max}} \simeq \sqrt{\frac{\theta_{\text{Ein}}}{\sqrt{\mu_{\text{av}}\sigma_{\text{W}}}} \left( \frac{1}{f_{\star}\kappa_{\text{tot}}\mu_{\text{av}}} \right)^{\frac{3}{4}}}. \quad (5.20)$$

By combining these results, we obtain the following expression for the maximum magnification

$$r_{\text{max}} \simeq \sqrt{\frac{\theta_{\text{Ein}}}{\sqrt{\mu_{\text{av}}\sigma_{\text{W}}}} \min\left(1, (C_0 f_{\star} \mu_{\text{av}} \kappa_{\text{tot}})^{-\frac{3}{4}}\right)}, \quad (5.21)$$

where we introduce an  $\mathcal{O}(1)$  fitting parameter,  $C_0$ , to account for the uncertainty in the estimation given by Eq. (5.20).

By analyzing the data from GERLUMPH, we find that the sigmoid function is suitable to capture the suppression,

$$S(r; r_{\text{max}}) = \frac{1 + e^{-1}}{1 + \exp\left(\frac{r - r_{\text{max}}}{r_{\text{max}}}\right)}. \quad (5.22)$$

The function approaches unity when the maximum magnification becomes infinite, corresponding to the point source case. In Fig. 5.4, we present the fitting results. The following relation is used here,

$$S(r; r_{\text{max}}) = r^2 \frac{dP}{d \log_{10} r} \left( r_0^2 \frac{dP}{d \log_{10} r} \Big|_{r=r_0} \right)^{-1}, \quad (5.23)$$

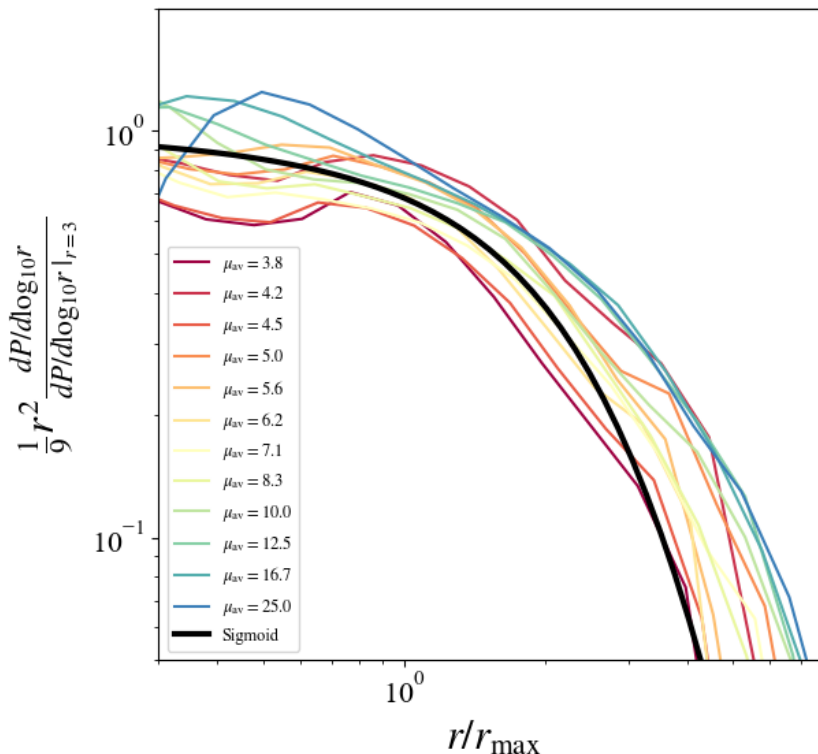


Figure 5.4: The suppression of the PDF obtained from GERLUMPH data and fitting with the sigmoid function. The color lines correspond to the different average magnifications. Here we use the data with  $f_* = 0.2$ . The black line shows our sigmoid modeling of the suppression with the fitting parameter  $C_0 = 2.0$ . This figure is taken from [48].

which is derived from Eq. (5.17), and we normalize the  $x$ -axis by the maximum magnification using Eq. (5.21), while the  $y$ -axis represents the right-hand side of Eq. (5.23) with  $r_0 = 3$ . Figure 5.4 shows that the sigmoid function with the maximum magnification derived by Eq. (5.21) fits the simulation data well, with the fitting parameter  $C_0 = 2.0$ . Figure 5.3 shows the comparison of the integrated PDF between our model including the suppression (blue line) and the simulation data (green points). In contrast to the point source case, the data points for a finite source size do not exactly align in a single line due to the additional dependence of  $\mu_{av}$  in the suppression function through the maximum magnification. However, this effect is relatively small and the data points still closely align in a single line. We use a typical average magnification of  $\mu_{av} = 6.25$  ( $\kappa_{tot} = 0.42$ ) to calculate the maximum magnification for plotting our theoretical predictions in Fig. 5.3. Note that since realizations are generated by varying only the source position while keeping the microlens distribution fixed for the GERLUMPH, the central value may be biased, or the errors may be underestimated due to unaccounted systematic uncertainties.

Combining all the results presented here, we conclude that the high magnification tail of the PDF can be represented as

$$\frac{dP}{d\log_{10} r} = 2 \ln 10 P^{\text{PS}}(r > r_{\text{th}}) \frac{1 + e^{-1}}{1 + \exp\left(\frac{r - r_{\text{max}}}{r_{\text{max}}}\right)} \left(\frac{r}{r_{\text{th}}}\right)^{-2}. \quad (5.24)$$

The fitting parameters are  $A_0 = 0.057$ ,  $B_0 = 0.394$ , and  $C_0 = 2.0$ . We observe that this model accurately captures the simulation results.

By integrating the PDF above the magnification threshold for the finite source size case, we can derive the following ratio,

$$\begin{aligned} \frac{P^{\text{FS}}(r > r_{\text{th}})}{P^{\text{PS}}(r > r_{\text{th}})} &= 2 \ln 10 r_{\text{th}}^2 \int_{r_{\text{th}}}^{\infty} \frac{1}{r^2} \frac{1 + e^{-1}}{1 + \exp\left(\frac{r - r_{\text{max}}}{r_{\text{max}}}\right)} d \log_{10} r \\ &\simeq \left(1 - \frac{r_{\text{th}}}{r_{\text{max}}}\right) e^{-\frac{r_{\text{th}}}{r_{\text{max}}}} + \left(\frac{r_{\text{th}}}{r_{\text{max}}}\right)^2 \left\{ -\text{CI}\left(\frac{r_{\text{th}}}{r_{\text{max}}}\right) + \text{SI}\left(\frac{r_{\text{th}}}{r_{\text{max}}}\right) \right\}. \end{aligned} \quad (5.25)$$

Here, CI and SI refer to the hyperbolic cosine integral and the hyperbolic sine integral, respectively. They are expressed as  $\text{CI}(x) = \int_0^x dt \cosh(t)/t$  and  $\text{SI}(x) = \int_0^x dt \sinh(t)/t$ . In the point source limit, where  $r_{\text{max}} \gg r_{\text{th}}$ , the first term on the right-hand side becomes dominant and simplifies to unity, as anticipated.

## 5.4 Total probability distribution function

Our analytic model discussed in Sec. 5.2 focuses solely on the high-magnification tail. In this section, we explain how the total PDF is modeled.

A ray-shooting simulation indicates that the PDF around the average magnification follows a log-normal distribution [226]. The average magnification and its variance are analytically examined in [209], as shown in Sec. 4.8. Based on the average magnification  $\mu_{\text{av}}$  and its standard deviation  $\text{Std}[\mu_{\text{av}}]$ , Eq. (4.146), we model the PDF near the average magnification as

$$\left. \frac{dP}{d \log_{10} \mu} \right|_{\text{middle}} = \frac{1}{\sqrt{2\pi\sigma_{\log_{10} \mu_{\text{av}}}^2}} \exp\left(-\frac{(\log_{10} \mu - \log_{10} \mu_{\text{av}})^2}{2\sigma_{\log_{10} \mu_{\text{av}}}^2}\right), \quad (5.26)$$

with the standard deviation for the log-normal distribution being

$$\sigma_{\log_{10} \mu_{\text{av}}} = \frac{\text{Std}[\mu_{\text{av}}]}{\mu_{\text{av}} \ln 10}. \quad (5.27)$$

The high-magnification tail of the PDF given in Eq. (5.24), can be expressed with  $r$  replaced by  $\mu$  as,

$$\left. \frac{dP}{d \log_{10} \mu} \right|_{\text{high}} = 2 \ln 10 P^{\text{PS}}(\mu > \mu_{\text{th}}) \frac{1 + e^{-1}}{1 + \exp\left(\frac{\mu - \mu_{\text{max}}}{\mu_{\text{max}}}\right)} \left(\frac{\mu}{\mu_{\text{th}}}\right)^{-2}. \quad (5.28)$$

Combining the above PDFs, we can obtain the total PDF,

$$\left. \frac{dP}{d \log_{10} \mu} \right|_{\text{tot}} = \begin{cases} A_{\text{norm}} \left. \frac{dP}{d \log_{10} \mu} \right|_{\text{middle}} & (\mu \leq \mu_0) \\ \left. \frac{dP}{d \log_{10} \mu} \right|_{\text{high}} & (\mu \geq \mu_0), \end{cases} \quad (5.29)$$

where  $\mu_0 > \mu_{\text{av}}$  represents the matching magnification between the log-normal distribution and the high-magnification tail, and  $A_{\text{norm}}$  is the normalization constant ensuring that the total probability is normalized to unity.

In Fig. 5.5, we present an example of the total PDF at  $\theta = 0.039$  arcsec away from the macro-critical curve in the Icarus-like system, reviewed in Sec. 5.5.1. It can be observed that the transition between the middle region and high magnification tails occurs at  $\mu_0 \simeq 3\mu_{\text{av}}$  in this case.

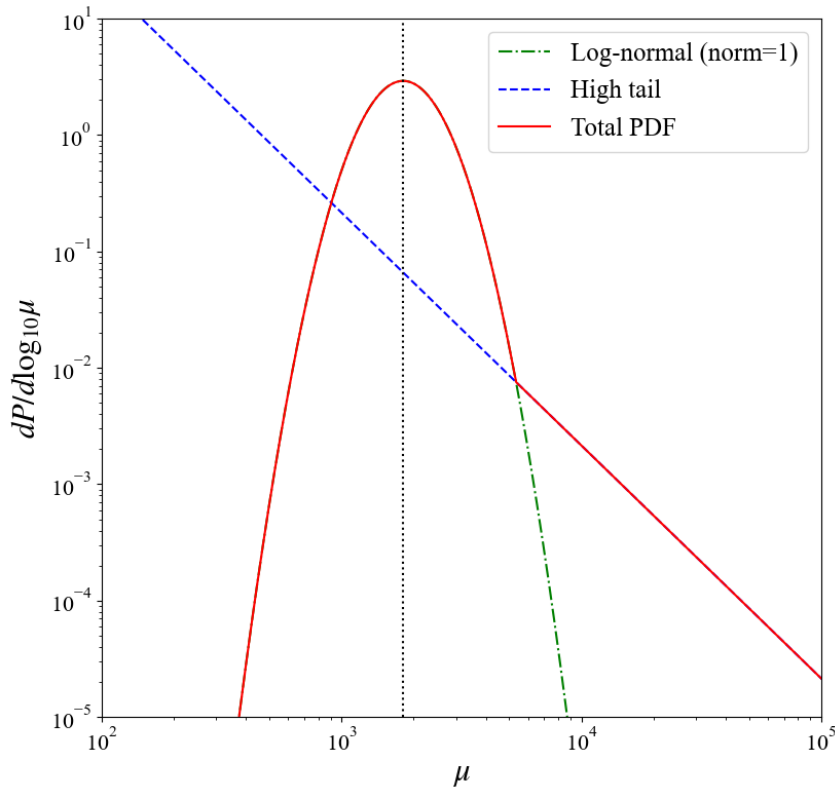


Figure 5.5: The total PDF of the magnification at  $\theta = 0.039$  arcsec away from the macro-critical curve in the Icarus-like system, which corresponds to  $\beta = 7.0 \times 10^{-5}$  arcsec away from the macro-caustic. The average magnification is calculated from Eq. (5.30) and its variance is calculated from Eq. (4.148), where we consider the constant background convergence and the shear. The constant background convergence is calculated from the average magnification assuming the shear equals the convergence. The green dash-dot line shows the PDF around the average magnification, which is shown in a vertical dotted line. The blue dashed line represents the high-magnification tail of the PDF. The red solid line is the total PDF with the normalization factor  $A_{\text{norm}} = 0.9986$  as introduced in Eq. (5.29). This figure is taken from [48].

## 5.5 Application to Icarus-like system

In this section, we apply our analytic model to the Icarus-like system, predicting the number of high-magnification events and the probability distribution of their observed positions. Additionally, we constrain the mass and mass fraction of microlenses and PBHs based on the number of high-magnification events. We begin by reviewing the properties of the MACS J1149 cluster and Icarus, as primarily discussed in [136], in Sec. 5.5.1. In Sec. 5.5.2, we calculate the probability of exceeding a certain magnification threshold and its associated image location. Here, we ignore the correlation between the source size and the intrinsic luminosity of the source star, as well as the threshold in apparent magnitude. These factors are incorporated in Sec. 5.5.3 for a more accurate prediction of the number of Icarus-like events. In the same section, we also present the constraint on the microlens parameter space. Finally, we provide the constraint on the mass and mass fraction of PBHs in the presence of ICL stars in Sec. 5.5.4.

### 5.5.1 MACS J1149 cluster and Icarus

#### Average magnification

Icarus is an extremely magnified blue supergiant star within a spiral galaxy at redshift  $z = 1.49$ , observed in the MACS J1149 galaxy cluster at redshift  $z = 0.544$ . The average magnification,  $\mu_{\text{av}}$ , near Icarus can be described as a function of the distance  $\beta$  from the macro-caustic of the galaxy cluster, given by

$$\mu_{\text{av}}(\beta) = \mu_{\text{h}}\mu_{\text{r}} \frac{1}{\sqrt{2\pi(\sigma_{\text{ml}}^2 + \sigma_{\text{W}}^2)}} \int_0^\infty d\beta' \sqrt{\frac{\beta_0}{\beta'}} \exp\left[-\frac{(\beta' - \beta)^2}{2(\sigma_{\text{ml}}^2 + \sigma_{\text{W}}^2)}\right], \quad (5.30)$$

with  $\mu_{\text{h}} = 13$ ,  $\mu_{\text{r}} = 3$ , and  $\beta_0 = 0.045$  arcsec [136]. The tangential magnification as a function of the distance  $\theta$  to the macro-critical curve is expressed as

$$\mu_{\text{t}}(\theta) = \mu_{\text{h}} \sqrt{\frac{\beta_0}{\beta(\theta)}} = \mu_{\text{h}} \left(\frac{\theta}{\text{arcsec}}\right)^{-1}. \quad (5.31)$$

The source size  $\sigma_{\text{W}}$ , expressed in arcseconds, is connected to the physical source size  $R$  by

$$\sigma_{\text{W}} = 2.7 \times 10^{-12} \left(\frac{R}{R_{\odot}}\right) \text{ arcsec}. \quad (5.32)$$

The effective source size,  $\sigma_{\text{ml}}$ , which represents the variance in the random deflection angle induced by microlenses, is expressed by Eq. (4.134), where the Einstein radius of a microlens with mass  $M_{\star}$  is given by

$$\theta_{\text{Ein}} = 1.8 \times 10^{-6} \left(\frac{M_{\star}}{M_{\odot}}\right)^{\frac{1}{2}} \text{ arcsec}. \quad (5.33)$$

Note that although  $R_{\star}$  is originally defined in Eq. (4.135), we adopt  $R_{\star} = 1500$  as stated in [209].

Icarus is observed at a distance of 0.13 arcsec from the macro-critical curve. The average magnification at this location is approximately  $\mu_{\text{av}} = 300$ , which is much lower than the expected magnification of  $\mathcal{O}(10^3)$ . This difference indicates that the star is significantly magnified by microlenses. The ICL stars can contribute to the microlensing effect. The surface mass density of the ICL stars is estimated to be  $\Sigma_{\text{ICL}} = 1.1 - 1.9 \times 10^7 M_{\odot}/\text{kpc}^2$ , which corresponds to an average convergence of  $\kappa_{\text{ICL}} = 0.0046 - 0.0079$  [44]. This estimation is based on the observed surface brightness of the ICL and the mass-to-light ratios, consistent with previous analysis [228]. The mass-to-light ratios primarily depend on the assumed initial mass functions (IMFs); the lower bound corresponds to the Chabrier IMF [229, 230], while the upper bound corresponds to the Salpeter IMF [231], introducing uncertainties in the estimation of the surface mass density. Given that the total convergence is  $\kappa_{\text{tot}} = 0.83$ , estimated from the mass modeling of the MACS J1149 cluster [232], the mass fraction of ICL stars is calculated as  $\kappa_{\text{ICL}}/\kappa_{\text{tot}} \simeq 0.005 - 0.009$ . The most likely mass of the ICL stars is  $M_{\star} \simeq 0.3 M_{\odot}$  [136]. This is reasonable by considering the Salpeter IMF, which is a bottom-heavy IMF preferred for early-type galaxies commonly found in galaxy clusters, and that substellar objects with masses below  $0.08 M_{\odot}$  cannot undergo star formation due to insufficient mass for hydrogen-burning. Conversely, stars with higher mass  $M_{\star} \gg 1.5 M_{\odot}$  are unlikely to survive the age of a galaxy cluster. Therefore, we consider the typical mass range of ICL stars to be  $0.1 - 10 M_{\odot}$ , with the most likely value around  $M_{\star} \simeq 0.3 M_{\odot}$ .

### Constraint on the radius of Icarus

The radius of Icarus can be constrained using the peak magnitude and the source crossing time. To examine this, we first establish the relationship between the source size and its luminosity. Assuming the source behaves like a blackbody with temperature  $T$ , this relation can be derived from the Stefan–Boltzmann law,

$$\frac{L}{L_{\odot}} = \left(\frac{R}{R_{\odot}}\right)^2 \left(\frac{T}{T_{\odot}}\right)^4. \quad (5.34)$$

The estimated temperature, derived from the spectral energy distribution (SED) shown in Fig. 5.6, is  $T \simeq 12000$  K, which is characteristic of a blue supergiant [44]. The absolute magnitude of the V-band can be expressed as

$$\begin{aligned} M_{L_{\star},V} &= M_{L_{\odot},V} - 2.5 \log_{10} \left(\frac{L}{L_{\odot}}\right) \\ &= 1.65 - 5 \log_{10} \left(\frac{R}{R_{\odot}}\right), \end{aligned} \quad (5.35)$$

where we use the V-band magnitude of the Sun  $M_{L_{\odot},V} = 4.83$  and the solar temperature  $T_{\odot} = 5777$  K, and apply Eq. (5.34) in the second equality. Including the bolometric correction of B.C. =  $-0.69$  [233, 234], the absolute magnitude can be expressed as

$$M_{L_{\star}} \simeq 1.0 - 5 \log_{10} \left(\frac{R}{R_{\odot}}\right). \quad (5.36)$$

For a source magnified by a factor of  $\mu$ , its apparent magnitude can be expressed as

$$\begin{aligned} m_{L_{\star}} &= M_{L_{\star}} + D - 2.5 \log_{10} \mu \\ &\simeq 45.1 - 5 \log_{10} \left(\frac{R}{R_{\odot}}\right) - 2.5 \log_{10} \mu, \end{aligned} \quad (5.37)$$

where  $D = 5 \log_{10} d - 5$  represents the distance modulus, with  $d$  denoting the luminosity distance in parsecs. Given the source redshift, the distance modulus is  $D = 45.2$ . Observations in the F125W band require a cross-filter K-correction to properly account for differences between the observed and rest-frame filter transmission. This correction is applied in the second equality to ensure consistent analysis. The observation of Icarus suggests that the peak apparent magnitude is  $m_{L_{\star}} \lesssim 26$ . The threshold of the magnification  $\mu_{\text{obsth}}$  required to reach this observed apparent magnitude can be derived from Eq. (5.37) as

$$\mu_{\text{obsth}}(R) = 4.4 \times 10^7 \left(\frac{R}{R_{\odot}}\right)^{-2}. \quad (5.38)$$

It is evident that smaller sources require higher magnifications to be observed due to their smaller absolute magnitude. Since the maximum magnification can be derived from Eq. (5.21) with Eqs. (5.32) and (5.33), the condition  $\mu_{\text{obsth}}(R) \lesssim \mu_{\text{max}}$  provides a lower limit for the radius of Icarus,

$$R_{\text{min}} = 69 \left(\frac{\mu_{\text{av}}}{300}\right)^{-\frac{1}{2}} \left(\frac{M_{\star}}{M_{\odot}}\right)^{-\frac{1}{6}} R_{\odot}. \quad (5.39)$$

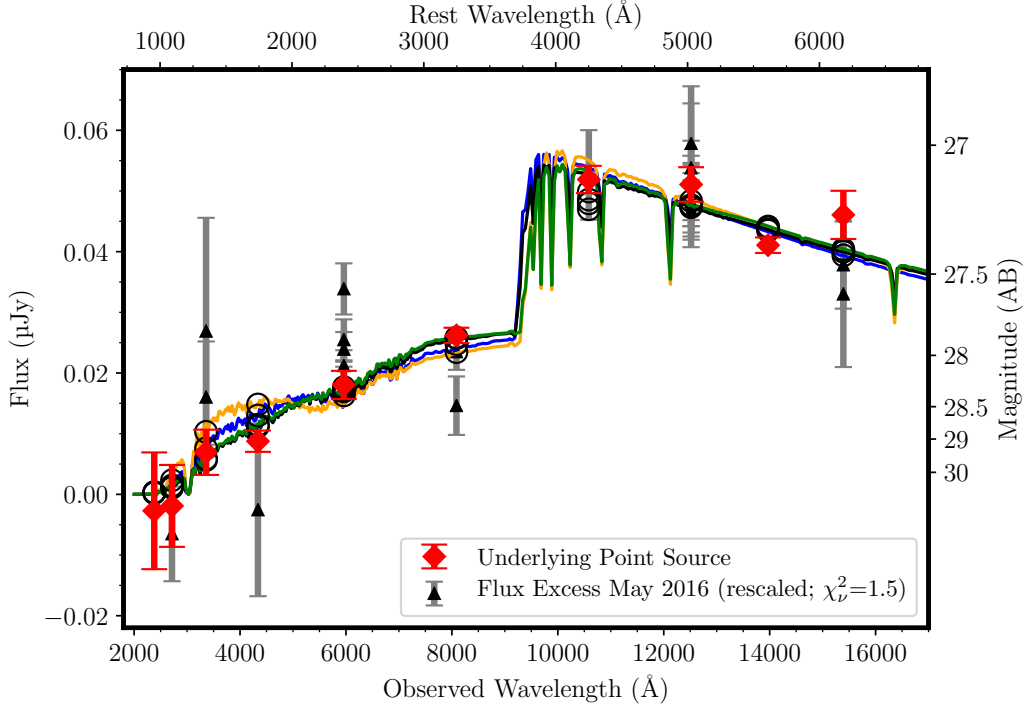


Figure 5.6: The SEDs of Icarus, measured during the HFF project (red diamonds) and during its peak magnification in May 2016 with a rescaling of the excess flux density by a factor of four (black triangles). The SED shows a strong Balmer break consistent with the host-galaxy redshift of 1.49. The stellar atmosphere models [235] for a mid-to-late B-type star provide a reasonable fit, with the temperature and surface gravity parameters given as  $T = 11180$  K and  $\log g = 2$  (blue),  $T = 12250$  K and  $\log g = 4$  (orange),  $T = 12375$  K and  $\log g = 2$  (black), and  $T = 13591$  K and  $\log g = 4$  (green). This figure is taken from [44].

where the nonlinear suppression term in Eq. (5.21) is neglected for this derivation. Sources with radii larger than this minimum radius can be detected.

An additional constraint on the radius of Icarus can be derived from the source crossing time, which is estimated by [136]

$$t_{\text{src}} = 0.038 \left( \frac{R}{R_{\odot}} \right) \left( \frac{v}{500 \text{ km/s}} \right)^{-1} \text{ days.} \quad (5.40)$$

The velocity  $v$  has three main components: the transverse peculiar velocity of the galaxy cluster, the relative transverse motion of microlenses within the cluster, and the transverse velocity in the source plane. Among these, the dominant factor is the transverse peculiar velocity of the galaxy cluster [136]. This is because, when we consider the relative velocity in the source plane, the relative transverse motion of microlenses within the cluster is suppressed by a factor of large magnification, and the transverse velocity in the source plane becomes smaller than the transverse peculiar velocity of the galaxy cluster due to the larger distance and redshift. For the MACS J1149 cluster, the three-dimensional peculiar velocity is measured to be  $v_{3D} = 638_{-393}^{+1072}$  km/s at a 68% confidence interval (CI) [236]. This value is higher than the typical peculiar velocity because MACS J1149 is a merging cluster. The merger axis is inclined at an angle of  $\alpha \simeq 30^\circ$  relative to the plane of the sky

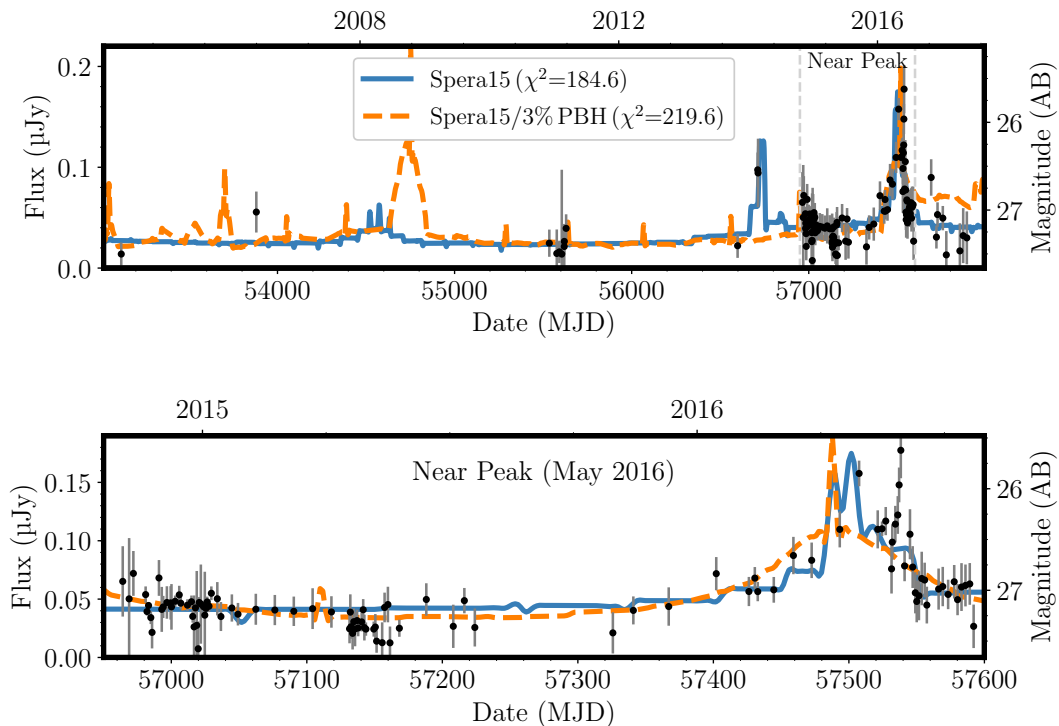


Figure 5.7: The observed fluxes of Icarus from 2004 to 2017 are shown in black circles measured through all wideband HST filters converted to the F125W band using the SED. The best-matching light curves, calculated with a microlens population incorporated the stellar evolution and core-collapse physics presented in [237], are also shown. The blue solid line represents the case without PBHs, while the orange solid line corresponds to a scenario where PBHs make up 3% of the total dark matter abundance. The upper panel shows the full light curve and the lower panel shows the most densely sampled part of the light curve including the peak magnification in May 2016. The peak magnification lasts for approximately 10 days. This figure is taken from [44].

[236]. Therefore, the transverse peculiar velocity can be estimated as  $v_{\text{pec}} = v_{3\text{D}} \cos \alpha$ . To account for the uncertainty in the peculiar velocity, we assume that its (transverse) probability distribution follows a log-normal distribution, which is marginalized over in Sec. 5.5.4. The light curve of Icarus indicates a source crossing time of less than 10 days as shown in Fig. 5.7, providing an upper bound on the radius of the source. The maximum radius can be expressed as

$$R_{\text{max}} \simeq 260 \left( \frac{v_{\text{pec}}}{500 \text{ km/s}} \right) R_{\odot}. \quad (5.41)$$

If the size of Icarus exceeds the maximum radius derived above, the duration of the peak magnification would be longer, contradicting the observed results.

### Star population in the arc

The width of the arc, which corresponds to the arm of the spiral galaxy that hosts Icarus, perpendicular to the macro-critical curve is  $w_{\text{arc}} = 0.2 \text{ arcsec}$ . The apparent magnitude of the arc in the F125W band is  $25 \text{ mag/arcsec}^2$ , corresponding to a luminosity density of  $6.5 \times 10^9 L_{\odot}/\text{arcsec}^2$ . This luminosity density can be converted into the number density

of source stars that are magnified. Assuming the stellar luminosity function follows a power-law distribution,  $dn_{\text{source}}/dL \propto L^{-2}$ , the number density of source stars can be determined from the luminosity density as

$$\frac{dn_{\text{source}}}{d(L/L_{\odot})} = \frac{6.5 \times 10^9 \text{ arcsec}^{-2}}{\mu_{\text{av}} \ln(L_{\text{max}}/L_{\text{min}})} \left( \frac{L}{L_{\odot}} \right)^{-2}, \quad (5.42)$$

with  $L_{\text{min}}$  and  $L_{\text{max}}$  being the minimum and maximum of the luminosity, respectively. By applying Eq. (5.34) with  $T = 12000$  K, the number density of source stars can be expressed as a function of radius as

$$\frac{dn_{\text{source}}}{d(R/R_{\odot})} = \frac{2n_0}{\mu_{\text{av}}} \left( \frac{R}{R_{\odot}} \right)^{-3}, \quad (5.43)$$

with  $n_0 = 1.9 \times 10^7 \text{ arcsec}^{-2}$  assuming  $L_{\text{min}} = 0.1 L_{\odot}$  and  $L_{\text{max}} = 10^7 L_{\odot}$ . The maximum luminosity can be used to estimate the maximum radius of the source, giving  $R_{\text{max}} = 730 R_{\odot}$ . Note that the assumption of  $T = 12000$  K for detectable individual stars reflects our focus on relatively rare blue supergiants. While red supergiants have approximately the same absolute magnitude as can be inferred from the Hertzsprung-Russell (HR) diagram and are expected to be more abundant, their larger source size due to lower temperature limits the maximum magnification, making them unobservable. Since the star formation is active in the spiral galaxies [238], a sufficient number of such blue supergiants is expected to be present.

### 5.5.2 Location of highly magnified events

In Sec. 5.4, we derive the total probability density function (PDF) at each point. In this section, we provide predictions for the locations of images where the magnification exceeds a given threshold  $\mu_{\text{obsth}}$ . As mentioned before, we ignore the correlation between the source size and the intrinsic luminosity of the source star, and the threshold in apparent magnitude in this section, which are included in Sec. 5.5.3 to calculate the number of Icarus-like events.

The probability that a source exceeds a given magnification threshold can be determined as follows. We first calculate the average magnification and the total PDF at each location from the macro-critical curve. Then, by integrating the PDF above the threshold  $r_{\text{th}} = \mu_{\text{obsth}}/\mu_{\text{av}}$ , we can obtain the probability  $P(r > r_{\text{th}})$  at each point. In Fig. 5.8, we present the probability of the magnification exceeding the thresholds  $\mu_{\text{obsth}} = 1000, 3000, 9000,$  and  $27000$ , as a function of the distance from the macro-critical curve, assuming model parameters for the Icarus-like system. For moderate magnification thresholds of 1000 and 3000, the probability increases as closer to the macro-critical curve since the average magnification becomes larger. Near the macro-critical curve, the probability approaches unity because the average magnification is large enough relative to the threshold. For higher thresholds, 9000 and 27000, there are local minima in the probability between 0.0 and 0.1 arcsec. Furthermore, we observe that the position where the probability reaches its maximum is not exactly on the macro-critical curve, but around  $\theta \simeq 0.05$  arcsec in the case of  $\mu_{\text{obsth}} = 27000$ .

To better understand this behavior, we break down the total PDF into two contributions: one from the middle PDF, and the other from the high-magnification tail of the PDF, as illustrated in Fig. 5.9. Regarding the middle PDF, which is around the

average magnification, the probability approaches unity when the average magnification exceeds the threshold, i.e.,  $\mu_{\text{av}} \gtrsim \mu_{\text{obsth}}$ . For the high-magnification tail, we observe a turnover near the macro-critical curve. Below this region, the probability is suppressed exponentially, which occurs in the nonlinear regime where  $\mu_{\text{av}} \gtrsim 1/(f_{\star}\kappa_{\text{tot}})$ . In contrast, in the linear regime, the probability increases as the distance to the macro-critical curve becomes closer due to the increase in the average magnification. This turnover behavior is consistent with the results shown in Fig. 5.8 for high values of  $\mu_{\text{obsth}}$ . The overall behavior of the contribution from the high-magnification tail of the PDF can be explained using Eq. (5.16). When we neglect the source size and approximate the relation between the average magnification and the distance as  $\mu_{\text{av}} \propto \theta^{-1}$ , the integrated probability follows

$$\begin{aligned} P(\mu > \mu_{\text{obsth}}) &\propto \mu_{\text{av}}^{\frac{5}{2}} \exp(-B_0 f_{\star} \kappa_{\text{tot}} \mu_{\text{av}}) \\ &\propto \theta^{-\frac{5}{2}} \exp(-B_0 f_{\star} \kappa_{\text{tot}} \mu_{\text{h}} \mu_{\text{r}} \theta^{-1}), \end{aligned} \quad (5.44)$$

from which the linear and nonlinear behavior can be understood. Another important feature in Fig. 5.8 is how varying magnification thresholds influence the overall normalization of the probability. This behavior can be easily understood from the relation  $P(\mu > \mu_{\text{obsth}}) \propto r_{\text{th}}^{-2} \propto \mu_{\text{obsth}}^{-2}$ .

The location of the observed Icarus is indicated by a vertical dashed line in Fig. 5.8. We observe that this position has a sufficiently high probability of being detected, though it is not the maximum. Note that a more detailed prediction for the observed position of Icarus-like events is provided in Sec. 5.5.3. Additionally, Earendel, whose magnification is expected to be more than a thousand, is observed precisely on a macro-critical curve, consistent with expectations including the middle PDF.

It is important to note that [239] develop a model for the probability distribution of the observed locations. In their model, within the corrugated region of the micro-critical curves near the macro-critical curve, the probability distribution is considered constant, with a decrease proportional to  $\theta^{-2}$  outside this region. Furthermore, their model alters the overall probability but maintains the same functional form across different magnification thresholds. These aspects differ slightly from our approach described above. As a result, by applying our new analytic model and repeating the analysis presented in [239], we anticipate being able to derive more robust constraints on the abundance of PBHs based on the observed positions of highly magnified stars. We leave this analysis for future work.

### 5.5.3 The number of Icarus-like events

Based on the analytic model presented in Sec. 5.2 and the properties of the Icarus system shown in Sec. 5.5.1, we estimate the number of highly magnified individual stars and predict their observed locations. While Sec. 5.5.2 focuses on the probability of exceeding the magnification threshold, we additionally account for the relation between the source size and luminosity. The number of high-magnification events is determined by evaluating whether the apparent magnitude surpasses a given threshold. The expected number of such events in a single snapshot is then calculated as

$$\begin{aligned} N &= 2 \int_{\theta_{\text{min}}}^{\theta_{\text{max}}} d\theta n_{\text{source}} w_{\text{arc}} \int_{\mu_{\text{obsth}}(R)}^{\infty} \frac{dP}{d \log_{10} \mu} \Big|_{\text{high}} d \log_{10} \mu \\ &= 2 \int_{\theta_{\text{min}}}^{\theta_{\text{max}}} d\theta \frac{2n_0 w_{\text{arc}}}{\mu_{\text{av}}(\theta)} \int_{R_{\text{min}}}^{R_{\text{max}}} dR \frac{R_{\odot}^2}{R^3} \int_{\mu_{\text{obsth}}(R)}^{\infty} \frac{dP}{d \log_{10} \mu} \Big|_{\text{high}} d \log_{10} \mu, \end{aligned} \quad (5.45)$$

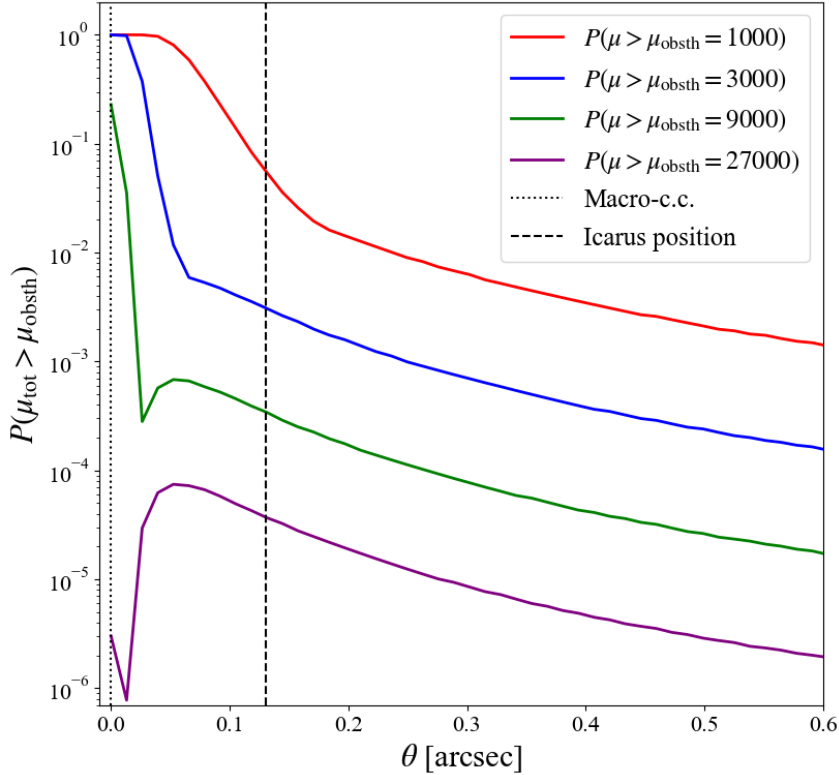


Figure 5.8: The probability of the total magnification exceeding the observational threshold  $\mu_{\text{obsth}}$  as a function of the distance from the macro-critical curve in the Icarus-like system. The red, blue, green, and purple lines indicate the cases with different magnification thresholds  $\mu_{\text{obsth}} = 1000, 3000, 9000,$  and  $27000$ , respectively. The vertical dotted line shows the position of the macro-critical curve. The vertical black dashed line represents the observed location of the Icarus. This figure is taken from [48].

where the factor of two reflects that images form on both sides of the macro-critical curve. In the second equality, we employ Eq. (5.43). It is important to note that Icarus, with a peak magnification duration of less than two weeks, is likely caused by the high-magnification tail. If this were not the case, the peak magnification would have lasted longer, similar to what was observed for Earendel. Consequently, the number of events is calculated based on the high-magnification tail of the PDF. The observation region is defined between  $\theta_{\text{min}} = 0.0$  arcsec and  $\theta_{\text{max}} = 1.3$  arcsec. The maximum source radius is determined as the smaller of the values given by Eq. (5.41) and  $730 R_{\odot}$ . The number of events, as expressed in Eq. (5.45), depends on three parameters: the peculiar velocity (or equivalently, the maximum source radius), the mass fraction of microlenses, and the microlens mass. Note again that all microlenses are assumed to have the same mass. Although the average magnification in Eq. (5.30) might exhibit a slight dependence on the microlens mass and mass fraction, we adopt the numerical results based on our fiducial parameters,  $f_{\star} = 6 \times 10^{-3}$  and  $M_{\star} = 0.3 M_{\odot}$ , as the parameter dependence has been verified to be minimal.

Figure 5.10 shows the predicted number of highly magnified stars as a function of the distance from the macro-critical curve with different assumed peculiar velocities of the MACS J1149 cluster. The fiducial parameters are selected to represent those of ICL stars [136]. As closer to the macro-critical curve, the expected number of events increases due

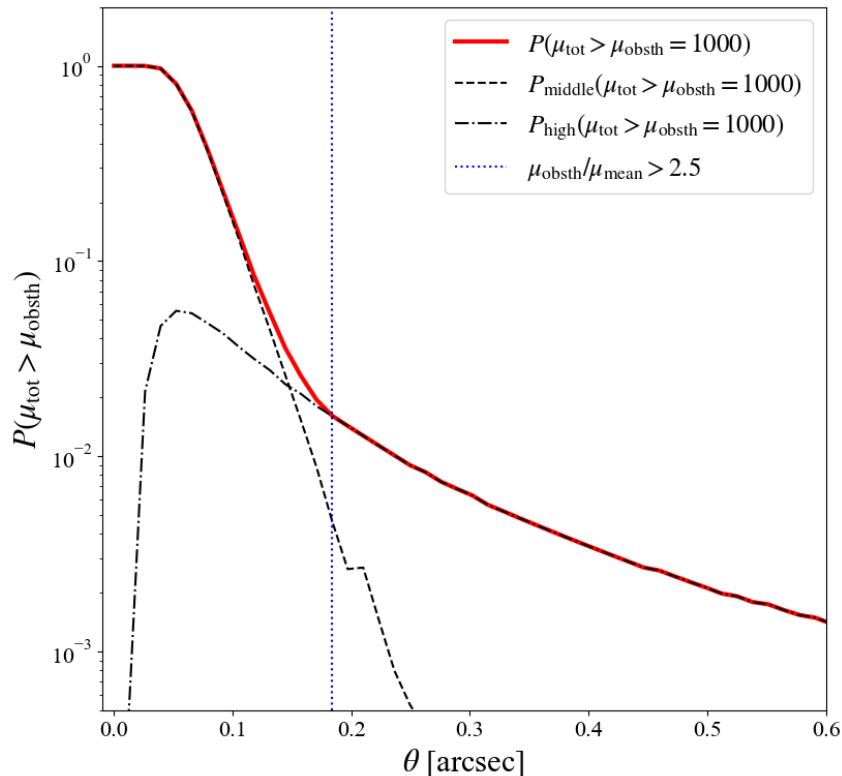


Figure 5.9: The probability of the total magnification exceeding the observational threshold  $\mu_{\text{obsth}} = 1000$ . Dashed and dash-dot lines represent contributions from the middle PDF and the high-magnification tail of the PDF, respectively. The vertical blue dotted line indicates the approximate position of the transition between them. This figure is taken from [48].

to the larger average magnification. However, at the center of the macro-critical curve, the number of events decreases since the system enters the nonlinear regime,  $f_{\star} \kappa_{\text{tot}} \mu_{\text{av}} \gtrsim 1$ . With the fiducial parameters that correspond to ICL stars, we find that the highest probability of detecting highly magnified stars aligns with the observed location of Icarus. A higher peculiar velocity results in a larger maximum source radius, thereby increasing the expected number of events. Figure 5.11 shows the case for different mass fractions of microlenses. When the mass fraction of microlenses increases, the turnover point moves farther from the macro-critical curve, as depicted by the green solid line. Conversely, if the mass fraction is sufficiently small, the nonlinear regime disappears and the turnover vanishes, as indicated by the red solid line. Figure 5.12 shows the case for different microlens masses. Since the minimum source radius,  $R_{\text{min}}$ , depends on the microlens mass as described by Eq. (5.39), a smaller microlens mass reduces the integration range, leading to a smaller expected number of events. This can also be understood as follows. For smaller microlens masses, the maximum magnification decreases due to the reduced size of the micro-critical curve relative to the source size. Consequently, only larger sources with higher absolute magnitudes have the possibility to be observed, and the suppression of the high-magnification tail of the PDF is further enhanced, leading to the suppressed number of events. When the microlens mass increases sufficiently, the expected number of events tends to stabilize. This convergence can be understood based on the following two points. First, the high-magnification tail of the PDF is largely independent of the microlens

mass, aside from the suppression due to the maximum magnification. Since the number density of microlenses scales as  $n_* \propto M_*^{-1}$  and the PDF scales as  $dP/d\log_{10}\mu \propto n_*\theta_{\text{Ein}}^2$ , the effect of microlens mass on the high-magnification tail is relatively modest. Second, sources with sufficiently small radii do not contribute significantly to high-magnification events. Since luminosity scales as  $L \propto R^2$  and the maximum magnification as  $\mu_{\text{max}} \propto \theta_{\text{Ein}}^{1/2}R^{-1/2} \propto M_*^{1/4}R^{-1/2}$ , we obtain  $L\mu_{\text{max}} \propto M_*^{1/4}R^{3/2}$ , indicating that larger sources tend to have higher magnitudes. Although smaller sources are more numerous, with  $dn_{\text{source}}/dR \propto R^{-3}$ , they do not significantly contribute to such events. Therefore, while increasing the microlens mass lowers the minimum source radius, thus extending the integration range, the expected number of events does not change much. Note that the dashed lines in Fig. 5.10 to Fig. 5.12 represent the results derived using the total PDF. Near the center, where the average magnification exceeds the observational threshold, the log-normal distribution dominates, resulting in a higher expected number of events. As stated before, since Icarus exhibits a short period of peak magnification, the event is likely associated with the high-magnification tail. Consequently, we focus on the high-magnification tail and disregard the log-normal contribution in the following analysis.

By integrating the expected number of events shown in Fig. 5.10 to Fig. 5.12 over the distance from the macro-critical curve, the expected total number of observed high-magnification events can be determined. Since Icarus is the only event with a peak magnification lasting approximately two weeks during the HST two-year observation, we estimate 52 independent snapshots. Therefore, we multiply 52 by the prediction from Eq. (5.45) for comparison with observational results.

Given that Icarus represents a single event observed over two years, the mean number of Icarus-like events,  $\bar{N}$ , can be constrained. Assuming a Poisson distribution,

$$P(N) = \frac{\bar{N}^N}{N!}e^{-\bar{N}}, \quad (5.46)$$

the probability of observing at least one event is given by  $1 - e^{-\bar{N}}$ . Thus, the mean number of events consistent with the observation is constrained to  $\bar{N} \geq 0.051$  at the 95% CI.

By comparing the analytically estimated number of events with the observed mean number of Icarus-like events, we can constrain the microlens parameter space. Figure 5.13 presents the 95% CI constraints on the mass and mass fraction of microlenses for various peculiar velocities of the galaxy cluster, assuming a single microlens population with uniform mass. A lower peculiar velocity reduces the expected number of events, leading to tighter constraints. The results are consistent with the properties of ICL stars, suggesting that the ICL stars alone can account for the observation of Icarus. For a fixed microlens mass, the number of events is reduced when the microlens mass fraction is either very small or very large. In the former case, the suppression occurs due to the absence of microlenses in the linear regime, where the PDF scales with the microlens number density. In the latter case, the suppression arises from the exponential damping of the PDF in the nonlinear regime. At a fixed mass fraction, the predicted number of events grows with increasing microlens mass and eventually saturates at sufficiently high masses, leaving the upper bound on the microlens mass unconstrained.

Note that [136] also explores the microlens parameter space using event rates (see Fig. 3 in their paper). However, there are two key differences between their approach and ours. First, the influence of microlens mass on the probability of high magnification is treated differently. In our analytic model, the dependence on microlens mass is negligible, whereas their model scales as  $M_*^{-1/2}$ . This leads to their framework predicting higher event

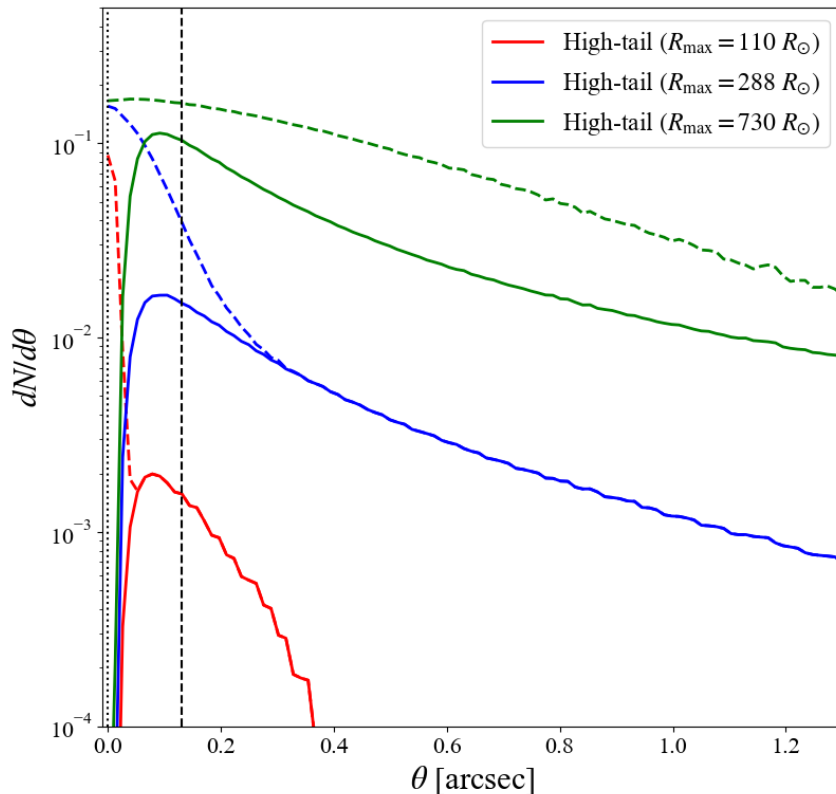


Figure 5.10: The expected number of the observed Icarus-like ultrahigh magnification events as a function of distance from the macro-critical curve for different maximum source radii, reflecting the different peculiar velocities of the cluster. The fiducial parameters are  $R_{\max} = 288 R_{\odot}$ ,  $f_{\star} = 6 \times 10^{-3}$ , and  $M_{\star} = 0.3 M_{\odot}$ , represented by the blue lines. Solid lines correspond to calculations using the high-magnification tail of the PDF, and dashed lines correspond to those using the total PDF. The vertical black dotted and dashed lines show the position of the macro-critical curve and the location of Icarus, respectively. This figure is adapted from [50].

rates for lower microlens masses. Second, their method does not account for the relation between the source radius and the magnification threshold. As previously noted, smaller microlenses require a larger source radius to achieve the observed apparent magnitude, which subsequently reduces the number of predicted events. These distinctions result in different constraints: our analysis does not set an upper limit on larger microlens masses, while their constraints are unable to limit smaller microlens masses. As a result, we expect our constraints to be more precise.

#### 5.5.4 Constraint on the PBH

PBHs are a potential alternative to the standard CDM model, and they would also be microlenses alongside the ICL stars. In this section, we use the observed number of events to constrain the PBH parameter space while accounting for the uncertainty in the peculiar velocity of the galaxy cluster. Here,  $M_{\text{PBH}}$  represents the mass of PBHs, and  $f_{\text{PBH}}$  denotes the mass fraction of PBHs relative to the total dark matter.

The analytic model for the high-magnification tail of the PDF assumes that all microlenses have identical masses, restricting our constraints on the PBHs to the mass range

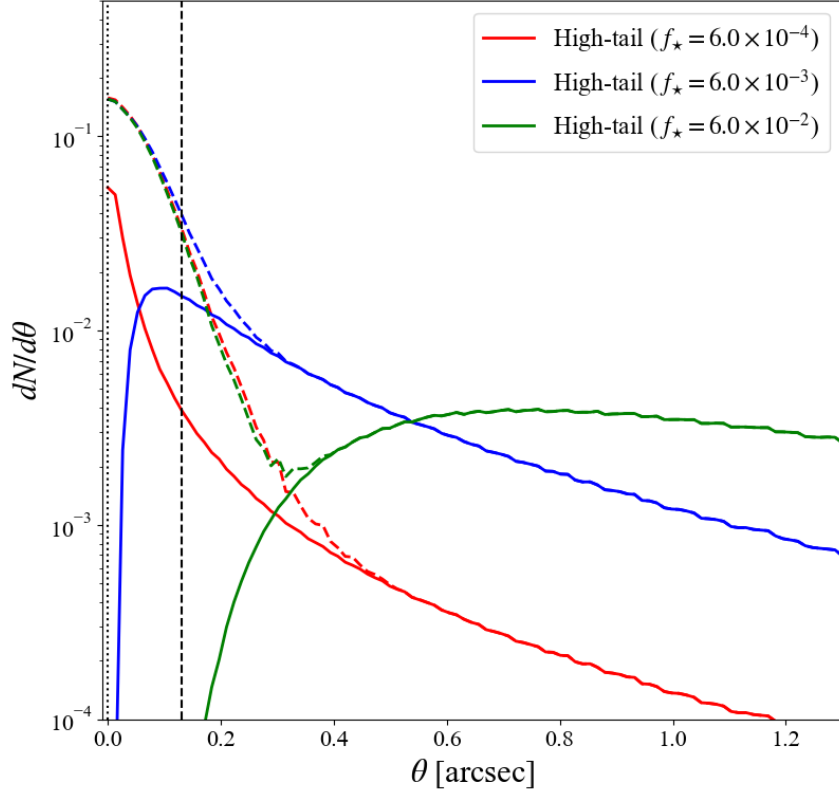


Figure 5.11: Similar to Fig. 5.10, but for different mass fractions of microlenses. This figure is adapted from [50].

of ICL stars,  $0.1 \lesssim M_{\text{PBH}}/M_{\odot} \lesssim 10$ . Additionally, considering the presence of the ICL stars, meaningful constraints can only be obtained for  $f_{\text{PBH}} \gtrsim f_{\text{ICL}} \simeq 0.01$ . This is because the suppression of the PDF in the nonlinear regime at high  $f_{\text{PBH}}$  is unaffected by the inclusion of ICL stars. To account for the uncertainty in peculiar velocity, we adopt a log-normal distribution, as detailed in Sec. 5.5.1. Figure 5.14 shows our constraints on the PBH parameters alongside existing ones from the literature. Our analysis constrains the PBH mass fraction to  $f_{\text{PBH}} \gtrsim 0.2$  for the PBH masses between  $0.1 M_{\odot}$  and  $10 M_{\odot}$  at the 95% CI. While these constraints are less stringent than those from earlier studies, they are consistent with existing results.

Note that [136] also provide constraints on the PBH parameter space in the presence of ICL stars. They focus on peak magnifications rather than the number of events, which differs from ours. However, for microlens masses in the range  $0.1 M_{\odot}$  and  $10 M_{\odot}$ , our findings are broadly consistent with theirs. An additional distinction is that our analysis incorporates the uncertainty in peculiar velocity, whereas [136] assumes a fixed peculiar velocity of  $v_{\text{pec}} = 500$  km/s.

## 5.6 Summary and discussions

Recently, highly magnified stars such as Icarus and Earendel have been detected within the galaxy cluster. To understand such observations and predict similar occurrences in future observations, it is essential to examine how the high-magnification tail of the PDF is influenced by parameters such as the microlens mass fraction  $f_{\star}$  and the average

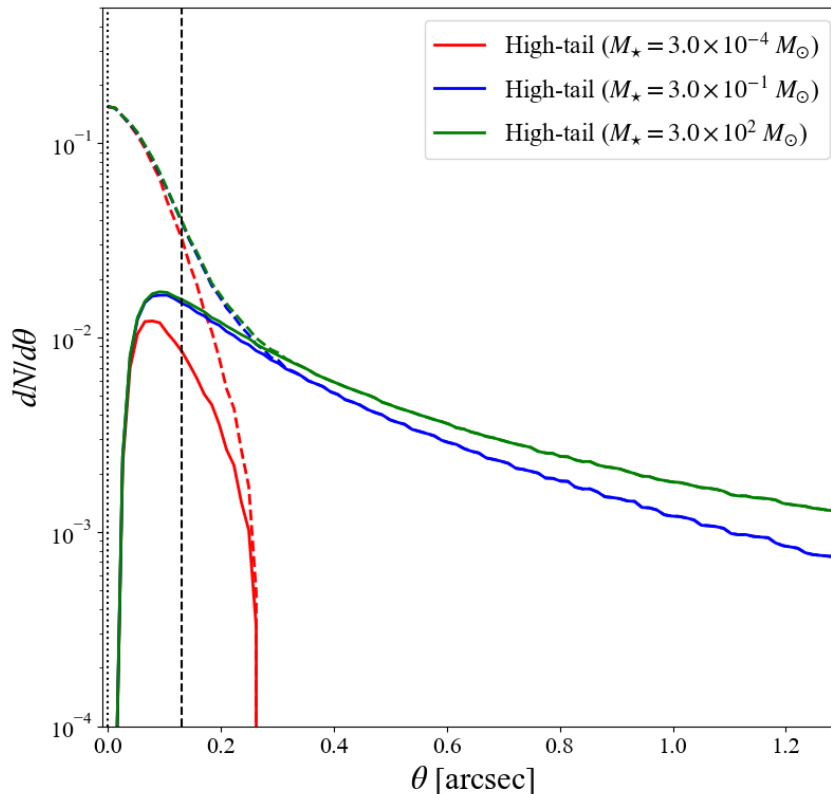


Figure 5.12: Similar to Fig. 5.10, but for different microlens masses. This figure is adapted from [50].

magnification  $\mu_{\text{av}}$ . To achieve this goal, we develop an analytic model for the high-magnification tail, using ray-tracing simulations of CCTRAIN and GERLUMPH.

Our analytical model assumes that the PDF is proportional to the number of "independent" microlenses, whose inter-microlens distance to the nearest neighbor is larger than the size of the micro-critical curve. We start by analyzing the case of a point source, where there is no maximum magnification, and show that the parameter dependencies of the PDF can be encapsulated in the parameter combination of  $X = f_{\star} \kappa_{\text{tot}} \mu_{\text{av}}$ . In the linear regime, where  $X \lesssim 1$ , the number of independent micro-critical curves approximately matches the number of microlenses, causing the integrated probability to scale linearly with  $X$ . Conversely, in the nonlinear regime, where  $X \gtrsim 1$ , micro-critical curves merge, reducing the number of independent microlenses exponentially and suppressing the probability exponentially. The validity of the model for a point source is confirmed using CCTRAIN simulation data. Next, we extend the analysis to the case with finite-sized sources. Due to the averaging effect across the source size, a maximum magnification exists, leading to the suppression of the high-magnification tail of the PDF above the maximum magnification. To account for this, we define a suppression factor,  $S(r; r_{\text{max}})$ , and find that a sigmoid function effectively captures the suppression, as verified with simulation data from GERLUMPH, where we treat the source plane resolution in GERLUMPH as an effective source size. Combining these findings, we obtain the analytic model for the high-magnification tail of the PDF described in Eq. (5.24), with Eqs. (5.16) and (5.21).

Two parameter degeneracies regarding the high-magnification tail of the PDF can be inferred from our model. The first involves the parameter combination  $f_{\star} \kappa_{\text{tot}} \mu_{\text{av}}$ , which plays an important role in understanding the high-magnification tail. This degeneracy

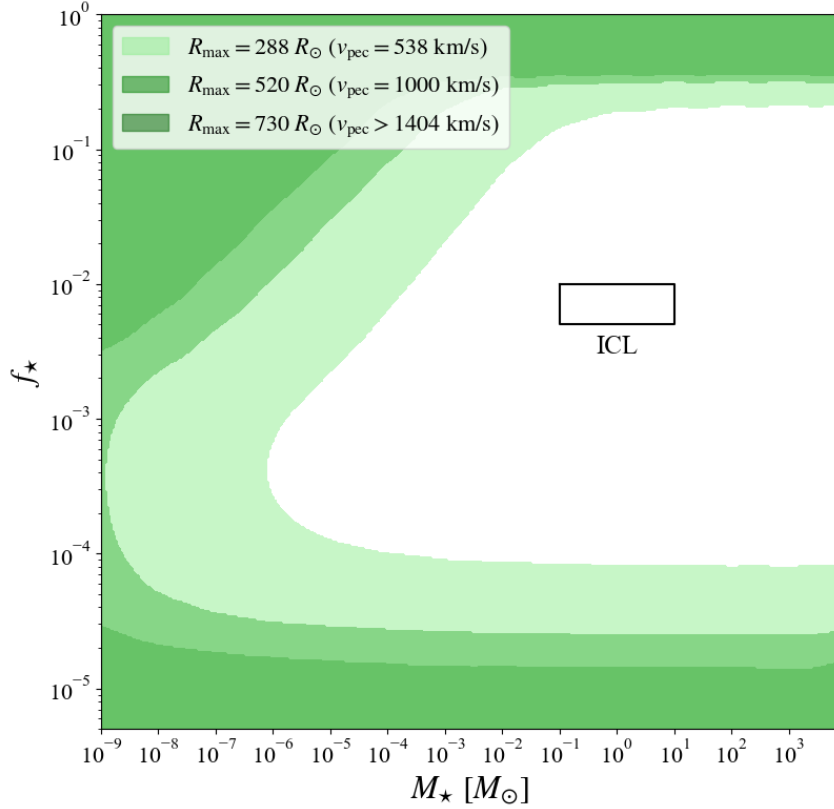


Figure 5.13: Constraints on the microlens parameters derived from the observed number of high-magnification events during the two-year HST observation period, assuming a single microlens component with a monochromatic mass function. The shaded regions indicate the excluded parameter spaces at the 95% CI. The three contours represent cases where different maximum source radii are applied, which corresponds to varying the peculiar velocities of the galaxy cluster. The parameter space of the ICL stars is shown in the black rectangular. This figure is taken from [50].

implies that uncertainties in the smooth lens mass distribution influence the estimation of the mass fraction of microlenses. It may be alleviated through precise mass modeling, leveraging many strong lensed images. The second degeneracy arises in the maximum magnification  $r_{\max}$ . The combination  $\theta_{\text{Ein}}/(\sqrt{\mu_{\text{av}}}\sigma_{\text{W}})$  indicates that the microlens mass is degenerate with the source size.

One simplified assumption in our model is that all microlenses have the same mass. In reality, the mass function of ICL stars and stellar black holes is shaped by factors such as the initial mass function, stellar evolution, and core-collapse physics, resulting in a diverse range of microlens masses [240, 241, 237]. Additionally, PBHs, which are potential alternatives to CDM and contribute to microlensing effects, are also expected to have a broad mass spectrum [123, 242] as reviewed in Sec. 2.3.2. Although our model does not account for the scenarios with multiple microlens masses, we expect that the PDF remains unaffected significantly in the linear regime. This is because the total area of each magnification bin remains constant, as evident from the following relations. The Einstein radius is proportional to the square root of the microlens mass,  $\theta_{\text{Ein}} \propto M_{\star}^{1/2}$ , while the number density of microlenses scales inversely with mass,  $n_{\star} \propto M_{\star}^{-1}$ . Consequently, the total area, which scales with  $n_{\star}\theta_{\text{Ein}}^2$ , does not change. In the nonlinear

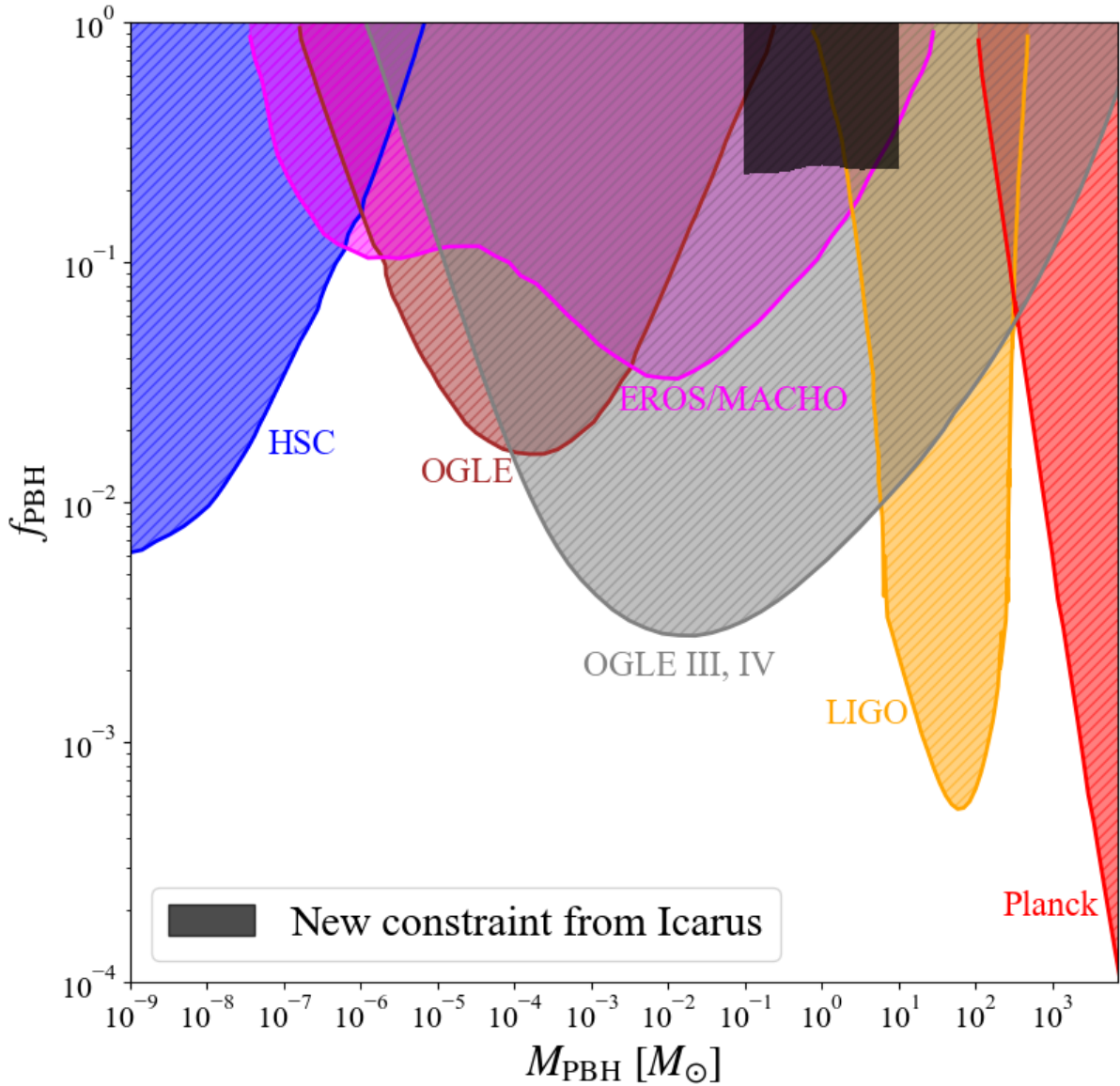


Figure 5.14: Constraints on the PBH parameters derived from the observed number of high-magnification events in the Icarus-like system during the two-year HST observation period, shown in black shaded region. The contribution of ICL stars is taken into account to obtain the constraint. The other constraints are obtained by HSC [134] (blue), OGLE [139] (brown), OGLE III, IV [140] (gray), LIGO [150] (yellow), EROS/MACHO [137, 138] (magenta), and Planck [149] (red). All the constraints are shown at the 95% CI. This figure is taken from [50].

regime, however, the impact of a mass spectrum could introduce complex modifications to the PDF. For instance, if the microlens population follows a power-law distribution and there are many low-mass objects, we expect that the high-magnification tail of the PDF would be suppressed. This is because the number of independent micro-critical curves from relatively large microlens masses would be suppressed by the presence of numerous smaller micro-critical curves around them. Conversely, some of the numerous smaller micro-critical curves would be independent, potentially amplifying the PDF in certain magnifications. As the typical magnification depends on the size of the micro-critical curves as shown in Eq. (4.130), the amplification of the PDF would occur only in the middle region of the high-magnification tail, while the very high-magnification tail would be suppressed as stated above. Extending our analytic model to incorporate a mass spectrum remains a subject for future research.

Another simplified assumption in our model is that microlenses are randomly and uniformly distributed in the lens plane. The spatial scale required for this assumption to remain valid and for the model to be accurate is several times larger than the size of a typical micro-critical curve. However, some microlenses may form binary systems, which introduces deviations from uniformity on scales smaller than the size of micro-critical curves. This non-uniformity could change the number of independent micro-critical curves. Moreover, the size and shape of the micro-critical curves are largely influenced by their masses and relative separations of binary systems, potentially leading to deviations in the PDF from our model predictions. We expect that the impact of microlens spatial distribution on the magnification PDF is likely more pronounced in the linear regime than in the nonlinear regime, where such clustering effects might play a less significant role.

For the application of our model, we focus on the Icarus system. Specifically, we first calculate the spatial probability distribution of highly magnified images exceeding a given magnification threshold. To do this, we also model the PDF near the average magnification in addition to the high-magnification tail, which we approximate using a log-normal distribution. For each location in the vicinity of the macro-critical curve (caustic), we compute the average magnification and determine the probability of exceeding the observational threshold. Closer to the macro-critical curve, the probability generally increases due to the increase in average magnification. However, if the magnification threshold is set to a value that exceeds the maximum average magnification (achieved on the critical curve), the behavior becomes non-trivial due to the contribution of nonlinear regime of the high magnification tail. Next, we calculate the expected number of Icarus-like events. In this calculation, we incorporate the relation between the source radius and luminosity, considering the constraints on the source radius derived from the peak magnification, source crossing time, and the luminosity of the arc. We use the high-magnification tail of the PDF to calculate the event number, as Icarus is expected to be an event in the high-magnification tail, given that its peak magnification lasts less than two weeks. Assuming all microlenses have the same mass, we identify the parameter space consistent with observations, specifically a single event with peak magnification lasting less than two weeks during the two-year HST monitoring period. We find that the parameter space where the number of events aligns with observations is consistent with the properties of ICL stars. Furthermore, we impose constraints on the parameter space for PBHs, demonstrating that a PBH mass fraction  $f_{\text{PBH}} \gtrsim 0.2$  for PBH masses ranging from  $0.1 M_{\odot}$  and  $10 M_{\odot}$  is excluded at the 95% CI, due to the exponential suppression of the event number in the nonlinear regime. This result is consistent with previous studies.

Uncertainties in the source temperature and the peculiar velocity of the MACS J1149 cluster affect our constraints on the parameter space for microlenses and PBHs. The temperature of Icarus is assumed to be  $T \simeq 12000$  K, but it has an uncertainty within the range 11000 K to 14000 K [235]. This variation affects the inferred blackbody luminosity, which directly impacts both the absolute and apparent magnitudes. These magnitudes are critical in determining the minimum source radius  $R_{\min}$  and the magnification threshold  $\mu_{\text{obsth}}$ . A lower temperature increases  $R_{\min}$  and  $\mu_{\text{obsth}}$ , reducing the integration range and, consequently, the expected number of highly magnified events. As a result, the parameter space consistent with the observed number of events becomes narrower. Moreover, the assumption of a uniform temperature for other source stars might not be entirely accurate. Refining this assumption could alter the estimated event rates, potentially modifying the constraints on the parameter space. As illustrated in Fig. 5.13, variations in the peculiar velocity have a large impact on the excluded parameter space. More accurate measurements of the peculiar velocity, especially if they align closely with the mean velocity, would tighten the constraints and potentially expand the excluded parameter space.

While this study focuses solely on the single Icarus event, the number of observed highly magnified stars is rapidly growing (e.g., [217]). Future analyses incorporating additional ultrahigh magnification events are expected to provide much tighter constraints. For instance, in the Icarus system, if two (three) events were observed instead of a single event, the excluded parameter space for PBHs would expand, ruling out  $f_{\text{PBH}} \gtrsim 0.08$  (0.01) at the 95% CI. This demonstrates that increasing the number of observed events could significantly expand the excluded parameter space, emphasizing the importance of further investigations.

While analyzing the number of highly magnified events is an effective approach for constraining the parameter space of microlenses and PBHs, the current PBH constraints are limited to the mass range of ICL stars. This limitation arises because the analytic model for the high-magnification tail assumes a single microlens mass. To extend the constraints on PBHs across a broader mass range, it is crucial to investigate the high-magnification tail of the PDF under a bimodal mass function for microlenses. Such studies are expected to refine the parameter space for a wider variety of microlens masses, offering insights into stellar evolution history and the fundamental nature of dark matter.

# Chapter 6

## Perturbation of macro-critical curves by substructures

### 6.1 Introduction

In the previous chapter, we examine how the distribution of microlenses affects strong lensing signals, specifically the event number of high-magnification events. In this chapter, we focus on more massive substructures such as subhalos. Strong gravitational lensing is also a powerful tool for studying substructures, where their mass distribution and abundance are influenced by the nature of dark matter. For example, substructures within lensing objects cause flux anomalies ratios of the strong gravitational lens images [243, 244, 245, 246, 247, 248, 249, 250, 251, 252]. In [252], seven gravitational lensing events involving radio quasars are analyzed, yielding a mass fraction of substructures relative to the total mass of  $f_{\text{sub}} = 0.012^{+0.007}_{-0.004}$ . This result agrees with predictions from cold dark matter (CDM) hydrodynamical simulations within  $1\sigma$ . The study also explored the thermal warm dark matter (WDM) model, where small-scale substructures are suppressed, deriving a lower limit for the WDM mass of  $m_{\text{WDM}} > 5.58 \text{ keV}/c^2$  at the 95% confidence interval (CI). Other dark matter models such as self-interacting dark matter (SIDM) and fuzzy dark matter (FDM) also affect the flux ratios in quadruple imaged quasars [114, 168]. Another example is that substructures distort the surface brightness patterns of lensed galaxies [253, 254, 255, 256, 257]. This phenomenon also provides direct evidence of the substructures.

A new method for searching substructures within galaxy clusters is proposed by [218], where they focus on the astrometric perturbations of the macro-critical curves due to substructures. In the absence of substructures, the smooth mass distribution forms a smooth macro-critical curve, with images observed on both sides symmetrically. The presence of substructures, however, can introduce localized distortions along these macro-critical curves, disrupting the expected symmetry of lensing events. Since the highly magnified individual stars have been observed [44, 216] as discussed in Chap. 5, the detailed shape of the macro-critical curve can be determined. Fluctuations caused by CDM subhalos with masses ranging from  $10^6 M_{\odot}$  and  $10^8 M_{\odot}$  are expected to perturb the macro-critical curve by  $\mathcal{O}(10)$  milli-arcseconds [218]. Such perturbations could be detectable through the James Webb Space Telescope (JWST) in near-infrared bands, requiring integration times of approximately ten hours (see also [219]).

It has been recently reported that a high-magnified huge star, likely a binary system of two supergiant stars, called Mothra, is observed near the macro-critical curve of the

galaxy cluster MACS0416 [45]. Unlike nearby sources, which are observed on both sides of the macro-critical curve, the counterimage of Mothra has not yet been detected. Several scenarios have been proposed to explain the absence of the counterimage, including time delays, the influence of foreground objects, and local microlensing or millilensing. They conclude that the Mothra event is likely attributed to millilensing caused by substructures with masses ranging from  $10^4 M_\odot$  and  $2.5 \times 10^6 M_\odot$ , given that the peak magnification persists for at least eight years. However, there is another possibility that they do not consider in their analysis: the perturbation of the macro-critical curve due to substructures.

In this chapter, we derive a general formula that relates fluctuations in macro-critical curves to fluctuations in the surface density caused by substructures. This formula allows us to analytically estimate the amplitude of the fluctuations of macro-critical curves using the surface density power spectrum of the substructures. As a practical application, we utilize our formula to examine whether the positional anomaly observed in Mothra can be attributed to macro-critical curve distortions caused by substructures, such as CDM subhalos, and the granular structures within the FDM halos.

This chapter is structured as follows. In Sec. 6.2, we derive a general formula that relates fluctuations in macro-critical curves to surface density fluctuations caused by substructures. In Sec. 6.3, we use this formula to propose an alternative explanation for the observation of Mothra with CDM and FDM models. Finally, the summary and discussions are presented in Sec. 6.4. This chapter is based on our recent work presented in [46].

## 6.2 Fluctuations of macro-critical curves

To study the fluctuation of the macro-critical curve due to substructures, it is convenient to start with the smooth lens potential given in Eq. (4.68),

$$\psi(\boldsymbol{\theta}) = \frac{1}{2} \{ \kappa_0(\theta_1^2 + \theta_2^2) + (1 - \kappa_0)(\theta_1^2 - \theta_2^2) \} - \frac{\epsilon}{6} \theta_1^3, \quad (6.1)$$

where the origins of the lens plane and source plane are placed on the critical curve and caustic, respectively, and an orthogonal configuration is considered, with the micro-image train oriented perpendicular to the macro-critical curve. Again,  $\epsilon$  is defined as  $\epsilon = -\psi_{,111}(\boldsymbol{\theta} = \mathbf{0})$ , and it is inversely proportional to the Einstein radius. The Jacobian matrix is given in Eq (4.72),

$$A(\boldsymbol{\theta}) = \begin{pmatrix} \epsilon\theta_1 & 0 \\ 0 & 2(1 - \kappa_0) \end{pmatrix}, \quad (6.2)$$

from which we can see that the macro-critical curve corresponds to the  $\theta_2$  axis.

Now, let us examine the fluctuations of the macro-critical curve induced by substructures. When considering fluctuations at a point on the original macro-critical curve caused by substructures, i.e.,  $\boldsymbol{\theta} = (0, \theta_2) \rightarrow \tilde{\boldsymbol{\theta}} = (\delta\theta_1, \theta_2 + \delta\theta_2)$ , the Jacobian matrix to linear order is given by

$$A(\tilde{\boldsymbol{\theta}}) \simeq \begin{pmatrix} \epsilon\delta\theta_1 - \delta\kappa - \delta\gamma_1 & -\delta\gamma_2 \\ -\delta\gamma_2 & 2(1 - \kappa_0) - \delta\kappa + \delta\gamma_1 \end{pmatrix}, \quad (6.3)$$

with  $\delta\kappa$ ,  $\delta\gamma_1$ , and  $\delta\gamma_2$  representing the convergence and two shear components due to substructures, respectively. The determinant of the Jacobian matrix is expressed as

$$\begin{aligned}\det A &= (\epsilon\delta\theta_1 - \delta\kappa - \delta\gamma_1)\{2(1 - \kappa_0) - \delta\kappa + \delta\gamma_1\} - \delta\gamma_2^2 \\ &\simeq 2(1 - \kappa_0)(\epsilon\delta\theta_1 - \delta\kappa - \delta\gamma_1),\end{aligned}\quad (6.4)$$

where we ignore the higher-order terms in the second equality. Since the critical curve is defined where the determinant of the Jacobian matrix is equal to zero, the fluctuated macro-critical curve satisfies

$$\delta\theta_1 = \frac{1}{\epsilon}(\delta\kappa + \delta\gamma_1). \quad (6.5)$$

While the original macro-critical curve corresponds to  $\theta_1 = 0$ , fluctuations in the  $\theta_1$  direction can be observed due to the presence of substructures.

Using the relation obtained in Eq. (6.5), we can express the auto two-dimensional power spectrum of  $\delta\theta_1$  as

$$P_{\delta\theta_1} = \frac{1}{\epsilon^2} (P_{\delta\kappa} + 2P_{\delta\kappa\delta\gamma_1} + P_{\delta\gamma_1}). \quad (6.6)$$

Here,  $P_{\delta\kappa}$ , and  $P_{\delta\gamma_1}$  are the auto two-dimensional power spectrum of  $\delta\kappa$  and  $\delta\gamma_1$ , respectively, and the cross-power spectrum between  $\delta\kappa$  and  $\delta\gamma_1$  is denoted by  $P_{\delta\kappa\delta\gamma_1}$ . Note that the cross-power spectrum of  $X$  and  $Y$  is defined as

$$\langle \tilde{X}(\mathbf{K})\tilde{Y}(\mathbf{K}') \rangle = (2\pi)^2 \delta_{\mathbf{D}}^{(2)}(\mathbf{K} + \mathbf{K}') P_{XY}(K), \quad (6.7)$$

where  $\tilde{X}$  and  $\tilde{Y}$  are the Fourier transform of  $X$  and  $Y$ ,  $\mathbf{K}$  is a two-dimensional wavenumber, and  $K = |\mathbf{K}|$ . Equation (6.6) can be expressed in a simpler form. To see this, let us start with Fourier transformation of the relation between the convergence and the lens potential given in Eq. (4.45), and the relations between the shear components and the lens potential given in Eqs. (4.46) and (4.47). We can obtain

$$\tilde{\kappa}(\mathbf{K}) = -\frac{K^2}{2}\tilde{\psi}(\mathbf{K}), \quad (6.8)$$

$$\tilde{\gamma}_1(\mathbf{K}) = -\frac{K_1^2 - K_2^2}{2}\tilde{\psi}(\mathbf{K}) = \cos(2\phi_K)\tilde{\kappa}(\mathbf{K}), \quad (6.9)$$

$$\tilde{\gamma}_2(\mathbf{K}) = -K_1K_2\tilde{\psi}(\mathbf{K}) = \sin(2\phi_K)\tilde{\kappa}(\mathbf{K}), \quad (6.10)$$

where  $\phi_K$  is the polar angle of the wavenumber vector  $\mathbf{K}$  and  $\tilde{\psi}$  denotes the Fourier transform of the lens potential. Therefore, the power spectrum can be expressed as

$$P_{\delta\gamma_1} = \cos^2(2\phi_K)P_{\delta\kappa}, \quad (6.11)$$

$$P_{\delta\kappa\delta\gamma_1} = \cos(2\phi_K)P_{\delta\kappa}. \quad (6.12)$$

By substituting them into Eq. (6.6), we can obtain

$$P_{\delta\theta_1} = \frac{1}{\epsilon^2}(1 + 2\cos(2\phi_K) + \cos^2(2\phi_K))P_{\delta\kappa}. \quad (6.13)$$

Furthermore, by taking the average of  $\phi_K$ , we can finally express the power spectrum of the fluctuation of the macro-critical curve as

$$P_{\delta\theta_1} = \frac{3}{2\epsilon^2}P_{\delta\kappa}. \quad (6.14)$$

Returning from Fourier space to real space, the fluctuation can be represented by

$$\epsilon^2 \langle \delta\theta_1^2 \rangle = \epsilon^2 \int d \log K \frac{K^2}{2\pi} P_{\delta\theta_1}(K) = \frac{3}{2} \int d \log K \frac{K^2}{2\pi} P_{\delta\kappa}(K) = \frac{3}{2} \langle \delta\kappa^2 \rangle. \quad (6.15)$$

Note that the left-hand-side of Eq. (6.15) represents the ratio of the fluctuation to the size of the macro-critical curve,  $\epsilon^2 \langle \delta\theta_1^2 \rangle \simeq \langle \delta\theta_1^2 \rangle / \theta_{\text{Ein}}^2$ . The derivation of the simple formulae in Eqs. (6.14) and (6.15) represents the main result of this chapter. While previous studies have examined the relation between image position fluctuations and surface density perturbations caused by substructures (e.g., [247]), this is the first time to derive the formulae connecting macro-critical curve fluctuations to surface density perturbations. These formulae provide a means to analytically estimate the variance of  $\delta\theta_1$  or the power spectrum  $P_{\delta\theta_1}$  from the power spectrum of surface density perturbations,  $P_{\delta\kappa}$ .

Although Eq. (6.14) is derived under the assumption of a fully orthogonal coordinate system, we argue that it holds rather generically. Near the fold critical curve, the tangential and radial magnifications generally exhibit the behavior  $\mu_t \simeq \mu_{t0} \delta\theta^{-1}$  and  $\mu_r \simeq \text{const.}$  with  $\delta\theta$  denotes the distance from the critical curve, as shown in Sec. 4.5. Considering the tangential magnification is given by  $\mu_t^{-1} = 1 - \kappa - \gamma$  with  $\gamma = \sqrt{\gamma_1^2 + \gamma_2^2}$ , substructures introduce modifications to the tangential magnification as

$$\mu_t^{-1} \simeq \frac{\delta\theta}{\mu_{t0}} - \delta\kappa - \left( \frac{\partial\gamma}{\partial\gamma_1} \right) \delta\gamma_1 - \left( \frac{\partial\gamma}{\partial\gamma_2} \right) \delta\gamma_2 = \frac{\delta\theta}{\mu_{t0}} - \delta\kappa - \frac{\gamma_1}{\gamma} \delta\gamma_1 - \frac{\gamma_2}{\gamma} \delta\gamma_2. \quad (6.16)$$

Again, the perturbed macro-critical curve satisfies the condition  $\mu_t^{-1} = 0$ , we can obtain the power spectrum expressed as

$$P_{\delta\theta} = \mu_{t0}^2 \left\{ P_{\delta\kappa} + \left( \frac{\gamma_1}{\gamma} \right)^2 P_{\delta\gamma_1} + \left( \frac{\gamma_2}{\gamma} \right)^2 P_{\delta\gamma_2} \right\} = \frac{3\mu_{t0}^2}{2} P_{\delta\kappa}, \quad (6.17)$$

which is essentially same as Eq. (6.14) if  $\mu_{t0} = 1/\epsilon$ . Note that we take an average of  $\phi_K$  in the second equality.

To validate the formula in Eq. (6.15), numerical simulations are performed using the open-source code GLAFIC [222]. These simulations are carried out by Doctor Katsuya T. Abe, the first author of [46]. Here, we briefly summarize the key findings, with additional details available in the original publication [46]. In the simulations, CDM subhalos are distributed near the macro-critical curve following a Poisson distribution, with the expected number determined by the subhalo mass function. Critical curves are then calculated for different subhalo populations and various subhalo mass ranges. The resulting fluctuations in the macro-critical curves are compared to the theoretical predictions. We find that the analytic formula is consistent with the numerical results, as long as the substructure power spectrum is not dominated by a small number of massive structures. With these numerical results, we confirm the validity of our analytic formulae.

### 6.3 Application to Mothra

In this section, we utilize our analytic formula given in Eq. (6.15) to investigate whether the position of Mothra, a highly magnified binary star at redshift  $z = 2.091$  observed near the macro-critical curve of the MACS J0416.1-403 cluster at  $z = 0.397$  with the JWST [45], can be explained by the astrometric perturbation of the macro-critical curve.

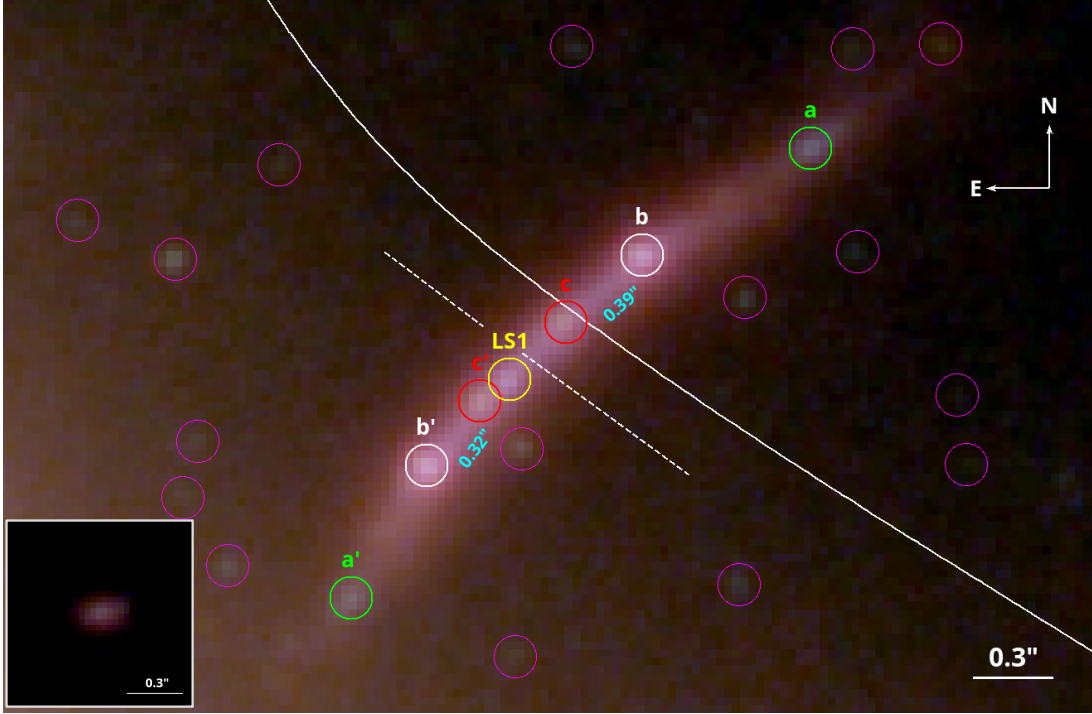


Figure 6.1: Color image of the ultrahigh magnified binary stars Mothra and its surroundings observed by the JWST. The LS1, circled in yellow, is the official name of Mothra. In the Mothra arc, there have been identified three pairs of images denoted by a, b, and c. The dashed white line indicates the local macro-critical curve estimated by these image pairs. The solid white line indicates the estimated macro-critical curve by the mass modeling of the MACS0416 cluster. This figure is taken from [45].

Unlike neighboring sources that appear as pairs on either side of the macro-critical curve, Mothra is observed only on the negative parity side of the macro-critical curve, and its counterimage is missing, as illustrated in Fig. 6.1. This anomaly could be due to a local millilensing effect from substructures that magnify the image only on the negative side [45]. Here, we explore an alternative explanation, attributing the observed location to macro-critical curve fluctuations induced by substructures. In this interpretation, Mothra is treated as a phenomenon akin to Earendel [216], located precisely on the macro-critical curve, and the absence of its counterimage is attributed to fluctuations in the macro-critical curve. Using our analytic formula, we evaluate substructure models that can explain the observed position of Mothra.

The parameters describing the MACS J0416.1-403 cluster are determined as follows. We first adopt a source redshift of  $z_s = 2.091$  and a lens redshift of  $z_l = 0.397$ . The virial halo mass of MACS J0416.1-403 is set to be  $M_{\text{hh}} = 1.24 \times 10^{15} M_{\odot}$  [258]. Using the mass model for MACS J0416.1-403 implemented in GLAFIC [222, 232], the Einstein radius for this source redshift is estimated as  $\theta_{\text{Ein}} \simeq 24.13$  arcsec. From the Einstein radius and the halo mass, we fix the concentration parameter of the NFW profile as  $c_{\text{vir}} = 7.59$ . Here, we use the stellar-to-halo mass relation [259] to determine the total stellar mass,  $M_s = 1.09 \times 10^{12} M_{\odot}$ , and the galaxy-size relation [74] to determine the effective radius of the Hernquist profile,  $\theta_b = 1.22$  arcsec. The parameter  $\epsilon$  is determined by the local properties of the macro-critical curve near Mothra. Using the mass model by GLAFIC, we estimate the tangential magnification as a function of the distance from the macro-critical

curve, finding the relation  $\mu_t \simeq 8 \text{ arcsec}/\delta\theta$ . From Eq. (6.17), we adopt  $\epsilon = 1/8 \text{ arcsec}^{-1}$ .

In our interpretation, explaining the observed position of Mothra requires a fluctuation of the macro-critical curve by approximately  $\simeq 0.07 \text{ arcsec}$ , particularly toward the negative parity side, as depicted in Fig. 6.1. Using Eq. (6.15), we can analytically connect the required macro-critical curve fluctuation to the surface density power spectrum of substructures. For a fluctuation amplitude of  $\langle\delta\theta_1^2\rangle^{1/2} \simeq 0.07 \text{ arcsec}$ , we estimate the variance in surface density perturbations  $\langle\delta\kappa^2\rangle \simeq 3.27 \times 10^{-5}$ . In the following, we consider two specific substructure models, CDM subhalos and granular strictures within FDM halos, and explore the possibility of explaining the observed location of Mothra.

### 6.3.1 CDM subhalos

First, we consider the CDM subhalos as perturbers of the macro-critical curve. Adopting the halo model framework [260] and assuming that subhalos are distributed without spatial correlation, the surface density power spectrum can be computed by integrating over the subhalo mass function weighted by their surface density profile as [256]

$$P_{\delta\kappa}(K) = \int_{M_{\text{sh},\text{min}}}^{M_{\text{sh},\text{max}}} \frac{d^2 N_{\text{sh}}}{dM_{\text{sh}} dS} |\tilde{\kappa}_{M_{\text{sh}}}(K)|^2 dM_{\text{sh}}, \quad (6.18)$$

with  $M_{\text{sh},\text{min}}$  and  $M_{\text{sh},\text{max}}$  being the minimum and maximum masses of subhalos, respectively. The surface number density of subhalos within the mass range of  $[M_{\text{sh}}, M_{\text{sh}} + dM_{\text{sh}}]$  is denoted by  $d^2 N_{\text{sh}}/dM_{\text{sh}} dS$ . This projected subhalo mass function is further described by Eq. (2.21), where the distribution of subhalos is assumed to be proportional to the surface density profile of the host halo. For the subhalo mass function, we adopt the model presented in [74]. The Fourier transform of the convergence is denoted by  $\tilde{\kappa}_{M_{\text{sh}}}(K)$ , which can be expressed with a subhalo mass as

$$\tilde{\kappa}_{M_{\text{sh}}}(K) = \frac{M_{\text{sh}}}{\Sigma_{\text{cr}}} \tilde{u}_{M_{\text{sh}}}(\mathbf{k} = (K_x, K_y, 0)), \quad (6.19)$$

where  $\Sigma_{\text{cr}}$  is the critical surface density given in Eq. (4.37), and  $\tilde{u}_{M_{\text{sh}}}(\mathbf{k})$  is the Fourier transform of the normalized mass function. It can be calculated by

$$\tilde{u}_{M_{\text{sh}}}(k) = \int_0^{r_{\text{vir}}} \frac{4\pi r^2}{M_{\text{sh}}} \frac{\sin kr}{kr} \rho_{M_{\text{sh}}}(r) dr, \quad (6.20)$$

where  $\rho_{M_{\text{sh}}}(r)$  denotes the subhalo density profile. Here, we adopt the Navarro-Frenk-White (NFW) profile for the subhalo density profile, leading to the expression of  $\tilde{u}_{M_{\text{sh}}}(k)$  as [261],

$$\tilde{u}_{M_{\text{sh}}}(k) = f(c_{\text{vir}}) \left\{ \sin(kr_{\text{vir}}) \{ \text{Si}(kr_{\text{vir}}(1 + c_{\text{vir}})) - \text{Si}(kr_{\text{vir}}) \} \right. \\ \left. + \cos(kr_{\text{vir}}) \{ \text{Ci}(kr_{\text{vir}}(1 + c_{\text{vir}})) - \text{Ci}(kr_{\text{vir}}) \} - \frac{\sin(kr_{\text{vir}}c_{\text{vir}})}{kr_{\text{vir}}(1 + c_{\text{vir}})} \right\}, \quad (6.21)$$

where  $\text{Si}(X) = \int_0^X dt \sin(t)/t$  is the sine integral function and  $\text{Ci}(X) = -\int_X^\infty dt \cos(t)/t$  is the cosine integral function. The function  $f(c_{\text{vir}})$  is the same function given in Eq. (2.8).

By substituting Eq. (6.18) into Eq. (6.15), we can estimate the mass range of CDM subhalos ( $M_{\text{sh},\text{min}}, M_{\text{sh},\text{max}}$ ) required to reproduce  $\langle\delta\kappa^2\rangle \simeq 3.27 \times 10^{-5}$ . Note that the

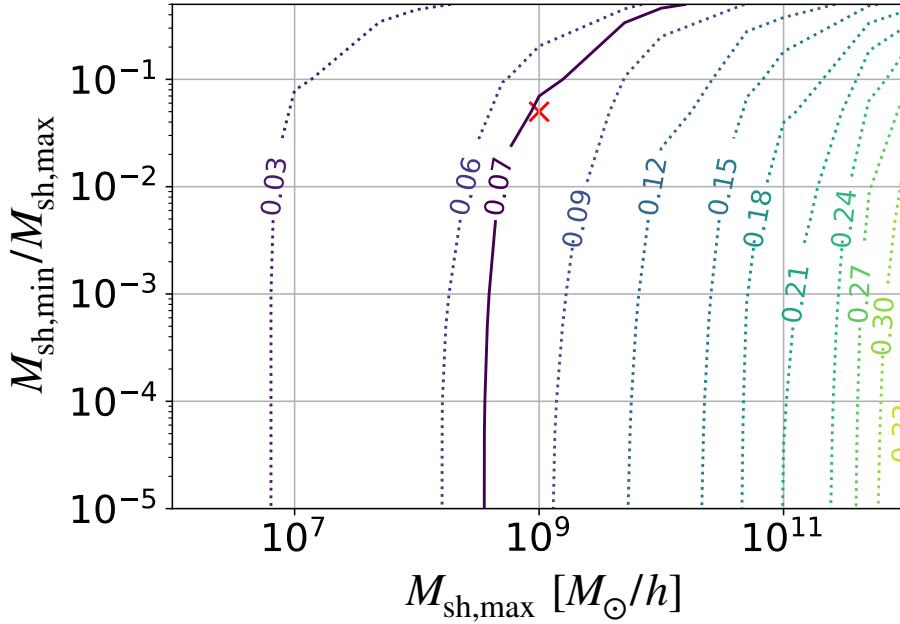


Figure 6.2: Contours of fluctuations of the macro-critical curve  $\langle \delta\theta_1^2 \rangle^{1/2}$  in the units of arcsec, as a function of maximum subhalo mass  $M_{\text{sh,max}}$  and mass ratio  $M_{\text{sh,min}}/M_{\text{sh,max}}$ , for the Mothra-like lensing system. The red cross shows the model that we calculate in detail to interpret the anomalous position of Mothra (see Fig. 6.3). This calculation is conducted by the first author of [46]. This figure is taken from [46].

minimum mass of CDM subhalos is predicted to be theoretically very small, for instance,  $10^{-12} - 10^{-3} M_\odot$  in the case of supersymmetric neutralinos [262, 263, 264, 265]. Therefore, the  $M_{\text{sh,min}}/M_{\text{sh,max}}$  ratio can be effectively considered as zero. From Fig. 6.2, we find that the maximum subhalo mass  $M_{\text{sh,max}}$  required to explain the Mothra-like lensing event is less than  $10^9 M_\odot/h$  for such small  $M_{\text{sh,min}}/M_{\text{sh,max}}$ . This is consistent with the absence of any visible galaxy near Mothra. Consequently, we conclude that CDM subhalos, particularly those with  $M_{\text{sh,max}} \simeq 10^{8-9} M_\odot/h$  might provide a plausible explanation for the observed location of Mothra.

While the observed location of Mothra can be attributed to perturbations in the macro-critical curve caused by CDM subhalos with a maximum mass of  $10^9 M_\odot/h$ , such subhalos could also influence the magnification ratios of multiple image pairs of nearby sources on either side of the critical curve. Here, we specifically examine the impact on the magnification ratios of the image pair  $c$  and  $c'$  shown in Fig. 6.1 using GLAFIC. Based on the configuration of the multiple image pairs, the magnification ratio between the images  $c$  and  $c'$  is expected to be approximately 1.22 [45]. We distribute the CDM subhalos with the mass range between  $(M_{\text{sh,min}}, M_{\text{sh,max}}) = (5 \times 10^7 M_\odot/h, 10^9 M_\odot/h)$  in ten different populations of subhalos, and obtain two thousand parameter sets of  $(\delta\theta_1, \mu_c, \mu_{c'})$ . The distribution of the parameter sets is shown in Fig. 6.3. When  $|\delta\theta_1| \simeq 0.2$  arcsec, the perturbed critical curve approaches the location of image  $c$  or  $c'$ , resulting in a strong correlation between  $\delta\theta_1$  and the magnification ratio  $\mu_c/\mu_{c'}$ . However, for smaller perturbations, specifically  $\delta\theta_1 \lesssim 0.1$  arcsec, this correlation becomes much weaker. This suggests that the Mothra lens system could be reproduced while preserving the observed magnification ratio of  $\mu_c/\mu_{c'} \simeq 1.22$ . It is important to note that subhalos can also introduce

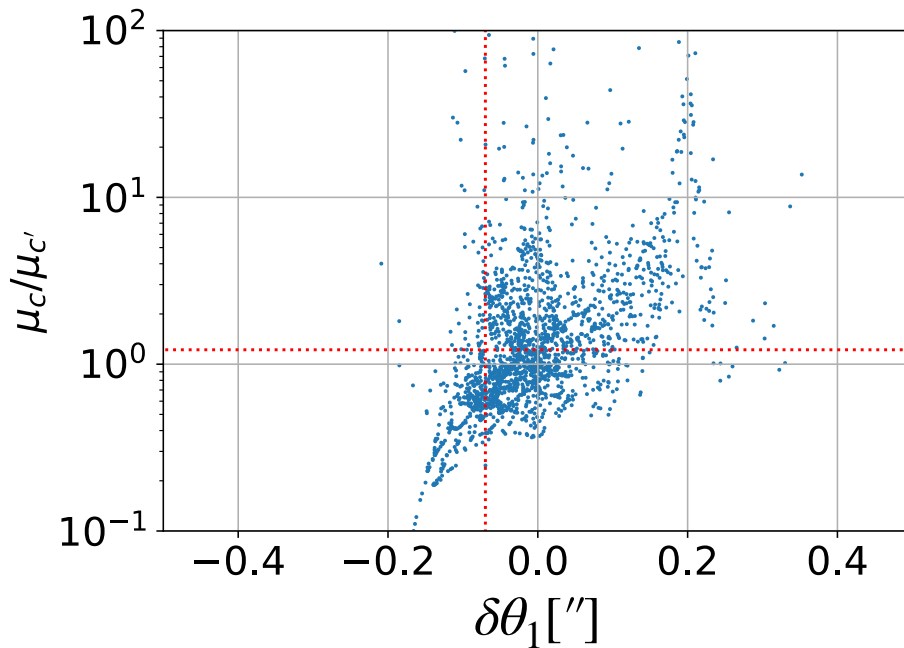


Figure 6.3: The correlation between  $\delta\theta_1$  and the magnification ratio between  $c$  and  $c'$ . The horizontal red dotted line represents the magnification ratio of the images  $c$  and  $c'$ , which is predicted to be about 1.22. The vertical red dotted line shows  $\delta\theta_1$  to explain the observed location of Mothra with the fluctuations of the macro-critical curve. This calculation is conducted by the first author of [46]. This figure is taken from [46].

positional perturbations to other multiple image pairs. Ensuring that these perturbations do not significantly alter the observed positions of those images is crucial for confirming the viability of the scenario. However, further investigation is beyond the scope of this chapter and is left for future studies.

### 6.3.2 Granular structures in FDM halos

Due to the wave nature of FDM, the granular structures, which originate from the interference pattern, exist in FDM halos, as discussed in Chap. 3. The characteristic size of each granular structure corresponds to the de Broglie wavelength. The surface density perturbations from these granular features have been analytically explored in [164] as reviewed in Sec. 3.6. In their calculations, they assume that the granular structures are uniformly and randomly distributed with a number density  $\langle n \rangle = 1/V_c$ , where  $V_c$  represents the constant volume of an individual granular structure. The mass of each granular structure is determined by the local NFW density profile and the internal density profile is modeled as Gaussian.

Without baryon components, the surface density power spectrum is expressed by Eq. (3.116). Substituting the volume of the granular structure given by Eq. (3.57), the power spectrum can be represented by

$$P_{\delta\kappa, \text{FDMonly}}(K) = \frac{\pi \int dz \rho_{\text{NFW}}^2(r)}{6\Sigma_{\text{cr}}^2} \lambda_{\text{dB}}^3 \exp\left(-\frac{\lambda_{\text{dB}}^2 K^2}{4}\right), \quad (6.22)$$

with  $\lambda_{\text{dB}} = h/mv$  is the de Broglie wavelength where the halo velocity dispersion is set to

a constant value determined by Eq. (3.107). Then, the perturbation of the macro-critical curve in FDM halos can be estimated using Eqs. (6.14) and (6.15), as

$$\langle \delta\theta_{1,\text{FDMonly}}^2 \rangle = \frac{\lambda_{\text{dB}}}{4\epsilon^2} \frac{\int dz \rho_{\text{NFW}}^2(r)}{\Sigma_{\text{cr}}^2}. \quad (6.23)$$

Given that the de Broglie wavelength scales inversely with the FDM particle mass  $m$ , the simple relation of  $\langle \delta\theta_{x,\text{FDMonly}}^2 \rangle \propto 1/m$  satisfies. Equation (6.23) can be expressed in an alternative form,

$$\epsilon^2 \langle \delta\theta_{1,\text{FDMonly}}^2 \rangle = \frac{\lambda_{\text{dB}}}{4r_{\text{NFW}}(x)} \kappa_{\text{FDM}}^2(x), \quad (6.24)$$

where  $r_{\text{NFW}}(x)$  is the effective radius in FDM halos at the position of  $x = |\mathbf{x}|$  introduced in Eq. (3.115). Here,  $\kappa_{\text{FDM}}(x)$  is the convergence due to the overall FDM density profile, given as

$$\kappa_{\text{FDM}}(x) = \frac{1}{\Sigma_{\text{cr}}} \int dz \rho_{\text{NFW}}(r). \quad (6.25)$$

From Eq. (6.24), the fluctuation in the macro-critical curve is proportional to the convergence and inversely proportional to the square root of the number of granular structures along the effective radius.

When baryonic components are smoothly distributed, the surface density power spectrum takes the form given in Eq. (3.117). Compared to the FDM-only case described by Eq. (6.22), it is reduced by a factor of  $\{\Sigma_{\text{NFW}}/(\Sigma_{\text{NFW}} + \Sigma_{\text{Hern}})\}^2$ , reflecting the contribution of baryonic matter to the overall density distribution. Consequently, the perturbation in the critical curve can be expressed as

$$\epsilon^2 \langle \delta\theta_{1,\text{FDMbaryon}}^2 \rangle = \frac{\lambda_{\text{dB}}}{4r_{\text{NFW}}} \left( \frac{\kappa_{\text{FDM}}}{\kappa_{\text{tot}}} \right)^2 \kappa_{\text{tot}}^2, \quad (6.26)$$

where  $\kappa_{\text{tot}} = \kappa_{\text{FDM}} + \kappa_{\text{baryon}}$  denotes the total convergence. Assuming the baryon mass distribution follows the Hernquist profile,  $\kappa_{\text{baryon}}$  is expressed by

$$\kappa_{\text{baryon}}(x) = \frac{1}{\Sigma_{\text{cr}}} \int dz \rho_{\text{Hern}}(r). \quad (6.27)$$

It is evident that the presence of a smooth baryon profile suppresses fluctuations in the macro-critical curves.

Using these relations, we estimate the perturbation of the macro-critical curve in the Mothra system. Figure 6.4 shows the relation between the FDM mass and the fluctuation in the macro-critical curve due to the granular structures. We find that the FDM mass of  $m \simeq 5.5 \times 10^{-25} \text{ eV}/c^2$  is required to account for the observed position of Mothra. This value is much lower than the typical FDM mass range of  $m = 10^{-23}\text{-}10^{-21} \text{ eV}/c^2$ . There are two reasons why such a small FDM mass is necessary to produce a sizable effect. First, the de Broglie wavelength is relatively short due to the high-velocity dispersion in galaxy clusters. Second, the longer line-of-sight projection in galaxy clusters leads to a more pronounced averaging effect. When the FDM mass is small, each granular structure becomes larger, resulting in greater fluctuations. However, the preferred mass of  $m \simeq 5.5 \times 10^{-25} \text{ eV}/c^2$  is challenged by several constraints, including those from Lyman- $\alpha$  forest [182, 183, 184, 185], which suggests that scenarios in which all dark matter consists entirely of FDM may be excluded. Further exploration of hybrid dark matter models (e.g., FDM+CDM) would be beneficial, where we expect that our formalism is also applicable.

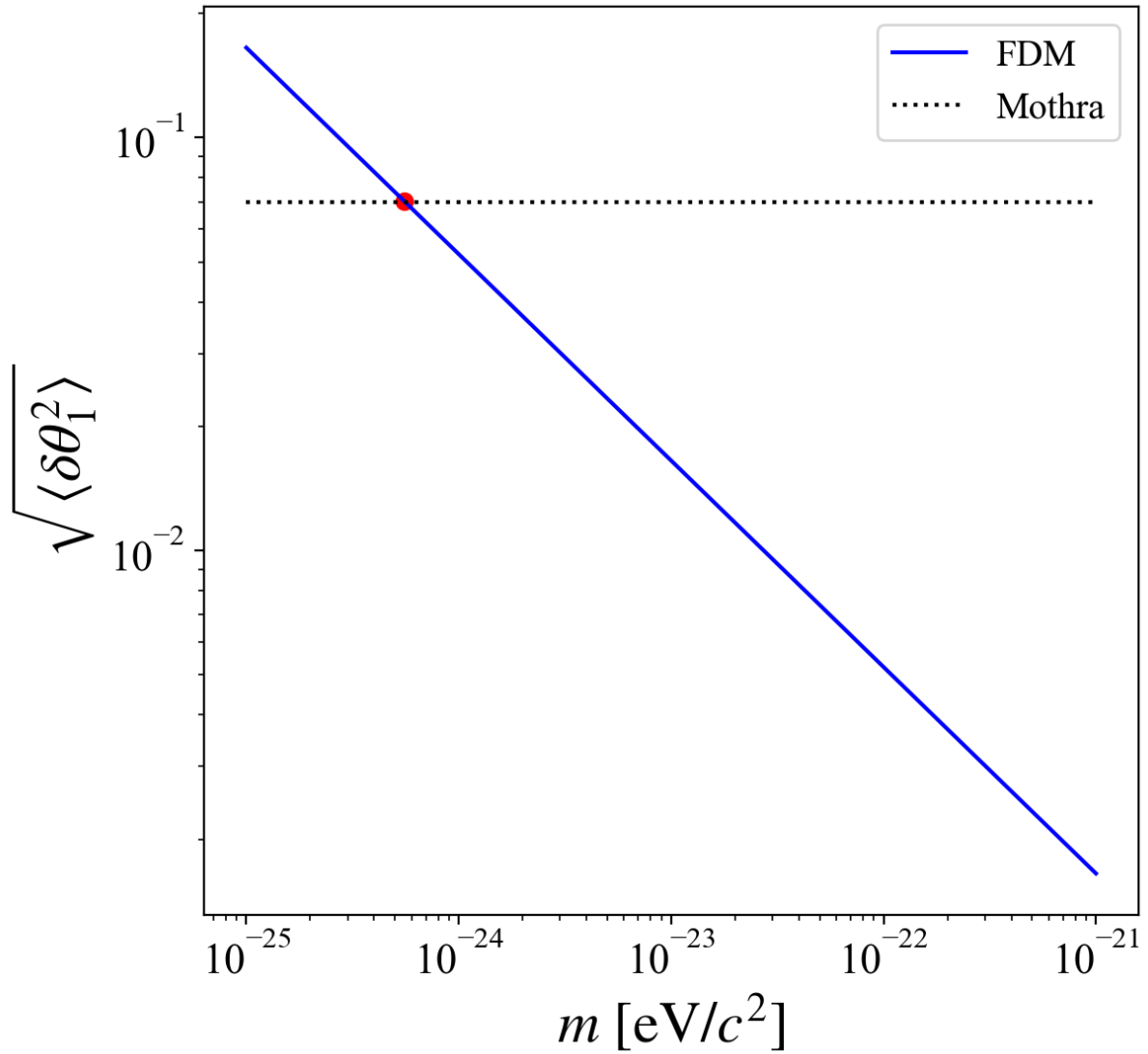


Figure 6.4: The FDM mass dependence of the fluctuation of the macro-critical curve in the Mothra-like system. The horizontal dotted line shows the fluctuation needed to explain the observed offset of Mothra. This figure is taken from [46].

## 6.4 Summary and discussions

Astrometric perturbations of critical curves in strong lensing systems provide a powerful tool for investigating small-scale substructures. A smooth mass distribution results in symmetric multiple images around macro-critical curves, however, the presence of substructures introduces small-scale fluctuations in the macro-critical curves, breaking the symmetry of the lensing configuration. In this chapter, we derive general formulae for how the surface density fluctuations induced by substructures affect the shape of the macro-critical curve. The formula, presented in Eq. (6.15), enables the analytic estimation of the fluctuation amplitude from the surface density power spectrum of substructures. To validate this formula, we conduct numerical tests using the open-source software GLAFIC. We find that the formula is accurate, provided that substructures are not dominated by a few very massive structures.

To demonstrate the application of our analytic formula, we examine the possibility that the recently observed extremely magnified binary star Mothra, whose counterimage has not been detected, can be explained by the fluctuation of the macro-critical curve caused by substructures. Our analysis reveals that CDM subhalos with masses between  $5 \times 10^7 M_\odot/h$  and  $10^9 M_\odot/h$  can successfully account for the anomalous position of Mothra, as well as the magnification ratio of the nearby image pair. Additionally, we find that FDM with a very small mass of  $\lesssim 10^{-24} \text{ eV}/c^2$  would be required to explain the observed offset of Mothra.

While both CDM subhalos and granular structures within FDM halos could potentially explain the observed location of Mothra, an increase in the number of such events would allow us to estimate the distribution function of the fluctuations (or the power spectrum in Fourier space), enabling a direct distinction between the CDM and FDM scenarios. Naively, since granular structures are distributed throughout the halo and massive CDM subhalos inducing large fluctuations are less abundant, fluctuations are expected to occur more frequently with FDM granular structures than with CDM subhalos. Therefore, it is crucial to observe more highly magnified stars, which can, for example, be achieved with the JWST, and to determine the detailed shape of the critical curve.

The analytic relation between fluctuations in the macro-critical curve and those in the surface mass density is expected to become a powerful tool when the shape of the critical curve can be measured in more detail. This will contribute to a deeper understanding of the nature of dark matter.



# Chapter 7

## Galaxy-galaxy strong lensing cross-section with FDM model

### 7.1 Introduction

The galaxy-galaxy strong lensing (GGSL) cross-section in galaxy clusters has recently been identified as one of the discrepancies between observation and the theoretical predictions with the standard  $\Lambda$  Cold Dark Matter ( $\Lambda$ CDM) model (see Fig. 7.1) [266, 267, 268]. The cross-section refers to the total area on the source plane enclosed by the secondary caustics, which are produced by substructures such as subhalos and galaxies. Observations show that the GGSL cross-section is approximately an order of magnitude larger than what is predicted by hydrodynamic  $\Lambda$ CDM simulations. This discrepancy could suggest that the actual mass distribution within substructures inside galaxy clusters is more concentrated than that of the CDM subhalos. This is in contrast to other small-scale issues discussed in Sec. 2.2, where the problem arises from an overdense mass distribution in the CDM model.

To address the small-scale issues, one potential approach is to incorporate baryonic physics and/or explore alternative dark matter models. These modifications could alter the mass distribution within halos and subhalos, as discussed in Sec. 2.3. Several investigations have already been conducted to determine whether such changes could resolve the GGSL cross-section discrepancy. The impact of baryonic physics on the cross-section has been examined through hydrodynamical simulations by [269] and [270]. Their findings suggest that subhalos with masses  $M_{\text{sh}} \gtrsim 10^{11} M_{\odot}$  might become more compact, which increases the cross-section, especially with low active galactic nuclei (AGN) efficiencies. However, these simulated subhalos contain more stellar components than are observed, making it unlikely that the discrepancy can be resolved solely by adjusting AGN physics [271]. In [272], they explore the effects of mass redistribution by modifying the concentration and tidal radius of CDM subhalos since the observations only provide constraints on the internal total mass, finding that tension persists within the CDM framework. Meanwhile, [273] investigate the GGSL cross-section within the context of the self-interacting dark matter (SIDM) model [31]. They show that the core-collapsed SIDM subhalos, with an inner density profile of  $\rho \propto r^{-\gamma}$  with a power-law index  $\gamma > 2.5$ , could help mitigate the discrepancy. However, further research is needed, as they do not consider factors such as the fraction of core-collapsed objects and the SIDM subhalo mass function. Additional detailed investigations of the GGSL cross-section within the SIDM framework would be possible using the recently developed simulations [274].

As an alternative to the CDM model, we investigate the fuzzy dark matter (FDM) model [34] and its potential impact on the GGSL cross-section. As discussed in Chap. 3, FDM is a scalar particle with a mass range of approximately  $m \simeq 10^{-24} - 10^{-20} \text{ eV}/c^2$ , and one possible candidate for FDM in particle physics is the axion-like particle (ALP), which appears in string theory [153]. A notable characteristic of FDM halos is the presence of a soliton core at the center, surrounded by a Navarro-Frenk-White (NFW) profile. This feature has been confirmed by cosmological FDM simulations [160, 163, 161]. The soliton core corresponds to the lowest energy state of the FDM, and its density profile can be expressed by the ground state solution to the Schrödinger-Poisson (SP) equation. The soliton core is characterized by two key parameters: the core mass (or core radius) and the FDM mass. For a given halo mass, the core mass can be uniquely determined by the core-halo mass relation [171, 162, 176, 47], as shown in Sec. 3.4. For a given core mass, the central density of the core increases, and the core radius shrinks, as the FDM mass becomes larger. Thus, it is expected that the GGSL cross-section would be influenced by the FDM mass, which is the basis for our investigation. By exploring the dependency of the GGSL cross-section on the FDM mass, we aim to determine whether the FDM model can yield a sufficiently large GGSL cross-section and identify the preferred mass range for FDM particles.

In this chapter, we begin by developing an analytic model to calculate the cross-section of a single FDM subhalo within a host halo. We examine how the cross-section depends on factors such as the FDM mass, the subhalo mass, and the distance from the host halo center. Next, we calculate the total cross-section by integrating the cross-section of an individual subhalo over both subhalo mass and distance, assuming a subhalo mass function. Additionally, we take into account the baryon distribution using a stellar-to-halo mass relation and investigate the impact of the baryon distribution on the overall cross-section.

This chapter is organized as follows. In Sec. 7.2, we present our analytic model for the GGSL cross-sections of FDM subhalos. In Sec. 7.3, we investigate the impact of the baryonic distribution and compare our analytic predictions with the observational result. Finally, we summarize our findings and provide discussions in Sec. 7.4. This chapter is based on our recent work presented in [49]. Throughout this chapter, we use the concentration-halo mass relation for CDM halos presented in [55] with the suppression below the half-mode mass for FDM halos modeled by Eq. (3.68). The expression of the FDM density profile is given in Eq. (3.104), where we apply the core-halo mass relation given in Eq. (3.98) and the soliton core density profile provided in Eq. (3.53).

## 7.2 GGSL cross-section with FDM subhalos

In this section, we present our model for the GGSL cross-section of FDM subhalos. We assume a total host halo mass of  $M_{\text{hh}} = 10^{15} M_{\odot}$ , with the host halo density profile following the NFW profile. Since the core radius of the host halo is sufficiently small due to the large velocity dispersion, we neglect the influence of the soliton core on the overall profile of the host halo. For simplicity, we consider spherical host and subhalos. The redshifts of the source and lens planes are set to  $z_s = 2.0$  and  $z_\ell = 0.5$ , respectively. With these parameters, the critical curve of the host halo has a size of approximately 14 arcsec. We begin by presenting the model for the GGSL cross-section of a single FDM subhalo in Sec. 7.2.1. Then in Sec. 7.2.2, we calculate the total cross-section contributed by all FDM subhalos by considering the subhalo mass function.

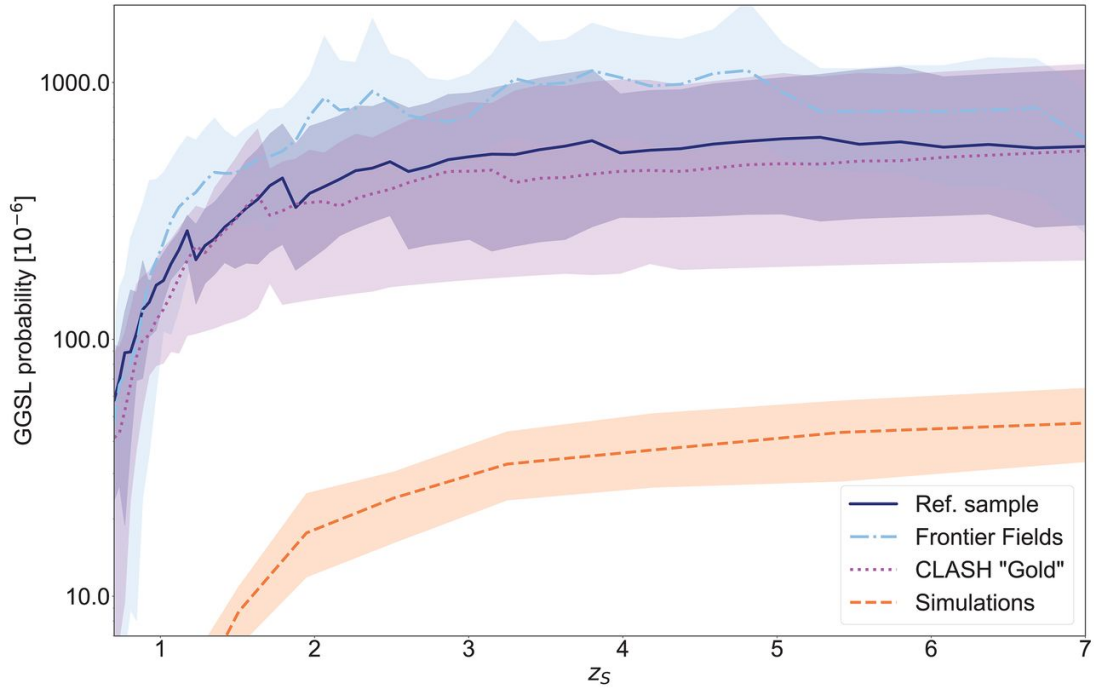


Figure 7.1: The GGSL probability in galaxy clusters between the observational results and the  $\Lambda$ CDM predictions as a function of the source redshift. The GGSL probability is defined by the total area enclosed by the secondary caustics divided by the area sampled by the cluster mass reconstruction mapped onto the source plane. The mean GGSL probability for eleven galaxy cluster samples is shown with a solid dark blue line, while the light blue dashdot and violet dotted lines plot the computed GGSL probability for the Hubble Frontier Field (HFF) [213] and Cluster Lensing and Supernova Survey with Hubble (CLASH) Gold [275, 276] samples, respectively. The orange dashed line shows the median GGSL probability measured from  $\Lambda$ CDM simulations. The colored bands show the 99.9% confidence interval (CI) for each dataset. The discrepancy between observations and simulations of an order of magnitude can be identified. This figure is taken from [266].

### 7.2.1 Single FDM subhalo

In this subsection, we examine the cross-section of a single FDM subhalo within the host halo. To calculate the cross-section, we perform numerical simulations using the same code as that employed in [266]. First, we generate convergence maps (projected density fields) and compute the deflection angle using ray-tracing simulations. By incorporating the deflection angle contribution from the host halo, we determine the secondary-critical curve associated with the subhalos.

In Fig. 7.2, we show the convergence maps of both CDM and FDM subhalos with different FDM masses, positioned 20 arcseconds from the center of the host halo. The core radius, denoted by red lines, shrinks as the FDM mass increases, as can be estimated from Eq. (3.55). The secondary-critical curves are indicated by white lines. As expected, the size of the critical curve varies with the FDM mass. In Fig. 7.3, we plot the corresponding GGSL cross-sections. We observe that for sufficiently small FDM masses, the cross-section is zero, as the central density of the soliton core is not high enough to generate the critical curve; the convergence is less than one at the center (see Sec. 4.4). For large FDM masses, the cross-section approaches the same value as that of the CDM subhalo, since the effect

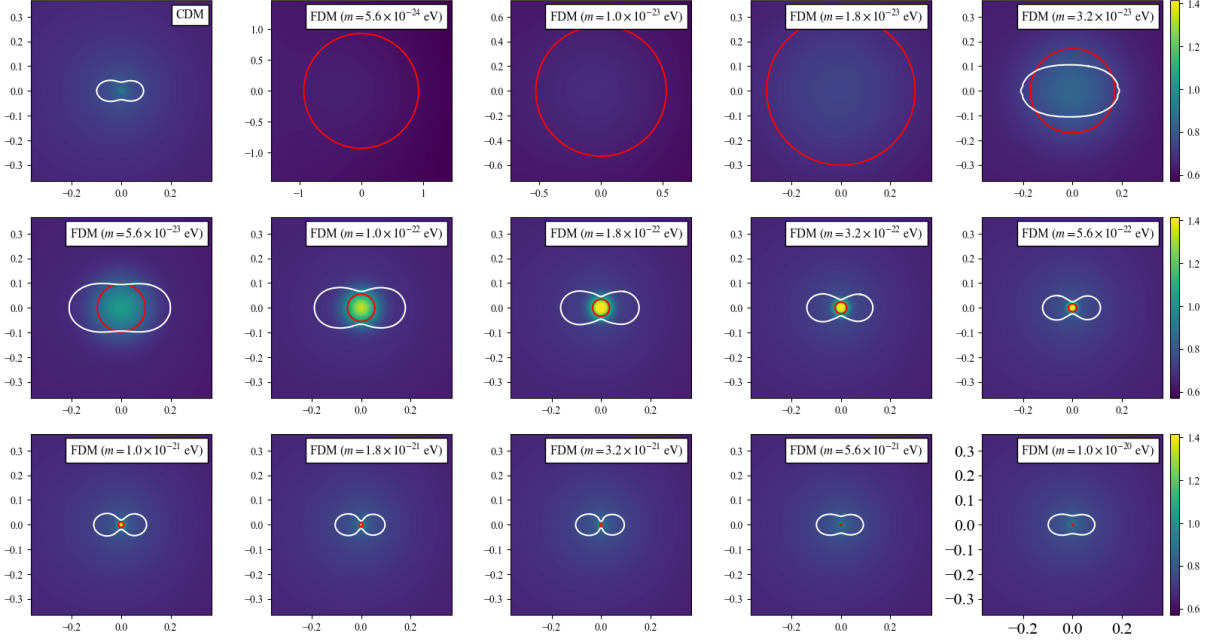


Figure 7.2: The convergence maps and secondary-critical curves around the position of the subhalos in the CDM model and the FDM model with different FDM masses. The location of subhalos is 20 arcsec from the center of the host halo,  $(x, y) = (-20, 0)$ , where the unit is arcsec. The masses of host halo and subhalos are set to  $10^{15} M_{\odot}$  and  $10^{11} M_{\odot}$ , respectively. The redshifts of the source plane and lens plane are set to  $z_s = 2.0$  and  $z_l = 0.5$ , respectively. The secondary-critical curves are shown in white lines and the core radii of the FDM subhalos are shown in red lines. Note that the box sizes are different for the cases with the FDM mass  $m = 5.6 \times 10^{-24} \text{ eV}/c^2$  and  $1.0 \times 10^{-23} \text{ eV}/c^2$ . This figure is taken from [49].

of the soliton core becomes negligible and the cylinder mass within critical curves is the same. Interestingly, for FDM masses between these extremes, where the core radii are comparable to the size of the critical curves, the cross-section exceeds that of the CDM case. The peak cross-section is roughly an order of magnitude larger than that for the CDM subhalo, suggesting that the GGSL discrepancy could be alleviated by considering the FDM model.

We find that the GGSL cross-section of a single FDM subhalo can be accurately represented by the following analytic formula,

$$\sigma_{\text{FDM}}(m; M_{\text{sh}}, d_{\text{sh}}) = \frac{1}{2} \left\{ 1 + \tanh \left( \frac{\log_{10} m - \log_{10} m_{\text{peak}}}{\Delta_{\log_{10} m}} \right) \right\} \times \left\{ \sigma_{\text{FDM}}^{\text{peak}} \left( \frac{m}{m_{\text{peak}}} \right)^{-1} + \sigma_{\text{CDM}}(M_{\text{sh}}, d_{\text{sh}}) \right\}. \quad (7.1)$$

We define the peak cross-section as  $\sigma_{\text{FDM}}^{\text{peak}}$ , which can be seen in Fig. 7.3, and denote the corresponding FDM mass as  $m_{\text{peak}}$ . The first term reflects that the cross-section becomes zero for FDM masses below the peak value due to the core density profile being too shallow. The second term represents the reduction in the cross-section, which scales inversely with the FDM mass for values above  $m_{\text{peak}}$ , eventually converging to the cross-section of a CDM subhalo. For FDM masses  $m \gtrsim m_{\text{peak}}$ , the core radius becomes smaller than the Einstein

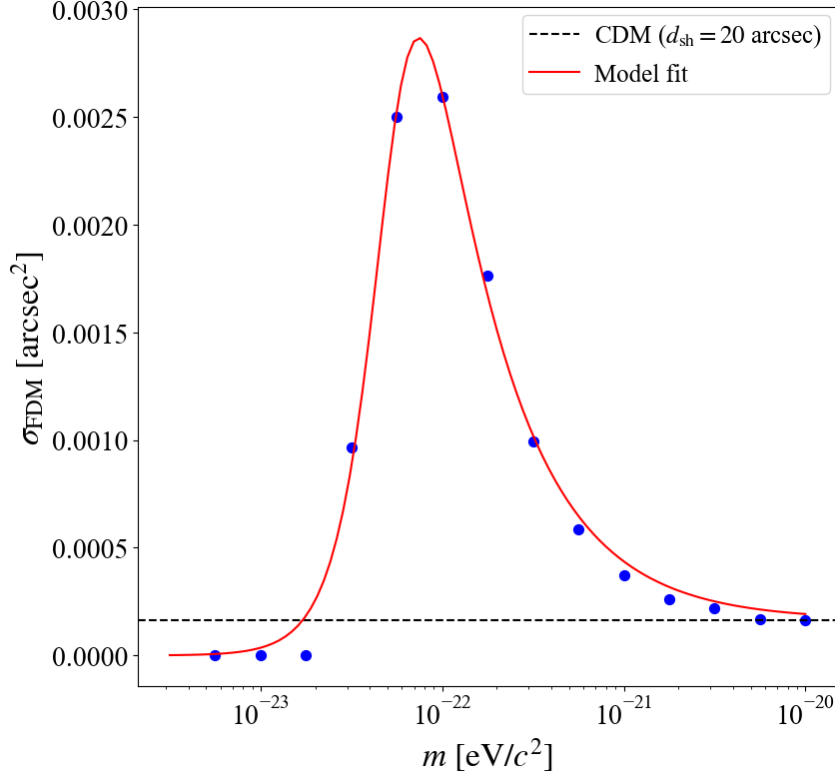


Figure 7.3: The GGSL cross-section of a single FDM subhalo in a galaxy cluster as a function of the FDM mass. The parameters are the same as Fig. 7.2. The cross-section of the CDM subhalo is shown in the horizontal dashed line. The red line shows the fitting result of our analytic model where the fitting parameters are  $m_{\text{peak}} = 10^{-22.3} \text{ eV}/c^2$ ,  $\sigma_{\text{FDM}}^{\text{peak}} = 0.005 \text{ arcsec}^2$ , and  $\Delta_{\log_{10} m} = 0.23$ . This figure is taken from [49].

radius,  $x_c \lesssim x_{\text{Ein}}$ , where  $x$  represents the two-dimensional coordinates on the projected plane. Considering the relation  $\sigma_{\text{FDM}} \propto x_{\text{Ein}}^2 \propto M(< x_{\text{Ein}}) \simeq M_c + M_{\text{NFW}}(< x_{\text{Ein}})$ , where  $M(< x)$  is the cylinder mass, and the dependence of the core mass on the FDM mass,  $M_c \propto m^{-1}$ , we can understand how the cross-section varies with the FDM mass as described in Eq. (7.1). In Fig. 7.3, we plot the fitting result of our analytic formula in the red solid line, which accurately captures the numerical results.

The peak cross-section and the corresponding peak FDM mass depend on two key parameters: the subhalo mass  $M_{\text{sh}}$  and the distance from the host center  $d_{\text{sh}}$ . As indicated by Fig. 7.2, the peak cross-section occurs when the core radius approximately matches the size of the critical curve, roughly corresponding to the Einstein radius (ignoring the expansion due to the smooth background mass distribution),  $x_c \simeq x_{\text{Ein}}$ . In this scenario, the cylinder mass within the critical curve can be approximated by the core mass,  $x_{\text{Ein}} \propto M_c^{1/2}$ . Using the relations  $x_c = r_c \propto M_{\text{sh}}^{-1/3} m^{-1}$  and  $M_c \propto M_{\text{sh}}^{1/3} m^{-1}$ , the dependence of the peak FDM mass on these parameters can be derived as

$$m_{\text{peak}}(M_{\text{sh}}, d_{\text{sh}}) \propto M_{\text{sh}}^{-1}. \quad (7.2)$$

It is important to note that the size of the critical curve is influenced by the position of the subhalo due to the contribution of the host halo. While this could affect the peak FDM mass, numerical results show negligible dependence on the distance. The dependence of the peak cross-section on the subhalo mass can be estimated as  $\sigma_{\text{FDM}}^{\text{peak}} \propto x_{c,\text{peak}}^2 \propto$

$M_{\text{sh}}^{-2/3} m_{\text{peak}}^{-2} \propto M_{\text{sh}}^{4/3}$ . For a fixed subhalo mass, we numerically find that the peak cross-section scales with distance as  $\sigma_{\text{FDM}}^{\text{peak}} \propto d_{\text{sh}}^{-2.3}$ . By combining these dependencies, the peak cross-section depends on the subhalo mass and its distance from the host halo center as

$$\sigma_{\text{FDM}}^{\text{peak}}(M_{\text{sh}}, d_{\text{sh}}) \propto M_{\text{sh}}^{4/3} d_{\text{sh}}^{-2.3}. \quad (7.3)$$

As expected, subhalos located closer to the macro-critical curve or with greater mass contribute to larger cross-sections. It is important to note that subhalos with secondary-critical curves exceeding 3 arcseconds are typically excluded from consideration, as such large critical curves are not observed [266]. The smoothing parameter  $\Delta_{\log_{10} m}$  in Eq. (7.1) is on the order of 0.1 and does not exhibit any clear dependence on either parameter.

For a host halo modeled with a spherical NFW profile and a mass of  $M_{\text{hh}} = 10^{15} M_{\odot}$ , with source and lens redshifts set to  $z_s = 2.0$  and  $z_l = 0.5$ , respectively, we numerically obtain the coefficients for the peak cross-section and the corresponding peak FDM mass. With the coefficients, they can be represented as

$$\sigma_{\text{FDM}}^{\text{peak}}(M_{\text{sh}}, d_{\text{sh}}) \simeq 5 \times 10^{-3} \text{ arcsec}^2 \left( \frac{M_{\text{sh}}}{10^{11} M_{\odot}} \right)^{4/3} \left( \frac{d_{\text{sh}}}{20 \text{ arcsec}} \right)^{-2.3}, \quad (7.4)$$

$$m_{\text{peak}}(M_{\text{sh}}) \simeq 1 \times 10^{-22} \text{ eV}/c^2 \left( \frac{M_{\text{sh}}}{10^{11} M_{\odot}} \right)^{-1}. \quad (7.5)$$

We also investigate the empirical relation for the cross-section of a single CDM subhalo, expressing it as a function of the subhalo mass and its distance from the center of the host halo. As a result, the following relationship is obtained,

$$\sigma_{\text{CDM}}(M_{\text{sh}}, d_{\text{sh}}) \simeq 1 \times 10^{-4} \text{ arcsec}^2 \left( \frac{M_{\text{sh}}}{10^{11} M_{\odot}} \right)^{2.3} \left( \frac{d_{\text{sh}}}{20 \text{ arcsec}} \right)^{-12}. \quad (7.6)$$

The coefficients in Eqs. (7.4), (7.5), and (7.6) are influenced by the mass and density profile of the host halo, as well as the redshifts of the source and lens planes. These parameters are set constant in this chapter.

## 7.2.2 Total GGS� cross-section

With the analytic expression for the cross-section of a single CDM and FDM subhalo, accounting for variations in FDM mass, subhalo mass, and distance from the host halo center, we can now compute the total cross-section contributed by all subhalos within the host halo.

The total cross-section is derived by multiplying the subhalo mass function, discussed in Sec. 2.1.3 for CDM subhalos and Sec. 3.5 for FDM subhalos, with the single subhalo cross-section and integrating over both the subhalo mass and distance from the host halo center. For FDM subhalos, the resulting total cross-section depends on the FDM mass,

$$\begin{aligned} \sigma_{\text{FDM}}^{\text{tot}}(m) &= \sum_{i=0}^{N_{\text{sh}}} \sigma_{\text{FDM}}(m; M_{\text{sh}}, d_{\text{sh}}) \\ &= \int_{M_{\text{sh},\text{min}}}^{M_{\text{sh},\text{max}}} dM_{\text{sh}} \int_{d_{\text{sh},\text{min}}}^{d_{\text{sh},\text{max}}} dd_{\text{sh}} \left. \frac{d^2 N_{\text{sh}}}{dM_{\text{sh}} dd_{\text{sh}}} \right|_{\text{FDM}} \sigma_{\text{FDM}}(m; M_{\text{sh}}, d_{\text{sh}}). \end{aligned} \quad (7.7)$$

For CDM subhalos, it can be expressed as

$$\sigma_{\text{CDM}}^{\text{tot}} = \int_{M_{\text{sh},\text{min}}}^{M_{\text{sh},\text{max}}} dM_{\text{sh}} \int_{d_{\text{sh},\text{min}}}^{d_{\text{sh},\text{max}}} dd_{\text{sh}} \left. \frac{d^2 N_{\text{sh}}}{dM_{\text{sh}} dd_{\text{sh}}} \right|_{\text{CDM}} \sigma_{\text{CDM}}(M_{\text{sh}}, d_{\text{sh}}). \quad (7.8)$$

In Fig. 7.4, we show the total cross-section of FDM subhalos normalized by that of CDM subhalos as a function of the FDM mass. The subhalo mass range is set between  $M_{\text{sh},\text{min}} = 10^{10} M_{\odot}$  and  $M_{\text{sh},\text{max}} = 10^{12} M_{\odot}$ . Although there is a large number of subhalos with lower masses,  $M_{\text{sh}} \lesssim 10^{10} M_{\odot}$ , their cross-sections are relatively small, and they do not significantly contribute to the total cross-section. There are two reasons why the maximum subhalo mass is set to  $10^{12} M_{\odot}$ . First, the number of high-mass subhalos is small, and second, these subhalos would produce critical curves larger than what we observe, as discussed in Sec. 7.2.1. We also choose the minimum and maximum distances from the host halo center to be  $d_{\text{sh},\text{min}} = 15$  arcsec and  $d_{\text{sh},\text{max}} = 100$  arcsec, respectively. The minimum distance ensures that subhalos are located outside the macro-critical curve of the host halo. We find that the total cross-section is nearly zero for FDM masses below  $m \lesssim 10^{-23} \text{ eV}/c^2$ . Interestingly, for  $m \gtrsim 10^{-23} \text{ eV}/c^2$ , the total cross-section exceeds that of the CDM case. The peak ratio of the total cross-section from FDM to CDM subhalos is approximately three when the FDM mass is  $m \simeq 10^{-22} \text{ eV}/c^2$ . As the FDM mass increases further, in the CDM limit, the total cross-section ratio approaches one, as expected. While FDM subhalos can produce a larger cross-section than CDM subhalos, no FDM mass is capable of generating a cross-section large enough to match the observed value, which is about an order of magnitude greater than that of CDM subhalos.

### 7.3 Effects of baryons

Cluster galaxies contain baryonic components, which we have previously neglected. In this section, we consider the impact of the baryon distribution on both the single and total cross-sections. We include the baryons without modifying the dark matter distribution, i.e., we ignore the back reaction of the dark matter distribution caused by the presence of baryons. This is because we still do not understand how the dark matter density profile is affected by the presence of central stellar distribution, particularly in the case of FDM. In Sec. 7.4, we discuss how the dark matter profile is changed and its impact on the cross-section. Although the total mass slightly exceeds  $10^{15} M_{\odot}$  due to the inclusion of the baryons, this increase is negligible since the baryon mass contributes only about 1% of the total dark matter mass. We assume the baryon distribution follows the Hernquist profile [78] as summarized in Sec. 2.1.4. To determine the Hernquist profile for a given halo mass, we use the stellar-to-halo mass relation [80] and the relation between the effective radius of the Hernquist profile and the virial radius of the host subhalo, given by  $r_e = 0.03 r_{\text{vir}}$  [277, 278].

We examine how the inclusion of the baryon profile affects the cross-section of each subhalo. In Fig. 7.5, we show the convergence maps and critical curves, using the same setup as in Fig. 7.2. The addition of the baryons results in an increase in the size of the secondary-critical curves around the subhalos. In Fig. 7.6, we show the corresponding cross-sections. It is evident that the ratio of the peak FDM cross-section to the CDM cross-section decreases when the baryon profile is included, compared to the case without baryons.

Although the coefficients and power-law indices are slightly altered, we find that the analytic model presented in Sec. 7.2.1 still provides a good description of the cross-section,

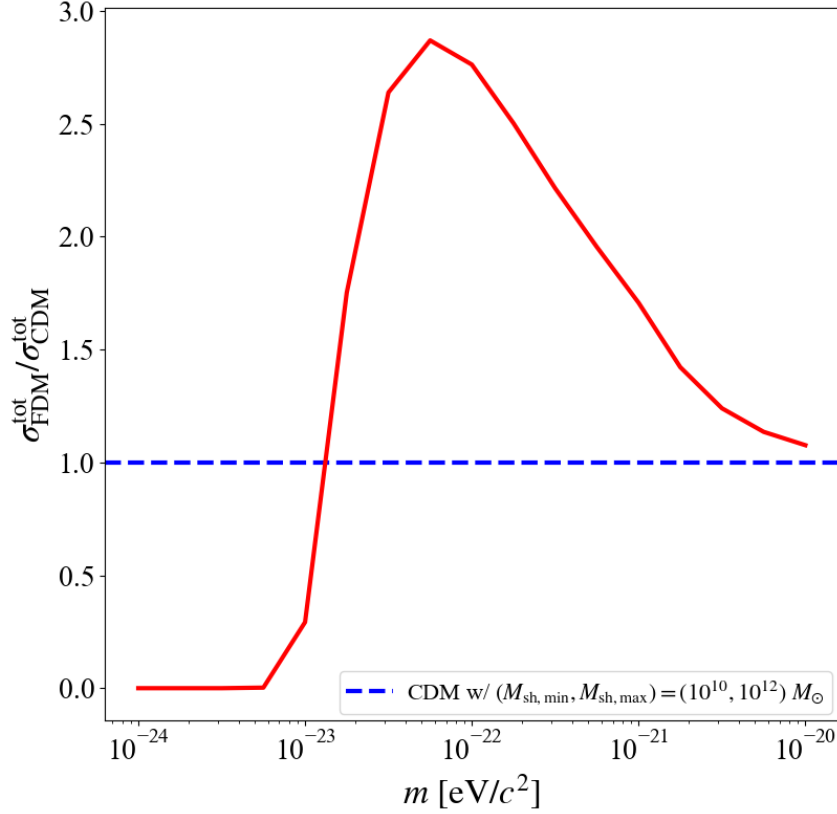


Figure 7.4: The ratio of the total GGSL cross-sections of the CDM and FDM subhalos as a function of the FDM mass. Host halo mass and the redshifts of the source and lens plane are the same as Fig. 7.2. The minimum and maximum subhalo masses are set to  $10^{10} M_{\odot}$  and  $10^{12} M_{\odot}$ , respectively. We set the minimum and maximum distances to 15 arcsec and 100 arcsec, respectively. This figure is taken from [49].

even when baryon components are included, as shown in Fig. 7.6. The peak cross-section and the corresponding peak FDM mass can be represented by

$$\sigma_{\text{FDM}}^{\text{peak}}(M_{\text{sh}}, d_{\text{sh}}) \simeq 7 \times 10^{-3} \text{ arcsec}^2 \left( \frac{M_{\text{sh}}}{10^{11} M_{\odot}} \right)^{1.3} \left( \frac{d_{\text{sh}}}{20 \text{ arcsec}} \right)^{-1.7}, \quad (7.9)$$

$$m_{\text{peak}}(M_{\text{sh}}) \simeq 8 \times 10^{-23} \text{ eV}/c^2 \left( \frac{M_{\text{sh}}}{10^{11} M_{\odot}} \right)^{-1}, \quad (7.10)$$

and the cross-section for a single CDM subhalo is

$$\sigma_{\text{CDM}}(M_{\text{sh}}, d_{\text{sh}}) \simeq 1 \times 10^{-3} \text{ arcsec}^2 \left( \frac{M_{\text{sh}}}{10^{11} M_{\odot}} \right)^{2.0} \left( \frac{d_{\text{sh}}}{20 \text{ arcsec}} \right)^{-2.3}. \quad (7.11)$$

The coefficient of the cross-section increases with the inclusion of the baryon profile. Meanwhile, the peak FDM mass is slightly smaller compared to the case without baryons. This occurs because the size of the critical curve expands due to the baryon distribution, requiring a smaller FDM mass for the same core size.

Taking into account the subhalo mass function, we can compute the total cross-section as done in Sec. 7.2.2. In Fig. 7.7, we plot the ratio of the total cross-section between FDM and CDM subhalos as a function of the FDM mass. The presence of the baryon profile

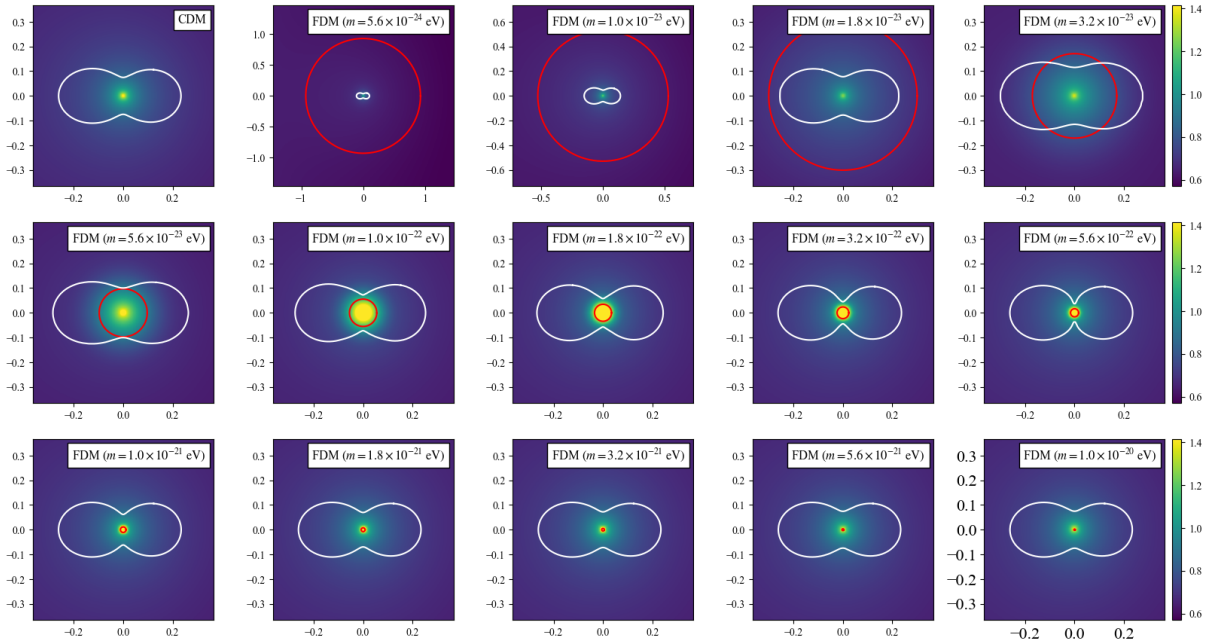


Figure 7.5: Similar to Fig. 7.2, but including the baryon distribution. The baryon distribution is determined by the Hernquist profile where we use the stellar-to-halo mass relation presented in [80] and the relation  $r_e = 0.03r_{\text{vir}}$ . This figure is taken from [49].

results in a suppression of the ratio compared to the case without baryons. The largest effect occurs when the FDM mass is approximately  $10^{-22}$  eV/ $c^2$ , with the ratio being less than two. Since the observations indicate that the total cross-section is about ten times larger than the CDM predictions, it might suggest that the FDM model, regardless of the mass, cannot fully explain the observational results. However, the assumptions of spherical host and subhalos, as well as the neglect of modifications of the dark matter profile due to the presence of baryons, should be revisited in future studies. These factors could potentially increase the cross-section.

## 7.4 Summary and discussions

A discrepancy regarding the GGSL cross-section in galaxy clusters has been identified between observations and the predictions based on the  $\Lambda$ CDM model, with the former being an order of magnitude larger. One potential solution to this discrepancy is to consider the FDM model, which is a viable alternative to CDM. In this chapter, we have developed an analytic model to describe the GGSL cross-section of FDM subhalos and compared it to that of CDM subhalos using numerical simulations. This analysis assumes spherical symmetry for both the host halo and the subhalos. The host halo mass distribution is modeled by the NFW profile, with a fixed mass of  $M_{\text{hh}} = 10^{15} M_{\odot}$ , while the source and lens redshifts are set to  $z_s = 2.0$  and  $z_l = 0.5$ , respectively.

We first consider a single subhalo with mass  $M_{\text{sh}}$ , located at a distance  $d_{\text{sh}}$  from the center of the host halo. When the FDM mass is sufficiently small, the core density is shallow, and no critical curves form around the subhalo, resulting in a zero cross-section. As the FDM mass increases, the core radius decreases, and the central core density increases. The cross-section reaches its maximum when the core radius is approximately

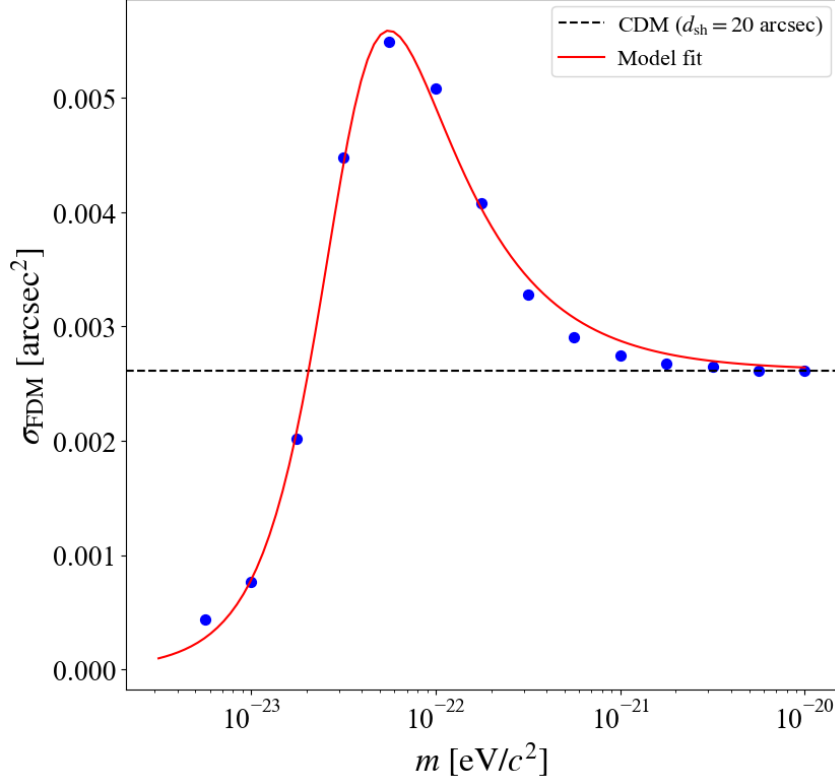


Figure 7.6: Similar to Fig. 7.3, but including the baryon distribution. The red line shows the fitting result of our analytic model with the fitting parameters being  $m_{\text{peak}} = 10^{-22.4} \text{ eV}/c^2$ ,  $\sigma_{\text{FDM}}^{\text{peak}} = 0.007 \text{ arcsec}^2$ , and  $\Delta_{\log_{10} m} = 0.31$ . This figure is taken from [49].

equal to the size of the critical curve. This is because the enclosed mass within the soliton core radius exceeds that of the NFW profile within the same radius. For larger FDM masses, the cross-section scales as  $\sigma_{\text{FDM}} \propto m^{-1}$ , approaching to the CDM case. The analytic model in Eq. 7.1 accurately describes the dependence of the single subhalo cross-section on the FDM mass. Additionally, we investigate how the two key quantities in the analytic model, the peak FDM mass  $m_{\text{peak}}$  and the peak cross-section  $\sigma_{\text{FDM}}^{\text{peak}}$ , depend on the subhalo mass  $M_{\text{sh}}$  and its distance from the host halo center  $d_{\text{sh}}$ .

The total cross-section, which is the sum of the cross-sections of all subhalos, is obtained by integrating the cross-section for each subhalo over both  $M_{\text{sh}}$  and  $d_{\text{sh}}$  under the consideration of the subhalo mass function. In this study, we assume that the spatial distribution of the subhalos follows the mass distribution of the host halo. Our findings show that the FDM mass around  $m \simeq 10^{-22} \text{ eV}/c^2$  results in the largest cross-section, which is several times larger than the total cross-section produced by CDM subhalos.

Subhalos with mass  $M_{\text{sh}} \gtrsim 10^{10} M_{\odot}$  contain a sufficient amount of baryon due to deep gravitational potential. Therefore, we investigate the effect of the baryon distribution on both the single and total cross-sections. We assume that the baryon distribution follows the Hernquist profile, with the total mass derived from the stellar-to-halo mass relation. While it is likely that the presence of stars in the central regions of galaxies would alter the dark matter distribution, we neglect this effect and simply add the baryon profile to the underlying dark matter density profile. This decision is made due to the current lack of an analytical description of how baryons modify the dark matter profile. As expected, the presence of baryons increases both the single and total cross-sections. The FDM

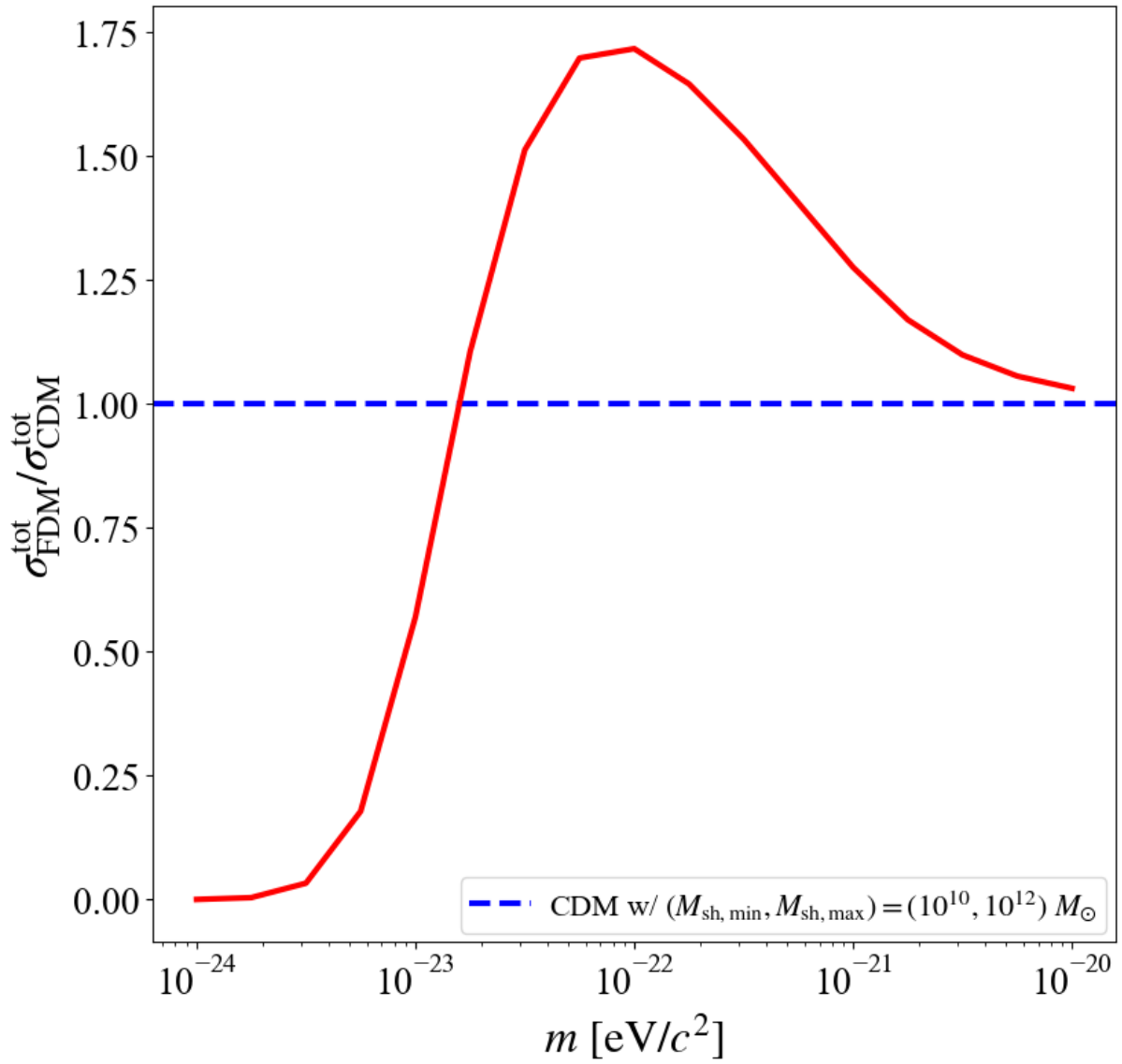


Figure 7.7: Similar to Fig. 7.4, but including the baryon contribution. This figure is taken from [49].

mass dependence of the single cross-section remains similar to the case without baryons. However, the ratio of the peak cross-section for FDM subhalos to that of CDM subhalos is reduced in the presence of baryons. This suppression is also reflected in the total cross-section, where the peak is about 1.8 times larger than the total cross-section for CDM subhalos. Given that the observed cross-section is approximately ten times larger than the CDM prediction, it indicates that the FDM model, regardless of mass, cannot produce a cross-section large enough to match the observations from cluster galaxies.

One key assumption that we need to discuss is the sphericity of the host and subhalos. If we take into account the ellipticity of the host and subhalos, we expect that the size of the critical curve would increase due to the effect of the enhanced shear. When the ellipticity is less than one, the peak FDM mass is expected to decrease to align the core radius with the enlarged critical curve. To obtain a reliable constraint on the FDM mass, further detailed modeling is required, including factors such as ellipticity. Additionally, precise modeling for the baryon distribution within subhalos, accurate redshifts for both the source and lens planes, and the detailed mass distribution of the host halo would provide robust constraints on the FDM mass.

An additional assumption that should be discussed is the neglect of any modifications of the dark matter profile in the presence of baryons. In this study, we simply add the baryon component because there is still uncertainty about how the dark matter density profile is altered when baryons are present. In the CDM case, this could be modeled by considering adiabatic contraction [279, 278]. In the FDM model, while the soliton core is known to be described by the ground state solution of the SP equation in the presence of a baryon potential, an additional condition, such as the core-halo mass relation, is required to determine the central density of the soliton core for a given halo mass, which has not yet been extensively explored. To the best of our knowledge, [280] is the only study that conducts a zoom-in simulation of a single FDM halo with baryon physics, finding that the soliton core becomes denser and the core radius decreases. We expect that the peak FDM mass would be smaller than what we find in this study, and the peak cross-section would be larger, potentially alleviating the discrepancy.

By refining our model and incorporating more realistic extensions specific to each galaxy cluster, we expect to assess the validity of the FDM model more rigorously. Since the cross-section varies with the FDM mass, a more detailed investigation could help place better constraints on the FDM mass. Additionally, because the soliton core influences other strong gravitational lensing phenomena, such as flux anomalies and time delays, our model could be extended to investigate these effects as well. We hope that our work in this chapter will be an important step toward a deeper understanding of the nature of dark matter.

# Chapter 8

## Conclusions

Understanding the nature of dark matter remains one of the most profound challenges in cosmology. Investigations on small scales are particularly crucial, as they offer unique insights into the distribution of dark matter and thus the nature of dark matter. Among the various methods, strong gravitational lensing is one of the most effective methods for probing small-scale structures. Recent advancements in observational techniques have yielded an increasing observed number of strong gravitational lensing events. Especially, highly magnified individual/binary stars such as Icarus, Earendel, Mothra, and Dragon, have been observed near the critical curve of galaxy clusters, where the magnification of background sources becomes mathematically infinite. From these detections, we can estimate in detail the shape and the distribution of the critical curves and thus the mass distribution within the lens objects. These observations indicate the need for theoretical studies of how small-scale structures, associated with the nature of dark matter, affect the shape and the distribution of critical curves. Combining these theoretical studies with observations can provide insights into the nature of dark matter.

In this thesis, we first study the effect of microlenses near the macro-critical curve of the galaxy cluster, focusing on how micro-critical curves influence the detection of highly magnified stars. We develop an analytic model for the high-magnification tail of the probability distribution function (PDF), showing that the probability scales with the independent number of micro-critical curves, consistent with lensing simulations. As an application of the model, we calculate the number of Icarus-like events near the macro-critical curve of the MACS J1149 cluster. We constrain the parameter space of microlens that is consistent with the observed event number of Icarus, finding that stars that contribute to the intra-cluster light (ICL stars) can explain the single event of Icarus. We further examine the existence of the primordial black holes (PBHs) as microlenses in addition to ICL stars, resulting in the mass fraction  $f_{\text{PBH}} \gtrsim 0.2$  is excluded at the 95% confidence interval (CI) when the PBH mass is around  $1 M_{\odot}$ , since such a high mass fraction reduce the number of independent micro-critical curves.

We then investigate how substructures, such as subhalos, perturb the macro-critical curve of the galaxy cluster. A possible observed example is Mothra, located 0.07 arcseconds from the estimated macro-critical curve of the MACS0416 cluster. However, its counter-image has not been observed. This phenomenon could be explained by the presence of milli-lensing, however, it also might be explained by astrometric shifts in the macro-critical curve. We derive the general analytic formula which relates the variance of fluctuation in the macro-critical curve and that in surface density due to substructures. As a specific example of substructures, we consider the cold dark matter (CDM) subhalos

and show that the position of Mothra can be explained if the maximum subhalo mass is around  $10^9 M_\odot/h$ . We also consider the granular structures in the fuzzy dark matter (FDM) model, finding that a particle mass of  $m \simeq 10^{-24} \text{ eV}/c^2$  is required to account for the observed location of Mothra.

Finally, we study the galaxy-galaxy strong lensing (GGSL) cross-section within the framework of the FDM model. The GGSL cross-section, defined as the total area enclosed by secondary caustics generated by substructures, is observed to exceed predictions of the CDM model by an order of magnitude. We numerically and analytically show that FDM subhalos can produce larger cross-sections than CDM subhalos due to the presence of soliton cores in FDM. The peak cross-section can be achieved when the soliton core radius coincides with the size of the (secondary) critical curve, with a maximum ratio of approximately two between FDM and CDM models when the baryon distribution is included. These findings suggest that while FDM subhalos enhance the cross-section, the FDM model may struggle to explain the observed GGSL cross-section.

While the constraints on the properties of dark matter obtained in this thesis are less stringent than those found in the literature, the methods developed here represent an important step toward uncovering the nature of dark matter through future observations. In particular, future observations of more highly magnified events (caustic crossing events) may provide evidence for PBHs or FDM. Although Icarus exhibits a single peak of caustic crossing during the observational period, discovering events where a source undergoes two caustic crossings could enable the direct estimation of the size of the caustic and, consequently, the size of the microlenses, providing more direct evidence for PBHs. For this purpose, long-term monitoring over many years would be essential. Furthermore, discovering a larger number of ultrahigh magnification images through such observations could lead to a more detailed understanding of the shape of the macro-critical curve. Investigating the distribution of fluctuations could provide evidence for FDM, as the numerous granular structures lead to frequent fluctuations. These highly magnified events are expected to be observed by the James Webb Space Telescope (JWST), the Nancy Grace Roman Space Telescope, the Rubin Observatory, and the Thirty Meter Telescope (TMT). The JWST has already identified more than 40 microlensed individual stars (red supergiant stars) near the critical curve of the Abell 370 galaxy cluster [217], demonstrating the feasibility of such observations. Regarding the GGSL, the Euclid mission and the Legacy Survey of Space and Time (LSST) through the Rubin Observatory are expected to increase the sample size of the galaxy cluster significantly. Such large statistical samples enable us a direct comparison of the number of the GGSL without relying on mass modeling, providing robust insights into dark matter subhalo abundance and its density profile.

We expect that these future observations, combined with a more realistic extension of our analytic models, will provide stronger implications on the fundamental properties of dark matter. By continuing such studies to constrain the nature of dark matter from the perspective of observational cosmology, it is expected that many dark matter models proposed in particle physics would be ruled out. Furthermore, it will help narrow the targets of collider experiments and direct and indirect detections. We hope that continued progress in these areas will lead to a breakthrough, allowing us to finally uncover the true nature of dark matter within our lifetime.

# Acknowledgement

First and foremost, I would like to express my deepest gratitude to Professor Masamune Oguri at Chiba University. He has always made time for weekly one-on-one discussions and welcomed me to his office on other days for additional discussions. Our group meetings, where we discuss the latest research shown in arXiv, have also been invaluable for broadening my understanding of gravitational lensing and observational cosmology. His quick and thoughtful responses have always been incredibly helpful. During my Master's program, he taught me how to conduct research and write papers. During my PhD program, I learned how to conduct research independently, including reading papers critically, finding new research topics, carrying out studies effectively, writing papers, making presentation slides, giving presentations, and engaging in meaningful discussions with others. Thanks to his guidance, I could independently contact and visit Professor Massimo Meneghetti, and complete a paper with him, as a single researcher. Moreover, he has always respected my career choices, both during and after my PhD period, for which I am deeply grateful. I cannot thank him enough for his invaluable support throughout my academic journey.

I would also like to express my gratitude to Professor Massimo Meneghetti at INAF OAS Bologna. I first met him at the Winter School on Cosmology in Tonale, where we had a fruitful discussion. I was very honored that he chose my poster as the best poster. The next year, he warmly welcomed me to INAF OAS Bologna and we were able to begin our collaboration. This experience was one of my first opportunities to collaborate with an international researcher, and I deeply appreciate him for providing this chance. Furthermore, he gave me the opportunity to have discussions with European researchers, allowing me to broaden my perspective outside of Japan.

During the review of my doctoral dissertation, I would like to thank the committee members: Professor Masahiro Takada, Professor Hitoshi Murayama, Professor Jun'ichi Yokoyama, Professor Yuta Michimura, and Professor Hideyuki Tagoshi. Their valuable comments helped me identify parts I did not understand sufficiently and allowed me to discuss them in more detail. I also learned the importance of future-oriented discussions. I realized that our models can be used not only to constrain the nature of dark matter from existing observational results but also to determine what kinds of observations should be performed to detect them in the future.

In the fuzzy dark matter project, I had numerous opportunities to collaborate and engage in discussions with outstanding researchers. First and foremost, I am deeply grateful to Professor Ayuki Kamada. I am impressed by his deep physics insight and broad knowledge of both particle physics and cosmology, my goal was to be able to make discussions as he does. Through discussion, I could identify gaps in my understanding, which helped me to improve my logical thinking. When I visited Warsaw University, I had productive discussions with him and he gave me useful advice on my presentation, which was invaluable to me. I would also like to express my heartfelt gratitude to Professor

Kohei Kamada. During my first year as a PhD student, I had weekly discussions with him, where he taught me how to understand and interpret the results of numerical calculations. These discussions provided the basis for developing analytic models, an important step that influenced my subsequent research. I am equally grateful to Professor Naoki Yoshida. He has always provided fresh perspectives throughout the project, allowing me to look at the results from different angles. Finally, I would like to thank Professor Atsushi Taruya. Our discussions during conferences were valuable and offered important opportunities for me to deepen my understanding.

During the gravitational lensing projects, I had the privilege of engaging in discussions with distinguished researchers. At Chiba University, where I conducted my PhD research, I am particularly grateful to Doctor Katsuya Abe. He was my closest researcher and I often questioned and had extensive discussions with him. Through our collaboration, I learned how to conduct research more efficiently. I also had the opportunity to discuss with Professor Jordi Miralda-Escudé during my visit to the University of Barcelona, as well as Professor José Maria Diego, Professor Tom Broadhurst, and Doctor José Maria Palencia during my visit to IFCA in Santander. Additionally, I had fruitful online discussions with Professor Georgios Vernardos. I had insightful discussions with Professor Jeremy Lim and Doctor Alfred Amruth at Chiba University. These experiences greatly broadened my knowledge and helped me expand my academic network beyond Japan.

The starting point of my journey in astrophysics and cosmology dates back to my high school days. Professor Shun Saito, a graduate of our high school, gave us a talk on dark matter and dark energy nine years ago. I was deeply impressed by his talk and found it very interesting, and I still clearly remember receiving a pamphlet from the IPMU with his signature. Finally, during my PhD period, I had the opportunity to meet him again in person. I am truly grateful to him for inspiring me at such an early stage.

I would also like to thank some of my best friends. Yugo Inutsuka has been my best friend since the beginning of junior high school. Since then, we have worked hard and encouraged each other, which has significantly shaped the foundation of my approach to learning physics and mathematics. Although we are now in different fields of physics, he still offers me insightful ideas whenever we talk. Shintaro Miki and I met during our first year of undergraduate studies. I often asked him about physics and mathematics and deeply admired his profound understanding. Masaya Amo and I met at a summer school during our first year of the master's program. Since then, even though we have been working on different topics, his energy and passion have always inspired me and driven me to keep going. Greta Toni is my best friend in Italy, whom I met at a winter school on cosmology. When I visited Bologna, she kindly helped me find my accommodation. Thanks to her, I was able to join a wonderful group in Bologna and do my research comfortably.

I would also like to thank the members of the astrophysics group at Chiba University, UTAP and RESCEU at the University of Tokyo, as well as INAF OAS Bologna and the University of Bologna. They have always provided me with comfortable and supportive research environments.

Finally, I am deeply grateful to my partner, Mina Uehara. She has always been by my side, offering unwavering support. Her presence allowed me to continue my studies comfortably. I am also profoundly thankful to my brother and parents. Their constant support and care, especially when I was unwell, have been invaluable.

# Bibliography

- [1] F. Zwicky, “Die Rotverschiebung von extragalaktischen Nebeln,” *Helvetica Physica Acta*, vol. 6, pp. 110–127, Jan. 1933.
- [2] H. Andernach and F. Zwicky, “English and Spanish Translation of Zwicky’s (1933) The Redshift of Extragalactic Nebulae,” *arXiv e-prints*, p. arXiv:1711.01693, Nov. 2017.
- [3] V. C. Rubin and J. Ford, W. Kent, “Rotation of the Andromeda Nebula from a Spectroscopic Survey of Emission Regions,” *ApJ*, vol. 159, p. 379, Feb. 1970.
- [4] K. C. Freeman, “On the Disks of Spiral and S0 Galaxies,” *ApJ*, vol. 160, p. 811, June 1970.
- [5] Planck Collaboration, “Planck 2018 results. VI. Cosmological parameters,” *A&A*, vol. 641, p. A6, Sept. 2020.
- [6] G. Bertone, D. Hooper, and J. Silk, “Particle dark matter: evidence, candidates and constraints,” *Phys. Rep.*, vol. 405, no. 5-6, pp. 279–390, Jan. 2005.
- [7] H. Baer, K.-Y. Choi, J. E. Kim, and L. Roszkowski, “Dark matter production in the early Universe: Beyond the thermal WIMP paradigm,” *Phys. Rep.*, vol. 555, pp. 1–60, Feb. 2015.
- [8] CMS Collaboration, “Search for dark matter produced in association with a single top quark or a top quark pair in proton-proton collisions at  $\sqrt{s} = 13$  TeV,” *arXiv e-prints*, p. arXiv:1901.01553, Jan. 2019.
- [9] ATLAS Collaboration, “Search for dark matter in events with missing transverse momentum and a Higgs boson decaying into two photons in  $pp$  collisions at  $\sqrt{s} = 13$  TeV with the ATLAS detector,” *arXiv e-prints*, p. arXiv:2104.13240, Apr. 2021.
- [10] E. Aprile, J. Aalbers, F. Agostini, M. Alfonsi, L. Althueser, F. D. Amaro, M. Anthony, F. Arneodo, L. Baudis, B. Bauermeister, M. L. Benabderrahmane, T. Berger, P. A. Breur, A. Brown, A. Brown, E. Brown, S. Bruenner, G. Bruno, R. Budnik, C. Capelli, J. M. R. Cardoso, D. Cichon, D. Coderre, A. P. Colijn, J. Conrad, J. P. Cussonneau, M. P. Decowski, P. de Perio, P. di Gangi, A. di Giovanni, S. Diglio, A. Elykov, G. Eurin, J. Fei, A. D. Ferella, A. Fieguth, W. Fulgione, A. Gallo Rosso, M. Galloway, F. Gao, M. Garbini, C. Geis, L. Grandi, Z. Greene, H. Qiu, C. Hasterok, E. Hogenbirk, J. Howlett, R. Itay, F. Joerg, B. Kaminsky, S. Kazama, A. Kish, G. Koltman, H. Landsman, R. F. Lang, L. Levinson, Q. Lin, S. Lindemann, M. Lindner, F. Lombardi, J. A. M. Lopes, J. Mahlstedt, A. Manfredini, T. Marrodán Undagoitia, J. Masbou, D. Masson, M. Messina, K. Micheneau,

- K. Miller, A. Molinario, K. Morâ, M. Murra, J. Naganoma, K. Ni, U. Oberlack, B. Pelssers, F. Piastra, J. Pienaar, V. Pizzella, G. Plante, R. Podviianiuk, N. Priel, D. Ramírez García, L. Rauch, S. Reichard, C. Reuter, B. Riedel, A. Rizzo, A. Rocchetti, N. Rupp, J. M. F. Dos Santos, G. Sartorelli, M. Scheibelhut, S. Schindler, J. Schreiner, D. Schulte, M. Schumann, L. Scotto Lavina, M. Selvi, P. Shagin, E. Shockley, M. Silva, H. Simgen, D. Thers, F. Toschi, G. Trincherro, C. Tunnell, N. Upole, M. Vargas, O. Wack, H. Wang, Z. Wang, Y. Wei, C. Weinheimer, C. Wittweg, J. Wulf, J. Ye, Y. Zhang, T. Zhu, and Xenon Collaboration, “Dark Matter Search Results from a One Ton-Year Exposure of XENON1T,” *Phys. Rev. Lett.*, vol. 121, no. 11, p. 111302, Sept. 2018.
- [11] J. Aalbers, D. S. Akerib, C. W. Akerlof, A. K. Al Musalhi, F. Alder, A. Alqah-tani, S. K. Alsum, C. S. Amarasinghe, A. Ames, T. J. Anderson, N. Angelides, H. M. Araújo, J. E. Armstrong, M. Arthurs, S. Azadi, A. J. Bailey, A. Baker, J. Balajthy, S. Balashov, J. Bang, J. W. Bargemann, M. J. Barry, J. Barthel, D. Bauer, A. Baxter, K. Beattie, J. Belle, P. Beltrame, J. Bensinger, T. Benson, E. P. Bernard, A. Bhatti, A. Biekert, T. P. Biesiadzinski, H. J. Birch, B. Birrittella, G. M. Blockinger, K. E. Boast, B. Boxer, R. Bramante, C. A. J. Brew, P. Brás, J. H. Buckley, V. V. Bugaev, S. Burdin, J. K. Busenitz, M. Buuck, R. Cabrera, C. Carels, D. L. Carlsmith, B. Carlson, M. C. Carmona-Benitez, M. Cascella, C. Chan, A. Chawla, H. Chen, J. J. Cherwinka, N. I. Chott, A. Cole, J. Coleman, M. V. Converse, A. Cottle, G. Cox, W. W. Craddock, O. Creaner, D. Curran, A. Currie, J. E. Cutter, C. E. Dahl, A. David, J. Davis, T. J. R. Davison, J. Delgado, S. Dey, L. de Viveiros, A. Dobi, J. E. Y. Dobson, E. Druskiewicz, A. Dushkin, T. K. Edberg, W. R. Edwards, M. M. Elnimr, W. T. Emmet, S. R. Eriksen, C. H. Faham, A. Fan, S. Fayer, N. M. Fearon, S. Fiorucci, H. Flaecher, P. Ford, V. B. Francis, E. D. Fraser, T. Fruth, R. J. Gaitskell, N. J. Gantos, D. Garcia, A. Geffre, V. M. Gehman, J. Genovesi, C. Ghag, R. Gibbons, E. Gibson, M. G. D. Gilchriese, S. Gokhale, B. Gomber, J. Green, A. Greenall, S. Greenwood, M. G. D. van der Grinten, C. B. Gwilliam, C. R. Hall, S. Hans, K. Hanzel, A. Harrison, E. Hartigan-O’Connor, S. J. Haselschwardt, M. A. Hernandez, S. A. Hertel, G. Heuermann, C. Hjermfelt, M. D. Hoff, E. Holtom, J. Y. K. Hor, M. Horn, D. Q. Huang, D. Hunt, C. M. Ignarra, R. G. Jacobsen, O. Jahangir, R. S. James, S. N. Jeffery, W. Ji, J. Johnson, A. C. Kaboth, A. C. Kamaha, K. Kamdin, V. Kasey, K. Kazkaz, J. Keefner, D. Khaitan, M. Khaleeq, A. Khazov, I. Khurana, Y. D. Kim, C. D. Kocher, D. Kodroff, L. Korley, E. V. Korolkova, J. Kras, H. Kraus, S. Kravitz, H. J. Krebs, L. Kreczko, B. Krikler, V. A. Kudryavtsev, S. Kyre, B. Landerud, E. A. Leason, C. Lee, J. Lee, D. S. Leonard, R. Leonard, K. T. Lesko, C. Levy, J. Li, F. T. Liao, J. Liao, J. Lin, A. Lindote, R. Linehan, W. H. Lippincott, R. Liu, X. Liu, Y. Liu, C. Loniewski, M. I. Lopes, E. Lopez Asamar, B. López Paredes, W. Lorenzon, D. Lucero, S. Luitz, J. M. Lyle, P. A. Majewski, J. Makkinje, D. C. Malling, A. Manalaysay, L. Manenti, R. L. Mannino, N. Marangou, M. F. Marzioni, C. Maupin, M. E. McCarthy, C. T. McConnell, D. N. McKinsey, J. McLaughlin, Y. Meng, J. Migneault, E. H. Miller, E. Mizrachi, J. A. Mock, A. Monte, M. E. Monzani, J. A. Morad, J. D. Morales Mendoza, E. Morrison, B. J. Mount, M. Murdy, A. S. J. Murphy, D. Naim, A. Naylor, C. Nedlik, C. Nehr Korn, F. Neves, A. Nguyen, J. A. Nikoleyczik, A. Nilima, J. O’Dell, F. G. O’Neill, K. O’Sullivan, I. Olcina, M. A. Olevitch, K. C. Oliver-Mallory, J. Orpwood, D. Pagenkopf, S. Pal, K. J. Palladino, J. Palmer, M. Pangilinan, N. Parveen, S. J.

- Patton, E. K. Pease, B. Penning, C. Pereira, G. Pereira, E. Perry, T. Pershing, I. B. Peterson, A. Piepke, J. Podczerwinski, D. Porzio, S. Powell, R. M. Preece, K. Pushkin, Y. Qie, B. N. Ratcliff, J. Reichenbacher, L. Reichhart, C. A. Rhyne, A. Richards, Q. Riffard, G. R. C. Rischbieter, J. P. Rodrigues, A. Rodriguez, H. J. Rose, R. Rosero, P. Rossiter, T. Rushton, G. Rutherford, D. Rynders, J. S. Saba, D. Santone, A. B. M. R. Sazzad, R. W. Schnee, P. R. Scovell, D. Seymour, S. Shaw, T. Shutt, J. J. Silk, C. Silva, G. Sinev, K. Skarpaas, W. Skulski, R. Smith, M. Solmaz, V. N. Solovov, P. Sorensen, J. Soria, I. Stancu, M. R. Stark, A. Stevens, T. M. Stiegler, K. Stifter, R. Studley, B. Suerfu, T. J. Sumner, P. Sutcliffe, N. Swanson, M. Szydagis, M. Tan, D. J. Taylor, R. Taylor, W. C. Taylor, D. J. Temples, B. P. Tennyson, P. A. Terman, K. J. Thomas, D. R. Tiedt, M. Timalsina, W. H. To, A. Tomás, Z. Tong, D. R. Tovey, J. Tranter, M. Trask, M. Tripathi, D. R. Tronstad, C. E. Tull, W. Turner, L. Tvrznikova, U. Utku, J. Va'Vra, A. Vacheret, A. C. Vaitkus, J. R. Verbus, E. Voirin, W. L. Waldron, A. Wang, B. Wang, J. J. Wang, W. Wang, Y. Wang, J. R. Watson, R. C. Webb, A. White, D. T. White, J. T. White, R. G. White, T. J. Whitis, M. Williams, W. J. Wisniewski, M. S. Witherell, F. L. H. Wolfs, J. D. Wolfs, S. Woodford, D. Woodward, S. D. Worm, C. J. Wright, Q. Xia, X. Xiang, Q. Xiao, J. Xu, M. Yeh, J. Yin, I. Young, P. Zarzhitsky, A. Zuckerman, E. A. Zweig, and Lux-Zeplin Collaboration, "First Dark Matter Search Results from the LUX-ZEPLIN (LZ) Experiment," *Phys. Rev. Lett.*, vol. 131, no. 4, p. 041002, July 2023.
- [12] Y. Meng, Z. Wang, Y. Tao, A. Abdukerim, Z. Bo, W. Chen, X. Chen, Y. Chen, C. Cheng, Y. Cheng, X. Cui, Y. Fan, D. Fang, C. Fu, M. Fu, L. Geng, K. Giboni, L. Gu, X. Guo, K. Han, C. He, J. He, D. Huang, Y. Huang, Z. Huang, R. Hou, X. Ji, Y. Ju, C. Li, M. Li, S. Li, S. Li, Q. Lin, J. Liu, X. Lu, L. Luo, W. Ma, Y. Ma, Y. Mao, N. Shaheed, X. Ning, N. Qi, Z. Qian, X. Ren, C. Shang, G. Shen, L. Si, W. Sun, A. Tan, A. Wang, M. Wang, Q. Wang, S. Wang, S. Wang, W. Wang, X. Wang, M. Wu, W. Wu, J. Xia, M. Xiao, X. Xiao, P. Xie, B. Yan, X. Yan, J. Yang, Y. Yang, C. Yu, J. Yuan, Y. Yuan, D. Zhang, M. Zhang, P. Zhang, T. Zhang, L. Zhao, Q. Zheng, J. Zhou, N. Zhou, X. Zhou, Y. Zhou, and PandaX-4T Collaboration, "Dark Matter Search Results from the PandaX-4T Commissioning Run," *Phys. Rev. Lett.*, vol. 127, no. 26, p. 261802, Dec. 2021.
- [13] D. Hooper and L. Goodenough, "Dark matter annihilation in the Galactic Center as seen by the Fermi Gamma Ray Space Telescope," *Physics Letters B*, vol. 697, no. 5, pp. 412–428, Mar. 2011.
- [14] R. Abbasi, M. Ackermann, J. Adams, S. K. Agarwalla, J. A. Aguilar, M. Ahlers, J. M. Alameddine, N. M. Amin, K. Andeen, G. Anton, C. Argüelles, Y. Ashida, S. Athanasiadou, S. N. Axani, X. Bai, A. Balagopal, M. Baricevic, S. W. Barwick, V. Basu, S. Baur, R. Bay, J. J. Beatty, K. H. Becker, J. Becker Tjus, J. Beise, C. Bellenghi, S. BenZvi, D. Berley, E. Bernardini, D. Z. Besson, G. Binder, D. Bindig, E. Blaufuss, S. Blot, F. Bontempo, J. Y. Book, C. Boscolo Meneguolo, S. Böser, O. Botner, J. Böttcher, E. Bourbeau, J. Braun, B. Brinson, J. Brostean-Kaiser, R. T. Burley, R. S. Busse, D. Butterfield, M. A. Campana, K. Carloni, E. G. Carnie-Bronca, S. Chattopadhyay, N. Chau, C. Chen, Z. Chen, D. Chirkin, S. Choi, B. A. Clark, L. Classen, A. Coleman, G. H. Collin, A. Connolly, J. M. Conrad, P. Coppin, P. Correa, S. Countryman, D. F. Cowen, P. Dave, C. De

Clercq, J. J. DeLaunay, D. Delgado López, H. Dembinski, K. Deoskar, A. Desai, P. Desiati, K. D. de Vries, G. de Wasseige, T. DeYoung, A. Diaz, J. C. Díaz-Vélez, M. Dittmer, A. Domi, H. Dujmovic, M. A. DuVernois, T. Ehrhardt, C. El Aisati, P. Eller, R. Engel, H. Erpenbeck, J. Evans, P. A. Evenson, K. L. Fan, K. Fang, A. R. Fazely, A. Fedynitch, N. Feigl, S. Fiedlschuster, C. Finley, L. Fischer, D. Fox, A. Franckowiak, E. Friedman, A. Fritz, P. Fürst, T. K. Gaisser, J. Gallagher, E. Ganster, A. Garcia, L. Gerhardt, A. Ghadimi, C. Glaser, T. Glauch, T. Glüsenkamp, N. Goehlke, J. G. Gonzalez, S. Goswami, D. Grant, S. J. Gray, S. Griffin, S. Griswold, C. Günther, M. Gustafsson, P. Gutjahr, C. Haack, A. Hallgren, R. Halliday, L. Halve, F. Halzen, T. Hambye, H. Hamdaoui, M. Ha Minh, K. Hanson, J. Hardin, A. A. Harnisch, P. Hatch, A. Haungs, K. Helbing, J. Hellrung, F. Henningsen, L. Heuermann, N. Heyer, S. Hickford, A. Hidvegi, C. Hill, G. C. Hill, K. D. Hoffman, K. Hoshina, W. Hou, T. Huber, K. Hultqvist, M. Hünnefeld, R. Hussain, K. Hymon, S. In, A. Ishihara, M. Jacquart, M. Jansson, G. S. Japaridze, K. Jayakumar, M. Jeong, M. Jin, B. J. P. Jones, D. Kang, W. Kang, X. Kang, A. Kappes, D. Kappesser, L. Kardum, T. Karg, M. Karl, A. Karle, U. Katz, M. Kauer, J. L. Kelley, A. Khatee Zathul, A. Kheirandish, J. Kiryluk, S. R. Klein, A. Kochocki, R. Koirala, H. Kolanoski, T. Kontrimas, L. Köpke, C. Kopper, D. J. Koskinen, P. Koundal, M. Kovacevich, M. Kowalski, T. Kozynets, K. Kruiswijk, E. Krupczak, A. Kumar, E. Kun, N. Kurahashi, N. Lad, C. Lagunas Gualda, M. Lamoureux, M. J. Larson, F. Lauber, J. P. Lazar, J. W. Lee, K. Leonard DeHolt, A. Leszczyńska, M. Lincetto, Q. R. Liu, M. Liubarska, E. Lohfink, C. Love, C. J. Lozano Mariscal, L. Lu, F. Lucarelli, A. Ludwig, W. Luszczyk, Y. Lyu, J. Madson, K. B. M. Mahn, Y. Makino, S. Mancina, W. Marie Sainte, I. C. Mariş, S. Marka, Z. Marka, M. Marsee, I. Martinez-Soler, R. Maruyama, F. Mayhew, T. McElroy, F. McNally, J. V. Mead, K. Meagher, S. Mechbal, A. Medina, M. Meier, S. Meighen-Berger, Y. Merckx, L. Merten, J. Micallef, T. Montaruli, R. W. Moore, Y. Morii, R. Morse, M. Moulai, T. Mukherjee, R. Naab, R. Nagai, M. Nakos, U. Naumann, J. Necker, M. Neumann, H. Niederhausen, M. U. Nisa, A. Noell, S. C. Nowicki, A. Obertacke Pollmann, V. O'Dell, M. Oehler, B. Oeyen, A. Olivas, R. Orsoe, J. Osborn, E. O'Sullivan, H. Pandya, N. Park, G. K. Parker, E. N. Paudel, L. Paul, C. Pérez de los Heros, J. Peterson, S. Philippen, S. Pieper, A. Pizzuto, M. Plum, A. Pontén, Y. Popovych, M. Prado Rodriguez, B. Pries, R. Procter-Murphy, G. T. Przybylski, J. Rack-Helleis, K. Rawlins, Z. Rechav, A. Rehman, P. Reichherzer, G. Renzi, E. Resconi, S. Reusch, W. Rhode, M. Richman, B. Riedel, E. J. Roberts, S. Robertson, S. Rodan, G. Roellinghoff, M. Rongen, C. Rott, T. Ruhe, L. Ruohan, D. Ryckbosch, S. Athanasiadou, I. Safa, J. Saffer, D. Salazar-Gallegos, P. Sampathkumar, S. E. Sanchez Herrera, A. Sandrock, M. Santander, S. Sarkar, S. Sarkar, J. Savelberg, P. Savina, M. Schaufel, H. Schieler, S. Schindler, B. Schlüter, F. Schlüter, T. Schmidt, J. Schneider, F. G. Schröder, L. Schumacher, G. Schwefer, S. Sclafani, D. Seckel, S. Seunarine, R. Shah, A. Sharma, S. Shefali, N. Shimizu, M. Silva, B. Skrzypek, B. Smithers, R. Snihur, J. Soedingrekso, A. Søggaard, D. Soldin, G. Sommani, C. Spannfellner, G. M. Spiczak, C. Spiering, M. Stamatikos, T. Stanev, T. Stezelberger, T. Stürwald, T. Stuttard, G. W. Sullivan, I. Taboada, S. Ter-Antonyan, W. G. Thompson, J. Thwaites, S. Tilav, K. Tollefson, C. Tönnis, S. Toscano, D. Tosi, A. Trettin, C. F. Tung, R. Turcotte, J. P. Twagirayezu, B. Ty, M. A. Unland Elorrieta, A. K. Upadhyay, K. Upshaw, N. Valtonen-Mattila, J. Vandenbroucke, N. van Eijndhoven, D. Vannerom, J. van

- Santen, J. Vara, J. Veitch-Michaelis, M. Venugopal, S. Verpoest, D. Veske, C. Walck, T. B. Watson, C. Weaver, P. Weigel, A. Weindl, J. Weldert, C. Wendt, J. Werthebach, M. Weyrauch, N. Whitehorn, C. H. Wiebusch, N. Willey, D. R. Williams, M. Wolf, G. Wrede, X. W. Xu, J. P. Yanez, E. Yildizci, S. Yoshida, F. Yu, S. Yu, T. Yuan, Z. Zhang, P. Zhelnin, and IceCube Collaboration, “Search for neutrino lines from dark matter annihilation and decay with IceCube,” *Phys. Rev. D*, vol. 108, no. 10, p. 102004, Nov. 2023.
- [15] K. Abe, Y. Hayato, K. Hiraide, K. Ieki, M. Ikeda, J. Kameda, Y. Kanemura, R. Kaneshima, Y. Kashiwagi, Y. Kataoka, S. Miki, S. Mine, M. Miura, S. Moriyama, Y. Nakano, M. Nakahata, S. Nakayama, Y. Noguchi, K. Okamoto, K. Sato, H. Sekiya, H. Shiba, K. Shimizu, M. Shiozawa, Y. Sonoda, Y. Suzuki, A. Takeda, Y. Takemoto, A. Takenaka, H. Tanaka, S. Watanabe, T. Yano, S. Han, T. Kajita, K. Okumura, T. Tashiro, T. Tomiya, X. Wang, J. Xia, S. Yoshida, G. D. Megias, P. Fernandez, L. Labarga, N. Ospina, B. Zaldivar, B. W. Pointon, E. Kearns, J. L. Raaf, L. Wan, T. Wester, J. Bian, N. J. Griskevich, W. R. Kropp, S. Locke, M. B. Smy, H. W. Sobel, V. Takhistov, A. Yankelevich, J. Hill, R. G. Park, B. Bodur, K. Scholberg, C. W. Walter, L. Bernard, A. Coffani, O. Drapier, S. El Hedri, A. Giampaolo, T. A. Mueller, A. D. Santos, P. Paganini, B. Quilain, T. Ishizuka, T. Nakamura, J. S. Jang, J. G. Learned, K. Choi, S. Cao, L. H. V. Anthony, D. Martin, M. Scott, A. A. Sztuc, Y. Uchida, V. Berardi, M. G. Catanesi, E. Radicioni, N. F. Calabria, L. N. Machado, G. De Rosa, G. Collazuol, F. Iacob, M. Lamoureux, M. Mattiuzzi, L. Ludovici, M. Gonin, G. Pronost, C. Fujisawa, Y. Maekawa, Y. Nishimura, M. Friend, T. Hasegawa, T. Ishida, T. Kobayashi, M. Jakkapu, T. Matsubara, T. Nakadaira, K. Nakamura, Y. Oyama, K. Sakashita, T. Sekiguchi, T. Tsukamoto, T. Boschi, F. Di Lodovico, J. Gao, A. Goldsack, T. Katori, J. Migenda, M. Taani, S. Zsoldos, Y. Kotsar, H. Ozaki, A. T. Suzuki, Y. Takeuchi, C. Bronner, J. Feng, T. Kikawa, M. Mori, T. Nakaya, R. A. Wendell, K. Yasutome, S. J. Jenkins, N. McCauley, P. Mehta, K. M. Tsui, Y. Fukuda, Y. Itow, H. Menjo, K. Ninomiya, J. Lagoda, S. M. Lakshmi, M. Mandal, P. Mijakowski, Y. S. Prabhu, J. Zalipska, M. Jia, J. Jiang, C. K. Jung, M. J. Wilking, C. Yanagisawa, M. Harada, H. Ishino, S. Ito, H. Kitagawa, Y. Koshio, F. Nakanishi, S. Sakai, G. Barr, D. Barrow, L. Cook, S. Samani, D. Wark, F. Nova, J. Y. Yang, M. Malek, J. M. McElwee, O. Stone, M. D. Thiesse, L. F. Thompson, H. Okazawa, S. B. Kim, J. W. Seo, I. Yu, A. K. Ichikawa, K. D. Nakamura, S. Tairafune, K. Nishijima, K. Iwamoto, K. Nakagiri, Y. Nakajima, N. Taniuchi, M. Yokoyama, K. Martens, P. de Perio, M. R. Vagins, M. Kuze, S. Izumiyama, M. Inomoto, M. Ishitsuka, H. Ito, T. Kinoshita, R. Matsumoto, Y. Ommura, N. Shigeta, M. Shinoki, T. Suganuma, K. Yamauchi, J. F. Martin, H. A. Tanaka, T. Towstego, R. Akutsu, V. Gousy-Leblanc, M. Hartz, A. Konaka, N. W. Prouse, S. Chen, B. D. Xu, B. Zhang, M. Posiadala-Zezula, D. Hadley, M. Nicholson, M. O’Flaherty, B. Richards, A. Ali, B. Jamieson, L. Marti, A. Minamino, G. Pintaudi, S. Sano, S. Suzuki, K. Wada, and Super-Kamiokande Collaboration, “Search for Cosmic-Ray Boosted Sub-GeV Dark Matter Using Recoil Protons at Super-Kamiokande,” *Phys. Rev. Lett.*, vol. 130, no. 3, p. 031802, Jan. 2023.
- [16] C. L. Bennett, D. Larson, J. L. Weiland, N. Jarosik, G. Hinshaw, N. Odegard, K. M. Smith, R. S. Hill, B. Gold, M. Halpern, E. Komatsu, M. R.olta, L. Page, D. N. Spergel, E. Wollack, J. Dunkley, A. Kogut, M. Limon, S. S. Meyer, G. S. Tucker,

- and E. L. Wright, “Nine-year Wilkinson Microwave Anisotropy Probe (WMAP) Observations: Final Maps and Results,” *ApJS*, vol. 208, no. 2, p. 20, Oct. 2013.
- [17] S. Chabanier, M. Millea, and N. Palanque-Delabrouille, “Matter power spectrum: from Ly  $\alpha$  forest to CMB scales,” *MNRAS*, vol. 489, no. 2, pp. 2247–2253, Oct. 2019.
- [18] B. Abolfathi, D. S. Aguado, G. Aguilar, C. Allende Prieto, A. Almeida, T. T. Ananna, F. Anders, S. F. Anderson, B. H. Andrews, B. Anguiano, A. Aragón-Salamanca, M. Argudo-Fernández, E. Armengaud, M. Ata, E. Aubourg, V. Avila-Reese, C. Badenes, S. Bailey, C. Balland, K. A. Barger, J. Barrera-Ballesteros, C. Bartosz, F. Bastien, D. Bates, F. Baumgarten, J. Bautista, R. Beaton, T. C. Beers, F. Belfiore, C. F. Bender, M. Bernardi, M. A. Bershadsky, F. Beutler, J. C. Bird, D. Bizyaev, G. A. Blanc, M. R. Blanton, M. Blomqvist, A. S. Bolton, M. Bouché, J. Borissova, J. Bovy, C. A. Bradna Diaz, W. N. Brandt, J. Brinkmann, J. R. Brownstein, K. Bundy, A. J. Burgasser, E. Burtin, N. G. Busca, C. I. Cañas, M. Cano-Díaz, M. Cappellari, R. Carrera, A. R. Casey, B. Cervantes Sodi, Y. Chen, B. Cherinka, C. Chiappini, P. D. Choi, D. Chojnowski, C.-H. Chuang, H. Chung, N. Clerc, R. E. Cohen, J. M. Comerford, J. Comparat, J. Correa do Nascimento, L. da Costa, M.-C. Cousinou, K. Covey, J. D. Crane, I. Cruz-Gonzalez, K. Cunha, G. da Silva Ilha, G. J. Damke, J. Darling, J. Davidson, James W., K. Dawson, M. A. C. de Icaza Lizaola, A. de la Macorra, S. de la Torre, N. De Lee, V. de Sainte Agathe, A. Deconto Machado, F. Dell’Agli, T. Delubac, A. M. Diamond-Stanic, J. Donor, J. J. Downes, N. Drory, H. du Mas des Bourboux, C. J. Duckworth, T. Dwelly, J. Dyer, G. Ebelke, A. Davis Eigenbrot, D. J. Eisenstein, Y. P. Elsworth, E. Emsellem, M. Eracleous, G. Erfanianfar, S. Escoffier, X. Fan, E. Fernández Alvar, J. G. Fernandez-Trincado, R. Fernando Cirolini, D. Feuillet, A. Finoguenov, S. W. Fleming, A. Font-Ribera, G. Freisclad, P. Frinchaboy, H. Fu, Y. Gómez Maqueo Chew, L. Galbany, A. E. García Pérez, R. Garcia-Dias, D. A. García-Hernández, L. A. Garma Oehmichen, P. Gaulme, J. Gelfand, H. Gil-Marín, B. A. Gillespie, D. Goddard, J. I. González Hernández, V. Gonzalez-Perez, K. Grabowski, P. J. Green, C. J. Grier, A. Gueguen, H. Guo, J. Guy, A. Hagen, P. Hall, P. Harding, S. Hasselquist, S. Hawley, C. R. Hayes, F. Hearty, S. Hekker, J. Hernandez, H. Hernandez Toledo, D. W. Hogg, K. Holley-Bockelmann, J. A. Holtzman, J. Hou, B.-C. Hsieh, J. A. S. Hunt, T. A. Hutchinson, H. S. Hwang, C. E. Jimenez Angel, J. A. Johnson, A. Jones, H. Jönsson, E. Jullo, F. S. Khan, K. Kinemuchi, D. Kirkby, I. Kirkpatrick, Charles C., F.-S. Kitaura, G. R. Knapp, J.-P. Kneib, J. A. Kollmeier, I. Lacerna, R. R. Lane, D. Lang, D. R. Law, J.-M. Le Goff, Y.-B. Lee, H. Li, C. Li, J. Lian, Y. Liang, M. Lima, L. Lin, D. Long, S. Lucatello, B. Lundgren, J. T. Mackereth, C. L. MacLeod, S. Mahadevan, M. A. G. Maia, S. Majewski, A. Manchado, C. Maraston, V. Mariappan, R. Marques-Chaves, T. Masseron, K. L. Masters, R. M. McDermid, I. D. McGreer, M. Melendez, S. Meneses-Goytia, A. Merloni, M. R. Merrifield, S. Meszaros, A. Meza, I. Minchev, D. Minniti, E.-M. Mueller, F. Muller-Sanchez, D. Muna, R. R. Muñoz, A. D. Myers, P. Nair, K. Nandra, M. Ness, J. A. Newman, R. C. Nichol, D. L. Nidever, C. Nitschelm, P. Noterdaeme, J. O’Connell, R. J. Oelkers, A. Oravetz, D. Oravetz, E. A. Ortíz, Y. Osorio, Z. Pace, N. Padilla, N. Palanque-Delabrouille, P. A. Palicio, H.-A. Pan, K. Pan, T. Parikh, I. Pâris, C. Park, S. Peirani, M. Pellejero-Ibanez, S. Penny, W. J. Percival, I. Perez-Fournon, P. Petitjean, M. M. Pieri, M. Pinsonneault, A. Pisani, F. Prada, A. Prakash, A. B.

- d. A. Queiroz, M. J. Raddick, A. Raichoor, S. Barboza Rembold, H. Richstein, R. A. Riffel, R. Riffel, H.-W. Rix, A. C. Robin, S. Rodríguez Torres, C. Román-Zúñiga, A. J. Ross, G. Rossi, J. Ruan, R. Ruggeri, J. Ruiz, M. Salvato, A. G. Sánchez, S. F. Sánchez, J. Sanchez Almeida, J. R. Sánchez-Gallego, F. A. Santana Rojas, B. X. Santiago, R. P. Schiavon, J. S. Schimoia, E. Schlafly, D. Schlegel, D. P. Schneider, W. J. Schuster, A. Schwobe, H.-J. Seo, A. Serenelli, S. Shen, Y. Shen, M. Shetrone, M. Shull, V. Silva Aguirre, J. D. Simon, M. Skrutskie, A. Slosar, R. Smethurst, V. Smith, J. Sobek, G. Somers, B. J. Souter, D. Souto, A. Spindler, D. V. Stark, K. Stassun, M. Steinmetz, D. Stello, T. Storchi-Bergmann, A. Streblyanska, G. S. Stringfellow, G. Suárez, J. Sun, L. Szigeti, M. Taghizadeh-Popp, M. S. Talbot, B. Tang, C. Tao, J. Tayar, M. Tembe, J. Teske, A. R. Thakar, D. Thomas, P. Tissera, R. Tojeiro, C. Tremonti, N. W. Troup, M. Urry, O. Valenzuela, R. van den Bosch, J. Vargas-González, M. Vargas-Magaña, J. A. Vazquez, S. Villanova, N. Vogt, D. Wake, Y. Wang, B. A. Weaver, A.-M. Weijmans, D. H. Weinberg, K. B. Westfall, D. G. Whelan, E. Wilcots, V. Wild, R. A. Williams, J. Wilson, W. M. Wood-Vasey, D. Wylezalek, T. Xiao, R. Yan, M. Yang, J. E. Ybarra, C. Yèche, N. Zakamska, O. Zamora, P. Zarrouk, G. Zasowski, K. Zhang, C. Zhao, G.-B. Zhao, Z. Zheng, Z. Zheng, Z.-M. Zhou, G. Zhu, J. C. Zinn, and H. Zou, “The Fourteenth Data Release of the Sloan Digital Sky Survey: First Spectroscopic Data from the Extended Baryon Oscillation Spectroscopic Survey and from the Second Phase of the Apache Point Observatory Galactic Evolution Experiment,” *ApJS*, vol. 235, no. 2, p. 42, Apr. 2018.
- [19] M. A. Troxel, N. MacCrann, J. Zuntz, T. F. Eifler, E. Krause, S. Dodelson, D. Gruen, J. Blazek, O. Friedrich, S. Samuroff, J. Prat, L. F. Secco, C. Davis, A. Ferté, J. DeRose, A. Alarcon, A. Amara, E. Baxter, M. R. Becker, G. M. Bernstein, S. L. Bridle, R. Cawthon, C. Chang, A. Choi, J. De Vicente, A. Drlica-Wagner, J. Elvin-Poole, J. Frieman, M. Gatti, W. G. Hartley, K. Honscheid, B. Hoyle, E. M. Huff, D. Huterer, B. Jain, M. Jarvis, T. Kacprzak, D. Kirk, N. Kokron, C. Krawiec, O. Lahav, A. R. Liddle, J. Peacock, M. M. Rau, A. Refregier, R. P. Rollins, E. Rozo, E. S. Rykoff, C. Sánchez, I. Sevilla-Noarbe, E. Sheldon, A. Stebbins, T. N. Varga, P. Vielzeuf, M. Wang, R. H. Wechsler, B. Yanny, T. M. C. Abbott, F. B. Abdalla, S. Allam, J. Annis, K. Bechtol, A. Benoit-Lévy, E. Bertin, D. Brooks, E. Buckley-Geer, D. L. Burke, A. Carnero Rosell, M. Carrasco Kind, J. Carretero, F. J. Castander, M. Crocce, C. E. Cunha, C. B. D’Andrea, L. N. da Costa, D. L. DePoy, S. Desai, H. T. Diehl, J. P. Dietrich, P. Doel, E. Fernandez, B. Flaugher, P. Fosalba, J. García-Bellido, E. Gaztanaga, D. W. Gerdes, T. Giannantonio, D. A. Goldstein, R. A. Gruendl, J. Gschwend, G. Gutierrez, D. J. James, T. Jeltema, M. W. G. Johnson, M. D. Johnson, S. Kent, K. Kuehn, S. Kuhlmann, N. Kuropatkin, T. S. Li, M. Lima, H. Lin, M. A. G. Maia, M. March, J. L. Marshall, P. Martini, P. Melchior, F. Menanteau, R. Miquel, J. J. Mohr, E. Neilsen, R. C. Nichol, B. Nord, D. Petravick, A. A. Plazas, A. K. Romer, A. Roodman, M. Sako, E. Sanchez, V. Scarpine, R. Schindler, M. Schubnell, M. Smith, R. C. Smith, M. Soares-Santos, F. Sobreira, E. Suchyta, M. E. C. Swanson, G. Tarle, D. Thomas, D. L. Tucker, V. Vikram, A. R. Walker, J. Weller, Y. Zhang, and DES Collaboration, “Dark Energy Survey Year 1 results: Cosmological constraints from cosmic shear,” *Phys. Rev. D*, vol. 98, no. 4, p. 043528, Aug. 2018.
- [20] B. A. Reid, W. J. Percival, D. J. Eisenstein, L. Verde, D. N. Spergel, R. A. Skibba,

- N. A. Bahcall, T. Budavari, J. A. Frieman, M. Fukugita, J. R. Gott, J. E. Gunn, Ž. Ivezić, G. R. Knapp, R. G. Kron, R. H. Lupton, T. A. McKay, A. Meiksin, R. C. Nichol, A. C. Pope, D. J. Schlegel, D. P. Schneider, C. Stoughton, M. A. Strauss, A. S. Szalay, M. Tegmark, M. S. Vogeley, D. H. Weinberg, D. G. York, and I. Zehavi, “Cosmological constraints from the clustering of the Sloan Digital Sky Survey DR7 luminous red galaxies,” *MNRAS*, vol. 404, no. 1, pp. 60–85, May 2010.
- [21] J. S. Bullock and M. Boylan-Kolchin, “Small-Scale Challenges to the  $\Lambda$ CDM Paradigm,” *ARA&A*, vol. 55, no. 1, pp. 343–387, Aug. 2017.
- [22] B. Moore, “Evidence against dissipation-less dark matter from observations of galaxy haloes,” *Nature*, vol. 370, no. 6491, pp. 629–631, Aug. 1994.
- [23] R. A. Flores and J. R. Primack, “Observational and Theoretical Constraints on Singular Dark Matter Halos,” *ApJ*, vol. 427, p. L1, May 1994.
- [24] B. Moore, S. Ghigna, F. Governato, G. Lake, T. Quinn, J. Stadel, and P. Tozzi, “Dark Matter Substructure within Galactic Halos,” *ApJ*, vol. 524, no. 1, pp. L19–L22, Oct. 1999.
- [25] K. A. Oman, J. F. Navarro, A. Fattahi, C. S. Frenk, T. Sawala, S. D. M. White, R. Bower, R. A. Crain, M. Furlong, M. Schaller, J. Schaye, and T. Theuns, “The unexpected diversity of dwarf galaxy rotation curves,” *MNRAS*, vol. 452, no. 4, pp. 3650–3665, Oct. 2015.
- [26] M. Boylan-Kolchin, J. S. Bullock, and M. Kaplinghat, “Too big to fail? The puzzling darkness of massive Milky Way subhaloes,” *MNRAS*, vol. 415, no. 1, pp. L40–L44, July 2011.
- [27] E. Tollet, A. V. Macciò, A. A. Dutton, G. S. Stinson, L. Wang, C. Penzo, T. A. Gutcke, T. Buck, X. Kang, C. Brook, A. Di Cintio, B. W. Keller, and J. Wadsley, “NIHAO - IV: core creation and destruction in dark matter density profiles across cosmic time,” *MNRAS*, vol. 456, no. 4, pp. 3542–3552, Mar. 2016.
- [28] A. Fitts, M. Boylan-Kolchin, O. D. Elbert, J. S. Bullock, P. F. Hopkins, J. Oñorbe, A. Wetzel, C. Wheeler, C.-A. Faucher-Giguère, D. Kereš, E. D. Skillman, and D. R. Weisz, “fire in the field: simulating the threshold of galaxy formation,” *MNRAS*, vol. 471, no. 3, pp. 3547–3562, Nov. 2017.
- [29] P. F. Hopkins, A. Wetzel, D. Kereš, C.-A. Faucher-Giguère, E. Quataert, M. Boylan-Kolchin, N. Murray, C. C. Hayward, S. Garrison-Kimmel, C. Hummels, R. Feldmann, P. Torrey, X. Ma, D. Anglés-Alcázar, K.-Y. Su, M. Orr, D. Schmitz, I. Escala, R. Sanderson, M. Y. Grudić, Z. Hafen, J.-H. Kim, A. Fitts, J. S. Bullock, C. Wheeler, T. K. Chan, O. D. Elbert, and D. Narayanan, “FIRE-2 simulations: physics versus numerics in galaxy formation,” *MNRAS*, vol. 480, no. 1, pp. 800–863, Oct. 2018.
- [30] S. Colombi, S. Dodelson, and L. M. Widrow, “Large-Scale Structure Tests of Warm Dark Matter,” *ApJ*, vol. 458, p. 1, Feb. 1996.
- [31] D. N. Spergel and P. J. Steinhardt, “Observational Evidence for Self-Interacting Cold Dark Matter,” *Phys. Rev. Lett.*, vol. 84, no. 17, pp. 3760–3763, Apr. 2000.

- [32] S. Hawking, “Gravitationally collapsed objects of very low mass,” *MNRAS*, vol. 152, p. 75, Jan. 1971.
- [33] B. J. Carr and S. W. Hawking, “Black holes in the early Universe,” *MNRAS*, vol. 168, pp. 399–416, Aug. 1974.
- [34] W. Hu, R. Barkana, and A. Gruzinov, “Fuzzy Cold Dark Matter: The Wave Properties of Ultralight Particles,” *Phys. Rev. Lett.*, vol. 85, no. 6, pp. 1158–1161, Aug. 2000.
- [35] A. Einstein, “Lens-Like Action of a Star by the Deviation of Light in the Gravitational Field,” *Science*, vol. 84, no. 2188, pp. 506–507, Dec. 1936.
- [36] F. Zwicky, “On the Probability of Detecting Nebulae Which Act as Gravitational Lenses,” *Physical Review*, vol. 51, no. 8, pp. 679–679, Apr. 1937.
- [37] D. Walsh, R. F. Carswell, and R. J. Weymann, “0957+561 A, B: twin quasistellar objects or gravitational lens?” *Nature*, vol. 279, pp. 381–384, May 1979.
- [38] R. Lynds and V. Petrosian, “Giant Luminous Arcs in Galaxy Clusters,” in *Bulletin of the American Astronomical Society*, vol. 18, Sept. 1986, p. 1014.
- [39] G. Soucail, Y. Mellier, B. Fort, G. Mathez, and M. Cailloux, “Discovery of the first gravitational Einstein ring - The luminous arc in Abell 370,” *The Messenger*, vol. 50, pp. 5–6, Dec. 1987.
- [40] J. N. Hewitt, E. L. Turner, D. P. Schneider, B. F. Burke, and G. I. Langston, “Unusual radio source MG1131+0456: a possible Einstein ring,” *Nature*, vol. 333, no. 6173, pp. 537–540, June 1988.
- [41] M. J. Irwin, R. L. Webster, P. C. Hewett, R. T. Corrigan, and R. I. Jedrzejewski, “Photometric Variations in the Q2237+0305 System: First Detection of a Microlensing Event,” *AJ*, vol. 98, p. 1989, Dec. 1989.
- [42] C. Alcock, C. W. Akerlof, R. A. Allsman, T. S. Axelrod, D. P. Bennett, S. Chan, K. H. Cook, K. C. Freeman, K. Griest, S. L. Marshall, H. S. Park, S. Perlmutter, B. A. Peterson, M. R. Pratt, P. J. Quinn, A. W. Rodgers, C. W. Stubbs, and W. Sutherland, “Possible gravitational microlensing of a star in the Large Magellanic Cloud,” *Nature*, vol. 365, no. 6447, pp. 621–623, Oct. 1993.
- [43] J. A. Tyson, F. Valdes, and R. A. Wenk, “Detection of Systematic Gravitational Lens Galaxy Image Alignments: Mapping Dark Matter in Galaxy Clusters,” *ApJ*, vol. 349, p. L1, Jan. 1990.
- [44] P. L. Kelly, J. M. Diego, S. Rodney, N. Kaiser, T. Broadhurst, A. Zitrin, T. Treu, P. G. Pérez-González, T. Morishita, M. Jauzac, J. Selsing, M. Oguri, L. Pueyo, T. W. Ross, A. V. Filippenko, N. Smith, J. Hjorth, S. B. Cenko, X. Wang, D. A. Howell, J. Richard, B. L. Frye, S. W. Jha, R. J. Foley, C. Norman, M. Bradac, W. Zheng, G. Brammer, A. M. Benito, A. Cava, L. Christensen, S. E. de Mink, O. Graur, C. Grillo, R. Kawamata, J.-P. Kneib, T. Matheson, C. McCully, M. Nonino, I. Pérez-Fournon, A. G. Riess, P. Rosati, K. B. Schmidt, K. Sharon, and B. J. Weiner, “Extreme magnification of an individual star at redshift 1.5 by a galaxy-cluster lens,” *Nature Astronomy*, vol. 2, pp. 334–342, Apr. 2018.

- [45] J. M. Diego, B. Sun, H. Yan, L. J. Furtak, E. Zackrisson, L. Dai, P. Kelly, M. Nonino, N. Adams, A. K. Meena, S. P. Willner, A. Zitrin, S. H. Cohen, J. C. J. D’Silva, R. A. Jansen, J. Summers, R. A. Windhorst, D. Coe, C. J. Conselice, S. P. Driver, B. Frye, N. A. Grogin, A. M. Koekemoer, M. A. Marshall, N. Pirzkal, A. Robotham, M. J. Rutkowski, R. E. Ryan, S. Tompkins, C. N. A. Willmer, and R. Bhatawdekar, “JWST’s PEARLS: Mothra, a new kaiju star at  $z = 2.091$  extremely magnified by MACS0416, and implications for dark matter models,” *A&A*, vol. 679, p. A31, Nov. 2023.
- [46] K. T. Abe, H. Kawai, and M. Oguri, “Analytic approach to astrometric perturbations of critical curves by substructures,” *Phys. Rev. D*, vol. 109, no. 8, p. 083517, Apr. 2024.
- [47] H. Kawai, A. Kamada, K. Kamada, and N. Yoshida, “Modeling the core-halo mass relation in fuzzy dark matter halos,” *Phys. Rev. D*, vol. 110, no. 2, p. 023519, July 2024.
- [48] H. Kawai and M. Oguri, “Analytic model for the statistics of ultrahigh magnification events,” *Phys. Rev. D*, vol. 110, no. 8, p. 083514, Oct. 2024.
- [49] H. Kawai and M. Meneghetti, “Galaxy-galaxy strong lensing cross-section with fuzzy dark matter model,” *arXiv e-prints*, p. arXiv:2410.14543, Oct. 2024.
- [50] H. Kawai and M. Oguri, “Constraints on primordial black holes from the observed number of Icarus-like ultrahigh magnification events,” *arXiv e-prints*, p. arXiv:2411.13816, Nov. 2024.
- [51] S. Profumo, *An Introduction to Particle Dark Matter*, 2017.
- [52] S. Dodelson and F. Schmidt, *Modern Cosmology*, 2020.
- [53] S. Chabanier, N. Palanque-Delabrouille, C. Yèche, J.-M. Le Goff, E. Armengaud, J. Bautista, M. Blomqvist, N. Busca, K. Dawson, T. Etourneau, A. Font-Ribera, Y. Lee, H. du Mas des Bourboux, M. Pieri, J. Rich, G. Rossi, D. Schneider, and A. Slosar, “The one-dimensional power spectrum from the SDSS DR14 Ly $\alpha$  forests,” *J. Cosmology Astropart. Phys.*, vol. 2019, no. 7, p. 017, July 2019.
- [54] Planck Collaboration, N. Aghanim, Y. Akrami, F. Arroja, M. Ashdown, J. Aumont, C. Baccigalupi, M. Ballardini, A. J. Banday, R. B. Barreiro, N. Bartolo, S. Basak, R. Battye, K. Benabed, J. P. Bernard, M. Bersanelli, P. Bielewicz, J. J. Bock, J. R. Bond, J. Borrill, F. R. Bouchet, F. Boulanger, M. Bucher, C. Burigana, R. C. Butler, E. Calabrese, J. F. Cardoso, J. Carron, B. Casaponsa, A. Challinor, H. C. Chiang, L. P. L. Colombo, C. Combet, D. Contreras, B. P. Crill, F. Cuttaia, P. de Bernardis, G. de Zotti, J. Delabrouille, J. M. Delouis, F. X. Désert, E. Di Valentino, C. Dickinson, J. M. Diego, S. Donzelli, O. Doré, M. Douspis, A. Ducout, X. Dupac, G. Efstathiou, F. Elsner, T. A. Enßlin, H. K. Eriksen, E. Falgarone, Y. Fantaye, J. Fergusson, R. Fernandez-Cobos, F. Finelli, F. Forastieri, M. Frailis, E. Franceschi, A. Frolov, S. Galeotta, S. Galli, K. Ganga, R. T. Génova-Santos, M. Gerbino, T. Ghosh, J. González-Nuevo, K. M. Górski, S. Gratton, A. Gruppuso, J. E. Gudmundsson, J. Hamann, W. Handley, F. K. Hansen, G. Helou, D. Herranz, S. R. Hildebrandt, E. Hivon, Z. Huang, A. H. Jaffe, W. C. Jones, A. Karakci,

- E. Keihänen, R. Keskitalo, K. Kiiveri, J. Kim, T. S. Kisner, L. Knox, N. Krachmalnicoff, M. Kunz, H. Kurki-Suonio, G. Lagache, J. M. Lamarre, M. Langer, A. Lasenby, M. Lattanzi, C. R. Lawrence, M. Le Jeune, J. P. Leahy, J. Lesgourgues, F. Levrier, A. Lewis, M. Liguori, P. B. Lilje, M. Lilley, V. Lindholm, M. López-Cañiego, P. M. Lubin, Y. Z. Ma, J. F. Macías-Pérez, G. Maggio, D. Maino, N. Mandolesi, A. Mangilli, A. Marcos-Caballero, M. Maris, P. G. Martin, M. Martinelli, E. Martínez-González, S. Matarrese, N. Mauri, J. D. McEwen, P. D. Meerburg, P. R. Meinhold, A. Melchiorri, A. Mennella, M. Migliaccio, M. Millea, S. Mitra, M. A. Miville-Deschênes, D. Molinari, A. Moneti, L. Montier, G. Morgante, A. Moss, S. Mottet, M. Münchmeyer, P. Natoli, H. U. Nørgaard-Nielsen, C. A. Oxborrow, L. Pagano, D. Paoletti, B. Partridge, G. Patanchon, T. J. Pearson, M. Peel, H. V. Peiris, F. Perrotta, V. Pettorino, F. Piacentini, L. Polastri, G. Polenta, J. L. Puget, J. P. Rachen, M. Reinecke, M. Remazeilles, C. Renault, A. Renzi, G. Rocha, C. Rosset, G. Roudier, J. A. Rubiño-Martín, B. Ruiz-Granados, L. Salvati, M. Sandri, M. Savelainen, D. Scott, E. P. S. Shellard, M. Shiraishi, C. Sirignano, G. Sirri, L. D. Spencer, R. Sunyaev, A. S. Suur-Uski, J. A. Tauber, D. Tavagnacco, M. Tenti, L. Terenzi, L. Toffolatti, M. Tomasi, T. Trombetti, J. Valiviita, B. Van Tent, L. Vibert, P. Vielva, F. Villa, N. Vittorio, B. D. Wandelt, I. K. Wehus, M. White, S. D. M. White, A. Zacchei, and A. Zonca, “Planck 2018 results. I. Overview and the cosmological legacy of Planck,” *A&A*, vol. 641, p. A1, Sept. 2020.
- [55] T. Ishiyama, F. Prada, A. A. Klypin, M. Sinha, R. B. Metcalf, E. Jullo, B. Altieri, S. A. Cora, D. Croton, S. de la Torre, D. E. Millán-Calero, T. Oogi, J. Ruedas, and C. A. Vega-Martínez, “The Uchuu simulations: Data Release 1 and dark matter halo concentrations,” *MNRAS*, vol. 506, no. 3, pp. 4210–4231, Sept. 2021.
- [56] J. F. Navarro, C. S. Frenk, and S. D. M. White, “The Structure of Cold Dark Matter Halos,” *ApJ*, vol. 462, p. 563, May 1996.
- [57] G. L. Bryan and M. L. Norman, “Statistical Properties of X-Ray Clusters: Analytic and Numerical Comparisons,” *ApJ*, vol. 495, no. 1, pp. 80–99, Mar. 1998.
- [58] J. S. Bullock, T. S. Kolatt, Y. Sigad, R. S. Somerville, A. V. Kravtsov, A. A. Klypin, J. R. Primack, and A. Dekel, “Profiles of dark haloes: evolution, scatter and environment,” *MNRAS*, vol. 321, no. 3, pp. 559–575, Mar. 2001.
- [59] A. J. Mead, J. A. Peacock, C. Heymans, S. Joudaki, and A. F. Heavens, “An accurate halo model for fitting non-linear cosmological power spectra and baryonic feedback models,” *MNRAS*, vol. 454, no. 2, pp. 1958–1975, Dec. 2015.
- [60] B. Diemer and A. V. Kravtsov, “A Universal Model for Halo Concentrations,” *ApJ*, vol. 799, no. 1, p. 108, Jan. 2015.
- [61] J. Lee, “The Formalism for the Subhalo Mass Function in the Tidal-Limit Approximation,” *ApJ*, vol. 604, no. 2, pp. L73–L76, Apr. 2004.
- [62] M. Oguri and J. Lee, “A realistic model for spatial and mass distributions of dark halo substructures: An analytic approach,” *MNRAS*, vol. 355, no. 1, pp. 120–128, Nov. 2004.

- [63] F. C. van den Bosch, G. Tormen, and C. Giocoli, “The mass function and average mass-loss rate of dark matter subhaloes,” *MNRAS*, vol. 359, no. 3, pp. 1029–1040, May 2005.
- [64] J. Diemand, M. Kuhlen, and P. Madau, “Formation and Evolution of Galaxy Dark Matter Halos and Their Substructure,” *ApJ*, vol. 667, no. 2, pp. 859–877, Oct. 2007.
- [65] C. Giocoli, G. Tormen, and F. C. van den Bosch, “The population of dark matter subhaloes: mass functions and average mass-loss rates,” *MNRAS*, vol. 386, no. 4, pp. 2135–2144, June 2008.
- [66] C. Giocoli, L. Pieri, and G. Tormen, “Analytical approach to subhalo population in dark matter haloes,” *MNRAS*, vol. 387, no. 2, pp. 689–697, June 2008.
- [67] V. Springel, J. Wang, M. Vogelsberger, A. Ludlow, A. Jenkins, A. Helmi, J. F. Navarro, C. S. Frenk, and S. D. M. White, “The Aquarius Project: the subhaloes of galactic haloes,” *MNRAS*, vol. 391, no. 4, pp. 1685–1711, Dec. 2008.
- [68] J. L. Tinker and A. R. Wetzel, “What does Clustering Tell us About the Buildup of the Red Sequence?” *ApJ*, vol. 719, no. 1, pp. 88–103, Aug. 2010.
- [69] J. Han, S. Cole, C. S. Frenk, and Y. Jing, “A unified model for the spatial and mass distribution of subhaloes,” *MNRAS*, vol. 457, no. 2, pp. 1208–1223, Apr. 2016.
- [70] F. Jiang and F. C. van den Bosch, “Statistics of dark matter substructure - I. Model and universal fitting functions,” *MNRAS*, vol. 458, no. 3, pp. 2848–2869, May 2016.
- [71] A. Rodríguez-Puebla, P. Behroozi, J. Primack, A. Klypin, C. Lee, and D. Hellinger, “Halo and subhalo demographics with Planck cosmological parameters: Bolshoi-Planck and MultiDark-Planck simulations,” *MNRAS*, vol. 462, no. 1, pp. 893–916, Oct. 2016.
- [72] N. Hiroshima, S. Ando, and T. Ishiyama, “Modeling evolution of dark matter substructure and annihilation boost,” *Phys. Rev. D*, vol. 97, no. 12, p. 123002, June 2018.
- [73] S. Ando, T. Ishiyama, and N. Hiroshima, “Halo Substructure Boosts to the Signatures of Dark Matter Annihilation,” *Galaxies*, vol. 7, no. 3, p. 68, July 2019.
- [74] M. Oguri and R. Takahashi, “Probing Dark Low-mass Halos and Primordial Black Holes with Frequency-dependent Gravitational Lensing Dispersions of Gravitational Waves,” *ApJ*, vol. 901, no. 1, p. 58, Sept. 2020.
- [75] N. Hiroshima, S. Ando, and T. Ishiyama, “Semi-analytical frameworks for subhaloes from the smallest to the largest scale,” *MNRAS*, vol. 517, no. 2, pp. 2728–2737, Dec. 2022.
- [76] Á. Moliné, M. A. Sánchez-Conde, A. Aguirre-Santaella, T. Ishiyama, F. Prada, S. A. Cora, D. Croton, E. Jullo, R. B. Metcalf, T. Oogi, and J. Ruedas, “ $\Lambda$ CDM halo substructure properties revealed with high-resolution and large-volume cosmological simulations,” *MNRAS*, vol. 518, no. 1, pp. 157–173, Jan. 2023.

- [77] M. Bartelmann, “Arcs from a universal dark-matter halo profile.” *A&A*, vol. 313, pp. 697–702, Sept. 1996.
- [78] L. Hernquist, “An Analytical Model for Spherical Galaxies and Bulges,” *ApJ*, vol. 356, p. 359, June 1990.
- [79] J. B. Hyde and M. Bernardi, “Curvature in the scaling relations of early-type galaxies,” *MNRAS*, vol. 394, no. 4, pp. 1978–1990, Apr. 2009.
- [80] G. Girelli, L. Pozzetti, M. Bolzonella, C. Giocoli, F. Marulli, and M. Baldi, “The stellar-to-halo mass relation over the past 12 Gyr. I. Standard  $\Lambda$ CDM model,” *A&A*, vol. 634, p. A135, Feb. 2020.
- [81] S. M. K. Alam, J. S. Bullock, and D. H. Weinberg, “Dark Matter Properties and Halo Central Densities,” *ApJ*, vol. 572, no. 1, pp. 34–40, June 2002.
- [82] W. J. G. de Blok, “The Core-Cusp Problem,” *Advances in Astronomy*, vol. 2010, p. 789293, Jan. 2010.
- [83] S.-H. Oh, D. A. Hunter, E. Brinks, B. G. Elmegreen, A. Schruba, F. Walter, M. P. Rupen, L. M. Young, C. E. Simpson, M. C. Johnson, K. A. Herrmann, D. Ficit-Vicas, P. Cigan, V. Heesen, T. Ashley, and H.-X. Zhang, “High-resolution Mass Models of Dwarf Galaxies from LITTLE THINGS,” *AJ*, vol. 149, no. 6, p. 180, June 2015.
- [84] D. Marchesini, E. D’Onghia, G. Chincarini, C. Firmani, P. Conconi, E. Molinari, and A. Zacchei, “ $H\alpha$  Rotation Curves: The Soft Core Question,” *ApJ*, vol. 575, no. 2, pp. 801–813, Aug. 2002.
- [85] I. K. Baldry, S. P. Driver, J. Loveday, E. N. Taylor, L. S. Kelvin, J. Liske, P. Norberg, A. S. G. Robotham, S. Brough, A. M. Hopkins, S. P. Bamford, J. A. Peacock, J. Bland-Hawthorn, C. J. Conselice, S. M. Croom, D. H. Jones, H. R. Parkinson, C. C. Popescu, M. Prescott, R. G. Sharp, and R. J. Tuffs, “Galaxy And Mass Assembly (GAMA): the galaxy stellar mass function at  $z < 0.06$ ,” *MNRAS*, vol. 421, no. 1, pp. 621–634, Mar. 2012.
- [86] A. Drlica-Wagner, K. Bechtol, E. S. Rykoff, E. Luque, A. Queiroz, Y. Y. Mao, R. H. Wechsler, J. D. Simon, B. Santiago, B. Yanny, E. Balbinot, S. Dodelson, A. Fausti Neto, D. J. James, T. S. Li, M. A. G. Maia, J. L. Marshall, A. Pieres, K. Stringer, A. R. Walker, T. M. C. Abbott, F. B. Abdalla, S. Allam, A. Benoit-Lévy, G. M. Bernstein, E. Bertin, D. Brooks, E. Buckley-Geer, D. L. Burke, A. Carnero Rosell, M. Carrasco Kind, J. Carretero, M. Crocce, L. N. da Costa, S. Desai, H. T. Diehl, J. P. Dietrich, P. Doel, T. F. Eifler, A. E. Evrard, D. A. Finley, B. Flaugher, P. Fosalba, J. Frieman, E. Gaztanaga, D. W. Gerdes, D. Gruen, R. A. Gruendl, G. Gutierrez, K. Honscheid, K. Kuehn, N. Kuropatkin, O. Lahav, P. Martini, R. Miquel, B. Nord, R. Ogando, A. A. Plazas, K. Reil, A. Roodman, M. Sako, E. Sanchez, V. Scarpine, M. Schubnell, I. Sevilla-Noarbe, R. C. Smith, M. Soares-Santos, F. Sobreira, E. Suchyta, M. E. C. Swanson, G. Tarle, D. Tucker, V. Vikram, W. Wester, Y. Zhang, J. Zuntz, and DES Collaboration, “Eight Ultra-faint Galaxy Candidates Discovered in Year Two of the Dark Energy Survey,” *ApJ*, vol. 813, no. 2, p. 109, Nov. 2015.

- [87] J. R. Hargis, B. Willman, and A. H. G. Peter, “Too Many, Too Few, or Just Right? The Predicted Number and Distribution of Milky Way Dwarf Galaxies,” *ApJ*, vol. 795, no. 1, p. L13, Nov. 2014.
- [88] B. P. Moster, T. Naab, and S. D. M. White, “Galactic star formation and accretion histories from matching galaxies to dark matter haloes,” *MNRAS*, vol. 428, no. 4, pp. 3121–3138, Feb. 2013.
- [89] P. S. Behroozi, R. H. Wechsler, and C. Conroy, “The Average Star Formation Histories of Galaxies in Dark Matter Halos from  $z = 0-8$ ,” *ApJ*, vol. 770, no. 1, p. 57, June 2013.
- [90] C. B. Brook, A. Di Cintio, A. Knebe, S. Gottlöber, Y. Hoffman, G. Yepes, and S. Garrison-Kimmel, “The Stellar-to-halo Mass Relation for Local Group Galaxies,” *ApJ*, vol. 784, no. 1, p. L14, Mar. 2014.
- [91] S. Y. Kim, A. H. G. Peter, and J. R. Hargis, “Missing Satellites Problem: Completeness Corrections to the Number of Satellite Galaxies in the Milky Way are Consistent with Cold Dark Matter Predictions,” *Phys. Rev. Lett.*, vol. 121, no. 21, p. 211302, Nov. 2018.
- [92] L. Wang, A. A. Dutton, G. S. Stinson, A. V. Macciò, C. Penzo, X. Kang, B. W. Keller, and J. Wadsley, “NIHAO project - I. Reproducing the inefficiency of galaxy formation across cosmic time with a large sample of cosmological hydrodynamical simulations,” *MNRAS*, vol. 454, no. 1, pp. 83–94, Nov. 2015.
- [93] F. Governato, A. Zolotov, A. Pontzen, C. Christensen, S. H. Oh, A. M. Brooks, T. Quinn, S. Shen, and J. Wadsley, “Cuspy no more: how outflows affect the central dark matter and baryon distribution in  $\Lambda$  cold dark matter galaxies,” *MNRAS*, vol. 422, no. 2, pp. 1231–1240, May 2012.
- [94] A. Di Cintio, C. B. Brook, A. A. Dutton, A. V. Macciò, G. S. Stinson, and A. Knebe, “A mass-dependent density profile for dark matter haloes including the influence of galaxy formation,” *MNRAS*, vol. 441, no. 4, pp. 2986–2995, July 2014.
- [95] A. Zolotov, A. M. Brooks, B. Willman, F. Governato, A. Pontzen, C. Christensen, A. Dekel, T. Quinn, S. Shen, and J. Wadsley, “Baryons Matter: Why Luminous Satellite Galaxies have Reduced Central Masses,” *ApJ*, vol. 761, no. 1, p. 71, Dec. 2012.
- [96] A. A. Dutton, A. V. Macciò, J. Frings, L. Wang, G. S. Stinson, C. Penzo, and X. Kang, “NIHAO V: too big does not fail - reconciling the conflict between  $\Lambda$ CDM predictions and the circular velocities of nearby field galaxies,” *MNRAS*, vol. 457, no. 1, pp. L74–L78, Mar. 2016.
- [97] M. Takahiko, *Modern cosmology; Coevolution of the spacetime and matter*, 2018.
- [98] P. Bode, J. P. Ostriker, and N. Turok, “Halo Formation in Warm Dark Matter Models,” *ApJ*, vol. 556, no. 1, pp. 93–107, July 2001.
- [99] M. Viel, J. Lesgourgues, M. G. Haehnelt, S. Matarrese, and A. Riotto, “Constraining warm dark matter candidates including sterile neutrinos and light gravitinos with

- WMAP and the Lyman- $\alpha$  forest,” *Phys. Rev. D*, vol. 71, no. 6, p. 063534, Mar. 2005.
- [100] A. Schneider, R. E. Smith, A. V. Macciò, and B. Moore, “Non-linear evolution of cosmological structures in warm dark matter models,” *MNRAS*, vol. 424, no. 1, pp. 684–698, July 2012.
- [101] D. Anderhalden, A. Schneider, A. V. Macciò, J. Diemand, and G. Bertone, “Hints on the nature of dark matter from the properties of Milky Way satellites,” *J. Cosmology Astropart. Phys.*, vol. 2013, no. 3, p. 014, Mar. 2013.
- [102] A. V. Macciò, O. Ruchayskiy, A. Boyarsky, and J. C. Muñoz-Cuartas, “The inner structure of haloes in cold+warm dark matter models,” *MNRAS*, vol. 428, no. 1, pp. 882–890, Jan. 2013.
- [103] E. Polisensky and M. Ricotti, “Constraints on the dark matter particle mass from the number of Milky Way satellites,” *Phys. Rev. D*, vol. 83, no. 4, p. 043506, Feb. 2011.
- [104] M. R. Lovell, C. S. Frenk, V. R. Eke, A. Jenkins, L. Gao, and T. Theuns, “The properties of warm dark matter haloes,” *MNRAS*, vol. 439, no. 1, pp. 300–317, Mar. 2014.
- [105] N. Banik, J. Bovy, G. Bertone, D. Erkal, and T. J. L. de Boer, “Novel constraints on the particle nature of dark matter from stellar streams,” *J. Cosmology Astropart. Phys.*, vol. 2021, no. 10, p. 043, Oct. 2021.
- [106] M. Kaplinghat, S. Tulin, and H.-B. Yu, “Dark Matter Halos as Particle Colliders: Unified Solution to Small-Scale Structure Puzzles from Dwarfs to Clusters,” *Phys. Rev. Lett.*, vol. 116, no. 4, p. 041302, Jan. 2016.
- [107] X. Shen, P. F. Hopkins, L. Necib, F. Jiang, M. Boylan-Kolchin, and A. Wetzel, “Dissipative dark matter on FIRE - I. Structural and kinematic properties of dwarf galaxies,” *MNRAS*, vol. 506, no. 3, pp. 4421–4445, Sept. 2021.
- [108] A. Kamada, M. Kaplinghat, A. B. Pace, and H.-B. Yu, “Self-Interacting Dark Matter Can Explain Diverse Galactic Rotation Curves,” *Phys. Rev. Lett.*, vol. 119, no. 11, p. 111102, Sept. 2017.
- [109] J. Koda and P. R. Shapiro, “Gravothermal collapse of isolated self-interacting dark matter haloes: N-body simulation versus the fluid model,” *MNRAS*, vol. 415, no. 2, pp. 1125–1137, Aug. 2011.
- [110] H. Nishikawa, K. K. Boddy, and M. Kaplinghat, “Accelerated core collapse in tidally stripped self-interacting dark matter halos,” *Phys. Rev. D*, vol. 101, no. 6, p. 063009, Mar. 2020.
- [111] H. C. Turner, M. R. Lovell, J. Zavala, and M. Vogelsberger, “The onset of gravothermal core collapse in velocity-dependent self-interacting dark matter subhaloes,” *MNRAS*, vol. 505, no. 4, pp. 5327–5339, Aug. 2021.

- [112] Z. C. Zeng, A. H. G. Peter, X. Du, A. Benson, S. Kim, F. Jiang, F.-Y. Cyr-Racine, and M. Vogelsberger, “Core-collapse, evaporation, and tidal effects: the life story of a self-interacting dark matter subhalo,” *MNRAS*, vol. 513, no. 4, pp. 4845–4868, July 2022.
- [113] S. Balberg and S. L. Shapiro, “Gravothermal Collapse of Self-Interacting Dark Matter Halos and the Origin of Massive Black Holes,” *Phys. Rev. Lett.*, vol. 88, no. 10, p. 101301, Mar. 2002.
- [114] D. Gilman, J. Bovy, T. Treu, A. Nierenberg, S. Birrer, A. Benson, and O. Sameie, “Strong lensing signatures of self-interacting dark matter in low-mass haloes,” *MNRAS*, vol. 507, no. 2, pp. 2432–2447, Oct. 2021.
- [115] M. Vogelsberger, J. Zavala, and A. Loeb, “Subhaloes in self-interacting galactic dark matter haloes,” *MNRAS*, vol. 423, no. 4, pp. 3740–3752, July 2012.
- [116] M. Rocha, A. H. G. Peter, J. S. Bullock, M. Kaplinghat, S. Garrison-Kimmel, J. Oñorbe, and L. A. Moustakas, “Cosmological simulations with self-interacting dark matter - I. Constant-density cores and substructure,” *MNRAS*, vol. 430, no. 1, pp. 81–104, Mar. 2013.
- [117] S. Adhikari, A. Banerjee, K. K. Boddy, F.-Y. Cyr-Racine, H. Desmond, C. Dvorkin, B. Jain, F. Kahlhoefer, M. Kaplinghat, A. Nierenberg, A. H. G. Peter, A. Robertson, J. Sakstein, and J. Zavala, “Astrophysical Tests of Dark Matter Self-Interactions,” *arXiv e-prints*, p. arXiv:2207.10638, July 2022.
- [118] K. E. Andrade, J. Fuson, S. Gad-Nasr, D. Kong, Q. Minor, M. G. Roberts, and M. Kaplinghat, “A stringent upper limit on dark matter self-interaction cross-section from cluster strong lensing,” *MNRAS*, vol. 510, no. 1, pp. 54–81, Feb. 2022.
- [119] J. Miralda-Escudé, “A Test of the Collisional Dark Matter Hypothesis from Cluster Lensing,” *ApJ*, vol. 564, no. 1, pp. 60–64, Jan. 2002.
- [120] A. H. G. Peter, M. Rocha, J. S. Bullock, and M. Kaplinghat, “Cosmological simulations with self-interacting dark matter - II. Halo shapes versus observations,” *MNRAS*, vol. 430, no. 1, pp. 105–120, Mar. 2013.
- [121] M. Markevitch, A. H. Gonzalez, D. Clowe, A. Vikhlinin, W. Forman, C. Jones, S. Murray, and W. Tucker, “Direct Constraints on the Dark Matter Self-Interaction Cross Section from the Merging Galaxy Cluster 1E 0657-56,” *ApJ*, vol. 606, no. 2, pp. 819–824, May 2004.
- [122] C. A. Correa, “Constraining velocity-dependent self-interacting dark matter with the Milky Way’s dwarf spheroidal galaxies,” *MNRAS*, vol. 503, no. 1, pp. 920–937, May 2021.
- [123] B. Carr and F. Kühnel, “Primordial Black Holes as Dark Matter: Recent Developments,” *Annual Review of Nuclear and Particle Science*, vol. 70, pp. 355–394, Oct. 2020.
- [124] B. Carr, K. Kohri, Y. Sendouda, and J. Yokoyama, “Constraints on primordial black holes,” *Reports on Progress in Physics*, vol. 84, no. 11, p. 116902, Nov. 2021.

- [125] T. Harada, C.-m. Yoo, K. Kohri, K.-i. Nakao, and S. Jhingan, “Primordial Black Hole Formation in the Matter-dominated Phase of the Universe,” *ApJ*, vol. 833, no. 1, p. 61, Dec. 2016.
- [126] S. Passaglia and M. Sasaki, “Primordial black holes from CDM isocurvature perturbations,” *Phys. Rev. D*, vol. 105, no. 10, p. 103530, May 2022.
- [127] C.-M. Yoo, T. Harada, S. Hirano, H. Okawa, and M. Sasaki, “Primordial black hole formation from massless scalar isocurvature,” *Phys. Rev. D*, vol. 105, no. 10, p. 103538, May 2022.
- [128] B. J. Carr, “The primordial black hole mass spectrum.” *ApJ*, vol. 201, pp. 1–19, Oct. 1975.
- [129] S. W. Hawking, “Particle creation by black holes,” *Communications in Mathematical Physics*, vol. 43, no. 3, pp. 199–220, Aug. 1975.
- [130] G.-W. Yuan, L. Lei, Y.-Z. Wang, B. Wang, Y.-Y. Wang, C. Chen, Z.-Q. Shen, Y.-F. Cai, and Y.-Z. Fan, “Rapidly growing primordial black holes as seeds of the massive high-redshift JWST Galaxies,” *Science China Physics, Mechanics, and Astronomy*, vol. 67, no. 10, p. 109512, Oct. 2024.
- [131] A. Afzal, G. Agazie, A. Anumalapudi, A. M. Archibald, Z. Arzoumanian, P. T. Baker, B. Bécsy, J. J. Blanco-Pillado, L. Blecha, K. K. Boddy, A. Brazier, P. R. Brook, S. Burke-Spolaor, R. Burnette, R. Case, M. Charisi, S. Chatterjee, K. Chatziioannou, B. D. Cheeseboro, S. Chen, T. Cohen, J. M. Cordes, N. J. Cornish, F. Crawford, H. T. Cromartie, K. Crowter, C. J. Cutler, M. E. Decesar, D. Degan, P. B. Demorest, H. Deng, T. Dolch, B. Drachler, R. von Eckardstein, E. C. Ferrara, W. Fiore, E. Fonseca, G. E. Freedman, N. Garver-Daniels, P. A. Gentile, K. A. Gersbach, J. Glaser, D. C. Good, L. Guertin, K. Gültekin, J. S. Hazboun, S. Hourihane, K. Islo, R. J. Jennings, A. D. Johnson, M. L. Jones, A. R. Kaiser, D. L. Kaplan, L. Z. Kelley, M. Kerr, J. S. Key, N. Laal, M. T. Lam, W. G. Lamb, T. J. W. Lazio, V. S. H. Lee, N. Lewandowska, R. R. Lino Dos Santos, T. B. Littenberg, T. Liu, D. R. Lorimer, J. Luo, R. S. Lynch, C.-P. Ma, D. R. Madison, A. McEwen, J. W. McKee, M. A. McLaughlin, N. McMann, B. W. Meyers, P. M. Meyers, C. M. F. Mingarelli, A. Mitridate, J. Nay, P. Natarajan, C. Ng, D. J. Nice, S. K. Ocker, K. D. Olum, T. T. Pennucci, B. B. P. Perera, P. Petrov, N. S. Pol, H. A. Radovan, S. M. Ransom, P. S. Ray, J. D. Romano, S. C. Sardesai, A. Schmiedekamp, C. Schmiedekamp, K. Schmitz, T. Schröder, L. Schult, B. J. Shapiro-Albert, X. Siemens, J. Simon, M. S. Siwek, I. H. Stairs, D. R. Stinebring, K. Stovall, P. Stratmann, J. P. Sun, A. Susobhanan, J. K. Swiggum, J. Taylor, S. R. Taylor, T. Trickle, J. E. Turner, C. Unal, M. Vallisneri, S. Verma, S. J. Vigeland, H. M. Wahl, Q. Wang, C. A. Witt, D. Wright, O. Young, K. M. Zurek, and Nanograv Collaboration, “The NANOGrav 15 yr Data Set: Search for Signals from New Physics,” *ApJ*, vol. 951, no. 1, p. L11, July 2023.
- [132] W. H. Press and P. Schechter, “Formation of Galaxies and Clusters of Galaxies by Self-Similar Gravitational Condensation,” *ApJ*, vol. 187, pp. 425–438, Feb. 1974.
- [133] R. Arya, “Formation of primordial black holes from warm inflation,” *J. Cosmology Astropart. Phys.*, vol. 2020, no. 9, p. 042, Sept. 2020.

- [134] H. Niikura, M. Takada, N. Yasuda, R. H. Lupton, T. Sumi, S. More, T. Kurita, S. Sugiyama, A. More, M. Oguri, and M. Chiba, “Microlensing constraints on primordial black holes with Subaru/HSC Andromeda observations,” *Nature Astronomy*, vol. 3, pp. 524–534, Apr. 2019.
- [135] N. Smyth, S. Profumo, S. English, T. Jeltema, K. McKinnon, and P. Guhathakurta, “Updated constraints on asteroid-mass primordial black holes as dark matter,” *Phys. Rev. D*, vol. 101, no. 6, p. 063005, Mar. 2020.
- [136] M. Oguri, J. M. Diego, N. Kaiser, P. L. Kelly, and T. Broadhurst, “Understanding caustic crossings in giant arcs: Characteristic scales, event rates, and constraints on compact dark matter,” *Phys. Rev. D*, vol. 97, no. 2, p. 023518, Jan. 2018.
- [137] P. Tisserand, L. Le Guillou, C. Afonso, J. N. Albert, J. Andersen, R. Ansari, É. Aubourg, P. Bareyre, J. P. Beaulieu, X. Charlot, C. Coutures, R. Ferlet, P. Fouqué, J. F. Glicenstein, B. Goldman, A. Gould, D. Graff, M. Gros, J. Haissin-ski, C. Hamadache, J. de Kat, T. Lasserre, É. Lesquoy, C. Loup, C. Magneville, J. B. Marquette, É. Maurice, A. Maury, A. Milsztajn, M. Moniez, N. Palanque-Delabrouille, O. Perdureau, Y. R. Rahal, J. Rich, M. Spiro, A. Vidal-Madjar, L. Vigroux, S. Zylberajch, and EROS-2 Collaboration, “Limits on the Macho content of the Galactic Halo from the EROS-2 Survey of the Magellanic Clouds,” *A&A*, vol. 469, no. 2, pp. 387–404, July 2007.
- [138] C. Alcock, R. A. Allsman, D. R. Alves, T. S. Axelrod, A. C. Becker, D. P. Bennett, K. H. Cook, N. Dalal, A. J. Drake, K. C. Freeman, M. Geha, K. Griest, M. J. Lehner, S. L. Marshall, D. Minniti, C. A. Nelson, B. A. Peterson, P. Popowski, M. R. Pratt, P. J. Quinn, C. W. Stubbs, W. Sutherland, A. B. Tomaney, T. Vandehei, and D. L. Welch, “MACHO Project Limits on Black Hole Dark Matter in the 1-30  $M_{solar}$  Range,” *ApJ*, vol. 550, no. 2, pp. L169–L172, Apr. 2001.
- [139] H. Niikura, M. Takada, S. Yokoyama, T. Sumi, and S. Masaki, “Constraints on Earth-mass primordial black holes from OGLE 5-year microlensing events,” *Phys. Rev. D*, vol. 99, no. 8, p. 083503, Apr. 2019.
- [140] P. Mróz, A. Udalski, M. K. Szymański, I. Soszyński, Ł. Wyrzykowski, P. Pietrukowicz, S. Kozłowski, R. Poleski, J. Skowron, D. Skowron, K. Ulaczyk, M. Gromadzki, K. Rybicki, P. Iwanek, M. Wrona, and M. Ratajczak, “No massive black holes in the Milky Way halo,” *Nature*, vol. 632, no. 8026, pp. 749–751, Aug. 2024.
- [141] K. Griest, A. M. Cieplak, and M. J. Lehner, “New Limits on Primordial Black Hole Dark Matter from an Analysis of Kepler Source Microlensing Data,” *Phys. Rev. Lett.*, vol. 111, no. 18, p. 181302, Nov. 2013.
- [142] K. Griest, A. M. Cieplak, and M. J. Lehner, “Experimental Limits on Primordial Black Hole Dark Matter from the First 2 yr of Kepler Data,” *ApJ*, vol. 786, no. 2, p. 158, May 2014.
- [143] M. Zumalacárregui and U. Seljak, “Limits on Stellar-Mass Compact Objects as Dark Matter from Gravitational Lensing of Type Ia Supernovae,” *Phys. Rev. Lett.*, vol. 121, no. 14, p. 141101, Oct. 2018.

- [144] P. N. Wilkinson, D. R. Henstock, I. W. Browne, A. G. Polatidis, P. Augusto, A. C. Readhead, T. J. Pearson, W. Xu, G. B. Taylor, and R. C. Vermeulen, “Limits on the Cosmological Abundance of Supermassive Compact Objects from a Search for Multiple Imaging in Compact Radio Sources,” *Phys. Rev. Lett.*, vol. 86, no. 4, pp. 584–587, Jan. 2001.
- [145] S. M. Koushiappas and A. Loeb, “Dynamics of Dwarf Galaxies Disfavor Stellar-Mass Black Holes as Dark Matter,” *Phys. Rev. Lett.*, vol. 119, no. 4, p. 041102, July 2017.
- [146] T. D. Brandt, “Constraints on MACHO Dark Matter from Compact Stellar Systems in Ultra-faint Dwarf Galaxies,” *ApJ*, vol. 824, no. 2, p. L31, June 2016.
- [147] S. L. Zoutendijk, J. Brinchmann, L. A. Boogaard, M. L. P. Gunawardhana, T.-O. Husser, S. Kamann, A. F. Ramos Padilla, M. M. Roth, R. Bacon, M. den Brok, S. Dreizler, and D. Krajnović, “The MUSE-Faint survey. I. Spectroscopic evidence for a star cluster in Eridanus 2 and constraints on MACHOs as a constituent of dark matter,” *A&A*, vol. 635, p. A107, Mar. 2020.
- [148] M. A. Monroy-Rodríguez and C. Allen, “The End of the MACHO Era, Revisited: New Limits on MACHO Masses from Halo Wide Binaries,” *ApJ*, vol. 790, no. 2, p. 159, Aug. 2014.
- [149] Y. Ali-Haïmoud and M. Kamionkowski, “Cosmic microwave background limits on accreting primordial black holes,” *Phys. Rev. D*, vol. 95, no. 4, p. 043534, Feb. 2017.
- [150] V. Vaskonen and H. Veermäe, “Lower bound on the primordial black hole merger rate,” *Phys. Rev. D*, vol. 101, no. 4, p. 043015, Feb. 2020.
- [151] M. Andrés-Carcasona, A. J. Iovino, V. Vaskonen, H. Veermäe, M. Martínez, O. Pujolàs, and L. M. Mir, “Constraints on primordial black holes from LIGO-Virgo-KAGRA O3 events,” *Phys. Rev. D*, vol. 110, no. 2, p. 023040, July 2024.
- [152] B. J. Carr, K. Kohri, Y. Sendouda, and J. Yokoyama, “New cosmological constraints on primordial black holes,” *Phys. Rev. D*, vol. 81, no. 10, p. 104019, May 2010.
- [153] L. Hui, J. P. Ostriker, S. Tremaine, and E. Witten, “Ultralight scalars as cosmological dark matter,” *Phys. Rev. D*, vol. 95, no. 4, p. 043541, Feb. 2017.
- [154] M. Mina, D. F. Mota, and H. A. Winther, “Solitons in the dark: non-linear structure formation with fuzzy dark matter,” *arXiv e-prints*, p. arXiv:2007.04119, July 2020.
- [155] L. Hui, “Wave Dark Matter,” *ARA&A*, vol. 59, pp. 247–289, Sept. 2021.
- [156] E. G. M. Ferreira, “Ultra-light dark matter,” *A&A Rev.*, vol. 29, no. 1, p. 7, Dec. 2021.
- [157] E. Madelung, “Quantentheorie in hydrodynamischer Form,” *Zeitschrift für Physik*, vol. 40, no. 3-4, pp. 322–326, Mar. 1927.
- [158] T. C. Wallstrom, “Inequivalence between the Schrödinger equation and the Madelung hydrodynamic equations,” *Phys. Rev. A*, vol. 49, no. 3, pp. 1613–1617, Mar. 1994.

- [159] H.-Y. Schive, T. Chiueh, T. Broadhurst, and K.-W. Huang, “Contrasting Galaxy Formation from Quantum Wave Dark Matter,  $\psi$ DM, with  $\Lambda$ CDM, using Planck and Hubble Data,” *ApJ*, vol. 818, no. 1, p. 89, Feb. 2016.
- [160] H.-Y. Schive, T. Chiueh, and T. Broadhurst, “Cosmic structure as the quantum interference of a coherent dark wave,” *Nature Physics*, vol. 10, no. 7, pp. 496–499, July 2014.
- [161] S. May and V. Springel, “Structure formation in large-volume cosmological simulations of fuzzy dark matter: impact of the non-linear dynamics,” *MNRAS*, vol. 506, no. 2, pp. 2603–2618, Sept. 2021.
- [162] H. Y. J. Chan, E. G. M. Ferreira, S. May, K. Hayashi, and M. Chiba, “The diversity of core-halo structure in the fuzzy dark matter model,” *MNRAS*, vol. 511, no. 1, pp. 943–952, Mar. 2022.
- [163] P. Mocz, L. Lancaster, A. Fialkov, F. Becerra, and P.-H. Chavanis, “Schrödinger-Poisson-Vlasov-Poisson correspondence,” *Phys. Rev. D*, vol. 97, no. 8, p. 083519, Apr. 2018.
- [164] H. Kawai, M. Oguri, A. Amruth, T. Broadhurst, and J. Lim, “An Analytic Model for the Subgalactic Matter Power Spectrum in Fuzzy Dark Matter Halos,” *ApJ*, vol. 925, no. 1, p. 61, Jan. 2022.
- [165] N. Dalal, J. Bovy, L. Hui, and X. Li, “Don’t cross the streams: caustics from fuzzy dark matter,” *J. Cosmology Astropart. Phys.*, vol. 2021, no. 3, p. 076, Mar. 2021.
- [166] L. M. Widrow and N. Kaiser, “Using the Schroedinger Equation to Simulate Collisionless Matter,” *ApJ*, vol. 416, p. L71, Oct. 1993.
- [167] M. Dentler, D. J. E. Marsh, R. Hložek, A. Laguë, K. K. Rogers, and D. Grin, “Fuzzy dark matter and the Dark Energy Survey Year 1 data,” *MNRAS*, vol. 515, no. 4, pp. 5646–5664, Oct. 2022.
- [168] A. Laroche, D. Gilman, X. Li, J. Bovy, and X. Du, “Quantum fluctuations masquerade as haloes: bounds on ultra-light dark matter from quadruply imaged quasars,” *MNRAS*, vol. 517, no. 2, pp. 1867–1883, Dec. 2022.
- [169] A. Schneider, “Structure formation with suppressed small-scale perturbations,” *MNRAS*, vol. 451, no. 3, pp. 3117–3130, Aug. 2015.
- [170] B. Diemer, “COLOSSUS: A Python Toolkit for Cosmology, Large-scale Structure, and Dark Matter Halos,” *ApJS*, vol. 239, no. 2, p. 35, Dec. 2018.
- [171] H.-Y. Schive, M.-H. Liao, T.-P. Woo, S.-K. Wong, T. Chiueh, T. Broadhurst, and W. Y. P. Hwang, “Understanding the Core-Halo Relation of Quantum Wave Dark Matter from 3D Simulations,” *Phys. Rev. Lett.*, vol. 113, no. 26, p. 261302, Dec. 2014.
- [172] V. H. Robles, J. S. Bullock, and M. Boylan-Kolchin, “Scalar field dark matter: helping or hurting small-scale problems in cosmology?” *MNRAS*, vol. 483, no. 1, pp. 289–298, Feb. 2019.

- [173] N. Bar, D. Blas, K. Blum, and S. Sibiryakov, “Galactic rotation curves versus ultralight dark matter: Implications of the soliton-host halo relation,” *Phys. Rev. D*, vol. 98, no. 8, p. 083027, Oct. 2018.
- [174] J. L. Zagorac, I. Sands, N. Padmanabhan, and R. Easther, “Schrödinger-Poisson solitons: Perturbation theory,” *Phys. Rev. D*, vol. 105, no. 10, p. 103506, May 2022.
- [175] T. D. Yavetz, X. Li, and L. Hui, “Construction of wave dark matter halos: Numerical algorithm and analytical constraints,” *Phys. Rev. D*, vol. 105, no. 2, p. 023512, Jan. 2022.
- [176] A. Taruya and S. Saga, “Analytical approach to the core-halo structure of fuzzy dark matter,” *Phys. Rev. D*, vol. 106, no. 10, p. 103532, Nov. 2022.
- [177] X. Li, L. Hui, and T. D. Yavetz, “Oscillations and random walk of the soliton core in a fuzzy dark matter halo,” *Phys. Rev. D*, vol. 103, no. 2, p. 023508, Jan. 2021.
- [178] J. Binney and S. Tremaine, *Galactic Dynamics: Second Edition*, 2008.
- [179] E. Kendall, M. Gosenca, and R. Easther, “Aspherical ULDM collapse: variation in the core-halo mass relation,” *MNRAS*, vol. 526, no. 1, pp. 1046–1056, Nov. 2023.
- [180] R. Hlozek, D. Grin, D. J. E. Marsh, and P. G. Ferreira, “A search for ultralight axions using precision cosmological data,” *Phys. Rev. D*, vol. 91, no. 10, p. 103512, May 2015.
- [181] R. Hložek, D. J. E. Marsh, and D. Grin, “Using the full power of the cosmic microwave background to probe axion dark matter,” *MNRAS*, vol. 476, no. 3, pp. 3063–3085, May 2018.
- [182] E. Armengaud, N. Palanque-Delabrouille, C. Yèche, D. J. E. Marsh, and J. Baur, “Constraining the mass of light bosonic dark matter using SDSS Lyman- $\alpha$  forest,” *MNRAS*, vol. 471, no. 4, pp. 4606–4614, Nov. 2017.
- [183] V. Iršič, M. Viel, M. G. Haehnelt, J. S. Bolton, and G. D. Becker, “First Constraints on Fuzzy Dark Matter from Lyman- $\alpha$  Forest Data and Hydrodynamical Simulations,” *Phys. Rev. Lett.*, vol. 119, no. 3, p. 031302, July 2017.
- [184] M. Nori, R. Murgia, V. Iršič, M. Baldi, and M. Viel, “Lyman  $\alpha$  forest and non-linear structure characterization in Fuzzy Dark Matter cosmologies,” *MNRAS*, vol. 482, no. 3, pp. 3227–3243, Jan. 2019.
- [185] K. K. Rogers and H. V. Peiris, “Strong Bound on Canonical Ultralight Axion Dark Matter from the Lyman-Alpha Forest,” *Phys. Rev. Lett.*, vol. 126, no. 7, p. 071302, Feb. 2021.
- [186] A. Lidz and L. Hui, “Implications of a preionization 21-cm absorption signal for fuzzy dark matter,” *Phys. Rev. D*, vol. 98, no. 2, p. 023011, July 2018.
- [187] A. Schneider, “Constraining noncold dark matter models with the global 21-cm signal,” *Phys. Rev. D*, vol. 98, no. 6, p. 063021, Sept. 2018.
- [188] D. Jones, S. Palatnick, R. Chen, A. Beane, and A. Lidz, “Fuzzy Dark Matter and the 21 cm Power Spectrum,” *ApJ*, vol. 913, no. 1, p. 7, May 2021.

- [189] K. Schutz, “Subhalo mass function and ultralight bosonic dark matter,” *Phys. Rev. D*, vol. 101, no. 12, p. 123026, June 2020.
- [190] M. Benito, J. C. Criado, G. Hütsi, M. Raidal, and H. Veermäe, “Implications of Milky Way substructures for the nature of dark matter,” *Phys. Rev. D*, vol. 101, no. 10, p. 103023, May 2020.
- [191] S.-R. Chen, H.-Y. Schive, and T. Chiueh, “Jeans analysis for dwarf spheroidal galaxies in wave dark matter,” *MNRAS*, vol. 468, no. 2, pp. 1338–1348, June 2017.
- [192] A. X. González-Morales, D. J. E. Marsh, J. Peñarrubia, and L. A. Ureña-López, “Unbiased constraints on ultralight axion mass from dwarf spheroidal galaxies,” *MNRAS*, vol. 472, no. 2, pp. 1346–1360, Dec. 2017.
- [193] M. Safarzadeh and D. N. Spergel, “Ultra-light Dark Matter Is Incompatible with the Milky Way’s Dwarf Satellites,” *ApJ*, vol. 893, no. 1, p. 21, Apr. 2020.
- [194] K. Hayashi, E. G. M. Ferreira, and H. Y. J. Chan, “Narrowing the Mass Range of Fuzzy Dark Matter with Ultrafaint Dwarfs,” *ApJ*, vol. 912, no. 1, p. L3, May 2021.
- [195] A. Maleki, S. Baghran, and S. Rahvar, “Constraint on the mass of fuzzy dark matter from the rotation curve of the Milky Way,” *Phys. Rev. D*, vol. 101, no. 10, p. 103504, May 2020.
- [196] L. Lancaster, C. Giovanetti, P. Mocz, Y. Kahn, M. Lisanti, and D. N. Spergel, “Dynamical friction in a Fuzzy Dark Matter universe,” *J. Cosmology Astropart. Phys.*, vol. 2020, no. 1, p. 001, Jan. 2020.
- [197] B. V. Church, P. Mocz, and J. P. Ostriker, “Heating of Milky Way disc stars by dark matter fluctuations in cold dark matter and fuzzy dark matter paradigms,” *MNRAS*, vol. 485, no. 2, pp. 2861–2876, May 2019.
- [198] D. J. E. Marsh and J. C. Niemeyer, “Strong Constraints on Fuzzy Dark Matter from Ultrafaint Dwarf Galaxy Eridanus II,” *Phys. Rev. Lett.*, vol. 123, no. 5, p. 051103, Aug. 2019.
- [199] H. Davoudiasl and P. B. Denton, “Ultralight Boson Dark Matter and Event Horizon Telescope Observations of M 87\*,” *Phys. Rev. Lett.*, vol. 123, no. 2, p. 021102, July 2019.
- [200] M. J. Stott and D. J. E. Marsh, “Black hole spin constraints on the mass spectrum and number of axionlike fields,” *Phys. Rev. D*, vol. 98, no. 8, p. 083006, Oct. 2018.
- [201] O. Masamune, *Gravitational Lensing*, 2025.
- [202] P. Schneider, C. Kochanek, and J. Wambsganss, *Gravitational Lensing: Strong, Weak and Micro*, 2006.
- [203] P. Schneider, “A new formulation of gravitational lens theory, time-delay, and Fermat’s principle,” *A&A*, vol. 143, no. 2, pp. 413–420, Feb. 1985.
- [204] R. S. Ellis, “Gravitational lensing: a unique probe of dark matter and dark energy,” *Philosophical Transactions of the Royal Society of London Series A*, vol. 368, no. 1914, pp. 967–987, Feb. 2010.

- [205] P. Schneider, “The amplification caused by gravitational bending of light,” *A&A*, vol. 140, no. 1, pp. 119–124, Nov. 1984.
- [206] W. L. Burke, “Multiple Gravitational Imaging by Distributed Masses,” *ApJ*, vol. 244, p. L1, Feb. 1981.
- [207] L. Weisenbach, T. Anguita, J. Miralda-Escudé, M. Oguri, P. Saha, and P. L. Schechter, “Microlensing near macro-caustics,” *arXiv e-prints*, p. arXiv:2404.08094, Apr. 2024.
- [208] P. Schneider, J. Ehlers, and E. E. Falco, *Gravitational Lenses*, 1992.
- [209] L. Dai and M. Pascale, “New Approximation of Magnification Statistics for Random Microlensing of Magnified Sources,” *arXiv e-prints*, p. arXiv:2104.12009, Apr. 2021.
- [210] G. P. Lepage, “A new algorithm for adaptive multidimensional integration,” *Journal of Computational Physics*, vol. 27, no. 2, pp. 192–203, May 1978.
- [211] G. P. Lepage, “Adaptive multidimensional integration: VEGAS enhanced,” *Journal of Computational Physics*, vol. 439, p. 110386, Aug. 2021.
- [212] P. L. Kelly, S. A. Rodney, T. Treu, R. J. Foley, G. Brammer, K. B. Schmidt, A. Zitrin, A. Sonnenfeld, L.-G. Strolger, O. Graur, A. V. Filippenko, S. W. Jha, A. G. Riess, M. Bradač, B. J. Weiner, D. Scolnic, M. A. Malkan, A. von der Linden, M. Trenti, J. Hjorth, R. Gavazzi, A. Fontana, J. C. Merten, C. McCully, T. Jones, M. Postman, A. Dressler, B. Patel, S. B. Cenko, M. L. Graham, and B. E. Tucker, “Multiple images of a highly magnified supernova formed by an early-type cluster galaxy lens,” *Science*, vol. 347, no. 6226, pp. 1123–1126, Mar. 2015.
- [213] J. M. Lotz, A. Koekemoer, D. Coe, N. Grogin, P. Capak, J. Mack, J. Anderson, R. Avila, E. A. Barker, D. Borncamp, G. Brammer, M. Durbin, H. Gunning, B. Hilbert, H. Jenkner, H. Khandrika, Z. Levay, R. A. Lucas, J. MacKenty, S. Ogaz, B. Porterfield, N. Reid, M. Robberto, P. Royle, L. J. Smith, L. J. Storrie-Lombardi, B. Sunnquist, J. Surace, D. C. Taylor, R. Williams, J. Bullock, M. Dickinson, S. Finkelstein, P. Natarajan, J. Richard, B. Robertson, J. Tumlinson, A. Zitrin, K. Flanagan, K. Sembach, B. T. Soifer, and M. Mountain, “The Frontier Fields: Survey Design and Initial Results,” *ApJ*, vol. 837, no. 1, p. 97, Mar. 2017.
- [214] S. Refsdal, “On the possibility of determining Hubble’s parameter and the masses of galaxies from the gravitational lens effect,” *MNRAS*, vol. 128, p. 307, Jan. 1964.
- [215] P. L. Kelly, S. Rodney, T. Treu, S. Birrer, V. Bonvin, L. Dessart, R. J. Foley, A. V. Filippenko, D. Gilman, S. Jha, J. Hjorth, K. Mandel, M. Millon, J. Pierel, S. Thorp, A. Zitrin, T. Broadhurst, W. Chen, J. M. Diego, A. Dressler, O. Graur, M. Jauzac, M. A. Malkan, C. McCully, M. Oguri, M. Postman, K. B. Schmidt, K. Sharon, B. E. Tucker, A. von der Linden, and J. Wambsganss, “The Magnificent Five Images of Supernova Refsdal: Time Delay and Magnification Measurements,” *ApJ*, vol. 948, no. 2, p. 93, May 2023.
- [216] B. Welch, D. Coe, J. M. Diego, A. Zitrin, E. Zackrisson, P. Dimauro, Y. Jiménez-Teja, P. Kelly, G. Mahler, M. Oguri, F. X. Timmes, R. Windhorst, M. Florian,

- S. E. de Mink, R. J. Avila, J. Anderson, L. Bradley, K. Sharon, A. Vikaeus, S. McCandliss, M. Bradač, J. Rigby, B. Frye, S. Toft, V. Strait, M. Trenti, S. Sharma, F. Andrade-Santos, and T. Broadhurst, “A highly magnified star at redshift 6.2,” *Nature*, vol. 603, no. 7903, pp. 815–818, Mar. 2022.
- [217] Y. Fudamoto, F. Sun, J. M. Diego, L. Dai, M. Oguri, A. Zitrin, E. Zackrisson, M. Jauzac, D. J. Lagattuta, E. Egami, E. Iani, R. A. Windhorst, K. T. Abe, F. E. Bauer, F. Bian, R. Bhatawdekar, T. J. Broadhurst, Z. Cai, C.-C. Chen, W. Chen, S. H. Cohen, C. J. Conselice, D. Espada, N. Foo, B. L. Frye, S. Fujimoto, L. J. Furtak, M. Golubchik, T. Y.-Y. Hsiao, J.-B. Jolly, H. Kawai, P. L. Kelly, A. M. Koekemoer, K. Kohno, V. Kokorev, M. Li, Z. Li, X. Lin, G. E. Magdis, A. K. Meena, A. Nabizadeh, J. Richard, C. L. Steinhardt, Y. Wu, Y. Zhu, and S. Zou, “JWST Discovery of 40+ Microlensed Stars in a Magnified Galaxy, the “Dragon” behind Abell 370,” *arXiv e-prints*, p. arXiv:2404.08045, Apr. 2024.
- [218] L. Dai, T. Venumadhav, A. A. Kaurov, and J. Miralda-Escud, “Probing Dark Matter Subhalos in Galaxy Clusters Using Highly Magnified Stars,” *ApJ*, vol. 867, no. 1, p. 24, Nov. 2018.
- [219] L. L. R. Williams, P. L. Kelly, T. Treu, A. Amruth, J. M. Diego, S. Kei Li, A. K. Meena, A. Zitrin, and T. J. Broadhurst, “Flashlights: Properties of Highly Magnified Images Near Cluster Critical Curves in the Presence of Dark Matter Subhalos,” *arXiv e-prints*, p. arXiv:2304.06064, Apr. 2023.
- [220] T. Venumadhav, L. Dai, and J. Miralda-Escudé, “Microlensing of Extremely Magnified Stars near Caustics of Galaxy Clusters,” *ApJ*, vol. 850, no. 1, p. 49, Nov. 2017.
- [221] J. M. Diego, N. Kaiser, T. Broadhurst, P. L. Kelly, S. Rodney, T. Morishita, M. Oguri, T. W. Ross, A. Zitrin, M. Jauzac, J. Richard, L. Williams, J. Vega-Ferrero, B. Frye, and A. V. Filippenko, “Dark Matter under the Microscope: Constraining Compact Dark Matter with Caustic Crossing Events,” *ApJ*, vol. 857, no. 1, p. 25, Apr. 2018.
- [222] M. Oguri, “The Mass Distribution of SDSS J1004+4112 Revisited,” *PASJ*, vol. 62, p. 1017, Aug. 2010.
- [223] L. Dai and J. Miralda-Escudé, “Gravitational Lensing Signatures of Axion Dark Matter Minihalos in Highly Magnified Stars,” *AJ*, vol. 159, no. 2, p. 49, Feb. 2020.
- [224] N. Katz, S. Balbus, and B. Paczynski, “Random Scattering Approach to Gravitational Microlensing,” *ApJ*, vol. 306, p. 2, July 1986.
- [225] G. Vernardos, C. J. Fluke, N. F. Bate, and D. Croton, “GERLUMPH Data Release 1: High-resolution Cosmological Microlensing Magnification Maps and eResearch Tools,” *ApJS*, vol. 211, no. 1, p. 16, Mar. 2014.
- [226] J. M. Palencia, J. M. Diego, B. J. Kavanagh, and J. Martínez-Arrizabalaga, “Statistics of magnification for extremely lensed high redshift stars,” *A&A*, vol. 687, p. A81, July 2024.

- [227] J. Wambsganss, “Gravitational lensing: numerical simulations with a hierarchical tree code.” *Journal of Computational and Applied Mathematics*, vol. 109, no. 1, pp. 353–372, Sept. 1999.
- [228] T. Morishita, L. E. Abramson, T. Treu, K. B. Schmidt, B. Vulcani, and X. Wang, “Characterizing Intracluster Light in the Hubble Frontier Fields,” *ApJ*, vol. 846, no. 2, p. 139, Sept. 2017.
- [229] G. Chabrier, “The Galactic Disk Mass Function: Reconciliation of the Hubble Space Telescope and Nearby Determinations,” *ApJ*, vol. 586, no. 2, pp. L133–L136, Apr. 2003.
- [230] —, “Galactic Stellar and Substellar Initial Mass Function,” *PASP*, vol. 115, no. 809, pp. 763–795, July 2003.
- [231] E. E. Salpeter, “The Luminosity Function and Stellar Evolution.” *ApJ*, vol. 121, p. 161, Jan. 1955.
- [232] R. Kawamata, M. Oguri, M. Ishigaki, K. Shimasaku, and M. Ouchi, “Precise Strong Lensing Mass Modeling of Four Hubble Frontier Field Clusters and a Sample of Magnified High-redshift Galaxies,” *ApJ*, vol. 819, no. 2, p. 114, Mar. 2016.
- [233] D. C. Morton and T. F. Adams, “Effective Temperatures and Bolometric Corrections of Early-Type Stars,” *ApJ*, vol. 151, p. 611, Feb. 1968.
- [234] M. J. Pecaut and E. E. Mamajek, “Intrinsic Colors, Temperatures, and Bolometric Corrections of Pre-main-sequence Stars,” *ApJS*, vol. 208, no. 1, p. 9, Sept. 2013.
- [235] F. Castelli and R. L. Kurucz, “New Grids of ATLAS9 Model Atmospheres,” in *Modelling of Stellar Atmospheres*, ser. IAU Symposium, N. Piskunov, W. W. Weiss, and D. F. Gray, Eds., vol. 210, Jan. 2003, p. A20.
- [236] N. Golovich, W. A. Dawson, D. Wittman, G. Ogle, R. van Weeren, and A. Bonafede, “MC<sup>2</sup>: Dynamical Analysis of the Merging Galaxy Cluster MACS J1149.5+2223,” *ApJ*, vol. 831, no. 1, p. 110, Nov. 2016.
- [237] M. Spera, M. Mapelli, and A. Bressan, “The mass spectrum of compact remnants from the PARSEC stellar evolution tracks,” *MNRAS*, vol. 451, no. 4, pp. 4086–4103, Aug. 2015.
- [238] S. Koyama, Y. Koyama, T. Yamashita, M. Hayashi, H. Matsuhara, T. Nakagawa, S. V. Namiki, T. L. Suzuki, N. Fukagawa, T. Kodama, L. Lin, K. Morokuma-Matsui, R. Shimakawa, and I. Tanaka, “Do Galaxy Morphologies Really Affect the Efficiency of Star Formation During the Phase of Galaxy Transition?” *ApJ*, vol. 874, no. 2, p. 142, Apr. 2019.
- [239] C. Vall Müller and J. Miralda-Escudé, “Limits on Dark Matter Compact Objects implied by Supermagnified Stars in Lensing Clusters,” *arXiv e-prints*, p. arXiv:2403.16989, Mar. 2024.
- [240] S. E. Woosley, A. Heger, and T. A. Weaver, “The evolution and explosion of massive stars,” *Reviews of Modern Physics*, vol. 74, no. 4, pp. 1015–1071, Nov. 2002.

- [241] C. L. Fryer, K. Belczynski, G. Wiktorowicz, M. Dominik, V. Kalogera, and D. E. Holz, “Compact Remnant Mass Function: Dependence on the Explosion Mechanism and Metallicity,” *ApJ*, vol. 749, no. 1, p. 91, Apr. 2012.
- [242] A. M. Green and B. J. Kavanagh, “Primordial black holes as a dark matter candidate,” *Journal of Physics G Nuclear Physics*, vol. 48, no. 4, p. 043001, Apr. 2021.
- [243] S. Mao and P. Schneider, “Evidence for substructure in lens galaxies?” *MNRAS*, vol. 295, no. 3, pp. 587–594, Apr. 1998.
- [244] R. B. Metcalf and P. Madau, “Compound Gravitational Lensing as a Probe of Dark Matter Substructure within Galaxy Halos,” *ApJ*, vol. 563, no. 1, pp. 9–20, Dec. 2001.
- [245] M. Chiba, “Probing Dark Matter Substructure in Lens Galaxies,” *ApJ*, vol. 565, no. 1, pp. 17–23, Jan. 2002.
- [246] R. B. Metcalf and H. Zhao, “Flux Ratios as a Probe of Dark Substructures in Quadruple-Image Gravitational Lenses,” *ApJ*, vol. 567, no. 1, pp. L5–L8, Mar. 2002.
- [247] N. Dalal and C. S. Kochanek, “Direct Detection of Cold Dark Matter Substructure,” *ApJ*, vol. 572, no. 1, pp. 25–33, June 2002.
- [248] M. Bradač, P. Schneider, M. Steinmetz, M. Lombardi, L. J. King, and R. Porcas, “B1422+231: The influence of mass substructure on strong lensing,” *A&A*, vol. 388, pp. 373–382, June 2002.
- [249] R. B. Metcalf and A. Amara, “Small-scale structures of dark matter and flux anomalies in quasar gravitational lenses,” *MNRAS*, vol. 419, no. 4, pp. 3414–3425, Feb. 2012.
- [250] A. M. Nierenberg, T. Treu, G. Brammer, A. H. G. Peter, C. D. Fassnacht, C. R. Keeton, C. S. Kochanek, K. B. Schmidt, D. Sluse, and S. A. Wright, “Probing dark matter substructure in the gravitational lens HE 0435-1223 with the WFC3 grism,” *MNRAS*, vol. 471, no. 2, pp. 2224–2236, Oct. 2017.
- [251] D. Gilman, S. Birrer, A. Nierenberg, T. Treu, X. Du, and A. Benson, “Warm dark matter chills out: constraints on the halo mass function and the free-streaming length of dark matter with eight quadruple-image strong gravitational lenses,” *MNRAS*, vol. 491, no. 4, pp. 6077–6101, Feb. 2020.
- [252] J. W. Hsueh, W. Enzi, S. Vegetti, M. W. Auger, C. D. Fassnacht, G. Despali, L. V. E. Koopmans, and J. P. McKean, “SHARP - VII. New constraints on the dark matter free-streaming properties and substructure abundance from gravitationally lensed quasars,” *MNRAS*, vol. 492, no. 2, pp. 3047–3059, Feb. 2020.
- [253] S. Vegetti, L. V. E. Koopmans, A. Bolton, T. Treu, and R. Gavazzi, “Detection of a dark substructure through gravitational imaging,” *MNRAS*, vol. 408, no. 4, pp. 1969–1981, Nov. 2010.

- [254] S. Vegetti, D. J. Lagattuta, J. P. McKean, M. W. Auger, C. D. Fassnacht, and L. V. E. Koopmans, “Gravitational detection of a low-mass dark satellite galaxy at cosmological distance,” *Nature*, vol. 481, no. 7381, pp. 341–343, Jan. 2012.
- [255] Y. Hezaveh, N. Dalal, G. Holder, M. Kuhlen, D. Marrone, N. Murray, and J. Vieira, “Dark Matter Substructure Detection Using Spatially Resolved Spectroscopy of Lensed Dusty Galaxies,” *ApJ*, vol. 767, no. 1, p. 9, Apr. 2013.
- [256] Y. Hezaveh, N. Dalal, G. Holder, T. Kisner, M. Kuhlen, and L. Perreault Levasseur, “Measuring the power spectrum of dark matter substructure using strong gravitational lensing,” *J. Cosmology Astropart. Phys.*, vol. 2016, no. 11, p. 048, Nov. 2016.
- [257] S. Asadi, E. Zackrisson, and E. Freeland, “Probing cold dark matter subhaloes with simulated ALMA observations of macrolensed sub-mm galaxies,” *MNRAS*, vol. 472, no. 1, pp. 129–140, Nov. 2017.
- [258] K. Umetsu, E. Medezinski, M. Nonino, J. Merten, M. Postman, M. Meneghetti, M. Donahue, N. Czakon, A. Molino, S. Seitz, D. Gruen, D. Lemze, I. Balestra, N. Benítez, A. Biviano, T. Broadhurst, H. Ford, C. Grillo, A. Koekemoer, P. Melchior, A. Mercurio, J. Moustakas, P. Rosati, and A. Zitrin, “CLASH: Weak-lensing Shear-and-magnification Analysis of 20 Galaxy Clusters,” *ApJ*, vol. 795, no. 2, p. 163, Nov. 2014.
- [259] P. Behroozi, R. H. Wechsler, A. P. Hearin, and C. Conroy, “UNIVERSEMACHINE: The correlation between galaxy growth and dark matter halo assembly from  $z = 0-10$ ,” *MNRAS*, vol. 488, no. 3, pp. 3143–3194, Sept. 2019.
- [260] A. Cooray and R. Sheth, “Halo models of large scale structure,” *Phys. Rep.*, vol. 372, no. 1, pp. 1–129, Dec. 2002.
- [261] R. Scoccimarro, R. K. Sheth, L. Hui, and B. Jain, “How Many Galaxies Fit in a Halo? Constraints on Galaxy Formation Efficiency from Spatial Clustering,” *ApJ*, vol. 546, no. 1, pp. 20–34, Jan. 2001.
- [262] S. Hofmann, D. J. Schwarz, and H. Stöcker, “Damping scales of neutralino cold dark matter,” *Phys. Rev. D*, vol. 64, no. 8, p. 083507, Oct. 2001.
- [263] A. M. Green, S. Hofmann, and D. J. Schwarz, “The power spectrum of SUSY-CDM on subgalactic scales,” *MNRAS*, vol. 353, no. 3, pp. L23–L27, Sept. 2004.
- [264] S. Profumo, K. Sigurdson, and M. Kamionkowski, “What Mass Are the Smallest Protohalos?” *Phys. Rev. Lett.*, vol. 97, no. 3, p. 031301, July 2006.
- [265] R. Diamanti, M. E. C. Catalan, and S. Ando, “Dark matter protohalos in a nine parameter MSSM and implications for direct and indirect detection,” *Phys. Rev. D*, vol. 92, no. 6, p. 065029, Sept. 2015.
- [266] M. Meneghetti, G. Davoli, P. Bergamini, P. Rosati, P. Natarajan, C. Giocoli, G. B. Caminha, R. B. Metcalf, E. Rasia, S. Borgani, F. Calura, C. Grillo, A. Mercurio, and E. Vanzella, “An excess of small-scale gravitational lenses observed in galaxy clusters,” *Science*, vol. 369, no. 6509, pp. 1347–1351, Sept. 2020.

- [267] M. Meneghetti, A. Ragagnin, S. Borgani, F. Calura, G. Despali, C. Giocoli, G. L. Granato, C. Grillo, L. Moscardini, E. Rasia, P. Rosati, G. Angora, L. Bassini, P. Bergamini, G. B. Caminha, G. Granata, A. Mercurio, R. B. Metcalf, P. Natarajan, M. Nonino, G. V. Pignataro, C. Ragone-Figueroa, E. Vanzella, A. Acebron, K. Dolag, G. Murante, G. Taffoni, L. Tornatore, L. Tortorelli, and M. Valentini, “The probability of galaxy-galaxy strong lensing events in hydrodynamical simulations of galaxy clusters,” *A&A*, vol. 668, p. A188, Dec. 2022.
- [268] M. Meneghetti, W. Cui, E. Rasia, G. Yepes, A. Acebron, G. Angora, P. Bergamini, S. Borgani, F. Calura, G. Despali, C. Giocoli, G. Granata, C. Grillo, A. Knebe, A. V. Macciò, A. Mercurio, L. Moscardini, P. Natarajan, A. Ragagnin, P. Rosati, and E. Vanzella, “A persistent excess of galaxy-galaxy strong lensing observed in galaxy clusters,” *A&A*, vol. 678, p. L2, Oct. 2023.
- [269] Y. M. Bahé, “Strongly lensed cluster substructures are not in tension with  $\Lambda$ CDM,” *MNRAS*, vol. 505, no. 1, pp. 1458–1463, July 2021.
- [270] A. Robertson, “The galaxy-galaxy strong lensing cross-sections of simulated  $\Lambda$ CDM galaxy clusters,” *MNRAS*, vol. 504, no. 1, pp. L7–L11, June 2021.
- [271] A. Ragagnin, M. Meneghetti, L. Bassini, C. Ragone-Figueroa, G. L. Granato, G. Despali, C. Giocoli, G. Granata, L. Moscardini, P. Bergamini, E. Rasia, M. Valentini, S. Borgani, F. Calura, K. Dolag, C. Grillo, A. Mercurio, G. Murante, P. Natarajan, P. Rosati, G. Taffoni, L. Tornatore, and L. Tortorelli, “Galaxies in the central regions of simulated galaxy clusters,” *A&A*, vol. 665, p. A16, Sept. 2022.
- [272] Y. M. Tokayer, I. Dutra, P. Natarajan, G. Mahler, M. Jauzac, and M. Meneghetti, “The galaxy-galaxy strong lensing cross section and the internal distribution of matter in  $\Lambda$ CDM substructure,” *arXiv e-prints*, p. arXiv:2404.16951, Apr. 2024.
- [273] I. Dutra, P. Natarajan, and D. Gilman, “Self-Interacting Dark Matter, Core Collapse and the Galaxy-Galaxy Strong Lensing Discrepancy,” *arXiv e-prints*, p. arXiv:2406.17024, June 2024.
- [274] A. Ragagnin, M. Meneghetti, F. Calura, G. Despali, K. Dolag, M. S. Fischer, C. Giocoli, and L. Moscardini, “Dianoga SIDM: Galaxy cluster self-interacting dark matter simulations,” *A&A*, vol. 687, p. A270, July 2024.
- [275] M. Postman, D. Coe, N. Benítez, L. Bradley, T. Broadhurst, M. Donahue, H. Ford, O. Graur, G. Graves, S. Jouvel, A. Koekemoer, D. Lemze, E. Medezinski, A. Molino, L. Moustakas, S. Ogaz, A. Riess, S. Rodney, P. Rosati, K. Umetsu, W. Zheng, A. Zitrin, M. Bartelmann, R. Bouwens, N. Czakon, S. Golwala, O. Host, L. Infante, S. Jha, Y. Jimenez-Teja, D. Kelson, O. Lahav, R. Lazkoz, D. Maoz, C. McCully, P. Melchior, M. Meneghetti, J. Merten, J. Moustakas, M. Nonino, B. Patel, E. Regös, J. Sayers, S. Seitz, and A. Van der Wel, “The Cluster Lensing and Supernova Survey with Hubble: An Overview,” *ApJS*, vol. 199, no. 2, p. 25, Apr. 2012.
- [276] G. B. Caminha, P. Rosati, C. Grillo, G. Rosani, K. I. Caputi, M. Meneghetti, A. Mercurio, I. Balestra, P. Bergamini, A. Biviano, M. Nonino, K. Umetsu, E. Vanzella, M. Annunziatella, T. Broadhurst, C. Delgado-Correal, R. Demarco,

- A. M. Koekemoer, M. Lombardi, C. Maier, M. Verdugo, and A. Zitrin, “Strong lensing models of eight CLASH clusters from extensive spectroscopy: Accurate total mass reconstructions in the cores,” *A&A*, vol. 632, p. A36, Dec. 2019.
- [277] C. R. Keeton, “Cold Dark Matter and Strong Gravitational Lensing: Concord or Conflict?” *ApJ*, vol. 561, no. 1, pp. 46–60, Nov. 2001.
- [278] C. Giocoli, M. Meneghetti, M. Bartelmann, L. Moscardini, and M. Boldrin, “MOKA: a new tool for strong lensing studies,” *MNRAS*, vol. 421, no. 4, pp. 3343–3355, Apr. 2012.
- [279] G. R. Blumenthal, S. M. Faber, R. Flores, and J. R. Primack, “Contraction of Dark Matter Galactic Halos Due to Baryonic Infall,” *ApJ*, vol. 301, p. 27, Feb. 1986.
- [280] J. Veltmaat, B. Schwabe, and J. C. Niemeyer, “Baryon-driven growth of solitonic cores in fuzzy dark matter halos,” *Phys. Rev. D*, vol. 101, no. 8, p. 083518, Apr. 2020.

